Universität Stuttgart
Institut für Physikalische Chemie

Dissertation

Chemical Design and Probing of Novel Molecular 2-Qubit Systems

Dennis Schäfter

2023

Chemical Design and Probing of Novel Molecular 2-Qubit Systems

Von der
Fakultät Chemie der Universität Stuttgart
zur Erlangung der Würde eines
Doktors der Naturwissenschaften (Dr. rer. nat.)
genehmigte Abhandlung

Vorgelegt von

Dennis Dominik Schäfter

aus Heilbronn-Neckargartach

Hauptberichter: Prof. Dr. Joris van Slageren
Mitberichter: Prof. Dr. Biprajit Sarkar
Prüfungsvorsitzender: Prof. Dr. Andreas Köhn

Tag der mündlichen Prüfung:
14. Dezember 2023

Ph.D. Thesis:

Chemical Design and Probing of Novel Molecular 2-Qubit Systems

Doktorarbeit:

Chemisches Design und Untersuchung
von Neuartigen Molekularen Zweiquantenbitsystemen

University of Stuttgart, Germany

October 2017 – November 2021

I hereby certify that the dissertation entitled "Chemical Design and Probing of Novel Molecular 2-Qubit Systems" is entirely my own work except where otherwise indicated. Passages and ideas from other sources have been clearly indicated.

_____   _____

Date   Signature

"Don't let anyone think for you. Most people can barely think for themselves."

Evan Hadfield, Rare Earth

ACKNOWLEDGEMENT

Mama für Oma & T

TABLE OF CONTENTS

ABBREVIATIONS AND SYMBOLS

Abbreviations

AI.	Artificial intelligence
approx.	approximately
AWG	Arbitrary waveform generator
DEER	Double electron-electron resonance
DQC	Double quantum coherence
DQF	Double quantum filter
EPR	Electron paramagnetic resonance
EI	Electron impact ionization
EWG	Electron withdrawal group
exTTF	Extended tetrathiafulvalene
ILCT	Interligand charge transfer
LMCT	Ligand to metal charge transfer
MLCT	Metal to ligand charge transfer
MOF	Metal organic framework
PELDOR	Pulsed electron double resonance, see DEER
PTM	Perchlorinated trityl
QC	Quantum computer / quantum computing
QIP	Quantum information processing
Qubit	Quantum bit
Qugate	Quantum gate
RSA	Rivest-Shamir-Adleman (cryptography)
Rxn	Reaction
SEC	Spectroelectrochemical
SIFTER	Single-frequency technique for refocusing dipolar couplings
SOC	Spin-orbit coupling
TBDMS	Bis(tert-butyldimethylsilyl)
TD-DFT	Time dependent DFT
TTF	Tetrathiafulvalene

tzvp	triple-ζ valence polarized
UFF	Universal force field

Symbols

$\boldsymbol{a_{iso}}$	isotropic part of the hyperfine coupling tensor ($= a_{iso}\boldsymbol{I}$)
$\boldsymbol{A}$	hyperfine coupling tensor
A_f	factor for the fast component in exponential fits
A_s	factor for the slow component in exponential fits
$\boldsymbol{B}$	magnetic field
g	g-factor
$\boldsymbol{g}$	g-tensor
$\hat{\boldsymbol{I}}$	nuclear spin operator
$\boldsymbol{I}$	unitary matrix
I	total nuclear spin quantum number, intensity
M_0	magnetization
m_s	magnetic electron spin quantum number
$N_{\text{upper}}/N_{\text{lower}}$	Boltzmann distribution
S	spin
$\hat{\boldsymbol{S}}$	spin operator
$\boldsymbol{T}$	dipolar or anisotropic part of the hyperfine coupling tensor
T	temperature, electron nuclear coupling constant
T_1	longitudinal relaxation time
T_2	transversal relaxation time
T_{m}	phase memory time
x	stretch factor
α, β	spin state
γ	gyromagnetic ratio
$\tilde{\nu}$	wave numbers
σ	spin density operator
τ	time delay
Ω	Larmor frequency

ZUSAMMENFASSUNG

Molekulare Quantenbits haben in den letzten Jahrzehnten viel Aufmerksamkeit auf sich gezogen. Dabei wurden vor allem molekulare Einquantenbitsysteme untersucht. Um molekulare Quantencomputer zu realisieren, werden neben diesen Systemen auch entsprechende Zweiquantenbitsysteme benötigt, die zusammen ein vollständiges Set von Quantengattern für den Einsatz in Quantenoperationen bilden. Diese Arbeit beschäftigt sich daher mit der Herstellung und Untersuchung von Zweiquantenbitsystemen, die zusammen mit den bekannten Einquantenbitsystemen als Prototypen für den Einsatz in molekularen Quantencomputern dienen können.

Das Ziel des ersten und zweiten Kapitels war dabei die Planung, Entwicklung und Synthese eines neuartigen modularen Zweiquantenbitsystems und dessen detaillierte spektroskopische Analyse. Dazu wurden zunächst Prototypen, basierend auf den bisher bekannten Spitzenreitern unter den molekularen Einquantenbitsystemen, bestehend aus dem kernspinfreiem Dimercaptotrithion-Liganden **dmit** sowie verschiedenen starren Verbindungseinheiten, entworfen. Die daraus resultierenden theoretischen Verbindungen wurden dann hinsichtlich geeigneter Geometrie und passender Abstände der einzelnen Quantenbits evaluiert und schließlich retrosynthetisch auf ihre Realisierbarkeit hin untersucht. Zwei Archetypen von Liganden wurden dabei als besonders vielversprechend angesehen: Zum einen Liganden mit Adamantan als Platzhalter, zum anderen Liganden mit chinoiden Platzhaltern. Nach mehrstufiger Synthese konnten einige dieser Archetypen dann in Form von **dmdt₂Ad** auf Adamantylbasis, **dmdt₂Anthra** und **dmdt₂Dptba** auf Anthrachinonbasis und **dmdt₂Penta** auf Pentachinonbasis erhalten werden. Die Komplexierung dieser zu Zweiquantenbitsystemen war dabei ursprünglich mit Vanadium(IV) geplant, da das Vanadyl-dmit-System **V(dbddto)₃²⁻** derzeit der Spitzenreiter unter den Einzelquantenbitsystemen ist. Es zeigte sich jedoch, dass das Komplexverhalten des modifizierten Dithiols stark von dem des regulären **dmit**-Liganden abweicht, so dass eine Komplexierung mit Vanadium(IV) nicht erfolgreich war. Von allen Liganden konnten jedoch diamagnetische Titan(IV)-Dimere erhalten werden, die anschließend spektroskopisch charakterisiert wurden. Neben den Standardcharakterisierungsmethoden wie Kernspinresonanzspektroskopie (NMR) und Massenspektrometrie wurde das Redoxverhalten mittels Cyclovoltammetrie und UV/Vis-Spektroelektrochemie untersucht.

Mit den daraus gewonnenen Informationen konnten die Verbindungen anschließend elektrochemisch in die reduzierten Titan(III)-Dimer umgewandelt werden und mittels X-Band Elektronenspinresonanzspektroskopie (ESR) untersucht werden. Letztendlich war es dadurch auch möglich, die hergestellten Dimere ebenfalls durch chemische Reduktion zu erhalten und **dmdt₂Anthra[Ti(III)Cp₂]** mittels gepulster Q-Band ESR Spektroskopie auf seine Kohärenzeigenschaften hin zu untersuchen. Die dabei gefundenen Phasengedächtniszeiten bei 7 K in THF betrugen 3.0(3) µs und konnten durch Verwendung von deuteriertem THF als Lösungsmittel auf 5.2(6) µs erhöht werden. Des Weiteren verhalten sich diese bis um 40 K stabil. Diese Zeiten sind im oberen Bereich der bekannten Titan(III)-Qubits und ebenso im oberen Bereich unter den bekannten Zweiquantenbitsystemen anzusiedeln.

Im dritten Kapitel wurde eine Familie von drei PTM-Radikalen – zwei Monomere (**PTM-mono**, **PTM-tail**) und ein Dimer (**PTM-di**) – mittels gepulster Q-Band ESR-Spektroskopie untersucht. Alle drei Radikale zeigten ein sehr ähnliches Verhalten, einschließlich extrem langer Spin-Gitter-Relaxationszeiten um 1 s bei 7 K. Die Phasengedächtniszeiten wurden bei tiefen Temperaturen von 7 K auf über 100 µs für die beiden Monomere und knapp 80 µs für das Dimer bestimmt. Diese Zeiten sind einige der besten publizierten Phasengedächtniszeiten, nur übertroffen von den bereits erwähnten **V(dbddto)₃²⁻** und **N@C₆₀**. Zusätzlich zu diesen Ergebnissen wurde das Dimer **PTM-di** mittels dipolarer ESR-Spektroskopie untersucht. Mit Hilfe von Double Electron-Electron Resonance (DEER), Single-Frequency Technique for Refocusing Dipolar Couplings (SIFTER) und Double Quanum Coherence (DQC) konnte festgestellt werden, dass die beiden Qubits 2.4(1) nm voneinander entfernt sind. Dabei zeigten SIFTER und DQC jedoch deutlich besserer experimentelle Resultate als DEER – geschuldet der sehr schmalen Resonanzlinie von wenigen Millitesla und der experimentellen Technik des DEER-Experiments. Obwohl der Abstand zwischen den einzelnen Qubits für Gatteroperationen bei ~1.6 nm liegen sollte, sind die erhaltenen Ergebnisse vielversprechend und zeigen die individuelle Adressierbarkeit der beiden Spins.

Das letzte Kapitel befasst sich mit dem Einfluss der Spin-Bahn-Kopplung auf die Kohärenzeigenschaften von porphyrinbasierten Zweiquantenbitsystemen innerhalb der Gruppe 11 – Kupfer, Silber und Gold. Die Porphyrine wurden zum Teil rotationsflexibel (**mmPorph[M]**) und zum Teil starr verbunden (**fsPorph[M]**). Bei fünf der sechs

Verbindungen konnte Quantenkohärenz beobachtet werden, darunter erstmals in der Literatur beschrieben auch für Gold(II) in Form von **mmPorph[Au]**. Interessanterweise zeigen alle Verbindungen dabei über sehr ähnliche Phasengedächtniszeiten von etwa 2 μs bei tiefen Temperaturen von 5 K – 30 K, weitgehend unabhängig vom Zentralion der einzelnen Qubits. Auch für die Goldverbindung **mmPorph[Au]** konnte noch eine Phasengedächtniszeit von ca. 1.7 μs bei tiefen Temperaturen von 5 K bis 15 K gemessen werden.

Eine große Überraschung stellen jedoch die gemessenen Spin-Gitter-Relaxationszeiten dar. Diese sollten stark abnehmen, da Schweratome durch ihre Spin-Bahn-Kopplung stark zur Dekohärenz beitragen. So wird erwartet, dass die Relaxationszeit von Kupfer nach Gold abnimmt. Dies konnte jedoch experimentell nicht bestätigt werden: Die untersuchten Silberporphyrine **monoPorph[Ag]** und **mmPorph[Ag]** zeigen eine Verdopplung der Kohärenzzeiten im Vergleich zu ihrem leichteren Kupferanalogon. Obwohl ein ähnliches Ergebnis für ein verwandtes Silberporphyrin bei 1996 von Eaton und Eaton beobachtet wurde, konnte eine Erklärung für diese Resultate ebenso nicht gefunden werden.

SUMMARY

Molecular quantum bits have attracted much attention in the last decades. In particular, molecular one-quantum bit systems have been studied. In order to realize molecular quantum computers, in addition to these systems, corresponding two-quantum bit systems are also needed, which together form a complete set of quantum gates for use in quantum operations. This work is therefore concerned with the synthesis and investigation of two-quantum bit systems, which together with the known one-quantum bit systems can serve as prototypes for use in molecular quantum computers.

In this regard, the goal of the first and second chapters was to design, develop, and synthesize a novel modular two-quantum bit system and to analyze it in detail spectroscopically. To this end, prototypes were first designed based on the previously known frontrunners among molecular single-quantum bit systems, consisting of the nuclear spin-free dimercaptotrithione ligand **dmit** and various rigid linking units. The resulting compounds were then evaluated in terms of appropriate geometry and suitable spacing of the individual quantum bits, and finally retrosynthetically investigated for their producibility. Two archetypes of ligands were found to be particularly promising: First, ligands with adamantane as a spacer, and second, ligands with quinoid spacers. After multistep synthesis, some of these archetypes were then obtained in the form of adamantyl-based **dmdt$_2$Ad**, anthraquinone-based **dmdt$_2$Anthra** and **dmdt$_2$Dptba**, and pentachinone-based **dmdt$_2$Penta**. The complexation of these to two-quantum bit systems was originally planned to incorporate vanadium(IV), since the vanadyl-dmit system **V(dbddto)$_3$$^{2-\cdot}$** is one of the frontrunners among the single-quantum bit systems at this time. However, the complexation behavior of the modified dithiol was found to be very different from that of the regular **dmit** ligand, so complexation with vanadium(IV) was not successful. However, diamagnetic titanium(IV) dimers could be obtained from all ligands, which were subsequently characterized spectroscopically. In addition to standard characterization methods such as nuclear spin resonance (NMR) spectroscopy and mass spectrometry, the redox behavior was investigated by cyclic voltammetry and UV/Vis spectroelectrochemistry. With the information obtained from these studies, the compounds could then be converted electrochemically into the reduced titanium(III) dimers and studied by X-band electron paramagnetic resonance (EPR) spectroscopy. Ultimately, this also allowed the prepared

dimers to also be obtained by chemical reduction and **dmdt₂Anthra[Ti(III)Cp₂]** to be investigated for its coherence properties using pulsed Q-band ESR spectroscopy. The phase memory times found at 7 K in THF were 3.0(3) µs and could be increased to 5.2(6) µs by using deuterated THF as solvent. Furthermore, these behave stably up to around 40 K. These times are in the upper range of known titanium(III) qubits and likewise in the upper range among known two-quantum bit systems.

In the third chapter, a family of three PTM radicals – two monomers (**PTM-mono**, **PTM-tail**) and one dimer (**PTM-di**) – was studied by pulsed Q-band ESR spectroscopy. All three radicals showed very similar behavior, including extremely long spin-lattice relaxation times around 1 s at 7 K. The phase memory times were determined to be over 100 µs for the two monomers and just under 80 µs for the dimer at low temperatures of 7 K. These times are some of the best published phase memory times, exceeded only by **V(dbddto)₃²⁻** and **N@C₆₀** mentioned earlier. In addition to these results, the dimer **PTM-di** was studied by dipolar ESR spectroscopy. Using Double Electron-Electron Resonance (DEER), Single-Frequency Technique for Refocusing Dipolar Couplings (SIFTER) and Double Quantum Coherence (DQC), the two qubits were found to be 2.4(1) nm apart. However, SIFTER and DQC showed much better experimental results than DEER - owed to the very narrow resonance line of a few millitesla and the experimental technique of the DEER experiment. Although the distance between qubits for gate operations should be ~1.6 nm, the obtained results are promising and show the individual addressability of the two spins.

The last chapter deals with the influence of spin-orbit coupling on the coherence properties of porphyrin-based two-quantum bit systems within group 11 – copper, silver and gold. Some of the porphyrins were rotationally flexible (**mmPorph[M]**) and some were rigidly coupled (**fsPorph[M]**). Quantum coherence was observed for five of the six compounds, including, for the first time described in the literature, gold(II) in the form of **mmPorph[Au]**. Interestingly, all compounds thereby exhibit very similar phase memory times of about 2 µs at low temperatures of 5 K – 30 K, largely independent of the central ion of the individual qubits. Even for the gold compound **mmPorph[Au]**, a phase memory time of about 1.7 µs could still be measured at low temperatures from 5 K to 15 K.

However, the measured spin-lattice relaxation times are a big surprise. These should decrease sharply, since heavy atoms contribute strongly to decoherence through their spin-

orbit coupling. Thus, the relaxation time is expected to decrease from copper to gold. However, this could not be confirmed experimentally: The studied silver porphyrins **monoPorph[Ag]** and **mmPorph[Ag]** show a doubling of the coherence times compared to their lighter copper analogue. Although a similar result was observed for a related silver porphyrin in 1996 by Eaton and Eaton, an explanation for these results could likewise not be found.

1

INTRODUCTION

1.   INTRODUCTION

The basic ideas of quantum computers were first described by Feynman in his paper "Simulating Physics with Computers" in 1982 [1]. Shortly thereafter, Deutsch described in his "Universal Quantum Computer" that such a device could perform tasks that cannot be done by classical computers, although he did not specify how [2]. Since then, the use of quantum states for information processing has been a long-standing goal of scientists.

This has led to several algorithms in which quantum computers (QC) are far superior to their classical counterparts: In 1996, Grover [3] described an algorithm for searching through unsorted databases. He proved that his algorithm is suitable for searching a database with N entries in $\sqrt{N}$ steps. In the era of Big Data, the implementation of Grover's algorithm would be a significant improvement over conventional search algorithms since these algorithms scale only linearly in the best case. Another addition to the possible applications of QC is the algorithm of Shor [4]. In 1994 he proposed an algorithm that can factor numbers with the scalability order of a polynomial. By comparison, the currently fastest conventional algorithm – the General Number Field Sieve [5] – scales in a sub-exponential order. A working implementation of this algorithm would break all currently used RSA cryptography [6], which heavily relies heavily on the inability to factor large integers in a reasonable time. In addition to algorithms, as the field of artificial intelligence (AI) continues to grow, it is also worth considering the impact that quantum computing could have on AI [7]. The first steps in this direction have now been taken by Google with its TensorFlow Quantum library [8], which implements hybrid quantum-classical models.

All of these algorithms involve the use of quantum bits (qubits). Unlike classical bits, quantum bits are consisting of (at least) two states, which can also be in a coherent superposition. Although theoretically, all multilevel systems can act as a qubit, practical limitations exclude many of them. From well-defined systems of qubits and their initialization to long coherence times to actually perform a computation and the need for a universal set of quantum gates, these limitations are given by the DiVincenzo [9] criteria defined in the early 2000s.

In the last decades, the big players in the field of computing, such as IBM, Google, NVIDIA, and others, have stepped forward and invested heavily in the research of quantum

computers and the satisfaction of the aforementioned criteria. However, while these companies base their research on, e.g., superconducting quantum bits, a different approach has been taken with molecular-based designs for quantum bits, as they have several advantages that are not easily applicable to the other techniques: They are theoretically easy to arrange into ordered arrays and easy to initialize in a magnetic field at low temperatures. But a key advantage over other types of qubits is the ease of chemical tuning, which has made them a prime target for chemists. This has also led to much success in this field: Over the years, better and better qubit systems with very long coherence times have been found. Among the best are currently vanadium-based systems with relaxation times at low temperatures of up to 675 μs at low temperature [10].

However, successful implementation beyond a single qubit or a few qubits has not been achieved, even though a full set of quantum gates – equivalent to traditional transistor gates – is needed to perform the sophisticated quantum operations that make a theoretical quantum computer work. Without this set, no useful computation can be performed.

This is what this thesis addresses: The design and study of potential molecular multi-qubit systems, ideally based on known single-qubit systems.

Prior to the research part of this thesis, a general introduction given in the theoretical section should serve the reader as a guide to the design of molecular qubits as well as the current state of the art and some insights into the more advanced dipolar pulsed EPR spectroscopy methods to evaluate possible 2-qubit systems.

A major goal of this work was to develop a novel type of 2-qubit system that was tailored to fit the requirements outlined in the theoretical section. This involved the evaluation of possible target molecules beforehand, the retrosynthetic planning of the candidates, the synthesis, and finally, the evaluation of possible qubits.

In addition to this overarching part of this work, the role of spin-orbit coupling in 2-qubit systems was investigated with group 11 porphyrin systems as it has a direct impact on the expected spin relaxation times. These systems were provided by the Sarkar group at the University of Stuttgart. Finally, the properties of another potential, purely organic, and stable 2-qubit system were evaluated using more advanced pulsed EPR methods at the University of Manchester. The PTM radicals used here were provided by the Crivillers group at the University of Barcelona.

2

BACKGROUND

2. BACKGROUND

This chapter gives a brief overview of the theoretical background to the systems studied in this thesis as well as the employed techniques to investigate these. It goes over the requirements of (molecular) quantum bits and the quantum bits to assess their performance as quantum bits. In addition, a short overview of dipolar spectroscopy in EPR and the associated experimental techniques is given.

2.1. Requirements for Qubits

Quantum systems to be used in quantum computing must meet a number of requirements. These requirements have been generalized by DiVincenzo and are listed in a general overview in 2.1.1. For molecular qubits, however, some of these criteria will be described in more detail after 2.1.1.

2.1.1. DiVincenzo Criteria

In 2000, DiVincenzo [9] proposed five conditions quantum bits must fulfill in order to be successfully employed in quantum computation. These are:

A scalable system of well-characterized qubits.

With spin qubits, a well-characterized system should consist of a two-level spin system where the levels $|\uparrow\rangle$ and $|\downarrow\rangle$ are well separated from other states. True two-level systems are highly preferred over multilevel systems because they do not suffer from switching errors due to spin leakage to states not included in the qubit basis. "Scalability" refers to the requirement that the quantum computer can contain a large number of interacting qubits without losing any of the other requirements listed here. Since this property is satisfied by molecules in well-ordered arrays, chemical design certainly seems to be a promising and attractive method.

The possibility to set the state of the qubits to a specific state.

At any given time, a well-defined initialization state should be obtainable. This requirement is one of the easier ones to fulfill since; for molecular spins with relaxation properties, simply cooling the sample in a magnetic field forces the spins into their ground state.

Long decoherence times, which are much longer than the gate operation time.

The loss of quantum information due to the interaction of a spin with its environment is called decoherence. The time for this to occur should be at least several orders of magnitude larger than the quantum operation time τ_{gate}. Therefore, it is essential to increase the coherence times in molecular qubits. Since spin-based systems lose their coherence mainly due to the interaction with phonons and surrounding nuclear spins, chemical design and the use of low-spin systems can be a way to slow down the decoherence. Decoherence due to nuclear spins can be attributed to the hyperfine interaction of the electrons with the nuclear spins, as observed by Ardavan et al. in Cr_7Ni qubits [11]. And since molecular qubits usually include an organic ligand shell to protect the spin center from the environment, it is difficult to eliminate nuclear spins since the ligands usually contain hydrogen with a nuclear spin of $I = \frac{1}{2}$.

A universal set of quantum gates.

In analogy to classical computing, a quantum computer needs a universal set of quantum gates to compute. Quantum gates represent the quantum interpretations of classical Boolean gates that are necessary for computation. It has been shown that to obtain a universal set only two gates are needed to perform any quantum computational operation. A simple one qubit gate and the quantum XOR gate [12].

A measurement capability to read out individual qubits.

One of the biggest problems scientists face is reading out the individual state of a qubit state after a manipulation. Even if all the requirements and specifications are met, and a calculation can be performed, it is useless if the result cannot be retrieved. This, in consequence, means that every single quantum bit in the system must be selectively addressable in some way.

2.1.2. Benefits of Nuclear Spin-Free Coordination Sites

The fact that nuclear-spin-free ligands have a positive influence on the decoherence time of complexed metals has already been described in literature [13]–[18]. The contribution of nuclear spins to the decoherence of electron spin states results from several factors:

- Nuclear Spin Diffusion:
  Electrons experience magnetic field fluctuations due to flip-flop processes of nearby nuclear spins. This modulation drives the loss of the spin coherence of the electron and is known as nuclear spin diffusion. The rate at which such nuclear spin flip-flops occur is low, but the abundance of nuclear spins causes these processes to occur at a relevant rate. However: Nuclear spin diffusion does not simply just follow a r^{-3} dependence, as might be expected from the dipolar nature of the coupling. Instead, there is a radius called the spin diffusion barrier, within which the nuclei are so tightly coupled that no flip-flops occur. This means that they do not contribute to the overall decoherence [17],[19],[20].

- Spectral Diffusion:
  In addition to this process, the actual motion of the nuclear spins provides a contribution to dephasing, commonly referred to as spectral diffusion [16]. This effect can be comparable to that of nuclear spin diffusion in the case of protons.

Intuitively this, in consequence, might mean that you "just" have to remove all nuclear spins from your compound. While this is, of course, a valid and reasonable thought, a chemist will be very much challenged in his synthetic strategies.

To get an overview of all valid options for use in possible qubits, one must look at how the nuclear spin is distributed among elements and isotopes: Isotopes with an odd number of protons never have $I = 0$. Consequently, at least one isotope of the elements with an even number of protons will inherit a nuclear spin of $I = 0$. Looking at a nuclide chart [21], one will indeed find an above-average occurrence of nuclear spin-free isotopes, which are among the most abundant in the elements with an even number of protons.

As metals are generally not used in ligand design, this number reduces even further and drastically shrinks the number of options. Isotopic purification is generally not feasible due to availability and cost. This leaves only a handful of elements that are truly useful in the design of a nuclear spin-free ligand. These are Carbon (98.9% ^{12}C), Oxygen (99.8% ^{16}O),

Silicon (92.2% ^{28}Si), and Sulfur (95.0% ^{32}S). Heavier elements tend to increase their metallic character and are generally not useful in basic organic transformations.

While all of this has a significant impact on which elements to use in molecular quantum bits, it has been shown that some more atoms are valuable assets in creating quantum bits: **Cu(mnt)₂**, for example, is a good quantum bit [22] even though it contains several nitrogen atoms in the **mnt** ligand. This is thought to be the result from the fact that ^{14}N is not sufficiently abundant and has a much weaker magnetic moment to form a spin bath and therefore does not affect the relaxation behavior too much. Another example is chlorine, whose two common quadrupole nuclei ^{35}Cl and ^{37}Cl also have a much smaller magnetic moment relative to ^{1}H but, in addition, also have the wrong time scale of spin dynamics to interact with the electron spin [11],[23], as they relax very fast and any interactions with electrons are averaged to zero [24].

Figure 2.1. Periodic table with elements where (green) major parts ($>$ 50%), (yellow) minor parts ($\leq$ 50%) of the natural isotopic constitution are nuclear spin-free or (red) no natural isotope is nuclear spin-free or (grey) no natural isotopes exist. Compiled from [21].

2.1.3. Additional Considerations for Designing 2-Qubit Gates

As already mentioned in the DiVincenzo criteria, 2-qubit systems are needed in addition to 1-qubit systems. These systems must be individually addressable. This problem can, for instance, be solved by different orientations of the g-tensors of the individual qubits inside the molecule or by having two completely different g-tensors.

The second important issue is the adjustment of the interaction strength of the qubits. In practice, this means that the phase memory time T_m must be longer than both the operation time of the qubits gate τ_{gate} and the time of a quantum operation $\tau_{operation}$.

The τ_{gate} time must lie in between these aforementioned times because if it were shorter than the time for a quantum operation, the coupled state would not be usable, and if it were longer than T_m it would simply take too long, and the coherence would decay before the operation is completed.

This implies that the τ_{gate} time should be of the order of 100 ns, or the qubits should be coupled at about 10 MHz, which for a purely dipolar coupling of two spin-1/2-systems corresponds to a distance of 1.7 nm between the qubits.

2.2. Basics of EPR Spectroscopy

Electron Paramagnetic Resonance (EPR) is used to describe substances with unpaired electrons. It has some similarities to Nuclear Magnetic Resonance (NMR) spectroscopy.

Like NMR, EPR relies on the Zeeman effect. The degeneracy of the spin state S is lifted in a magnetic field. This external magnetic field is typically chosen to be parallel to the spatial quantization axis of the magnetic moments. This effect can be described by the electronic Zeeman Hamiltonian $\mathcal{H}_{EZ}$:

$$\mathcal{H}_{EZ} = \mu_B \cdot \boldsymbol{B}^T \boldsymbol{g}\, \widehat{\boldsymbol{S}} \tag{1}$$

Where $\boldsymbol{g}$ is the g-tensor of the system, μ_B is the Bohr magneton, $\boldsymbol{B}$ is the magnetic field vector and $\widehat{\boldsymbol{S}}$ is the spin operator.

The energy of spins whose magnetic moment is parallel to the outer magnetic field is reduced by the Zeeman effect. The energy of the antiparallel spins is consequently increased. Here, the eigenvalues of the Hamiltonian in **Equation (1)**, where the magnetic field $\boldsymbol{B}$ is in the z-direction, define the energy of the states $E(m_\mathrm{s})$:

$$E(m_\mathrm{s}) = g\,\mu_B\,B_z\,m_s \tag{2}$$

Therefore, a transition between two adjacent energy levels can be induced by the introduction of electromagnetic radiation, which satisfies the selection rule $\Delta m_s = \pm 1$ for an allowed transition:

$$\Delta E = h\nu = g\,\mu_B\,B_z \tag{3}$$

With Planck's constant h and the frequency of the electromagnetic radiation ν.

The population ratio in **Equation (4)** is quite large compared to that of the NMR population difference at the same field and temperature, which explains the greatly increased sensitivity of an EPR experiment compared to an NMR experiment. This is because the gyromagnetic ratio $\gamma = g\,\mu\,\hbar^{-1}$ of an electron spin exceeds that of a proton by a factor of more than 600. In addition, this allows the observation of the spin-spin interaction over larger distances and provides sensitivity to molecular motion on a smaller time scale.

$$\frac{N_{\mathrm{upper}}}{N_{\mathrm{lower}}} = \exp\left(-\frac{\Delta E}{k_\mathrm{B}T}\right) \tag{4}$$

With the temperature T and the Boltzmann constant k_B.

As nuclear spins, independent of the electron spin, are also impacted by magnetic fields, a nuclear Zeeman Hamiltonian $\mathcal{H}_\mathrm{NZ}$ can be used in analogy to the electronic one:

$$\mathcal{H}_\mathrm{NZ} = g_N \mu_N \boldsymbol{B}^T \hat{\boldsymbol{I}} \tag{5}$$

Furthermore, the hyperfine Hamiltonian $\mathcal{H}_{HF}$ describes the interaction of an electronic spin with the surrounding nuclear spins:

$$\mathcal{H}_{HF} = \widehat{S}^T A \widehat{I} \tag{6}$$

With the hyperfine tensor A of the interacting nuclei and the nuclear spin operator $\widehat{I}$.

The hyperfine tensor A in **Equation (6)** represents a composite of an isotropic a_{iso} and dipolar or anisotropic part T:

$$A = \begin{bmatrix} A_{xx} & A_{xy} & A_{xz} \\ A_{yx} & A_{yy} & A_{yz} \\ A_{zx} & A_{zy} & A_{zz} \end{bmatrix} = a_{iso} + T \tag{7}$$

Where $a_{iso} = a_{iso}I$; the use of the identity matrix I is herein omitted for clarity.

As the matrix A is usually symmetric, it can be transformed into a diagonal form:

$$A = \begin{bmatrix} A_{xx} & 0 & 0 \\ 0 & A_{yy} & 0 \\ 0 & 0 & A_{zz} \end{bmatrix} = a_{iso} + T \begin{bmatrix} -1 & 0 & 0 \\ 0 & -1 & 0 \\ 0 & 0 & 2 \end{bmatrix} \tag{8}$$

Where T represents the electron-nuclear coupling constant.

2.3. Evaluation of a Qubit's Performance

Qubits are generally characterized by two parameters: The phase memory time T_2 and the spin-lattice relaxation time T_1. The spin-spin relaxation time T_2 describes the lifetime of the superposition state of two levels in the system. It is important because it is the time within which a quantum computation must be performed. T_1 can be considered as the time needed for an inverted magnetization to return to its equilibrium state by exchanging energy with its surroundings. It is important for qubit performance as it correlates with the initialization time of a qubit.

2.3.1. The Hahn Echo Sequence

The above-mentioned parameters are accessible via pulsed EPR spectroscopy, in which many spins are excited simultaneously, resulting in the detection of the sum of the many spins. Once excited, they begin to dephase and decay due to inhomogeneities in the static magnetic field and slight differences in g-factors.

To detect this decay, the spin echo sequence is essential. This so-called Hahn echo sequence can be visually explained using a Bloch sphere in **Figure 2.2**, which shows the evolution of the spin state during the experiment. Assuming that all magnetization vectors are aligned parallel to the z-axis, the initial $\frac{\pi}{2}$-pulse first rotates the magnetization vectors by 90° onto the xy-plane, where they start to dephase for a time τ. The then applied second pulse, a π-pulse, flips all vectors by 180° on the xy-plane. As the spins themselves continue to dephase, they will realign after a time of 2τ, resulting in a detectable echo in the xy-plane:

Figure 2.2.   Evolution of the spin state on the Bloch sphere during the Hahn echo pulse sequence.

2.3.2. Spin-Lattice Relaxation Time T$_1$

The spin-lattice relaxation time describes the return of the spin system to its thermal equilibrium. While returning, it releases its energy to the surrounding lattice. T_1 is important because it controls the initialization time of the qubit [25].

Experimentally, the spin-lattice relaxation time T_1 can be measured with the inversion recovery sequence shown in (**Equation (9)**). In this sequence, the magnetization of all spins is first inverted by a π-pulse, which is followed by a standard Hahn echo detection sequence after a variable time T.

$$\pi - T - \frac{\pi}{2} - \tau - \pi - \tau - \text{echo} \tag{9}$$

Both the monoexponential (**Equation (10)**) and the biexponential function (**Equation (11)**) are common approaches for fitting the decay curves obtained from the intensity of the echo in an inversion recovery experiment over the varying time T. In the equations T_{SD} is the spectral diffusion time constant, which is usually an order of magnitude smaller than T_1 [25].

$$A(T) = A(0) + A_1 \exp\left(-\frac{T}{T_1}\right) \tag{10}$$

$$A(T) = A(0) + A_1 \exp\left(-\frac{\text{T}}{T_1}\right) + A_{\text{SD}} \exp\left(-\frac{\text{T}}{T_{\text{SD}}}\right) \tag{11}$$

T_1 usually varies strongly with temperature. This can be explained by the different spin-lattice relaxation mechanisms involved in decoherence, as shown in **Figure 2.3**. In the direct process, relaxation occurs by a single phonon having the same energy as the energy difference between the two spin microstates (e.g., $m_s = \pm1/2$). In both the Raman process and the Orbach processes, phonons are absorbed and re-emitted. The only difference is that in the Orbach process, the absorption and reemission occur with a real intermediate state being involved, while in the Raman process, it occurs only through a virtual excited state.

Figure 2.3. The level scheme of the direct process, Orbach process, and Raman process in spin-lattice relaxation theory [26],[27]. Indicated energies are phonon energies.

2.3.3. Phase Memory Time T_m

Experimentally, the spin-spin relaxation time T_2 can be extracted by fitting an exponential decay of a Hahn echo experiment, in which the echo intensity is plotted against the interpulse delay τ.

$$A(2\tau) = A(0) \ \exp\left(-\frac{2\tau}{T_2}\right) \tag{12}$$

Where I is the echo intensity at a given interpulse delay τ.

Although this is theoretically the case, such an experiment measures only the lower limit of T_2, since the echo decay is affected by both coherence transfer to neighboring electrons and nuclear spins. This lower limit is commonly referred to as the phase memory time T_m and is often used interchangeably with T_2. Often, electron spin and nuclear spin diffusion or

multiple observed spin systems can result in decay profiles that are not perfectly fitted by a simple exponential but by a stretched exponential function.

$$A(2\tau) = A(0) \, \exp\left(-\left(\frac{2\tau}{T_\mathrm{m}}\right)^x\right) \tag{13}$$

The stretch factor x for decoherence dominated by spin diffusion is typically $x = 2 \ldots 3$, while for relaxation dominated by the physical motion of the nuclei, this factor decreases to the range of $0.5 - 1$ [28].

If multiple spin systems are observed simultaneously, the use of a multi-exponential function such as a biexponential may be necessary for fitting:

$$A(2\tau) = A_\mathrm{f} \, \exp\left(-\frac{2\tau}{T_\mathrm{m,f}}\right) + A_\mathrm{s} \, \exp\left(-\frac{2\tau}{T_\mathrm{m,s}}\right) \tag{14}$$

Where A are the respective amplitude of the relaxation component with the accompanied phase memory times T_m. If two relaxation processes take place, they are often referred to as fast f and slow s.

2.4. Overview of Existing Molecular Qubit Solutions

In the last decades, a lot of work has been devoted to the use of electronic spins in molecules as potential qubits. They are proposed as a good alternative to other qubit systems, such as defects in semiconductor materials, trapped ions, superconducting electrical circuits, photons or nuclear spins, and others [29],[30]. In this chapter, we give a brief overview of the existing solutions proposed in literature, both for molecular single-qubit systems and for multi-qubit systems that can be used as qugates.

2.4.1. Single-Molecular Qubit Systems

With the goal of meeting DiVincenzo's criteria in mind, scientists have moved from the first molecular nanomagnets, which were readily used as qubits, to the development of new, dedicated qubit systems with reasonably long coherence times – and with success:

Figure 2.4. Representation of the molecular structure of **[Cu(mnt)$_2$]$^{2-}$** and **[V(C$_8$S$_8$)$_3$]$^{2-}$** in the crystal. Crystal data published by Dance et al. [31] and Kitagawa et al. [32]. Hydrogens and PPh$_4^-$ counter ions are omitted for clarity, and thermal ellipsoids are drawn at 50% probability level. Color code: Carbon (white), Copper (brown), Nitrogen (blue), Sulfur (yellow), Vanadium (grey).

Within a series of copper(II) complexes [15],[33] the nuclear-spin free **[Cu(mnt)$_2$][PPh$_4$-d$_{20}$]$_2$** was synthesized, exhibiting a coherence time of 68 µs at 7 K. A few years later, further progress in this direction led to the design of another series of vanadium-based nuclear spin-free qubits [10],[13],[18]. In this series, the **[V(C$_8$S$_8$)$_3$]$^{2-}$** exhibited an astonishing coherence time of 675 µs at 7 K in frozen CS$_2$ solution.

Encouraged by these results, more and more systems with better properties are being developed, including multi-qubit systems, as shown in the next chapter.

2.4.2. Multi-Qubit Systems

Multi-qubit-systems are required to implement more complex Quantum Information Processing (QIP) operations and to provide a complete set of instructions as defined by the DiVincenzo criteria. They can be considered the quantum equivalent of the classical transistor-based gates in a modern microchip and are therefore commonly referred to as quantum gates or qugates.

The bottom-up approach provided by molecular design facilitates the design of such gates. Molecular design allows multiple spin units to be linked together, for example, by forming covalent bonds, while providing the flexibility to precisely tune the distance between the spins.

Qubit Dimers with Organic Bridges

A common strategy for constructing qugates is to connect two-qubit units using an organic linker, resulting in a tailorable, very weak interaction between the individual qubits. However, the design of such qugates is quite challenging as there is a fine line between the communication being strong enough for entanglement and too strong where electronic exchange becomes a problem by changing the isolated qubit states.

Systems with two paramagnetic centers with bridges between them have been used extensively as molecular rulers. Since they consist of two spin probes on either end, often linked by a π-system, they can also be considered as a 2-qubit system. They have been synthesized by the Godt group and have also been used extensively in EPR development by groups around the world, especially the Jeschke group [34],[35]. These systems have several advantages: They can be prepared using well-known coupling chemistry and are highly tunable both in terms of the spin centers and the distance between them. However, the π-systems allow for through-bond spin-spin coupling, effectively removing the isolation of the individual spin centers. In addition, rigidity can only be achieved in two dimensions. Two literature examples of such long extended π-systems are shown in **Figure 2.5**.

Figure 2.5. Two molecular rulers developed by the Godt group with (a) a copper(II) center on one side and an organic radical on the other, spaced apart by a rigid ethynylbenzene chain [34], as well as (b) the molecular structure of a smaller, "early" ruler developed by Godt in the early 2000s [35]. Hydrogens are omitted for clarity, and thermal ellipsoids are drawn at 50% probability level. Color code: Carbon (white), Nitrogen (blue), Oxygen (red).

One type of qugate, the controlled NOT-gate (CNOT), has already been implemented by Takui et al. [36]. This gate inverts the second input if the first input is |1⟩. The molecule **[TEMPO,TEMPO]** shown in **Figure 2.6** contains two TEMPO molecules with different g-tensor orientations in the molecular coordinate frame, making them inequivalent. In addition, the hydrogens around the radicals have been replaced by deuterium to further increase the coherence times, and ^{15}N enrichment has been done to simplify the hyperfine structure. The distance between the radicals in this compound is 2.0 nm.

Figure 2.6. Representation of the molecular structure of **[TEMPO,TEMPO]** in the crystal. Published by Takui et al. [36] . Hydrogens are omitted for clarity, and thermal ellipsoids are drawn at 50% probability level. Color code: Carbon (white), Nitrogen (blue), Oxygen (red).

Figure 2.7. Representation of the molecular structure of **[Cr$_7$Ni,TEMPO]** in the crystal. Published by Winpenny et al. [37]. Hydrogens, CMe$_3$ groups, and additional solvent molecules are omitted for clarity, and thermal ellipsoids are drawn at 50% probability level. Color code: Carbon (white), Chromium (purple), Fluorine (lime), Nickel (pink), Nitrogen (blue), Oxygen (red).

Not only systems with two equivalent spin systems can be found in literature. Hetero-qubit systems have also been synthesized. Examples are **[Cr$_7$Ni,TEMPO]** reported by Winpenny et al. [37], shown in **Figure 2.7**, where a TEMPO molecule is attached to a Cr$_7$Ni ring system. Since the systems are not connected covalently, the interactions between the qubits are purely dipolar. Systems like these are interesting because they have significantly different g-values for the different spin types, making it much easier to address the qubits individually.

In addition to the purely organically linked systems, one of the first multi-qubit systems, **[Cr$_7$Ni,Co(SCN)$_2$,Cr$_7$Ni]**, was based on linked Cr$_7$Ni rings and is shown in **Figure 2.8** and was linked by a switchable Co(SCN)$_2$ linker unit that is reversibly switchable to Co(III).

Figure 2.8.   Representation of the molecular structure of **[Cr$_7$Ni,Co(SCN)$_2$,Cr$_7$Ni]** in the crystal. Published by Winpenny et al. [38]. Hydrogens, CMe$_3$, and additional solvent molecules are omitted for clarity, and thermal ellipsoids are drawn at 50% probability level. Color code: Carbon (white), Chromium (purple), Cobalt (green), Fluorine (lime), Nickel (pink), Nitrogen (blue), Sulfur (yellow), Oxygen (red).

Clamping Qubit Dimers

A fundamentally different approach to qugates is based on metal dimers linked by short clamping ligands such as hydroxyphenylpyrazolyl. This was first investigated by Aromí et al. [39] with a terbium dimer. The anisotropy of the dimer system results in a ground doublet of $m_J = \pm 6$, the tilt-angle between the two ions as well as a weak metal to metal interaction allow for two qugates operations: A CNOT and a SWAP gate.

However, one can also try to produce the heteroatomic analogs of such compounds. Although this is much more difficult since the coordination sites are the same and the atomic radii of the lanthanides are also very similar, resulting in essentially the same chemical reactivity, the problem has been overcome: Several compounds of the type **[Ln,Ln']** were prepared by using an asymmetric clamping ligand. Of the prepared compounds, the **[Ce,Er]**-system, shown in **Figure 2.9**, is theoretically usable as a CNOT gate since its Hilbert state consists of four states [39].

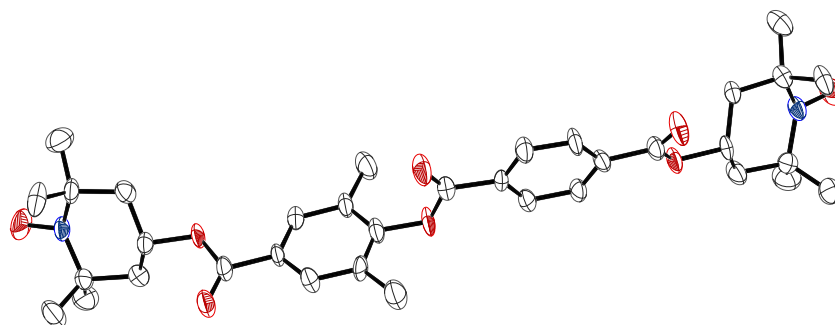**Figure 2.9**.   Representation of the molecular structure of **[Ce,Er]** in the crystal. Published by Aromí et al. [39]. Hydrogens and additional solvent molecules are omitted for clarity, and thermal ellipsoids are drawn at 50% probability level. Color code: Carbon (white), Cerium (green), Erbium (yellow), Nitrogen (blue), Oxygen (red).

In addition to the aforementioned lanthanide-based systems, also mixed-metal-based systems such as **[VO,Cu]** [40] and, more recently, **[VO,VO]** [41] have also been evaluated for their qubit properties. For the vanadium dimer, shown in **Figure 2.10**, it has been shown that the two vanadyl moieties allow for a weak dipolar interaction and have sufficient coherence times needed for qugate applications.

Figure 2.10.   Representation of the molecular structure of **[VO,VO]** in the crystal. Published by Aromí et al. [41]. Hydrogens and additional solvent molecules are omitted for clarity and thermal ellipsoids are drawn at 50% probability level. Color code: Carbon (white), Nitrogen (blue), Oxygen (red), Vanadium (olive).
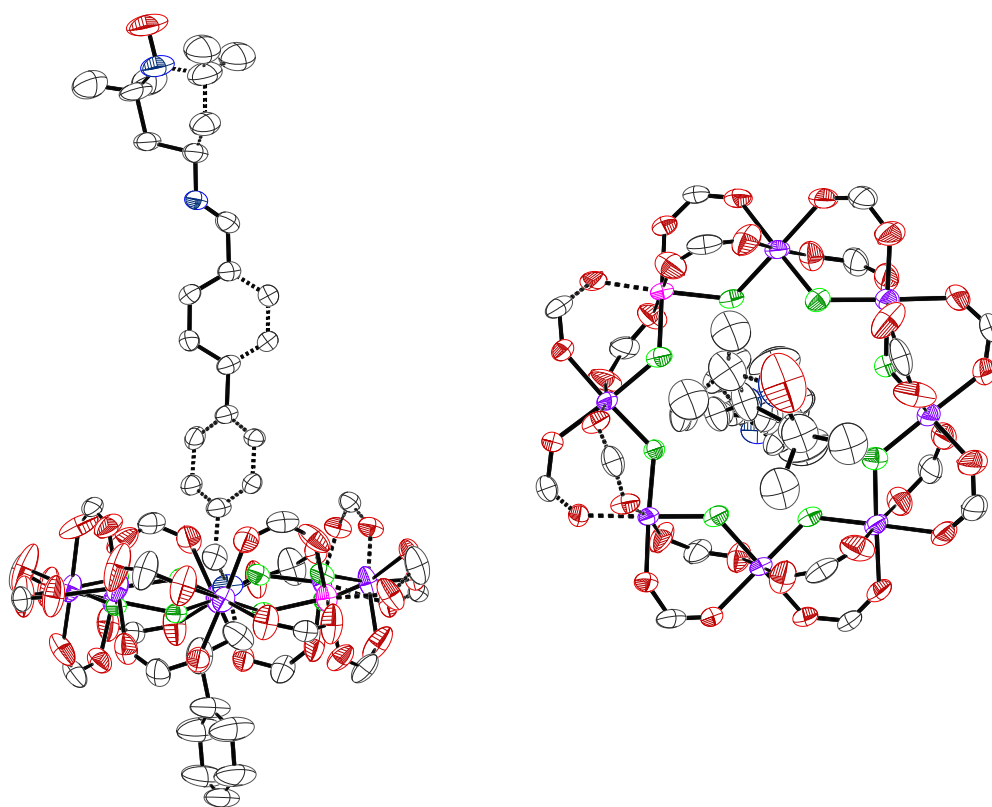
2.5. Basics of Pulsed Dipolar EPR Spectroscopy

This section is mainly based on the book chapter "Dipolar Spectroscopy – Single-resonance methods" [42] by Borbat and Freed in the book "EPR Spectroscopy: Fundamentals and Methods" [43]. In addition, the book by Schweiger and Jeschke, "Principles of Pulse Electron Paramagnetic Resonance" [44], and the Ph.D. thesis by Akhmetzyanov [45] were of great help.

2.5.1. Coupled Electron Spins and their Spin Hamiltonian

The Hamiltonian $\widehat{\mathcal{H}}_0$ of an isolated pair of spins S_1 and S_2, which are connected by the vector r_{12} with an angle θ relative to a static magnetic field B_0 is expressed as:

$$
\widehat{\mathcal{H}}_0 = \underbrace{\frac{\mu_B}{\hbar} B_0 g_1 \hat{S}_1 + \frac{\mu_B}{\hbar} B_0 g_2 \hat{S}_2}_{\text{EZ}}
$$

$$
+ \underbrace{\hat{I}_1^{(k)} \hat{A}_1^{(k)} \hat{S}_1^z + \hat{I}_2^{(l)} \hat{A}_2^{(l)} \hat{S}_2^z}_{\text{HF}}
$$

$$
- \underbrace{\left(\gamma_{1,N}^{(k)} B_0 \hat{I}_{1z}^{(k)} + \gamma_{2,N}^{(l)} B_0 \hat{I}_{2z}^{(l)} \right)}_{\text{NZ}}
$$

$$
+ \underbrace{\hat{I}_1^{(k)} \hat{P}_1^{(k)} \hat{I}_1^{(k)} + \hat{I}_2^{(l)} \hat{P}_2^{(l)} \hat{I}_2^{(l)}}_{\text{QDP}}
\tag{15}
$$

$$
+ \underbrace{d \left(3\hat{S}_{1z}\hat{S}_{2z} - \hat{S}_1\hat{S}_2 \right)}_{\text{ESDI}}
$$

$$
+ \underbrace{J \left(\frac{1}{2} - 2\hat{S}_1\hat{S}_2 \right)}_{\text{EX}}
$$

With EZ as the electron Zeeman, HF as the hyperfine, NZ as the nuclear Zeeman, QDP as the nuclear quadrupole, ESDI as the electron spin dipolar, and EX as the exchange interactions. k and l implying summation over the associated nuclei. $d = \omega_{dd}(1 - 3\cos^2\theta)$ and $\omega_{dd} = \frac{\gamma_e^2 \hbar}{2r_{12}^3}$. J is the electron exchange integral.

Figure 2.11.   Upon applying the π-pump on the S_2 spin, its contribution to the local field around S_1 changes its orientation, this resulting in an offset in resonance frequency and a change in ESE signal intensity.

To simplify the approach, the nuclear spin terms – Zeeman and quadrupole – are dropped, and the dipolar coupling term, which can be expressed as the so-called "dipolar alphabet" shown in **Equation (17)**, can be simplified in strong fields by ignoring all terms except $\hat{A}$ and $\hat{B}$:

$$
\begin{aligned}
\hat{\mathcal{H}}_{dd} &= d\left(3\hat{S}_{1z}\hat{S}_{2z} - \hat{S}_1\hat{S}_2\right) \\
&= \frac{\mu_0 g_1 g_2 \beta_e^2}{4\pi \hbar^2 r_{12}^3}\left(\hat{S}_1\hat{S}_2 - \frac{3}{r_{12}^2}(\hat{S}_1 r_{12})(\hat{S}_2 r_{12})\right)
\end{aligned}
\tag{16}
$$

$$
\begin{aligned}
&= D_{dip}\left(\hat{A} + \hat{B} + \hat{C} + \hat{D} + \hat{E} + \hat{F}\right) \\
\hat{A} &= \hat{S}_{1z}\hat{S}_{1z}(1 - 3\cos^2\theta) \\
\hat{B} &= \frac{1}{4}\left(\hat{S}_1^+\hat{S}_2^- + \hat{S}_2^-\hat{S}_1^+\right)(1 - 3\cos^2\theta) \\
\hat{C} &= -\frac{3}{2}\left(\hat{S}_1^+\hat{S}_{2z} + \hat{S}_{2z}\hat{S}_1^+\right)\sin\theta\cos\theta\exp{-i\phi} \\
\hat{D} &= -\frac{3}{2}\left(\hat{S}_1^-\hat{S}_{2z} + \hat{S}_{2z}\hat{S}_1^-\right)\sin\theta\cos\theta\exp{-i\phi} \\
\hat{E} &= -\frac{3}{4}\hat{S}_1^+\hat{S}_2^+\sin^2\theta\exp{-i2\phi} \\
\hat{F} &= -\frac{3}{4}\hat{S}_1^-\hat{S}_2^-\sin^2\theta\exp{-i2\phi}
\end{aligned}
\tag{17}
$$

Furthermore, the result can be simplified by including the Larmor frequency Ω_{Lk}:

$$
\hat{\mathcal{H}}_0 = \underbrace{\Omega_{L1}\hat{S}_{1z} + \Omega_{L2}\hat{S}_{2z}}_{\hat{\mathcal{H}}_{12}} + \underbrace{a\hat{S}_{1z}\hat{S}_{2z} + \frac{b_{ff}}{2}\left(\hat{S}_1^+\hat{S}_2^- + \hat{S}_1^-\hat{S}_2^+\right)}_{\hat{\mathcal{H}}_{dd}}
\tag{18}
$$

In **Equation (18)**, $\hat{H}_{12}$ is the representation of the Zeeman and hyperfine terms, giving the frequency spectrum in the EPR spectral dimension. $\hat{H}_{dd}$ however, has the secular part $a = d + 2J$ and the pseudosecular part $b_{ff} = -\frac{d}{2} + 2J$, including the exchange interaction.

When viewed in the rotating frame at the frequency ω_0, the Larmor frequencies Ω_{Lk} can be substituted by their offsets from the rotating frame frequency ω_0: $\Delta\omega_k = \Omega_{Lk} - \omega_0$.

The dipolar coupling will split the resonance lines at $\Delta\omega_k$ into a doublet with a distance of d for $\omega_{dd} \ll |\Delta\omega_1 - \Delta\omega_2|$ and a doublet of distance $3d/2$ for $\omega_{dd} \gg |\Delta\omega_1 - \Delta\omega_2|$. This, in consequence, leads to the characteristic Pake patterns [46].

Figure 2.12. Simulated Pake doublets resulting from (left) $\omega_{dd} \gg |\Delta\omega_1 - \Delta\omega_2|$ and (right) $\omega_{dd} \ll |\Delta\omega_1 - \Delta\omega_2|$.

2.5.2. Density Operator

The state of an ensemble of two coupled spins S_1 and S_2 is defined by a spin density operator $\hat{\sigma}(t)$. In the 4×4 representation of $\hat{\sigma}(t)$, the product eigenstates can serve as a convenient basis set for the spin states of $\omega_0(\hat{S}_{1z} + \hat{S}_{2z})$:

$$|1\rangle = |\alpha\alpha\rangle \tag{19}$$

$$|2\rangle = |\alpha\beta\rangle \tag{20}$$

$$|3\rangle = |\beta\alpha\rangle \tag{21}$$

$$|4\rangle = |\beta\beta\rangle \tag{22}$$

The values in the matrix are the values of the averages $\sigma_{ij}(t) = \langle i|\sigma|j\rangle = \overline{c_\iota(t)c_j^*(t)}$ (with $i, j = 1\ldots 4$) of an ensemble of N two-electron systems of state $|\Psi_n(t)\rangle = \sum_{i=1\ldots 4} c_i^n(i)|i\rangle$. These are shown in **Figure 2.13**, where the diagonal elements P_{ji} represent the state populations and the off-diagonal elements represent coherences.

Figure 2.13. (left) Elements of the density matrix of $\hat{\sigma}(t)$ in a system of two coupled electrons. The diagonal elements P_{jk} represent the state population, the off-diagonal elements coherences. SQ = Single Quantum Transition, ZQ = Zero Quantum Transition, and DQ = Double Quantum Transition. (right) Energy level diagram. Solid lines are allowed transitions, while dashed lines represent forbidden transitions. From [44].

Both $\sigma_{12}(t)$ and $\sigma_{34}(t)$ are coherences of the single-quantum transitions of the spin S_2 where α_1 flips to β_1 and vice versa. The zero-quantum-transition ZQ is represented in $\sigma_{23}(t)$, as both spins flip while being antiparallel, resulting in a net spin change of 0. Last, the double-quantum-transition DQ is represented by $\sigma_{14}(t)$, where two parallel spins flip, resulting in a net change of 2, hence DQ. Since $\sigma_{ji(t)} = \sigma_{ij(t)}^*$, the matrix is Hermitian.

In thermal equilibrium T this density operator is given by

$$\hat{\sigma}_{\mathrm{eq}} = \frac{\exp\!\left(-\hat{H}_0 k^{-1} T^{-1}\right)}{\mathrm{Tr}\!\left(\exp\!\left(-\hat{H}_0 k^{-1} T^{-1}\right)\right)} \tag{23}$$

with the Hamiltonian $\hat{H}_0 = \hbar\hat{\mathcal{H}}_0$, see **Equation (18)**.

If the sample being investigated is magnetically dilute, the spin pairs are described by the secular dipolar Hamiltonian. In dilute samples, the intermolecular couplings can be neglected and are much smaller than the intramolecular ones.

At high magnetic fields and high temperatures, the equilibrium density operator given in **Equation (23)** can be approximated by a series expansion of the exponential operator. The lowest order, ignoring all additional constants, is:

$$\hat{\sigma}_0 = -\left(\hat{S}_{1z} + \hat{S}_{2z}\right) \tag{24}$$

In this density matrix, at equilibrium, only the diagonal elements are present, corresponding to the energy levels with equilibrium population. When applying resonant radiation, the populations change creating non-zero off-diagonal elements that represent the coherences between states.

2.5.3. Evolving of Coupled Spins and the Liouville-von-Neumann Equation

As in all pulsed EPR experiments, microwave pulses, separated by free evolution periods, are applied to an initially equilibrated spin system. After a certain time t, the magnetization $M_y(t)$ is detected. The transverse magnetization can be prepared by applying a $\pi/2_x$-pulse to the equilibrium state, resulting in $\hat{\sigma}_{12}(0) = \hat{S}_{1y} + \hat{S}_{2y}$. Then free precession takes over according to the Larmor frequency offsets $\Delta\omega_k$ (with $k = (1,2)$) from the rotating frame frequency.

Spins can be characterized by a coherence order $\bar{p}$, where $\bar{p} = \pm 1$ indicates SQ, $\bar{p} = \pm 2$ indicates DQ and $\bar{p} = 0$ is simply the z-magnetization, whose maximum value is always $\bar{p} = \pm N$, with N being the number of spins and $\bar{p} = +1$ being the only observable order. In this case, each precessing spin is of order $\bar{p} = \pm 1$, and it evolves as $\exp(\mp i\Delta\omega_k t)$.

The detected signal is then given by

$$M_y(t) \sim -2 \, \text{Im} \left(\frac{\text{Tr}(\hat{\sigma}_{12}(t)\hat{S}^+)}{\text{Tr}(\hat{S}^-\hat{S}^+)} \right) \tag{25}$$

where $\hat{S}^\pm = \hat{S}_1^\pm + \hat{S}_2^\pm$.

The derivative of the density operator with respect to time is called the Liouville-von-Neumann **Equation (26)** and represents the free evolution of $\hat{\sigma}_{12}(t)$ for time-independent Hamiltonians, which equates to the spin dynamics of an ensemble of spin pairs. The solution to this equation is the unitary transformation of $\hat{\sigma}_{12}(0) = \hat{\sigma}_0$ in **Equation (27)**:

$$\frac{d\hat{\sigma}_{12}}{dt} = -i[\hat{\mathcal{H}}, \hat{\sigma}_{12}] \tag{26}$$

$$\hat{\sigma}_{12}(t) = \exp(-i\hat{\mathcal{H}}t) \, \hat{\sigma}_{12} \exp(i\hat{\mathcal{H}}t) \tag{27}$$

During a pulse sequence, the density operator evolves, and any element of the density matrix can be changed by the pulses. When applying an n-th pulse, the Hamiltonian becomes

$$\hat{\mathcal{H}}_n = \hat{\mathcal{H}}_0 + \hat{\mathcal{H}}_{1pn} \tag{28}$$

$$\hat{\mathcal{H}}_{1pn} = \frac{\omega_{1n}}{2}\left(\hat{S}^+ \exp(-i\phi_n) + \hat{S}^- \exp(i\phi_n)\right)$$
$$= \omega_{1n}\left(\hat{S}_x \cos\phi_n + \hat{S}_y \sin\phi_n\right) \tag{29}$$

with the n-th pulse being characterized by $\omega_{1n} = -\gamma_e B_{1n}$, the phase ϕ_n and the duration Δt_n.

The evolution of coherence can be represented by a coherence pathway transfer diagram, where pulses change the coherence order $\bar{p}$. A π-pulse intuitively changes the sign of the coherence order $\bar{p} \xrightarrow{\pi} -\bar{p}$. It also additionally inverts the polarizations, which are represented by the polarization operators $\hat{S}_k^\alpha \equiv \frac{\hat{E}_k}{2} + \hat{S}_{kz}$ and $\hat{S}_k^\beta \equiv \frac{\hat{E}_k}{2} - \hat{S}_{kz}$. With the identity operator $\hat{E}_k$ for spin k.

Any pulse can change a given coherence order $\bar{p}$ to any other available coherence order. This results in the following options for a single spin:

- Change coherence order: $\pm 1 \leftrightarrow 0$
- Refocusing or inverting: $\pm 1 \leftrightarrow \mp 1$

Also, a $\pi/2$-pulse can produce both coherence orders and z-magnetization as seen in:

$$\hat{S}^+ \xrightarrow{\pi/2_x} \frac{\hat{S}^+ + \hat{S}^-}{2} + i\hat{S}_z \tag{30}$$

2.5.4. Product Operator Formalism

Since it is very difficult to follow the time evolution of the density operator in the rotating frame using propagators of the Hamiltonians, a very simplified approach has been developed called the Product Operator (PO) formalism.

First, a simplification is made by assuming that $J = 0$ and, being in a weak coupling regime, by removing all flip-flop terms from the whole formalism. This means that the dipolar

Hamiltonian is $\widehat{\mathcal{H}}_{dd} = a\hat{S}_{1z}\hat{S}_{2z}$. A consequence of this is that $\widehat{\mathcal{H}}_{dd}$ commutes with the rest of $\widehat{\mathcal{H}}_0$.

The density operator in this formalism is built up from an appropriate operator basis. The density operator for the two-spin system $\hat{\sigma}_{12}$ in this case, can be described as the direct product of the individual density operator bases $\hat{\sigma}_1$ and $\hat{\sigma}_2$: $\frac{\hat{E}_k}{2}, \hat{S}_{kz}, \hat{S}_{kx}, \hat{S}_{ky}$ (with $k = (1,2)$) [47]. With the application of raising and lowering operators, this basis converts to $\frac{\hat{E}_k}{2}, \hat{S}_{kz}, \hat{S}_k^+, \hat{S}_k^-$, where $\hat{S}_k^{\pm} = \hat{S}_{kx} \pm i\hat{S}_{ky}$ [48].

The polarization states are given by the product operators $\hat{S}_{1z}, \hat{S}_{2z}$ (related to the population) and $2\hat{S}_{1z}\hat{S}_{2z}$ (related to the dipolar coupling). To follow the coherences and pulse sequences later, the following additional product operators are needed:

- Single-quantum in-phase: $\hat{I}_1^{\pm} = \hat{S}_1^{\pm}$ and $\hat{I}_2^{\pm} = \hat{S}_2^{\pm}$
- Single-quantum antiphase: $\hat{A}_1^{\pm} = 2\hat{S}_1^{\pm}\hat{S}_{2z}$ and $\hat{A}_2^{\pm} = 2\hat{S}_2^{\pm}\hat{S}_{1z}$
- Double-quantum: $\widehat{DQ}_{\pm} = \hat{S}_1^{\pm}\hat{S}_2^{\pm}$

2.5.5. Evolution of Single Quantum Coherence

As mentioned in 2.5.4, the approximations in the product operator formalism allow $\widehat{\mathcal{H}}_{12}$ and $\widehat{\mathcal{H}}_{dd}$ to commute. As a result, the coherence evolution can be treated separately for both offsets and couplings. This implies that the respective propagators of $\widehat{\mathcal{H}}_{12}$ and $\widehat{\mathcal{H}}_{dd}$ are used independently to describe the evolution of σ_{12}.

Although pulses can be conveniently described using the Cartesian form of the POs, evolution and coherence orders can be more easily followed in the spherical basis of the POs:

$$\hat{S}_k^{\pm} \xrightarrow{\widehat{\mathcal{H}}_{12}\tau} \hat{S}_k^{\pm} \exp(\mp i\Delta\omega_k\tau) \tag{31}$$

$$\hat{S}_k^{\pm} \xrightarrow{\widehat{\mathcal{H}}_{dd}\tau} \hat{S}_k^{\pm}\left(\cos\left(\frac{a\tau}{2}\right) \mp i2\hat{S}_{jz}\sin\left(\frac{a\tau}{2}\right)\right) = \hat{S}_k^{\pm}\left(c_\tau \mp i2\hat{S}_{jz}s_\tau\right) \tag{32}$$

with, $j \neq k$ and $j,k = (1,2)$ spins, $\Delta\omega_k$ as their Larmor frequency offsets, a their coupling and $c_\tau = \cos\left(\frac{a\tau}{2}\right)$ and $s_\tau = \sin\left(\frac{a\tau}{2}\right)$.

$\hat{S}_k^\pm$ evolves here under $\hat{\mathcal{H}}_{1\mathrm{p}2}$ (see **Equation (29)**) and describes the first-order coherences with $\bar{p} = \pm 1$ and thus the precession at $\Delta\omega_k$. The evolution of this phase is characterized as $\phi_{\mathrm{offset}} = \bar{p}\Delta\omega_k(\tau)$.

Under $\hat{\mathcal{H}}_{\mathrm{dd}}$, the evolution of $\hat{S}_k^\pm$ describes the conversion between the observable in-phase component and the non-observable antiphase component $2\hat{S}_k^\pm \hat{S}_{nz}$. The evolution of this phase can also be described with the dipolar phase $\phi_{\mathrm{dip}} = \bar{p}\bar{z}\left(\frac{a}{2}\right)$, where $\bar{z} = +1$ for $\hat{S}_n^\alpha$ and $\bar{z} = -1$ for $\hat{S}_n^\beta$, respectively. It is important to note that both phases describe reversible phases, allowing the offsets or couplings to be refocused.

It should be noted, however, that a real pulse will produce different coherence orders available for the observed spin, resulting in a whole set of possible pathways. The selection of the pathway of interest is then subject to phase cycling and interpulse interval constraints [44]. Also, each pulse along each pathway can generate alternative paths of $\Phi_{\mathrm{dip}}(\tau)$ for parts of the spin ensemble, resulting in several dipolar paths $\Phi_{\mathrm{dip},x}(\tau)$. However, these are treated by the product operator for ideal hard pulses; for arbitrary pulses, a more detailed description can be found in [42].

2.5.6. Refocusing Offsets and Couplings

In 2.5.5, it was shown how the free evolution of a spin pair works. What is missing from a complete description is the effect of pulses. For this, we look again at spins 1 and 2 with Larmor frequencies ω_1 and ω_2.

To detect an echo, π-pulses are needed to refocus the spins. The simplest sequence is a sandwiched π-pulse: $\tau - \pi - \tau$. Using the product operator formalism, the refocusing can be expressed as:

$$
\begin{aligned}
\hat{S}_k^\pm &\xrightarrow{\hat{\mathcal{H}}_0 \tau} \hat{S}_k^+ \exp(-\mathrm{i}\Delta\omega_k \tau) \\
&\xrightarrow{\pi} \hat{S}_k^- \exp(-\mathrm{i}\Delta\omega_k \tau) \\
&\xrightarrow{\hat{\mathcal{H}}_0 t} \hat{S}_k^- \exp\bigl(-\mathrm{i}\Delta\omega_k(\tau - t)\bigr)
\end{aligned}
\tag{33}
$$

Once $\tau = t$, any offsets are offset, and the signal is refocused, forming an echo. The equation shown above describes the coherence path $+1 \to -1$.

For a two-spin system, three different applications of a π-pulse can be considered and are shown in **Figure 2.14**: In (a) and (c), spin 1 is refocused. By evolving under the influence of the couplings, the pulses in the ω_2 channel in (b) and (c) indirectly change spin 1 in the ω_1 channel. The effect arises through the antiphase $2\hat{S}_1^+\hat{S}_{2z}$ term of **Equation (32)**.

The pulse in (a) flips spin 1, refocusing both the echo (**Equation (33)**) as well as the coupling (the latter by refocusing $2\hat{S}_1^+\hat{S}_{2z}$ to $2\hat{S}_1^-\hat{S}_{2z}$). In (b), the coupling is refocused, but this time through population inversion $\hat{S}_{2z} \to -\hat{S}_{2z}$. However, refocusing the offset of spin 1 needs an additional π-pulse.

(a) and (c) can be treated simultaneously by introducing the probability p to flip spin 2 and the probability to not flip it $q = 1 - p$. Applying this to $\hat{S}_1^+$ results in:

$$
\begin{aligned}
\hat{S}_1^+ &\xrightarrow{\hat{\mathcal{H}}_{dd}\tau} \hat{S}_1^+\left(c_\tau - i2\hat{S}_{2z}s_\tau\right) \\
&\xrightarrow{\pi} \hat{S}_1^-\left[(q + p)c_\tau - i2(q - p)\hat{S}_{2z}s_\tau\right] \\
&\xrightarrow{\hat{\mathcal{H}}_{dd}t} \hat{S}_1^-\left(q\left(c_\tau - i2\hat{S}_{2z}s_\tau\right) + p\left(c_\tau + i2\hat{S}_{2z}s_\tau\right)\right)\left(c_t + i2\hat{S}_{2z}s_t\right) \\
&= \hat{S}_1^-\left(q\left(c_{\tau-t} - i2\hat{S}_{2z}s_{\tau-t}\right) + p\left(c_{\tau+t} + i2\hat{S}_{2z}s_{\tau+t}\right)\right)
\end{aligned}
\tag{34}
$$

where $c_x = \cos\left(\frac{ax}{2}\right)$ and $s_x = \sin\left(\frac{ax}{2}\right)$.

When $t = \tau$, **Equation (34)** becomes $\hat{S}_1^-\left(q + p\left(c_{2\tau} + i2\hat{S}_{2z}s_{2\tau}\right)\right)$, which equals to $\hat{S}_1^-\left(c_{2\tau} + i2\hat{S}_{2z}s_{2\tau}\right)$ for a definite spin 2 flip ($p = 1$, hard pulse). This means, that $\Phi_{dip}(t)$ is unaffected by the π-pulse and is evolves as $at/2$. If there is no resonant pulse ($p = 0$) present on spin 2, only $\hat{S}_1^-$ is available for refocusing.

In (b), the applied π-pulse on ω_2 refocuses solely the Φ_{dip} by reversing its direction. By shifting the pulse on ω_2 with time while keeping the observing ω_1 static, the dipolar coupling can evolve.

Figure 2.14. Evolution of the coherences Φ_{off} and Φ_{dip} for different π-sandwich configurations on two coupled spins defined by their Larmor frequencies ω_1 and ω_2 [42].

However, panel (c), which best represents the single-resonance case if $\omega_1 \approx \omega_2$, provides no way to evolve the coupling other than to expand the $\tau - \pi - \tau$ sandwich. It is also limited by its dead time. This can be solved by adding another pulse, like the deadtime removal in the 3-pulse DEER sequence (which is obtained by merging (a) and (b)) with the 4-pulse DEER sequence (see 2.6.1). However, the timing $\tau - 2\tau - \tau - \mathrm{echo}$ from the DEER sequence was not that effective at evolving couplings and thus, the timing for the single resonance case was changed to $t_1 - (t_1 + t_2) - t_2 - \mathrm{echo}$ where $t_1 \ll t_2$ [19].

A comparison between the modified single-frequency case and the 4-pulse DEER sequence is therefore made in **Figure 2.15**.

Figure 2.15. Comparison of the single resonance (a) and double resonance (b) schemes based on refocused echo experiments with the evolution of Φ_{off} and Φ_{dip}. In (a), $\hat{U}$ represents a spin manipulation pulse [42].
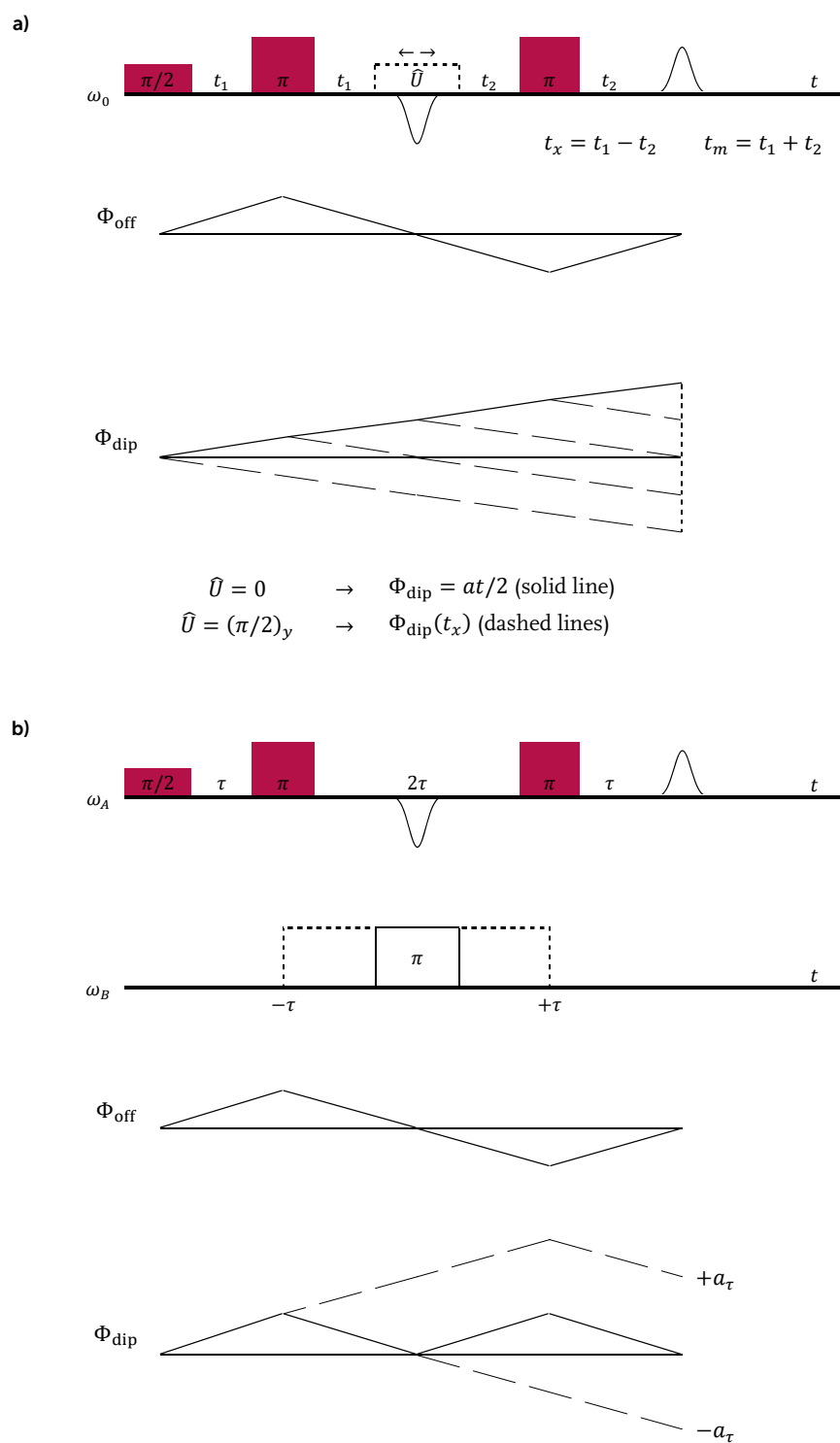
First, we will have a look at the refocusing in the case of double resonance as shown in **Figure 2.15**b). The refocusing for this case can be described as follows:

In the first pulse sandwich $\tau - \pi - \tau$, spin 1 evolves with:

$$\hat{S}_1^{\pm} \xrightarrow{\hat{\mathcal{H}}_{dd}\tau} \hat{S}_1^{\pm}\left(c_{\tau} \mp i2\hat{S}_{2z}s_{\tau}\right) \tag{35}$$

$$\xrightarrow{\pi} \hat{S}_1^{\mp}\left(c_{\tau} \pm i2\hat{S}_{2z}s_{\tau}\right)$$

$$\xrightarrow{\hat{\mathcal{H}}_{dd}t} \hat{S}_1^{\mp}\left(c_{\tau} \pm i2\hat{S}_{2z}s_{\tau}\right)\left(c_t \pm i2\hat{S}_{2z}s_t\right)$$

$$= \hat{S}_1^{\mp}\left(c_{\tau+t} \pm i2\hat{S}_{2z}s_{\tau+t}\right)$$

$$\rightarrow \hat{S}_1^{\mp}\left(c_{2\tau} \pm i2\hat{S}_{2z}s_{2\tau}\right) \tag{36}$$

And for $\hat{S}_2^{\pm}$ respectively by switching the indexes for the spins.

In this expression, however, the offset evolution is ignored because it is refocused for $t = \tau$ (see **Equation (33)**). Switching back to the Cartesian product operator after obtaining the evolution after 2τ for $\hat{S}_1^{\pm}$ (and $S_2^{\pm}$) leads to:

$$\hat{S}_{1y} = \frac{1}{2i}\left(\hat{S}_1^+ - \hat{S}_1^-\right)$$

$$= \frac{1}{2i}\left[\hat{S}_1^-\left(c_{2\tau} + i2\hat{S}_{2z}s_{2\tau}\right) - \hat{S}_1^+\left(c_{2\tau} - i2\hat{S}_{2z}s_{2\tau}\right)\right] \tag{37}$$

$$= -\hat{S}_{1y}c_{2\tau} + i2\hat{S}_{1x}\hat{S}_{2z}s_{2\tau}$$

And for $\hat{S}_{2y}$ respectively by switching the indexes for the spins.

Combining these to form $\hat{S}_{1y} + \hat{S}_{2y}$, as this is what is finally measured, leads to:

$$\hat{S}_{1y} + \hat{S}_{2y} = -\left(\hat{S}_{1y} + \hat{S}_{2y}\right)c_{2\tau} + i\left(2\hat{S}_{1x}\hat{S}_{2z} + 2\hat{S}_{2x}\hat{S}_{1z}\right)s_{2\tau} \tag{38}$$

Figure 2.15b) indicates that there is no dipolar coupling evolution in the refocused echo as a function of $t_x = t_1 - t_2$.

To describe the evolution of the coupling in a refocused echo as in **Figure 2.15**a), several parameters have to be introduced: $2t_m$ will be the length of the whole sequence, and the two pulse sandwiches will be denoted $t_1 - \pi - t_1$ and $t_2 - \pi - t_2$, resulting in $t_m = t_1 + t_2$. To emphasize that the sequence is of constant time, t_2 will be defined as $t_2 = t_m - t_p$. Additionally, the dipolar evolution variable $t_x = t_1 - t_2 = 2t_p - t_m$ must be defined. This variable can range from $-t_m$ to $+t_m$.

This allows us to describe the evolution of the spins during the refocusing of an echo as follows: Observing spin 1, after the first sandwich $t_1 - \pi - t_1$, in-phase and antiphase coherence is produced as in **Equation (37)**. After the second sandwich $t_2 - \pi - t_2$, the in-phase and anti-phase coherences evolve to a detectable in-phase coherence according to

$$\hat{I}_1(t_1) + \hat{A}_1(t_1) = -\hat{S}_{1y} \cos at_1 + 2\hat{S}_{1x}\hat{S}_{2z} \sin at_1 \tag{39}$$

$$\hat{I}_1(t_1) + \hat{A}_1(t_1) \to \hat{I}_1(t_1 + t_2)$$
$$= \hat{S}_{1y}(\cos at_1 \cos at_2 - \sin at_1 \sin at_2) \tag{40}$$
$$= \hat{S}_{1y} \cos a(t_1 + t_2)$$

With the cosines representing the evolution path $\hat{I}_1(0) \to \hat{I}_1(t_1) \to \hat{I}_1(t_1 + t_2)$ and the sines the path $\hat{I}_1(0) \to \hat{A}_1(t_1) \to \hat{I}_1(t_1 + t_2)$.

Single resonance techniques, in contrast to double resonance techniques, do not allow for refocusing Φ_{dip} only with π-pulses. However, it is possible to achieve this by introducing a suitable propagator $\hat{U}$ between the sequences that can refocus and is allowed to evolve the coherence orders to 0 and ± 2. To achieve this, $\hat{U}$ can make use of (several) pulses or use any other mechanism of spin manipulation. How this is done is up to the implementation, examples of which can be found in the SIFTER and DQC techniques described in 2.6.2 and 2.6.3.

The coherence transfer properties of $\hat{U}$ can be described arbitrarily by $C_I \hat{I}_k + C_A \hat{A}_k$ ($k = (1,2)$ and $(|C_I|, |C_A|) \leq 1$). In the orders $\bar{p} = 0, \pm 2$ there is no dipolar evolution takes place, so the dipolar phase is carried through the propagator $\hat{U}$ with the following effect:

$$\hat{I}_1(t_1) + \hat{A}_1(t_1) \xrightarrow{\hat{U}} C_I \hat{I}_1(t_1) + C_A \hat{A}_1(t_1)$$
$$\xrightarrow{t_2} \hat{S}_{1y}(C_I \cos at_1 \cos at_2 - C_A \sin at_1 \sin at_2) \tag{41}$$
$$= \hat{S}_{1y}\big((C_I + C_A) \cos at_m + (C_I - C_A) \cos at_x\big)$$

If in **Equation (41)** $C_I = -C_A$, only the $\cos at_x$ part remains. This means, that at $t_x = 0$ the coupling is completely refocused, which can be achieved by solid echo refocusing with, for example, $\hat{U} = \left(\frac{\pi}{2}\right)_y$.

$$-(\hat{S}_{1y} + \hat{S}_{2y})c_{2t_1} + i(2\hat{S}_{1x}\hat{S}_{2z} + 2\hat{S}_{2x}\hat{S}_{1z})s_{2t_1}$$

$$\xrightarrow{\left(\frac{\pi}{2}\right)_y} -(\hat{S}_{1y} + \hat{S}_{2y})c_{2t_1} \tag{42}$$

$$+ i(2\hat{S}_{2x}\hat{S}_{1z} + 2\hat{S}_{1x}\hat{S}_{2z})s_{2t_1}$$

Which is equivalent to $t_1 \rightarrow -t_1$ in $\sin at_1$, corresponding to time reversal with swapping of the antiphase coherences of the spins.

It is here that the similarity of the single and double resonance approaches, as shown in **Figure 2.15**, becomes apparent when comparing **Equation (38)** and **Equation (42)**.

2.6. Experiments in Pulsed Dipolar EPR Spectroscopy

Over time, a number of experimental techniques have been developed to measure the dipolar interactions of spins. This chapter describes three of the most prominent approaches: Double-Electron-Electron Resonance (DEER), Double Quantum Coherence (DQC), and Single-Frequency Technique for Refocusing Dipolar Couplings (SIFTER).

2.6.1. Double-Electron-Electron Resonance Experiment

Pulsed Electron Double Resonance (PELDOR) spectroscopy, also called DEER, is a resonance technique to study the interactions between radicals A and B. It was first described by Milov et al. in 1981 [49] by researchers from the Institute of Chemical Kinetics and Combustion at the Siberian Branch of the Russian Academy of Sciences in Novosibirsk and first observed 3 years later.
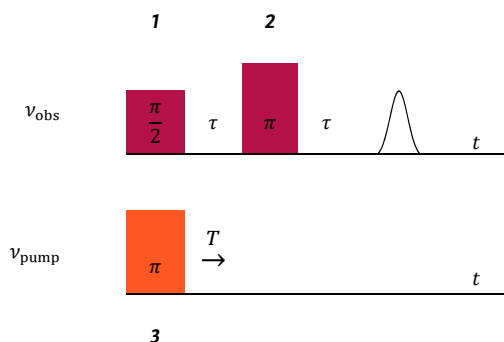
3-Pulse DEER

Figure 2.16.   3-pulse DEER sequence.

The first pulse sequence used to create a DEER trace consisted of 3 pulses and is therefore known as 3-pulse DEER. It consists of three pulses at two different frequencies – the pump and observer frequency – as shown in **Figure 2.16**.

Ideally, the pump pulse should excite only spin B, while the observer pulse should observe spin A.

In the observer pulse sequence, the first two pulses are used to generate an ESE signal at ω_A after time 2τ. The pump pulse at the frequency ω_B, however, will flip the B spin after time T. The result is the instantaneous change of the local magnetic field around spin B, which consequently shifts the EPR frequency of spin A. Since the detection is still at ω_A, the intensity of the observed signal will now change. If this is observed as a function of T, an oscillation of the altered spin B in the environment will be visible. This DEER signal contains the information about the spin-spin interaction.

Although very intuitive, this method has a major drawback which is the dead time t_{dead} just after $T = 0$ with a duration of at least half the sums of the π-pulse lengths [50], making it very difficult to characterize broad distance distributions.
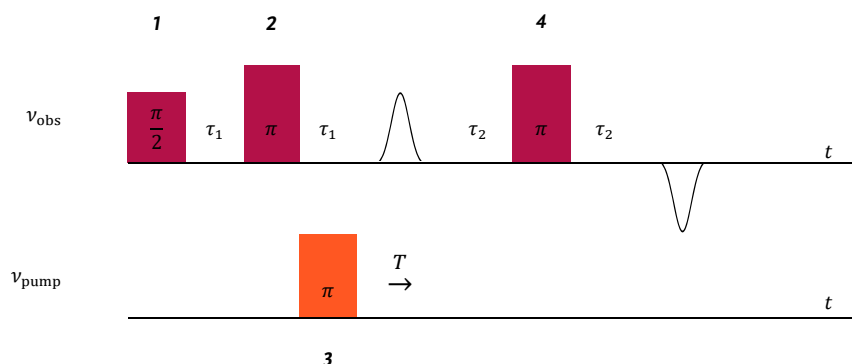
4-Pulse DEER

Figure 2.17. 4-pulse DEER sequence.

The major drawback of the 3-pulse DEER sequence led to the development of a 4-pulse sequence to overcome the dead time problems [51]. In this sequence, as shown in **Figure 2.17**, a Hahn echo is formed at the observer frequency after $2\tau_1$. An additional third pulse at $2\tau_1 + \tau_2$ refocuses the echo once more. If the pump pulse is then applied between the first refocusing pulse and the second one, the change in amplitude from $T = -\tau_1$ to $T = \tau_2$ can be measured. In this case, $T = 0$ is the time when the pump pulse coincides with the first generated echo.

Since this pulse sequence does not have an observer pulse at the same time as a pump pulse, there is no dead time as the effects of the two pulses interacting are not present.

2.6.2. Double Quantum Coherence Experiment

Another widely used single-frequency method is the Double Quantum Coherence (DQC) pulse sequence. A form of this "multiple-quantum coherence" has been known and used in NMR since the early 1980s. The DQC filtering technique selects electron double coherence, which allows the observation of weak dipolar couplings from relaxational decay [44].

All pulses in this sequence are applied at the same frequency, and it is important that they are very intense to be able to excite the entire spin distribution. As a consequence, very narrow EPR spectra are strongly preferred for this type of spectroscopy since they allow the use of regular microwave pulses.

Unfortunately, no intuitive model like the one used for DEER can be used in this context. In the following, only the most important parts of the pulse sequence are explained [42],[52]. For a more detailed mathematical interpretation, the reader is referred to the Ph.D. thesis of Akhmetzyanov [45].
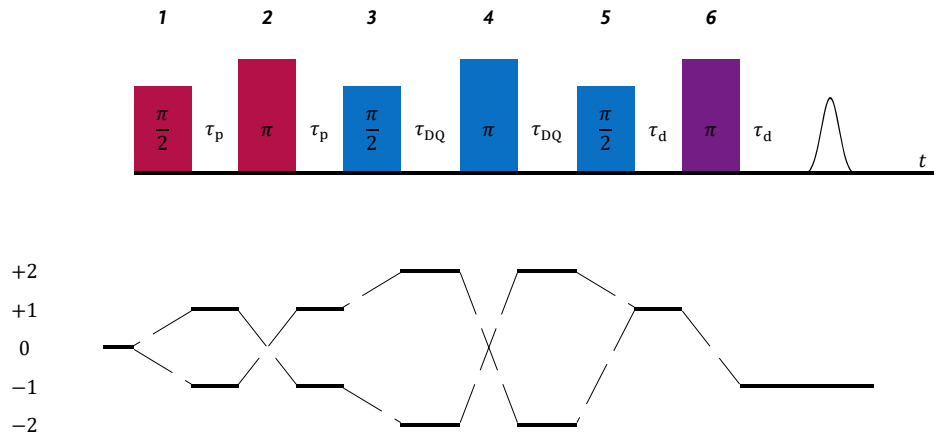
The Basic Principle of the DQC Sequence

Figure 2.18.   DQC pulse sequence including coherence pathway diagram.

- **Pulse *1* and *2* – Preparation:**

    First, in-phase coherence of character $\hat{I}_{12} = \hat{S}_{1y} + \hat{S}_{2y}$ is generated by applying a $\left(\frac{\pi}{2}\right)_x$ pulse (pulse 1) to the equilibrium state $\sigma_{12}(0)$. After that, the pulse sandwich $\tau_p - \pi_x - \tau_p$ (pulse 2) is used to evolve this in-phase coherence into $\hat{I}_{12} \rightarrow \hat{I}_{12} + \hat{A}_{12}$ with $\hat{I}_{12} = -\left(\hat{S}_{1y} + \hat{S}_{2y}\right)\cos a\tau_p$ and $\hat{A}_{12} = \left(\hat{S}_{1x}\hat{S}_{2z} + \hat{S}_{2x}\hat{S}_{1z}\right)\cos a\tau_p$ as well as refocusing any offsets.

- **Pulse 3 to 5 – Double Quantum Filter:**

  The $\left(\frac{\pi}{2}\right)_x - \tau_{DQ} - \pi_x - \tau_{DQ} - \left(\frac{\pi}{2}\right)_x$ sequence, also called as double-quantum filter (DQF), creates a double-quantum coherence with character $\hat{S}_{1x}\hat{S}_{2y} + \hat{S}_{1y}\hat{S}_{2x}$: This is achieved by first converting $\hat{A}_{12}$ to $DQ_y = -\frac{1}{2i}\left(\hat{S}_1^-\hat{S}_2^- - \hat{S}_1^+\hat{S}_2^+\right)\sin a\tau_p$ (pulse 3), while storing $\hat{I}_{12}$ as $-\left(\hat{S}_{1z} + \hat{S}_{2z}\right)$. The double quantum coherence then evolves to $DQ_y\left(2\tau_p + t\right) = \frac{1}{2i}\left(\hat{S}_1^-\hat{S}_2^- \exp(i(\Delta\omega_1 + \Delta\omega_2)t) - \hat{S}_1^+\hat{S}_2^+ \exp(i(\Delta\omega_1 + \Delta\omega_2)t)\right)\sin a\tau_p$. Refocusing using the $\tau_{DQ} - \pi_x - \tau_{DQ}$ sandwich (pulse 4) leads back to $DQ_y\left(2\tau_p + 2\tau_{DQ}\right) = \left(\hat{S}_1^-\hat{S}_2^- - \hat{S}_1^+\hat{S}_2^+\right)\sin a\tau_p$ and subsequent converting the DQ back to $\hat{A}_{12} = \left(\hat{S}_{1x}\hat{S}_{2z} + \hat{S}_{2x}\hat{S}_{1z}\right)\sin a\tau_p$ with the phase being labeled with the dipolar evolution at $2\tau_p$ (pulse 5).

- **Pulse 6 – Detection:**

  By refocusing with a final π-pulse (pulse 6), the signal reverts back to unobservable anti-phase coherence, which then evolves into observable coherence of character $S_{1y} + S_{2y}$, resulting in a detectable echo.

Labeling the Dipolar Contribution with the Double Quantum Filter

The term "filter" may be misleading in this case since it does not remove any signals but rather labels them for the following phase cycling. The result, however, is the same: DQF labels the double quantum signal parts from the interaction of the spins – the dipolar oscillations – and effectively separates them from the rest arising from the individual spins.

To achieve this separation, $\hat{I}_{12}$ with the phase $\Phi_{dip}\left(2\tau_p\right) = \cos a\tau_p$ is filtered to be $\hat{I}_{12} = -\left(\hat{S}_{1y} + \hat{S}_{2y}\right)\cos a\tau_p$, which further evolves into $\left(\hat{S}_{1y} + \hat{S}_{2y}\right)\cos a\tau_p \cos\left(a\tau_{DQ} - a\tau_p\right)$, which is observable.

It is important to emphasize that in this sequence, the targeted dipolar coupling is not refocused (as mentioned in 2.5.6). Only the suppression of the unwanted components by phase cycling isolates the desired dipolar coupling.

On the Importance of Phase Cycling

The aforementioned pulse sequence describes the desired path of coherence and the desired outcome. However, as one can immediately see from the pulse sequence, this is not the only thing that will happen in the sequence. Instead, a whole series of additional crossing echoes and interferences will occur because the pulse sequence consists of several subsets of what can be interpreted as Hahn echo sequences. To address these issues, proper and effective phase cycling must be conducted to isolate the pure dipolar coupling from all other contributions.

This phase cycling must be performed at the stage of the DQF. A basic cycle involves using the phases ϕ_k ($k = 1 \dots 3$) of the DQC pulses and the receiver phase ϕ_R in four steps, but it can be extended to be even more effective and robust [42],[53].

Table 2.1.   Basic phase cycle used to suppress unwanted coherence pathways in the DQC experiment.

Cycle	ϕ_1	ϕ_2	ϕ_3	ϕ_R
1	$+x$	$+x$	$+x$	$+y$
2	$+y$	$+y$	$+y$	$-y$
3	$-x$	$-x$	$-x$	$+y$
4	$-y$	$-y$	$-y$	$-y$

2.6.3. Single-Frequency Technique for Refocusing Dipolar Couplings Experiment

The "single-frequency technique for refocusing dipolar couplings" (SIFTER) pulse sequence, introduced in EPR by Jeschke and Spiess in the year 2000 [54], is – similar to DQC – best used when a strong non-selective pulse is able to excite almost the entire spectrum.
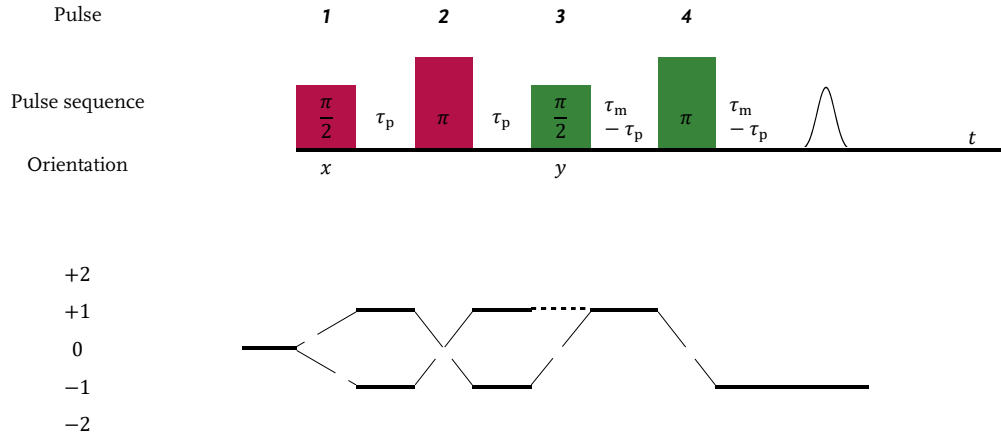
The Basic Principle of the SIFTER Sequence

Figure 2.19.   SIFTER pulse sequence including coherence pathway diagram.

- **Pulse *1* and *2* – Preparation:**

  The preparation stage consists of the same initial pulses used in the DQC sequence (see 2.6.2). It results in the evolution of $\hat{I}_{12}$ into $\hat{I}_{12} + \hat{A}_{12}$, where $\hat{I}_{12} = -\left(\hat{S}_{1y} + \hat{S}_{2y}\right)\cos a\tau_\mathrm{p}$ and $\hat{A}_{12} = \left(\hat{S}_{1x}\hat{S}_{2z} + \hat{S}_{2x}\hat{S}_{1z}\right)\cos a\tau_\mathrm{p}$.

- **Pulse *3* and *4* – Coherence Transfer and Detection:**

  If the sequence were not treated further, this would evolve and result in $\hat{\sigma}(2\tau_\mathrm{m}) = \left(\hat{S}_{1y} + \hat{S}_{2y}\right)\cos a\tau_\mathrm{m}$. Since the dipolar coupling is hidden in τ_m, this would not be very useful.

  However, applying a $\left(\frac{\pi}{2}\right)_y$ -pulse changes the sign of the antiphase term by coherence transfer according to $2\hat{S}_{1x}\hat{S}_{2z} \leftrightarrow -2\hat{S}_{2x}\hat{S}_{1z}$. This leads to the evolution that now results in $\hat{\sigma}(2\tau_\mathrm{m}) = \left(\hat{S}_{1y} + \hat{S}_{2y}\right)\cos a\tau_x$, with $\tau_x = 2\tau_\mathrm{p} - \tau_\mathrm{m}$. This can be recorded as a full echo, completely modulated by dipolar oscillations, and used for further analysis.

On the Effects of Finite Pulses

The previous discussion did not take into account that real pulses are not infinitely short but have finite lengths. This, in consequence, complicates everything. SIFTER itself is not capable of filtering, which effectively leads to all possible dipolar paths being used and detected. To neglect these, a finite π-pulse must be able to flip a large portion of spins contributing to the signal, which is only the case for very narrow spectra such as trityl. Isolated single spins can also cause contributions to the background signal, and the only way to address these is to use very intense shaped pulses that ensure a small unflipped fraction of spins.

2.7. From Time Trace to Distance – The Tikhonov Regularization

Extracting the distance distribution $P(r)$ from the experimental time trace $V(t)$ is mathematically non-trivial since an inverse problem must be solved. According to the Hadamard definition, many inverse problems do not fulfill one of the following criteria and are, therefore, ill-posed:

1. Existence. A solution to the problem exists.
2. Uniqueness. One solution to the problem exists.
3. Stability. The solution is stable and does not depend on small variations.

In the case of distance measurements, the third criterion of stability is a big problem because even small errors from noise or improper isolation of the signal can lead to large errors in the distance distribution.

The TIKHONOV Regularization

Several methods are known to "stabilize" these ill-posed inverse problems: One of the most powerful ones is the Tikhonov regularization [45],[55],[56]. It is defined as follows:

$$P_\alpha = \underset{P \geq 0}{\mathrm{argmin}} \left(\|V - KP\|^2 + \alpha \|LP\|^2 \right) \tag{43}$$

Where V is a discretized n_t-element vector with elements $V_i = V(t_i)/V_0$, K is the $n_t \times n_r$ kernel matrix with elements $K_{ij} = K(t_i, r_j)$, P as a n_r element vector with $P_i = P(r_i)$ and α is a regularization parameter; in the case of dipolar spectroscopy L is often chosen to be the second derivative operator, and the double vertical bars indicate the Euclidian norm of a vector.

If α is chosen appropriately here, the first term of **Equation (43)** yields a solution that is compatible with the experiment, while the second term smooths this estimate to remove unwanted properties of the solution.

From this, the regularized solution P_α is obtained by minimizing the functional in **Equation (43)**, giving rise to:

$$P_\alpha = (K^T K + \alpha L^T L)^{-1} K^T S \tag{44}$$

This expression is easily solved by using singular value decomposition available in most common computation software packages.

The L-curve Criterion

But how to choose an "appropriate" α? Choosing it too large will smooth the distance distribution $P(r)$ too much; choosing it too small will create artificial peaks. A common way to choose this parameter is based on inspecting the L-curve generated by plotting $\log(\eta_\alpha)$ against $\log(\rho_\alpha)$, where $\rho_\alpha = \|S - KP_\alpha\|^2$ is the mean square error to the solution and $\eta_\alpha = \|LP_\alpha\|^2$ is the smoothness.

Looking at the L-curves shown in the middle sub-figure of **Figure 2.20**, the optimal α is located at the intersection of the steeply sloped part and the non-steeply sloped part.

Practical Applications

Due to the reliability and robustness of the Tikhonov regularization, it has become the most widely used approach for extracting distance distributions from dipolar spectroscopy. It is also implemented by the widely used MATLAB toolbox for the analysis of dipolar time traces

"DeerAnalysis", its Python variant "DeerLab" and its standalone variant "ComparativeDeerAnalyzer" by the Jeschke group in Switzerland [57].
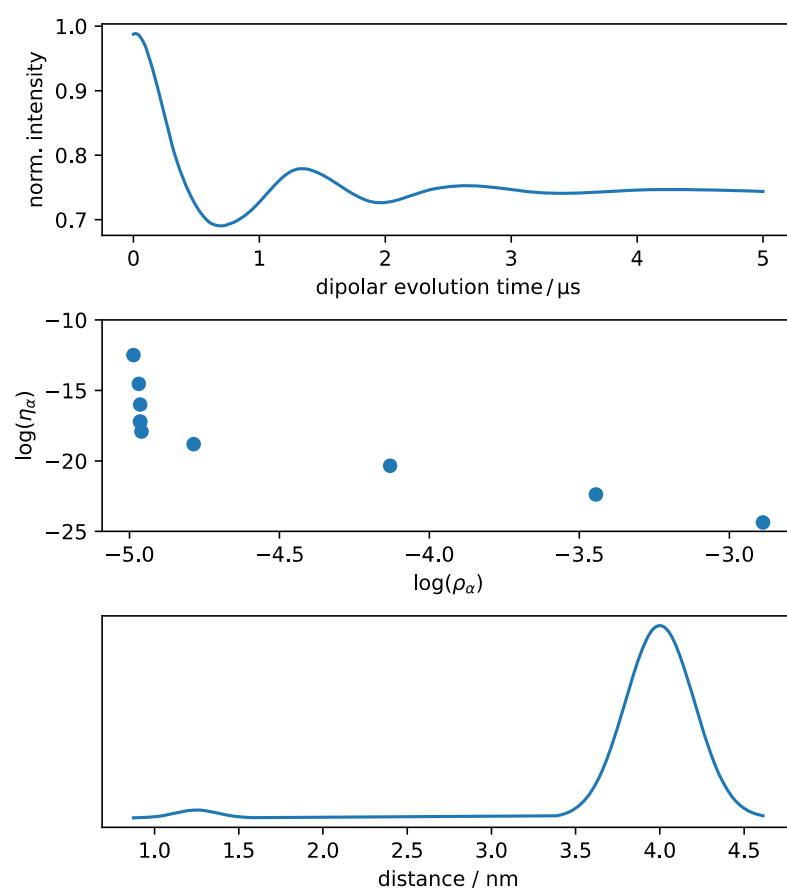

Figure 2.20.   Simulated dipolar evolution time trace (top) with its corresponding L-curve (middle) and resulting distance distribution (bottom). Adapted from Akhmetzyanov [45].

3

NOVEL BRIDGES FOR
MULTI-QUBIT SYSTEMS

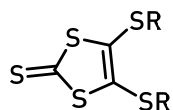# 3. NOVEL BRIDGES FOR MULTI-QUBIT-SYSTEMS

This chapter presents the process of designing and preparing novel bridges for multi-qubit systems. First, a thorough literature research for possible coordination sites and bridges was conducted in 3.1, which was based on the requirements outlined in 2.1. They were then elaborated to find the most suitable one for 2-qubit systems. These candidates were then analyzed retrosynthetically in 3.3, and the results of the synthesis are presented in Chapters 3.4 and 3.5.

In order to easily identify the new types of ligands and compounds, the nomenclature shown in **Figure 3.1** is introduced. The base designator for all compounds is **CS$_n$SP[R],** where the appropriate parts of the coordination site (**CS**) and the spacer part (**SP**) are substituted. In cases where **CS** is greater than one, the entire **CS$_n$SP** unit is referred to as a bridge.
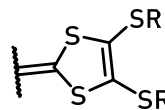
The group **R** designates either the protection group or, alternatively, the metal coordination sphere. For example, a compound named **dmdt$_2$Anthra[TiCp$_2$]** contains an anthraquinone spacer coupled to two dimercaptodithiole coordination sites that coordinate to two titanocene(IV) centers.
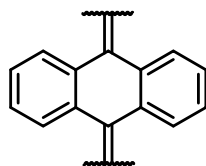
CS (Coordination Site):
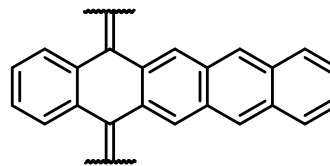

dmit
dimercaptoisotrithione

dmdt
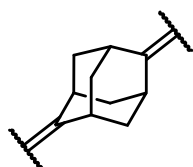4,5-dimercapto-1,3-dithiole-2-yl

SP (2-yl Modification, if applicable):

Anthra
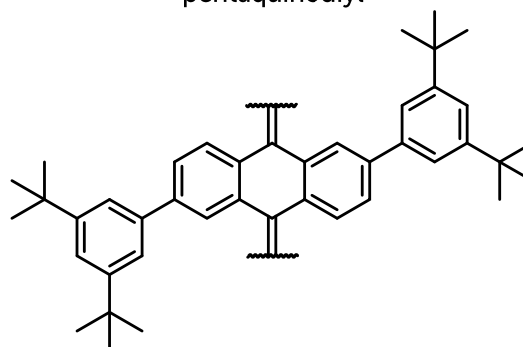anthraquinodiyl

Penta
pentaquinodiyl

Ad
2,6-adamantandiyl

Dtbpa
di-tert-butylphenylanthraquinodiyl

Figure 3.1.   Nomenclature of compounds used in Chapter 3 and 4.

3.1. Building Blocks of Qubit-Systems

As already previously discussed in 2.1, molecular qubits should have a well-defined spin-state S. In addition, the removal of weakly coupled nuclear spins in the environment improves the coherence time. For multi-qubit systems, some additional design criteria come into play: The inter-qubit coupling must be weak and is typically essentially dipolar in its nature. Therefore, it is crucial that the distance between the qubits is well defined – usually around 16 Å – and does not fluctuate. Preferably, they also do not exhibit a strong electron transfer behavior because this can interfere with the coordination environment of the two coordination metals. Hence, rigid, electronically inert bridges between the qubits are required.

3.1.1. The Spacer Unit: The Use of Rigid Spacers in Chemistry up to now

In general, all spacers discussed can be grouped into two archetypes – several examples thereof are shown in **Figure 3.2**.

On the one hand, spacers can be grouped into those that are mainly saturated, such as 2D and 3D alkyl structures. They can vary from adamantane to exotic stellane structures and are shown under (a). On the other hand, unsaturated structures that allow some degree of conjugation, such as quinoid structures or partially conjugated spiro-compounds, are shown under (b).

So far, saturated systems such as those shown in **Figure 3.2**a have not been used in the design of multi-qubits. Nevertheless, ligands that fit the criteria can be found in literature. Belser et al. published rigidly bridged osmium and ruthenium compounds in the 1990s, which are capable of binding metal ions at well-defined distances by using adamantane, cyclobutane, and similar rigid systems. However, these were not used for qubit applications at that time but rather for use in basic photophysical research on electron and energy transfer [58]–[62].
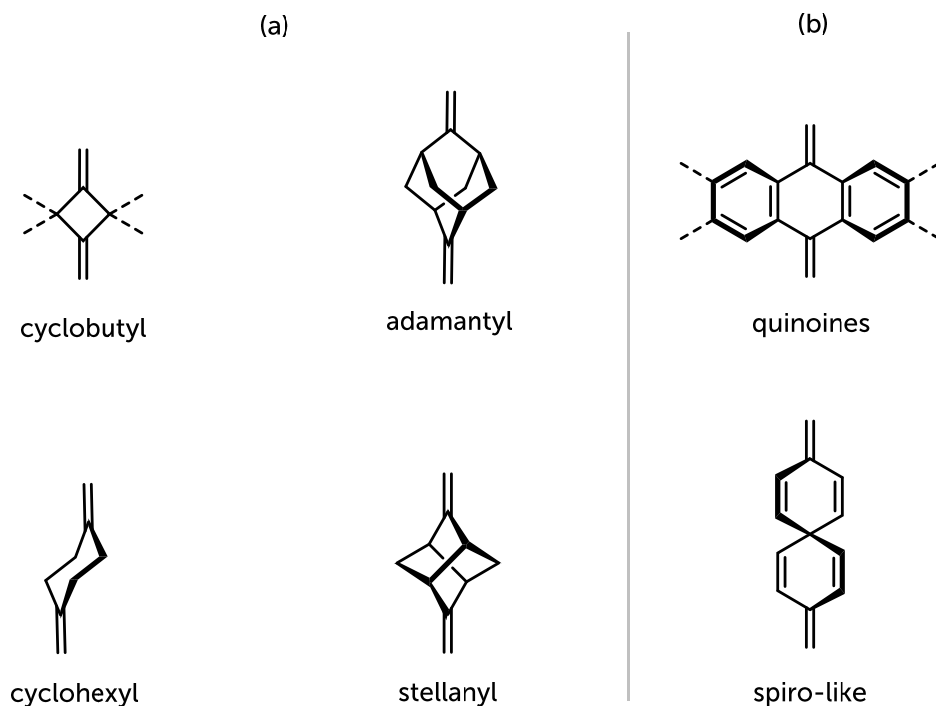
(a)   (b)

cyclobutyl   adamantyl   quinoines

cyclohexyl   stellanyl   spiro-like

Figure 3.2.   Examples of different types of central spacers. (a) shows saturated ligands, while (b) shows spacers with unsaturated character.

In addition, the group around Martin et al. [63] published another very rigid system, which was a spiro-conjugated tetrathiofulvalvene-type (**TTF**-type) ligand used as an alternative electroactive system, as shown in **Figure 3.3**b. Seemingly on par with the adamantyl systems in terms of structural rigidity, they share the major common drawback that the synthesis of the corresponding diketones is very tedious and over a total of 8 steps with a combined yield of 5 % unsatisfying. Nevertheless, the overall flexibility is immensely limited, and as such, they still seem to be an interesting choice for use in possible ligand design applications for molecular qubits.
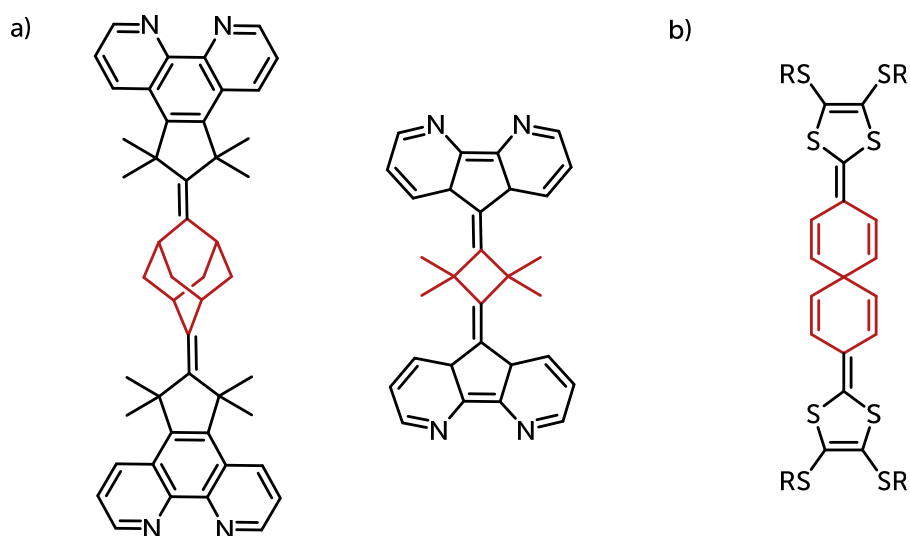
Figure 3.3.   Selection of compounds used by the group of (a) Belser [60],[62] in their research about photonic devices as well as (b) by Martin [63] in electroactive systems with their respective rigid part highlighted in red. R = alkyl

In addition to these systems, a large number of systems used in extended **TTF** (**exTTF**) chemistry are known, and some examples are shown in **Figure 3.4**. They also are vastly explored synthetically, which may prove beneficial in the development of a new qubit system.
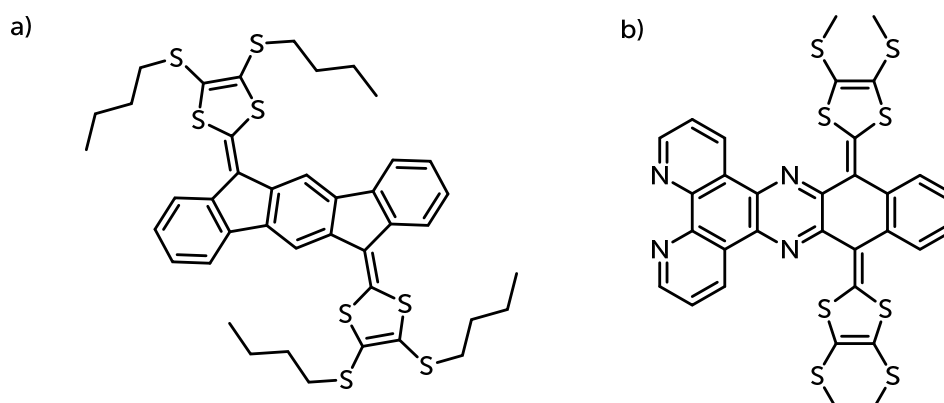

Figure 3.4.   (a) **exTTF**-indenofluorene used by the Nielson group [64] and (b) **exTTF**-dpq dyad used as an electrooptical cation chemosensor by the Hudhomme group [65].

Compared to the very rigid systems of Belser and Martin, these larger quinoid systems still retain some degree of flexibility. They can easily deform in the pseudo-aromatic plane, as can be seen in the example crystal structure shown in **Figure 3.5**.
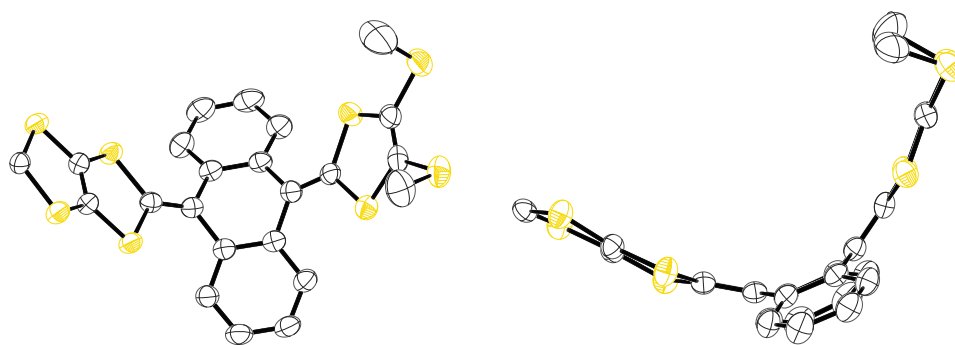

Figure 3.5.   An anthraquinone coupled to a dithiolene unit as described by Misaki [66]. Part of the structure, as well as hydrogens, were omitted for clarity; thermal ellipsoids are drawn at 50% probability level. Color code: Carbon (white), Sulfur (yellow).

Of these three structural motifs, compounds formed from the central spacers shown in **Figure 3.2** are the most interesting, although structures such as stellanyl-based or spiro-based are much harder to obtain than others.

3.1.2. The Coordination Site: 1,2-Dithiolenes vs. 1,3-Diketones

The question of choosing a suitable coordination site is answered by looking at two important properties of these sites: Synthetic modifiability and the influence on the electronic spin of a coordinated metal.

In quantum technology, qubits are mainly coordinated by either oxygen, sulfur, or nitrogen. Two of them belong to the group of (mostly) nuclear spin-free elements, with nitrogen being the exception. This leaves one with two main coordination sites worth considering based on their use in literature: 1,2-Dithiolenes, such as **dmit,** and 1,3-diketones, such as dibenzoylmethane **dbm**. Both should not affect the spin of the electron, which is located on the coordinated metal.

However, synthetic modifications work differently in the two systems. For the intended application, **dmit** will be more advantageous. As shown in **Figure 3.6**, it is a symmetric, planar molecule, whose backend can be heavily modified. Literature reports vast possibilities of modifying the thione functionality as it is still used heavily in **exTTF** chemistry for use in molecular conductors. For example, the preparation of a phosphonate or phosphonium salt gives the molecule the ability to undergo a Horner-Wadsworth-Emmons reaction or a Wittig reaction. This results in the formation of a C=C double bond, which is beneficial for the rigidity of a qubit system.
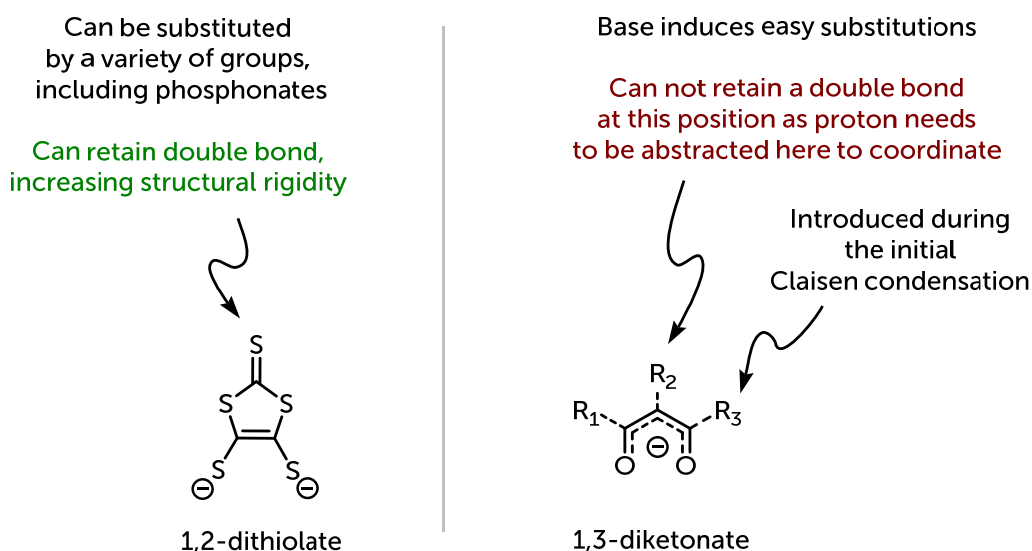
Can be substituted
by a variety of groups,
including phosphonates

Can retain double bond,
increasing structural rigidity

Base induces easy substitutions

Can not retain a double bond
at this position as proton needs
to be abstracted here to coordinate

Introduced during
the initial
Claisen condensation

1,2-dithiolate

1,3-diketonate

Figure 3.6.   Manipulations possible on the (left) 1,2-dithiolate **dmit** and (right) a generalized 1,3-diketonate. R = alkyl or aryl.

The formation of a rigid double bond at the backend will never be possible on a 1,3-diketone since deprotonation at the 2-position is essential for the formation of coordination compounds. These modifications would have to be introduced on either side of the diketone, making the molecule asymmetric and less rigid.

3.2. Evaluation of Hypothetical Dimeric Structures

In the previous section, the individual parts of the target systems were discussed. The next step is, therefore, to elaborate on how to chemically link the two parts together. The target structure is shown in **Figure 3.7**. It consists of two coordination sites, which contain the qubits, linked by double bonds to a rigid spacer.
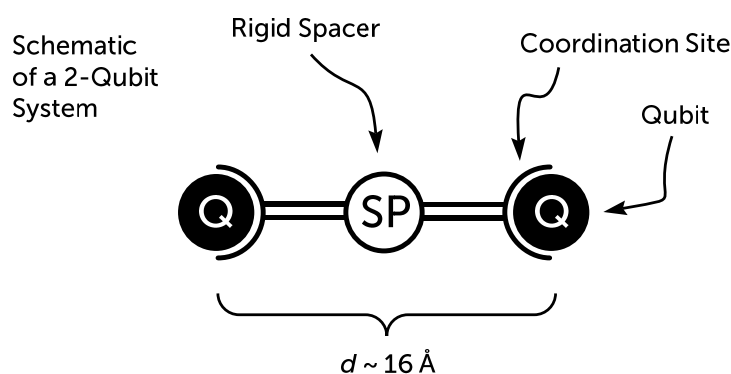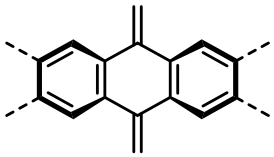
Schematic of a 2-Qubit System

Rigid Spacer

Coordination Site

Qubit

$$Q \!=\! SP \!=\! Q$$
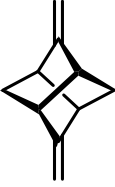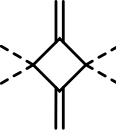
$$d \sim 16\,\text{Å}$$

Figure 3.7. Schematic design of a 2-qubit system aimed towards.

In order to evaluate promising candidates among the combinations formed by the spacers and coordination sites described in 3.1, structures based on **dmdt**-spacer-**dmdt** were crudely optimized by the universal force-field (UFF) method available in Avogadro and subsequently by DFT (B3LYP/def2-tvzp). The important results thereof are shown in **Table 3.1**.

Three parameters were used to characterize the structures: The first is the inter-spin distance d, which is the distance between two metal ions coordinated to the **dmdt** coordination sites. The second is the angle of intersection α of the planes of the **dmdt** ligands with each other since the ligand plane is likely directly connected to the principal magnetic axis of the coordinated metal ion. Third, the extent of potential electron delocalization over the ligand, which might affect the (non)-innocence of the ligand. For this, electron structure calculations were conducted, which through the Mayer bond indices, indicated this delocalization.

Table 3.1. Hypothetical structures of **dmdt**-spacer-**dmdt** ligands. d defines the approximated distance of coordination centers when attached to both available dithioles, while α is the angle the two ditholene rings are oriented to one another. Additionally, the electronic interaction capabilities of the two coordination sites as well as the difficulty of the synthesis are indicated. Colors indicate suitability, where green is optimal, yellow considerable, and red undesirable.

		d / Å	α / °	conjugation
1		13.79 (11.46[a])	108	π connected
2		19.96	90	isolated
3		16.70	90	isolated
4		16.73	53	isolated
5		15.66	0	σ connected[b]

[a] distance in different, but less likely, isomer.
[b] high chance of being electronically connected by σ-orbital overlap.

As shown **Table 3.1**. the preferred interspin distance of 16 Å is well met by the cyclobutyl compound due to its much smaller ring size. The adamantyl- (3) and the stellanyl-based (4) compounds follow closely with 16.7 Å, while the quinoid structures have estimated distances of 13 Å (1) and 20 Å (2).

Perpendicular orientation of the ligand planes is preferred to distinguish the two qubits more easily. This preference arises from the fact that the magnetic axes of the qubits will likely be perpendicular to each other. Two compounds fit this requirement best – the adamantyl-based (3) and the spiro-based (2) compound, with the coordination sites being truly 90° offset from each other. The stellanyl-based ligand, on the other hand, forces a geometry where the sites are offset by about 53°. Quinoid structures align the two sites at 108° to each other. The cyclobutyl-based unit is different, as it has coplanar **dmdt** ligand rings, thus an angle of 0°.

Since the qubit should be well localized on the central metal, the ability of electrons to hop through ligands, changing the position of the spin qubit, must be restricted. From the five prototypes shown, only the quinoid-based ligand is potentially conjugated. The cyclobutyl here is again different, as the ring size is so small that σ-overlap can occur. All other systems exhibit strong electron barrier properties by having multiple non-conjugating bonds or high torsion angles, also restricting orbital overlap.

In summary, only one motif is not very appealing to pursue in a synthetic sense: The cyclobutyl-basis is ruled out, as – although the interspin distance matches quite well – the fact that the coordination sites are coplanar, and the electronic situation is not fully clear. Much more preferred are the adamantyl and stellanyl spacers, closely followed by the quinoid spacers.

3.3. Development of the Retrosynthetic Approach

The retrosynthesis resulting from Section 3.2 is outlined in **Figure 3.8** and in the following paragraphs. It involves the modification of the coordination site and possibly the synthesis of the spacers.

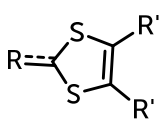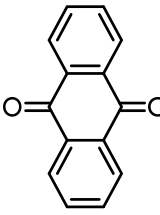### 3.3.1. Coupling of Coordination Site and Spacer

Since the goal is to obtain a rigid system, the thione functionality of the **dmit** unit must be replaced by a C=C double bond. Several ways are known to do this. Although a considerable amount of work has been done on the phosphite-mediated coupling of **dmit** units with electron-rich ketones, this route will not be applicable to some types of spacers as they can be electron-poor and hinder this type of reaction. Other coupling reactions to form C=C double bonds, such as the Barton-Kellogg reaction, are also not applicable because they require a diazo compound, which is not known to be formable from either **dmit** or from quinoid ketones or aliphatic ketones. Thus, literature proposes both Horner-Wadsworth-Emmons (HWE) reactions as well as Wittig reactions to couple a modified **dmit** bearing a phosphonate or phosphonium unit to ketones, as referred to in **Table 3.2**.

Overall, the most convenient and versatile preparation would be to pursue an HWE- or a Wittig-reaction. Both are applicable to both electron-rich ketones and electron-poor ketones, and reagents for these types of reactions have already been described in literature. In a direct comparison, however, the HWE reaction is clearly superior, as it has several advantages over the classical Wittig reaction:

- The byproduct of the Wittig reaction is rather inert and, therefore hard to remove triphenylphosphine oxide, whereas the byproduct of an HWE reaction is a phosphate ester that is highly water-soluble and can be easily removed by a simple organic work-up procedure.
- The reaction intermediate of the HWE reaction is much more reactive as it is a nucleophilic anion compared to the net-neutral ylide formed in a Wittig reaction.
- The formation of the triphenylphosphine species used in Wittig reactions tends to favor primary halides, whereas the Arbuzov reaction to form the HWE phosphonate generally tends to be less problematic in this respect.

The only drawback of a standard HWE reaction is the need for an electron-withdrawing group (EWG), whereas this is not a limitation for a Wittig reaction. In the case of dithiols, the sulfur atoms in the ring suffice as such an EWG, albeit a rather unconventional one. Upon deprotonation during the HWE reaction, the negative charge is delocalized over the dithiol ring, thus making the phosphonate a very good leaving group.

Table 3.2. Possible reaction mechanisms to couple a possible **dmit** system with linkers.

		electron-rich	electron-poor
Reaction Type	phosphite-mediated ketone coupling (R = O)	✔	✘
	Horner-Wadsworth-Emmons (R = PO(OR'')$_2$)	✔	✔
	Wittig (R = PR''$_3$)	✔	✔
	Barton-Kellogg (R = N$_2$ / S)	✘	✘

To summarize, the following retrosynthetic scheme can be deduced, as shown in **Figure 3.8**. The first step is to generate the dmit base ligand, which is then S-alkylated to then be replaced, over an iodo-intermediate, with a phosphonate that can be used as a reagent for an HWE reaction.
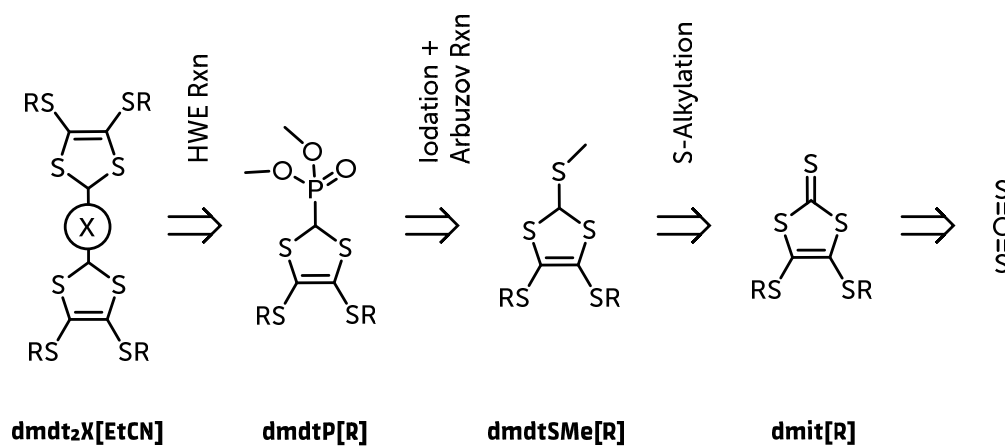

dmdt₂X[EtCN]   **dmdtP[R]**   **dmdtSMe[R]**   **dmit[R]**

Figure 3.8.   Retrosynthetic approach for preparing target ligands. X = **Ad**, **Anthra**, **Penta**, **Dtbpa**; R = protection group.

3.3.2. Commercial and Synthetic Accessibility of the Spacers

A preferred synthesis can be classified as easy to perform based on the length of the route to the ligand, the yields, and the availability of specific precursors.

Quinones have by far the best commercial availability. They are widely available as off-the-shelf chemicals in great variety. Cyclobutyl rings are also readily available in a permethylated form, although the use of such a system has been ruled out. Recently, 2,6-adamantandione has been available from smaller chemical suppliers, as this chemical is most likely a "waste" product of the hydroxylation of adamantanes. Targeted synthetic preparation of this compound is nearly impossible, with some yields in the low single-digits.

This brings us to the last two compounds, which are especially hard to obtain as they involve long synthetic routes or no convenient route in literature whatsoever. The spiro diketone, referred to as 2 in **Table 3.1**. is available through a 7-step synthesis as outlined in **Figure 3.9**, and the preparation of the stellane diketone, referred to as 4, is described with 6-steps involving photochemistry and ozonation as shown in **Figure 3.10**. Thus, although both molecules contain interesting spacer units, the approximate doubling of the synthetic steps to a useful ligand makes these spacers unattractive for first research.
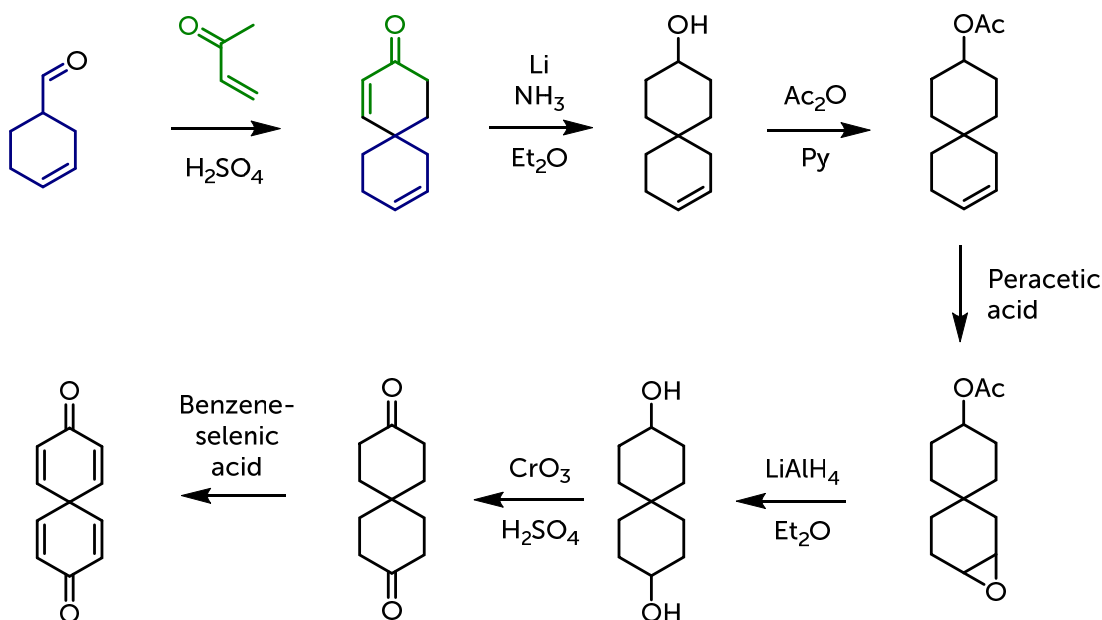

Figure 3.9.   Synthetic route to obtain the spiro diketone described in literature by Martín [63].
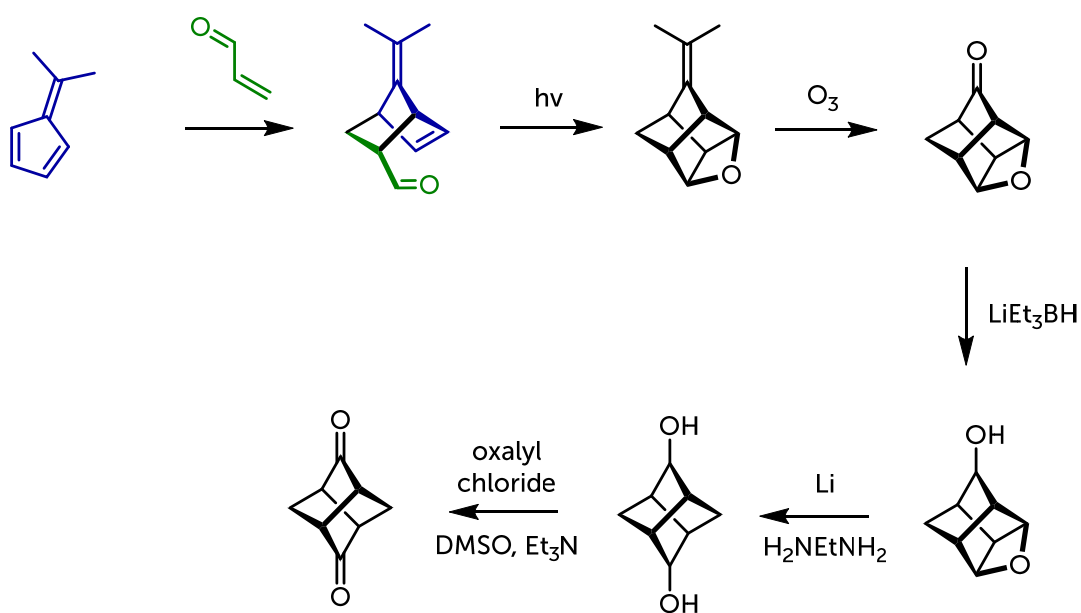
Figure 3.10. Synthetic route to obtain the stellanyl diketone described in literature by Oeser [67].

3.4. Modification of the Coordination Site: dmdtP

Synthetic modifications of the **dmit** motif have been known since the early 1980s. The modifications primarily relied on alkylthiole dmit derivates, which were rarely even pursued to be removed afterward. In this application, this is though crucial. Standard labile protection groups on the **dmit** thiols found in the literature are mainly benzoyl or propionitrile, as shown in **Figure 2.11**.
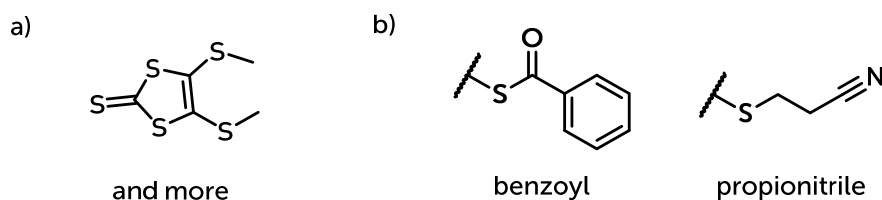

Figure 3.11. Commonly used protection groups of **dmit**. (a) Most widely spread protection groups if **dmit** is modified. (b) Most widely spread protection groups if **dmit** is used as a ligand.

The problem with the protection groups is that these also are prone to base attacks. This either drastically reduces yields or prevents the isolation of the target compounds altogether. The group needs to be stable towards the conditions later used in the HWE reaction, yielding **dmdtP**. As propionitrile appears stable in the presence of butyl lithium, which is used in the HWE reaction later, it was chosen as a protection group.

In addition to the mentioned stability reason, the deprotection group was used once to form the heavily modified **dmit** compounds from Kusamoto et al. [68]. In this paper, one of the crucial compounds needed to couple the dmit coordination site is reported but refers to literature where the deprotection group is never used. Sadly, crucial synthetic information is missing, and the ^{1}H NMR reported is inconsistent with what is expected and later found. This also presents the main reason why this chapter will highlight the synthetic challenges, which evolved from the synthesis of **dmdtP**.

As outlined in the retrosynthetic approach in **Figure 3.8**, the phosphonate **dmdtP** will be generated via an HWE-reaction of an intermediately formed iodo-compound **dmdtI**, which is generated by the cleavage of the methyl thioether **dmdtSMe**. This ether is accessible by methylating the thione of the starting **dmit**. **dmit** itself can easily and in large quantities be generated from the reaction of sodium with carbon disulfide.

The synthetic route toward **dmdtP** is accounted for in detail in the following section, including synthetic optimizations removing tedious purification steps and making medium-scale synthesis a treat.

3.4.1. Preparation of the Sulfur-Rich Heterocycle **dmit**

Most likely first described by Fetkenheuer et al. [69] by accident and later more purposefully by Hoyer et al. [70], the convenient preparation of large amounts of **dmit** has interested many research groups.

Hoyer's approach was surprisingly simple, cheap, and highly scalable and therefore became the standard method for preparing large quantities of this sulfur-rich ligand. He enhanced the procedure by precipitating **dmit** as its zincate rather than struggling with complicated

chromatographic purifications. As a bonus, the zincate proved far more stable than the alkali salts and thus provided a shelf-stable **dmit**-source:
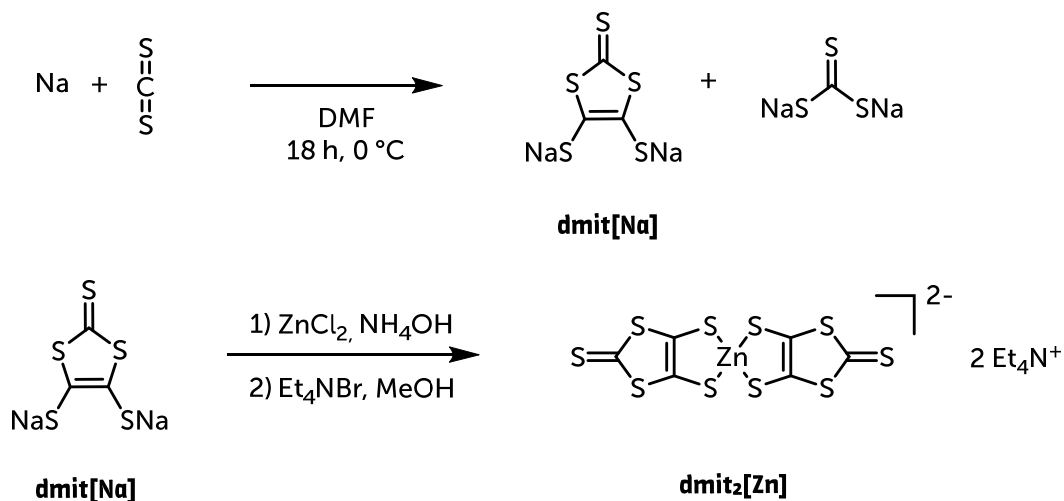

dmit[Na]

Figure 3.12. Generation and isolation of the **dmit** heterocycle described first by Hoyer et al. [70].

This thesis also employed the same route to access large quantities of this ligand. Generally, the synthetic route was employed on a multimolar scale, regularly yielding the zincate in good yields of up to 80 %. This carmine red powder can be used without further purification for the coming synthetic steps.

3.4.2. Protection

To use the **dmit** for synthetic applications, in the next step, the zincate intermediate was treated with the propionitrile protection group bromide in analogy to Recatalá [71].
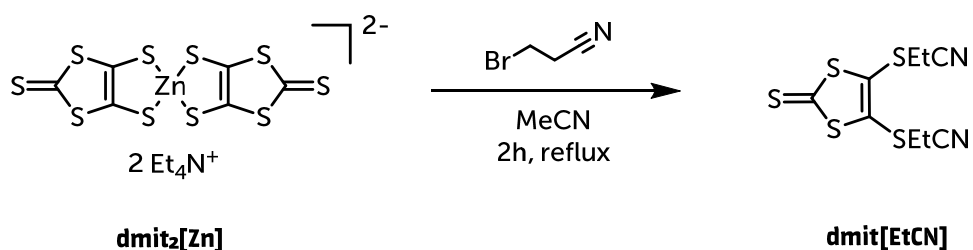

Figure 3.13. Preparation of **dmit[EtCN]**.

Therefore, an intensely pink-red zincate solution was prepared in regular acetonitrile and refluxed for 2 h after the addition of 3-bromopropionitrile. During this time, the solution changed color to ochre yellow. Removal of the formed precipitate and concentration on a rotary evaporator left a viscous oil. This oil was then crystallized by adding a large excess of ethanol, resulting in a bright yellow fine precipitate, which overnight condensed into long, golden needles in the freezer. Sometimes, a dark brown solid formed at the bottom of the flask. ^{1}H NMR analysis confirmed that this residue is also pure **dmit[EtCN]**, which, when crushed with a mortar and pestle, turned into a bright yellow powder suitable for further use. This precipitation is not necessarily required, and if the added purity of the crystalline product is not needed, it can be skipped by completely evaporating the solvent. As a result, **dmit[EtCN]** was isolated as both yellow needles and as a yellow powder in appropriate yields of 89%.

3.4.3. S-Alkylation

For the alkylation of the **dmit**'s thione function, two methods were chosen during the course of this thesis. The first one involved toxic dimethyl sulfate, which was quickly abandoned in favor of trimethyl orthoformate, as shown in **Figure 3.14**. The only negative effect of this change is the longer reaction time. However, since this was done overnight, it was considered a much more convenient and safe approach.

To obtain the crude dithiolium intermediate, a solution of **dmit[EtCN]** in chloroform was treated simultaneously with both the methylating agent trimethyl orthoformate as well as tetrafluoroboric acid diethyl ether complex overnight under stirring. The next day, the chloroform was removed utilizing rotary evaporation, leaving a red, viscous liquid of the crude product **(dmdtSMe[EtCN])BF$_4$**.

To obtain the S-alkylated **dmdtSMe[EtCN]**, the thiolium salt **(dmdtSMe[EtCN])BF$_4$** was immediately dissolved in MeCN and reduced with sodium borohydride. When the reaction mixture turned pale yellow, the reaction was stopped. If the mixture is stirred for longer, the pale yellow color changes more and more to orange, which then generally results in lower yields.

In literature, the crude product was purified by column chromatography. Since the preparation of these substances was usually done on a large scale with 20 g of product or more, this method was optimized. Vacuum-assisted dry column chromatography [72] with DCM was used to separate minor byproducts easily. Removal of the DCM from the purified thioether yields a very viscous light yellow liquid which solidifies overnight in the freezer to a pure off-white solid with good yields of up to 72%.
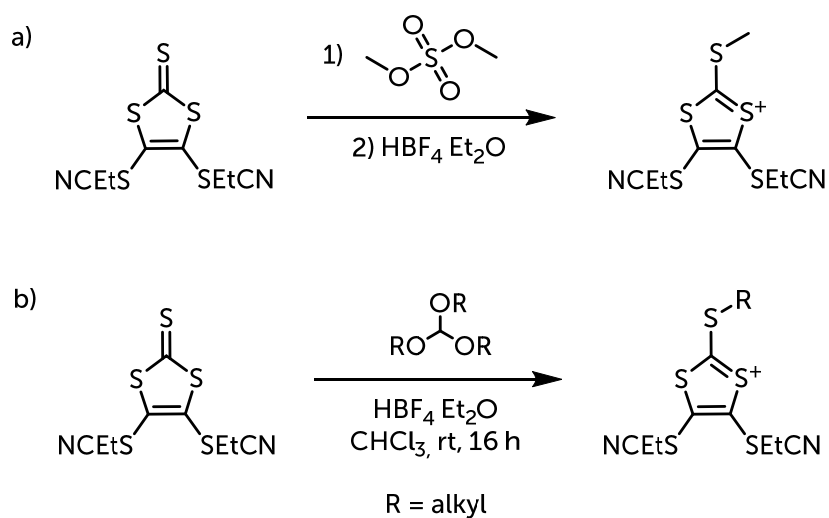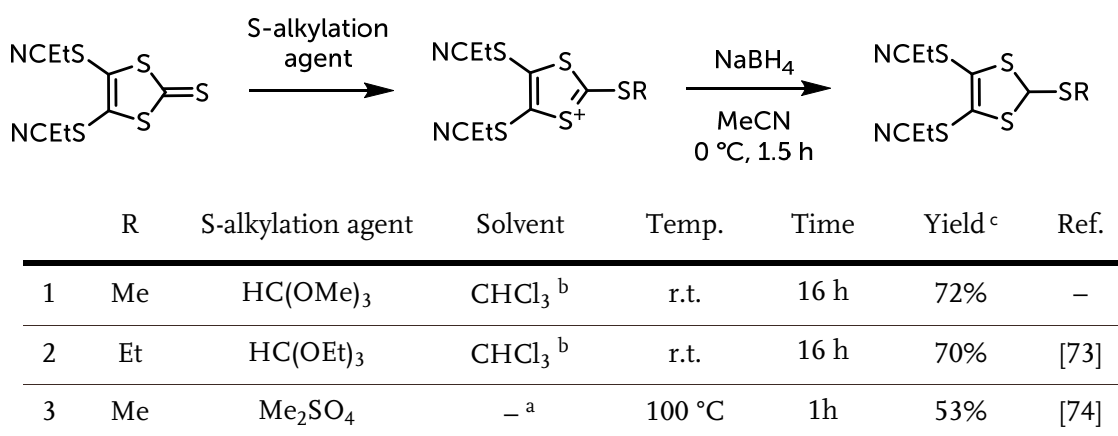

Figure 3.14.   Alkylation methods of the thione functionality of **dmit[EtCN]**.

As can be seen in Table 3.3, the alkylation without the use of dimethyl sulfate not only drastically reduced the hazardousness of the reaction but also improved yields quite a bit from ~50% to ~70%. This is probably due to the much longer reaction time.

Table 3.3. Reaction conditions of the alkylation of **dmit[EtCN]** with different S-alkylation agents.

	R	S-alkylation agent	Solvent	Temp.	Time	Yield[c]	Ref.
1	Me	HC(OMe)$_3$	CHCl$_3$ [b]	r.t.	16 h	72%	–
2	Et	HC(OEt)$_3$	CHCl$_3$ [b]	r.t.	16 h	70%	[73]
3	Me	Me$_2$SO$_4$	–[a]	100 °C	1h	53%	[74]

[a] neat. HBF$_4 \cdot$ Et$_2$O complex added afterwards.
[b] HBF$_4 \cdot$ Et$_2$O present during alkylation.
[c] Average yields acquired during this thesis.

3.4.4. Phosphonation

The phosphonation of the S-alkylated product proved to be the most challenging of the reactions. Despite an enormous amount of literature reports, this reaction was poorly reproducible initially. In particular, the purity of the thiolium intermediate is crucial for the subsequent reactions.

First, as described in literature, the thioether is cleaved from **dmdtSMe[EtCN]** in analogy to the formation of the thiolium salt described in Section 3.4.3: The addition of HBF$_4 \cdot$ Et$_2$O to a solution of the thioether in acetic anhydride produces a dark red solution of the thiolium salt over the course of 2 h. The crude salt was precipitated from the solution by adding a large volume of diethyl ether: The addition of approximately two times the volume of the reaction yields a brown viscous, sometimes semi-solid thiolium salt on the bottom of the flask, which in principle can be used further. However, it has been found that the purity of this **(dmdtH[EtCN])BF$_4$** is crucial for the next step. If it was not of sufficient purity, the next step – the precipitation of the **dmdtI[EtCN]** intermediate by the addition of sodium iodide – was highly unreproducible.
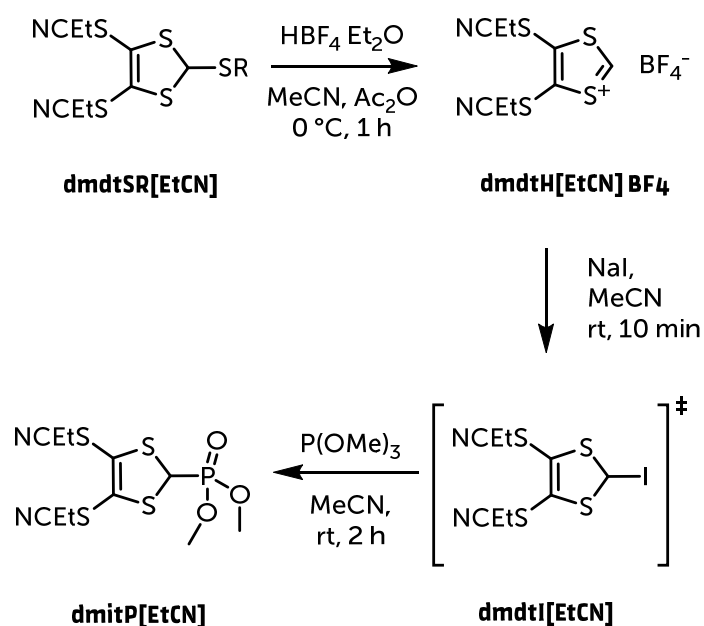
Figure 3.15. Reaction pathway of the Arbuzov reaction to obtain the HWE reagent **dmdtP[EtCN]** starting from **dmdtSMe[EtCN]**.

To solve this issue, precipitation was induced during the reaction rather than after. Unfortunately, the amount of diethyl ether present in the tetrafluoroboric acid diethyl ether complex is insufficient to cause the salt to precipitate. Adding more diethyl ether at the beginning of the reaction turned out to be the key to resolving this issue. Instead of using pure acetic anhydride as a solvent, a 1:1 mixture of acetic anhydride and diethyl ether consistently forced the formed thiolium salt to precipitate already during the reaction. Interestingly, the thiolium salt did not precipitate as a red, oily semisolid but as a beige, rather pale powder. ^{1}H-NMR analysis also confirmed that the precipitate was the desired thiolium salt. This solid was washed several times with diethyl ether to remove as much of the reaction mixture as possible. It was decided not to filter the substance, as it is unstable in air, and multiple washes also gave good results.

The second step was to prepare the Arbuzov intermediate – 2-iodo-dmdt **dmdtI[EtCN]**. This was easily accomplished by starting with the dithiolium salt, dissolving it in acetonitrile, and slowly adding solid sodium iodide to the solution. During this slow addition, a large amount of the yellow iodo compound was formed, turning the entire reaction mixture into a viscous slurry. The addition of trimethyl phosphite then rapidly cleared the yellow slurry

to become a vibrant orange solution. Extraction of the reaction solution with DCM and washing with large quantities of water yielded a sufficiently pure solution of the phosphate, which crystallized on concentration in a rotary evaporator, eliminating the need for column chromatography.

The compound itself is a pastel orange. An essential factor for determining its purity is the absence of any other phosphorus species that could interfere with the subsequent coupling reactions. Analysis of both proton decoupled and coupled ^{31}P NMR spectra confirmed the absence of such while also revealing a rather nice splitting pattern in the ^{13}C{^{1}H} NMR spectrum, as shown in **Figure 3.16**.

In the ^{13}C{^{1}H} NMR spectrum shown in **Figure 3.16**, two doublets result from the coupling with the ^{31}P nucleus ($I = 1/2$). The two coupling constants, $^1J_{P,C} = 164.6$ Hz and $^2J_{POC} = 7.7$ Hz are characteristic of carbon-phosphorus and carbon-oxygen-phosphorus couplings, respectively.
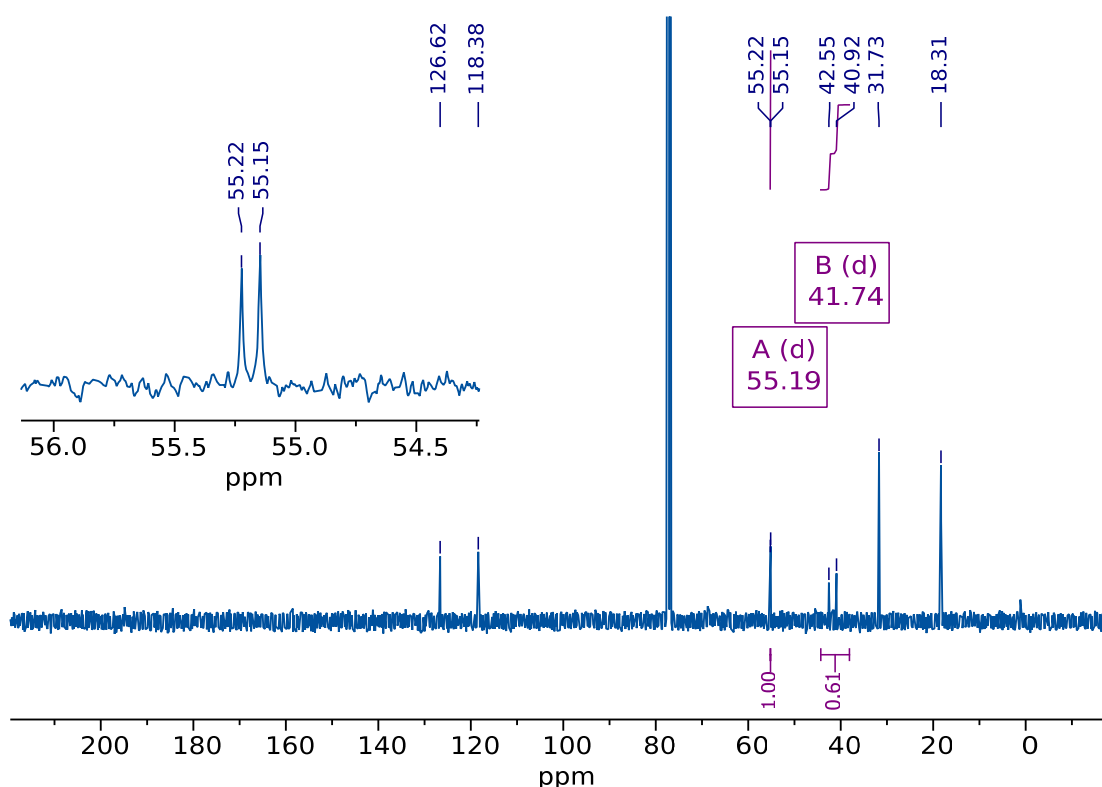

Figure 3.16. ^{13}C{^{1}H} NMR spectrum of **dmdtP[EtCN]** in CDCl$_3$.

3.5. Preparation of **dmdt**-Spacer-**dmdt**-Type Ligands

The previous section described the synthesis of the functionalized **dmit** derivative **dmdtP[EtCN]**, which will serve as the coordination site for the qubit systems. In this section, we discuss the coupling of this compound to adamantyl and quinone spacers.

3.5.1. Optimization of the Horner-Wadsworth-Emmons Reaction

The HWE reaction used here, outlined in **Figure 3.17**, is not traditional. Traditionally, the α-carbon of the phosphonate is attached to a strong electron-withdrawing group like an ester. In this case, the electron-withdrawing group consists of the 1,3-dithiole of the **dmdt** moiety, which generates an α-C heterosubstituted phosphorus ylide upon treatment with base. In the book by Kolodiazhnyi [75], a whole chapter is dedicated to the diverse chemical properties of non-traditional phosphates for use in HWE reactions. In this respect, **dmdt**-ylides can be quite remarkable because relatively weak bases like triethylamine already deprotonate them.
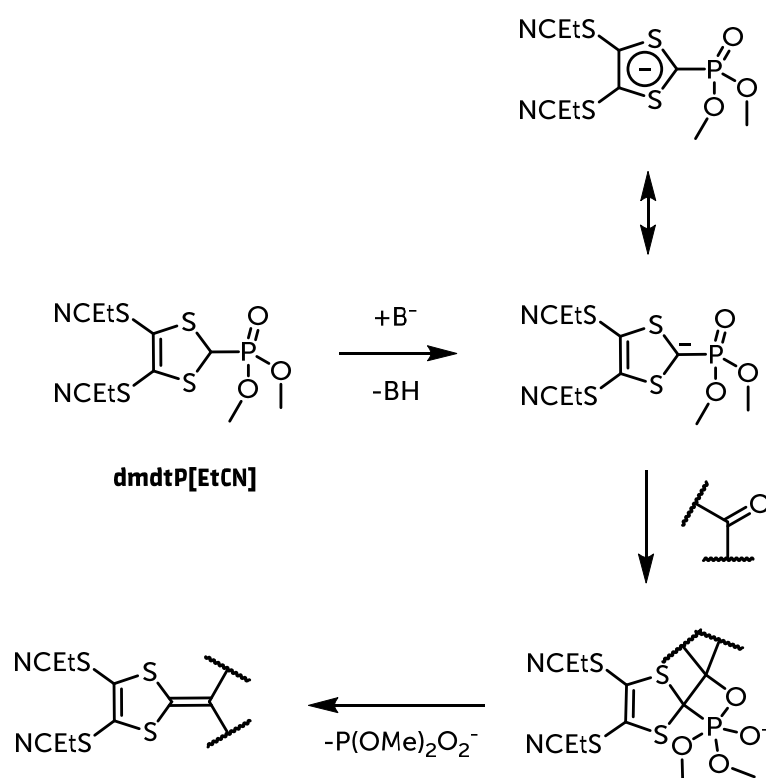

Figure 3.17.   Generation of the phosphonate anion and reaction to form the **dmdt** C=C bond.

This method is also widely used in literature to generate a modified backbone of a **dmdt** molecule, especially among the physically large **exTTF**s [65],[76].

To optimize the reaction conditions for this coupling with the propionitrile protecting group, which is labile towards reactions with bases, several mono-**dmdt** precursors were chosen as test compounds: Acetone as the simplest ketone and a monosubstituted adamantane itself as it is the central part of one of the target bridging spacers.
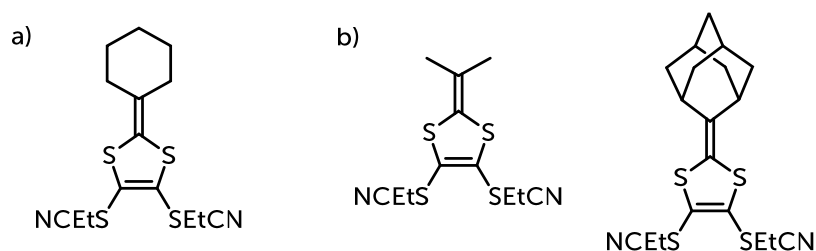

Figure 3.18.   (a) **dmdt** coupled system by Kusamoto et al. [68]. (b) Targets for the optimization of **dmdt** HWE reactions based on acetone and adamantanone as the ketones.

In order to optimize the HWE conditions for these reactions, the reaction conditions used in literature were used as a starting point. They are generally consistent with standard reaction procedures used in HWE reactions: Cooling to –78 °C, treatment with a base, stirring for an appropriate amount of time before and after adding the ketone, and a classical aqueous-organic work-up procedure.

In the case of the reaction of **dmdtP[EtCN]** with acetone and admantanone, it was found that a reaction time of 1.5 to 2 h in THF to generate the reactive phosphonate in combination with a gradual warming to room temperature over the course of 12 h after the addition of an undissolved ketone gave good results.

During the slow addition of butyl lithium, the orange solution of **dmdtP[EtCN]** underwent a color change to brown-green. An aqueous workup, often resulting in a purple aqueous phase and an orange organic phase, yielded the crude coupling product, which was subsequently purified either by column chromatography or, preferably, recrystallization.

After these optimization steps, a yield of about 59 % was obtained for the **dmdtAd[EtCN]**, and 93% for **dmdtiPr[EtCN]** as shown in **Table 3.4**.

3.5.2. Applying the Horner-Wadsworth-Emmons Reaction

As outlined, the synthetic plan included the preparation of a very rigid adamantane-based bridging ligand as well as an alternative with an anthraquinone core structure. However, during the course of this thesis, additional ligands were synthesized to expand the scope of this work. The evolution of the ligands is shown in **Figure 3.19**. The modifications made to the ligands served different purposes:

The quinone-based ligand was modified to also inherit a much more extended π-system, thus allowing for some degree of photoactivity, as well as another modification to make the ligand system much more soluble by introducing tert-butyl phenyl groups, thus reducing the chance of obtaining insoluble metal complexes upon coordination.

In total, two additional ligands were targeted and successfully synthesized using the optimized conditions determined by **dmdtiPr[EtCN]** and **dmdtAd[EtCN]**, shown in **Figure 3.19**.

The reactions proceeded therein as expected, although it should be noted that the adamantane-based systems **dmdt₂Ad[EtCN]** were much less soluble than their quinone-based counterparts **dmdt₂Anthra[EtCN]**, **dmdt₂Penta[EtCN]** and **dmdt₂Dtbpa[EtCN]**. As a result, much more solvent was needed to extract and purify them.

To avoid tedious column chromatography, the purification of these ligands was performed as follows:

1. Recrystallization from a mixture of hexanes and ethyl acetate, usually in a 5:1 ratio.
2. Precipitation by layering a DCM solution with hexanes.

The preferred method of purification was related to the type of spacer, as adamantyl was precipitated, and the quinones were recrystallized. The only exception in this series was the highly soluble **dmdt₂Dtbpa[EtCN]** ligand, the only ligand to be purified by column chromatography.
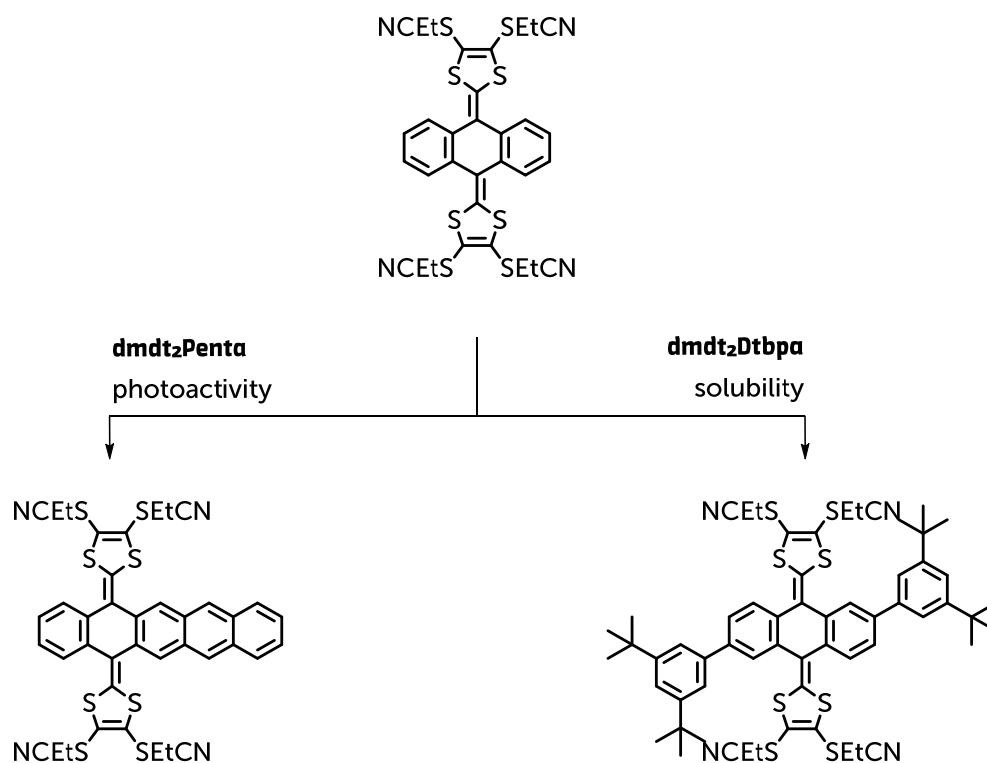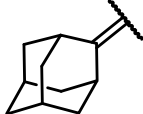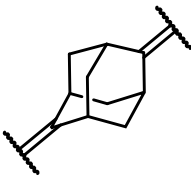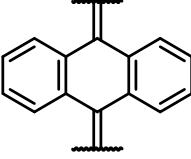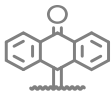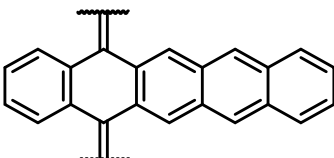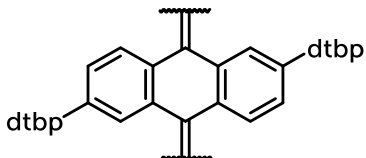
Figure 3.19.   Derivatives **dmdt₂Penta[EtCN]** and **dmdt₂Dtbpa[EtCN]** of the prototype **dmdt₂Anthra[EtCN]** with their respective property changes indicated.

In addition to the above, a monosubstituted byproduct was isolated from the **dmdt₂Anthra[EtCN]**, herein named **dmdtAnthrene[EtCN],** the crystal structure of which is shown in the appendix. A complete overview of the characteristics of the syntheses is given in **Table 3.4**. Overall, the double HWE reaction became well-behaved after initial coupling problems. Subsequently, these optimized synthetic routes could be easily transferred to the second generation of ligands with more modifications.

Table 3.4. Prepared HWE-coupling products throughout their generations with their yields and purposes. All products have the protection group **[EtCN]**.

		Name	Central spacer unit	Appearance	Purpose	Yield
0th generation	0a	**dmdtiPr**		off-white	synthetic optimization	93 %
	0b	**dmdtAd**		yellow		59 %
1st generation	1a	**dmdt₂Ad**		off-white powder	rigid isolation spacer	91 %
	1b	**dmdt₂Anthra**		yellow	semi-rigid spacer	46 %
	↳	**dmdtAnthrene**		red	(byproduct)	—[b]
2nd generation	2a	**dmdt₂Penta**		orange	semi-rigid barrier, photoactive	37 %
	2b	**dmdt₂Dtbpa**		brown	semi-rigid barrier, very soluble	49 %

[a] dtbp = 2,4-Di-tert-butylphenyl
[b] Yield not determined.

3.5.3. Crystal Structure of the Designed Bridges

Crystals suitable for X-ray diffraction of the protected ligands **dmdt₂Ad[EtCN]** and **dmdt₂Anthra[EtCN]** were obtained by slow evaporation from chloroform and dichloroethane, respectively.

The ligand **dmdt₂Ad[EtCN]** crystallizes in a triclinic crystal system with two additional chloroform molecules. The structure is shown in **Figure 3.20** and also in the appendix.
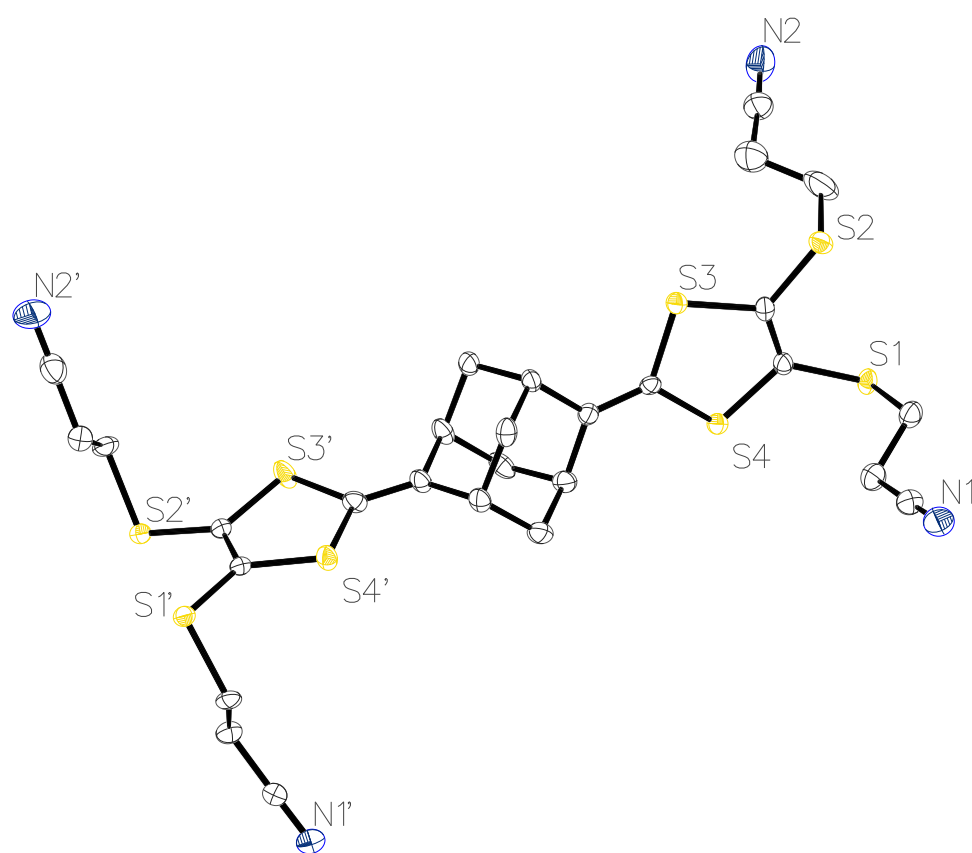

Figure 3.20.   Representation of the molecular structure of **dmdt₂Ad[EtCN]** in the crystal. Hydrogens and additional solvent molecules are omitted for clarity and thermal ellipsoids are drawn at 50% probability level. Color code: Carbon (white), Nitrogen (blue), Sulfur (yellow).
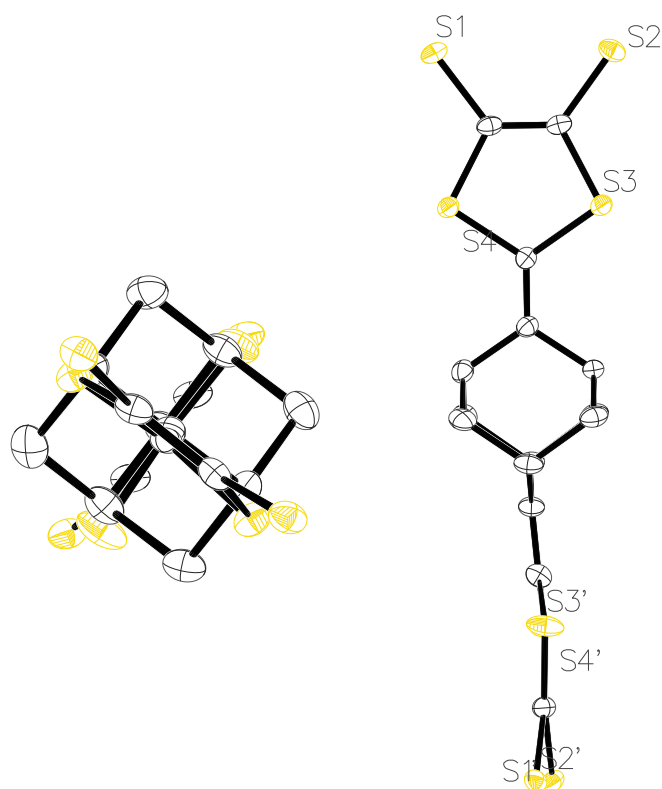
Figure 3.21. Molecular structure of **dmdt₂Ad[EtCN]** without EtCN protection groups. (left) View along the z-axis through the molecule. (right) Side-on view of the molecule. Hydrogens and additional solvent molecules are omitted for clarity. Color code: Carbon (white), Sulfur (yellow).

As previously suggested by careful analysis, the two coordination sites of **dmdt** are indeed perpendicular to each other: The angle of S3-C-S4 to S3'-C-S4' measured in the crystal is determined to be 96.2°, while the angle estimated in Chapter 3.2 was 90°. The **dmdt** ligand differs very little from the reported crystal data of **dmit** [77]. The dithiole ring system in **dmdt** is not completely planar but shows a slight curvature, as shown in **Figure 3.21**.

In contrast to the very rigid adamantane spacer, the crystal structure of the analogous **dmdt₂Anthra[EtCN]** shows quite well how flexible this type of system, in contrast, is. Chemical intuition would lead one to expect a more planar, conjugated system throughout

the ligand. In reality, the anthraquinone core is heavily bent, as is visible by looking at **Figure 3.22** and **Figure 3.23**.

This ligand **dmdt₂Anthra[EtCN]** also crystallizes in a triclinic crystal system with an additional dichloroethane molecule. The structure itself is shown in **Figure 3.22** and also in the appendix.
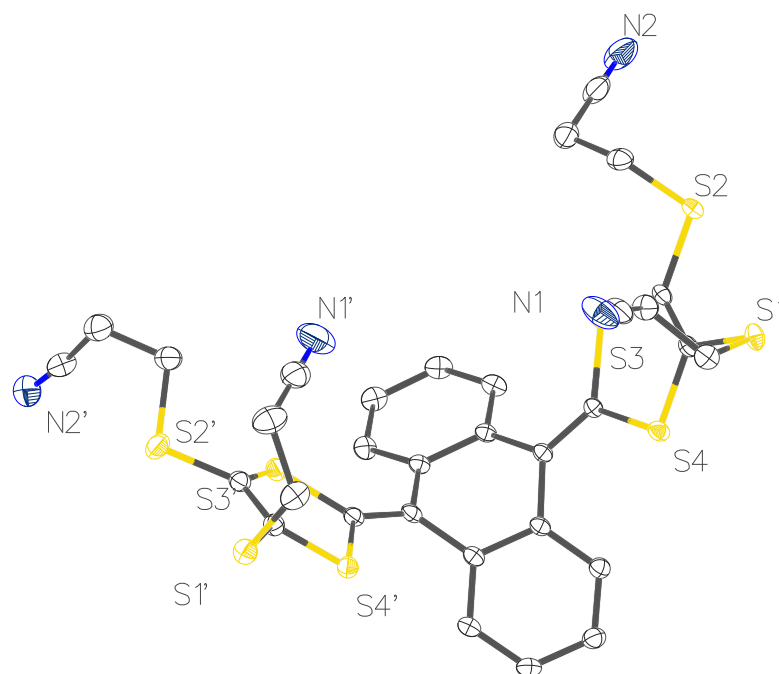

Figure 3.22. Representation of the molecular structure of **dmdt₂Anthra[EtCN]** in the crystal. Hydrogens and additional solvent molecules are omitted for clarity and thermal ellipsoids are drawn at 50% probability level. Color code: Carbon (white), Nitrogen (blue), Sulfur (yellow).
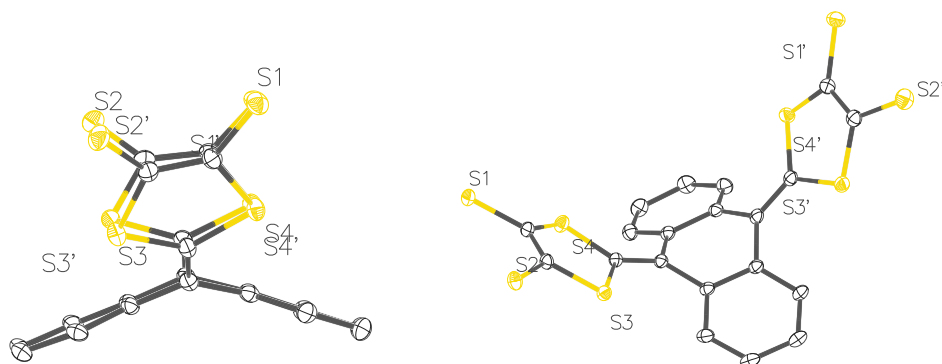
Figure 3.23.   Molecular structure of **dmdt₂Anthra[EtCN]** without EtCN protection groups. Hydrogens and additional solvent molecules are omitted for clarity. Color code: Carbon (white), Nitrogen (blue), Sulfur (yellow).

Besides the bent anthraquinone core unit, which flexes outwards, the coordination sites in this molecule are tilted 111.5° to each other, which agrees with the calculated angle of 108°. This can even have its benefits in contrast to a completely planar arrangement since, therefore, the S1-qubit-S2 planes will not be parallel to each other – the same reasoning for preferring a system like the adamantane-based one. The **dmdt** ligand in this molecule exhibits the same structural change to dmit as indicated in **dmdt₂Ad[EtCN]**.

An overview of the x-ray diffraction parameters and details of the two abovementioned structures are given in **Table 3.5**.

Table 3.5. X-ray details for **dmdt₂Ad[EtCN]** and **dmdt₂Anthra[EtCN]**.

	dmdt₂Ad[EtCN] · 2 CDCl₃	dmdt₂Anthra[EtCN] · DCE
empirical formula	$C_{30}H_{30}Cl_6N_4S_8$	$C_{32}H_{24}Cl_4N_4S_8$
fw / g mol^{-1}	915.84	862.913
T / K	130.0	140.01
cryst size / mm^3	$0.250 \times 0.212 \times 0.085$	$0.645 \times 0.325 \times 0.158$
cryst color	yellow	yellow
cryst system	triclinic	triclinic
space group	$P\bar{1}$	$P\bar{1}$
a / Å	11.5994(5)	11.9046(4)
b / Å	11.7233(6)	12.8093(4)
c / Å	14.3294(7)	14.2192(5)
α / °	93.677(2)	113.634(2)
β / °	97.814(2)	111.645(2)
γ / °	94.582(2)	92.816(2)
V / Å^3	1918.74(16)	1796.26(12)
Z	2	2
D_c / Mg m^{-3}	1.5851	1.595
μ / mm^{-1}	0.914	0.827
F(000)	940.0	883.4
θ range / °	2.88 – 52.96	3.46 – 61.20
reflns collected	30610	48839
unique reflns	7850	10978
R_{int}	0.0398	0.0321
R_{sigma}	0.0456	0.0300
data / restraints / params	7850 / 0 / 433	10978 / 0 / 433
GOF on F^2	1.035	0.827
R_1 [I > 2σ(I)]	0.0449	0.0414
wR$_2$ (F2)	0.1322	0.1095
max diff. peak and hole / e A^{-3}	2.01 / −1.13	2.03 / −1.11

3.6. Conclusion

In this chapter, novel rigid ligand systems have been designed from scratch for use in molecular multi-qubit quantum technologies based on the principles established in the community.

First, suitable targets derived from literature were screened by geometric optimization and electronic structure calculations based on the synthetic challenge of preparing large quantities of them. In this process, the synthesis of the ligands themselves was optimized to improve yields, reduce toxicity and shorten the preparation time.

The result was a new family of ligands called **dmdt₂X**, where **X** represents spacers ranging from quinoid structures to adamantane-based spacers that strongly inhibit electronic interactions and steric movement – they are shown in **Figure 3.24**. Such systems are not yet known in literature, especially with these goals in mind.
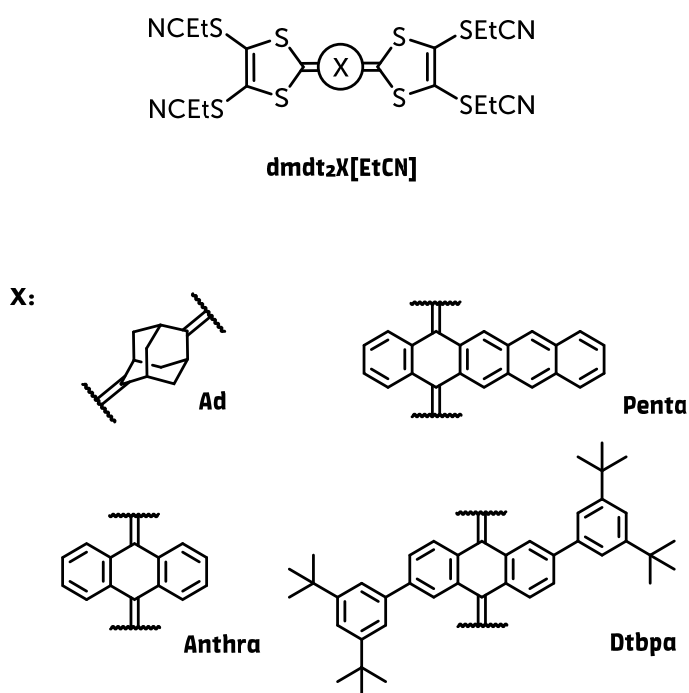

Figure 3.24. Varieties of **dmdt₂X** ligands evaluated and prepared.

3.7. Experimental Section

All manipulations were – unless stated otherwise – carried out under an atmosphere of argon or nitrogen using standard Schlenk line techniques. Dry solvents were purchased from Acros Organics in AcroSeal bottles or dried using standard techniques. Commercially available chemicals listed in the supporting information were used as received unless otherwise stated. For known compounds, spectral data were compared to literature to confirm identity, and if possible, new data was acquired, or changes in the synthetic approach were denoted.

Chromatography was performed on silica 60 (diameter 0.040 – 0.063 mm). Reaction control was performed with thin-layer chromatography plates (TLC) made from Silica 60 impregnated with F_{254} by Macherey-Nagel.

Solution NMR spectra were recorded on either a Bruker Avance AV250 (^{1}H 250 MHz), Bruker Avance AV300 (^{1}H 300 MHz; ^{13}C 63 MHz), a Bruker Ascend 400 (^{1}H 400 MHz; ^{13}C 101 MHz, ^{31}P 161.9 MHz), a Bruker Avance AV500 (^{1}H 500 MHz) or a Bruker Ascend 700 (^{1}H 700 MHz) at 303 K. Spectra are always referenced against residual solvent signals.

IR spectra were recorded on a Bruker Vektor 22 FT-IR spectrometer in ATR mode by the analytics division of the Institute of Organic Chemistry, University of Stuttgart.

ESI mass spectra were recorded on a Bruker Daltonics Micro-TOF Q spectrometer and **EI mass spectra** on a Finnigan MAT95 at 70 eV by the analytics division of the Institute of Organic Chemistry, University of Stuttgart.

Elemental analyses (C, H, N, S) were determined on an Elemental Micro Cube analyzer by Barbara Förtsch, Institute of Inorganic Chemistry, University of Stuttgart.

Single-crystal X-ray diffraction data was collected and partially resolved by Wolfgang Frey on a Bruker AXS Nanostar C diffractometer equipped with a Kappa APEX II Duo charge-coupled device detector. Structural solution was done with Olex2 [78]. Non-hydrogen atoms were refined anisotropically.

3.7.1. **dmdt** Modifications

[NBu₄]₂[Zn(dmit)₂]

#### Bis(tetraethylammonium)(bis(1,3-dithiole-2-thione-4,5-dithiol)zincate)

Finely ground sodium (14.5 g, 631 mmol, ground with a kitchen grater) was carefully covered with CS_2 (302 g, 240 mL, 4 mol) in a 2 l Schlenk flask equipped with a pressure-equalizing dropping funnel. While cooling at 0 °C, DMF (480 mL) was slowly added as a solvent over a period of 45 min to start the reaction. During this time, the solution turned dark red. The reaction was then allowed to warm to r.t. and was stirred overnight. The next day, MeOH (50 mL) was carefully added under cooling to quench any residual sodium metal under cooling. A solution of zinc chloride (21.5 g, 158 mmol) in concentrated ammonia (35%, 400 mL) and water (100 mL) was added through the dropping funnel. Finally, a solution of tetraethylammonium bromide (66.3 g, 315 mmol) in water (500 mL) was added over 30 min with vigorous stirring. Overnight, a very fine red-orange precipitate formed, which was collected by suction and washed with large quantities of water, ether and isopropanol, yielding a dusty carmine red powder.

Yield: 66% (70 g, 104 mmol).

dmit[EtCN]

4,5-Bis(cyanoethylthio)-1,3-dithiole-2-thione

To a solution of **[NEt₄][Zn(dmit)₂]** (15.0 g, 21 mmol) in MeCN (250 mL), 3-bromopropionitrile (8.7 mL, 13.9 g, 103 mmol, 5 eq.) was added. This solution was stirred at 100 °C for 2 h. After approx. 1 h the solution turned yellow. The yellowish-white precipitate formed was filtered off, the filtrate was diluted with DCM (250 mL) and washed with water (3 × 100 mL). The
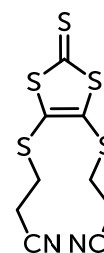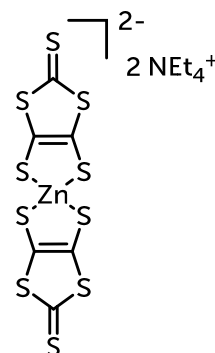
organic phase was dried with anhydrous sodium sulfate and concentrated by removing most of the solvent. Addition of a large excess of EtOH (600 mL) results in the formation of a bright yellow precipitate. Overnight, long golden-yellow needles and a brown solid formed in the freezer. The product was isolated by filtration, washing with cold EtOH and drying in vacuo as needles and a yellow powder (after crushing the brown solid).

Yield: 89% (15.2 g, 49.8 mmol).

^{1}H NMR (CDCl$_3$, 400 MHz): δ = 3.16 (t, J = 6.9 Hz, 4 H, CH$_2$CN), 2.80 (t, J = 6.9 Hz, 4 H, SCH$_2$).

Spectral data is consistent with reported data [71].

(dmdtSMe[EtCN])BF$_4$

2-Methylthio-4,5-bis(cyanoethylthio)-1,3-dithiolium tetrafluoroborate

Route A:

Dimethyl sulfate (13 mL, 17.4 g, 138 mmol, 7 eq.) was added to **dmit[EtCN]** (6.0 g, 20 mmol). The resulting suspension was heated to 100 °C for 1 h. After cooling, tetrafluoroboric acid diethyl ether complex (6.8 mL, 8.0 g, 49 mmol, 2.5 eq.) was added. 15 min later, Et$_2$O (200 mL) was added, causing the orange reaction solution to turn dark red and very viscous. After stirring for additional 15 min, the oil formed was then washed with Et$_2$O to remove any residual dimethyl sulfate and tetrafluoroboric acid to yield the product as a reddish brown viscous oil (sometimes a ockre solid) sufficiently pure for further use.
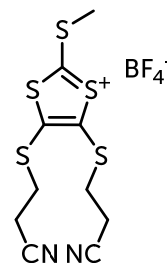
Route B:

To a solution of **dmit[EtCN]** (30.0 g, 99 mmol) in CHCl$_3$ (1500 mL) trimethyl orthoformate (43.1 mL, 41.8 g, 394 mmol, 4 eq.) and tetrafluoroboric acid diethyl ether complex (67.0 mL, 79.8 g, 493 mmol, 5 eq.) were added. The reaction mixture was stirred at room temperature overnight. *Caution: Be aware that pressure may build up in the reaction vessel if sealed.* After removing the solvent under vacuum, the crude dithiolium salt was washed with diethyl ether (3 x 100 ml). The dark brown, very viscous salt was used in the next step without further purification.

Yield was not determined as the product was used directly in the next step.

^{1}H NMR (CD$_3$CN, 400 MHz): δ = 3.37 (t, J =6.7 Hz, 2 × 2 H, SCH$_2$), 3.11 (s, 3 H, SMe), 2.85 (t, J = 6.7 Hz, 2 × 2 H, CH$_2$CN) ppm.

^{13}C NMR (CD$_3$CN, 101 MHz): δ = 208.20 (1 C, CSMe), 148.33 (2 C, C=C), 118.85 (2 C, CN), 33.90 (2 C, CH$_2$S), 24.14 (2 C, CCN), 19.23 (1 C, SCH$_3$) ppm.

HRMS (ESI+): *m/z*, calculated for [M]$^+$ (C$_{10}$H$_{11}$N$_2$S$_5$): 318.9520, found: 318.9512.

dmdtSMe[EtCN]

2-Methylthio-4,5-bis(cyanoethylthio)-1,3-dithiole

Sodium borohydride (9.3 g, 246 mmol) was added at 0°C to the tetrafluoroborate salt prepared from **dmit[EtCN]** (30.0 g, 99 mmol) dissolved in MeCN (500 mL). The solution was stirred for 1 h, during which time it lost its color. The solution was carefully quenched with cold water (50 mL) and extracted with DCM (1 L). The organic phase was separated, dried with anhydrous sodium sulfate and concentrated. After flash column chromatography (DCM, SiO$_2$) and removal of the
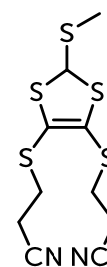
solvent, a yellow-white solid was obtained overnight in the freezer.

Yield: 73% (23.0 g, 71.8 mmol).

R_f = 0.37 (DCM, UV_{265} visible).

^{1}H NMR (CDCl$_3$, 400 MHz): δ = 5.73 (s, 1 H, CHSMe), 3.26 (m, 2 H, CH$_2$S), 2.95 (m, 2 H, CH$_2$S), 2.78 (m, 4 H, CH$_2$CN), 2.27 (s, 3 H, SMe) ppm.

^{13}C NMR (CDCl$_3$, 101 MHz): δ = 126.2 (2 C, C=C), 117.8 (2 C, CN), 58.3 (1 C, CHSMe), 31.5 (2 C, CH$_2$S), 18.7 (2 C, CCN), 15.3 (1 C, SCH$_3$) ppm.

HRMS (ESI+): *m/z*, calculated for [M+Na]$^+$ (C$_{10}$H$_{12}$NaN$_2$S$_5$): 342.9502, found: 342.9492.

dmdtSEt[EtCN]
2-Ethylthio-4,5-bis(cyanoethylthio)-1,3-dithiole

To a solution of **dmit[EtCN]** (15.2 g, 49.8 mmol) in CHCl$_3$ (600 mL) triethyl orthoformate (33 mL, 29.5 g, 199.0 mmol) and tetrafluoroboric acid diethyl ether complex (34 mL, 40.3 g, 248.8 mmol) were added. The reaction mixture was stirred at room temperature overnight. *Caution: Be aware that pressure may build up in the reaction vessel if sealed.* After removing the solvent under vacuum, the crude dithiolium salt was washed with diethyl ether (3 x 100 ml). The dark brown, very viscous salt was used in the next step without further purification.
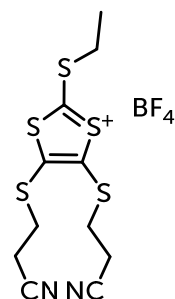
Sodium borohydride (4.7 g, 124.6 mmol) was added at 0°C to the tetrafluoroborate salt dissolved in MeCN (500 mL). The solution was stirred for 1 h, during which time it lost its color. The solution was quenched carefully with cold water (25 mL) and extracted with DCM (25 mL). The organic phase was separated, dried with anhydrous sodium sulfate and concentrated. After flash column chromatography (DCM, SiO_2) and removal of the solvent, an orange solid was obtained overnight in the freezer.

Yield: 70% (11.7 g, 35.0 mmol).

R_f = 0.35 (DCM, UV_{265} visible).

^{1}H NMR (CDCl$_3$, 500 MHz): δ = 5.77 (s, 1 H, CHSEt), 3.26–3.32 (m, 2 H, CH$_2$S), 2.89–2.96 (m, 2 H, CH$_2$S), 2.72–2.83 (m, 3 × 2 H, CH$_2$Me + CH$_2$CN), 1.31 (t, J = 7.4 Hz, 3 H, SMe) ppm.

^{13}C NMR (CDCl$_3$, 126 MHz): δ = 126.2 (2 C, C=C), 117.8 (2 C, CN), 56.3 (1 C, CHSEt), 31.4 (2 C, CH$_2$S), 26.6 (1 C, MeCH$_2$), 18.5 (2 C, CCN), 14.2 (1 C, SMeCH$_3$) ppm.

FT-IR: $\tilde{v}$ = 3464, 3352, 3247, 2969, 2927, 2871, 2360, 2321, 2250, 1648, 1593, 1451, 1416, 1280, 1264, 1166, 898, 728 cm^{-1}.

HRMS (ESI+): m/z, calculated for [M+Na]$^+$ (C$_{11}$H$_{14}$NaN$_2$S$_5$): 356.9653, found: 356.9655.

dmdtP[EtCN]

2-(Dimethylphosphonyl)-4,5-bis(cyanoethylthio)-1,3-dithiole

First, the methyl thioether is cleaved to give the thiolium salt **(dmdtH[EtCN])BF$_4$**: The methyl thioether **dmdtSMe[EtCN]** (10.0 g, 28.1 mmol) is suspended in a mixture of acetic anhydride (60 mL) and Et$_2$O (20 mL), cooled to 0 °C and tetrafluoroboric acid diethyl ether complex (14.8 mL, 17.6 g, 109.2 mmol, 3.5 eq.) is added slowly over the course of 10 min. After two-thirds
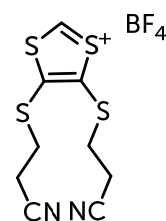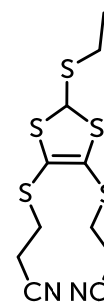
of the acid has been added, the solution becomes clear. Stirring for another 2 h at 0 °C yielded a beige precipitate of the desired thiolium salt. The remaining salt is precipitated by the further addition of Et$_2$O (50 mL). It is purified by decanting the supernatant and successive washes with Et$_2$O (2 × 25 mL). After drying in vacuo for 30 min, the solid is redissolved in acetonitrile (200 mL) and at r.t., sodium iodide (5.8 g, 39.0 mmol, 1.25 eq) is added slowly, resulting in the formation of a thick orange precipitate. After stirring for 10 min, trimethyl phosphite (6.2 mL, 6.6 g, 53.0 mmol, 1.7 eq.) was added slowly and dropwise, resulting in the solution clearing up to a bright orange color. This solution was left stirring o.n. at r.t. The solvent was evaporated, and the remaining oil was extracted with DCM (4 × 50 mL) and water (50 mL). Drying the organic extract with sodium sulfate and evaporating to dryness yields the fairly pure phosphonate as an oil, which solidifies over night in the freezer. For further purification two options are possible: For once, it is possible to column chromatograph (3:1 EtOAc/Hx, SiO$_2$) the crude product. The other option is to recrystallize from 1:1 EA/Hx and wash the filter cake with hexane. Both give an orange crystalline solid.
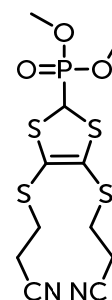
Yield: 76% (9.1 g, 23.8 mmol).

R$_f$ = 0.43 (DCM:EtOAc 1:1, anisaldehyde: lime-green spot, fades to red, UV$_{265}$ visible).

^{1}H NMR (CDCl$_3$, 400 MHz): δ = 4.60 (d, 2J = 7.1 Hz, 1 H, PCH), 3.91 (d, 3J = 10.6 Hz, 6 H, 2 × OMe), 3.38 – 3.29 (m, 2 H, SCH$_2$), 3.13 – 3.04 (m, 2 H, SCH$_2$), 2.96 – 2.84 (m, 4 H, CH$_2$CN) ppm.

^{13}C{^{1}H} NMR (CDCl$_3$, 101 MHz): δ = 126.6 (2 C, C=C), 118.4 (2 C, CN), 55.2 (d, ^{2}J$_{P,C}$ = 7.7 Hz, 2 C, POMe), 41.74 (d, ^{1}J$_{P,C}$ = 164.6 Hz, 1 C, PC), 37.7 (2 C, *C*H$_2$S), 18.3 (2 C, CCN) ppm.

^{31}P{^{1}H} NMR (CDCl$_3$, 162 MHz): δ = 18.9 (s) ppm.

^{31}P NMR (CDCl$_3$, 162 MHz): δ = 19.1 – 18.6 (pd) ppm.

IR: $\tilde{v}$ = 2953.92, 2248.73, 1250.79, 1179.86, 1030.83, 834.13, 798.93 cm^{-1}.

HRMS (ESI+): *m/z*, calculated for [M+Na]$^+$ (C$_{11}$H$_{15}$NaN$_2$O$_5$PS$_4$): 404.9601, found: 404.9567.

EA (C$_{11}$H$_{15}$N$_2$O$_3$PS$_4$): calc'd: C 34.54, H 3.95, N 7.32, found: C 34.54, H 3.92, N 7.43.

3.7.2. Spacer Modifications

Naphthalene-1,4-diole

To a solution of 1,4-napthoquinone (5.0 g, 32 mmol) in Et$_2$O (550 mL) an aqueous solution of sodium thionite (550 mL, 55.0 g, 316 mmol, 10 eq.) was added and the mixture was stirred vigorously to ensure mixing. After 1 h at r.t., the color had changed from yellow to colorless. The reaction was extracted with EtOAc (3 × 200 mL) and the combined phases were washed with brine (200 mL) and then dried subsequently with sodium sulfate. After evaporation of the solvent, a light beige, slightly air- and light-sensitive crystalline solid was obtained.
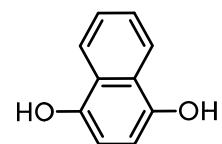

Yield: 93% (4.7 g, 29.3 mmol).

^{1}H NMR (CDCl$_3$, 400 MHz): δ = 8.10 – 8.16 (m, 2 H, isolated HCCH), 7.49 – 7.57 (m, 2 H), 6.67 (s, 2 H) ppm.

Spectral data is consistent with reported data [79].

Naphhalene-2,3-diylmethanol

Lithium aluminium hydride (1.53 g, 40.4 mmol) was suspended in THF (40 mL) and naphthalene-2,3-dicarboxylic anhydride (4.0 g, 20.2 mmol) was added at 0 °C. After stirring for 1 h, the mixture was quenched with water and 2 M HCl. The reaction mixture was extracted with $CHCl_3$ (3 × 30 mL) and the combined organic phases were washed with saturated sodium bicarbonate solution, brine and water. After drying with sodium sulfate, the colorless product was isolated by removing the solvent.
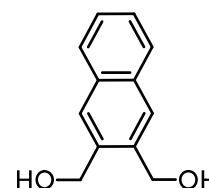
Yield: 76% (2.9 g, 15.4 mmol).

^{1}H NMR (CDCl$_3$, 400 MHz): δ = 7.82 (s, 4 H), 7.48 – 7.52 (m, 2 H), 4.91 (s, 4 H), 2.25 (s, 2 H) ppm.

Spectral data is consistent with reported data [80].

Naphhalene-2,3-dicarbaldehyde

Dimethyl sulfoxide (9.44 mL, 10.4 g, 132.9 mmol) in DCM (20 mL) was added dropwise to a solution of oxalyl chloride (5.74 mL, 8.5 g, 66.9 mmol) in DCM (100 mL). After stirring for 5 min, a solution of **naphthalene-2,3-diylmethanol** (4.5 g, 23.9 mmol) in THF (40 mL) and DMSO (3 mL) was added dropwise. The slurry was stirred for 1 h and triethylamine (40.0 mL, 29.0 g, 286.9 mmol) was added. After heating to r.t. and stirring for another 1.5 h, the reaction was quenched by pouring it into water. Extraction with Et$_2$O and washing of the combined organic phases with water, gave a crude solid after drying with sodium sulfate and removal of the solvent. The
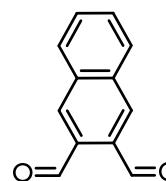
crude product was purified by recrystallization from EtOAc to give an orange, smelly solid.

Yield: 75% (3.3 g, 17.9 mmol).

^{1}H NMR (CDCl$_3$, 400 MHz): δ = 10.65 (s, 2 H, CHO), 8.47 (s, 2 H), 8.03 – 8.11 (m, 2 H), 7.71 – 7.80 (m, 2 H) ppm.

^{13}C{^{1}H} NMR (CDCl$_3$, 126 MHz): δ = 192.6 (2C, CO), 134.5 (2C, naphtha-C), 134.4 (2C, naphtha-C), 132.9 (2C, naphtha-C), 130.1 (2C, naphtha-C), 129.7 (2C, naphtha-C) ppm.

Spectral data is consistent with reported data [81].

Pentacene-5,14-dione

Over the course of 30 min, three solutions were added simultaneously to boiling EtOH (200 mL): **Naphthalene-1,4-diol** (200 mg, 1.25 mmol) in THF (20 mL), **2,3-naphthalene dicarboxaldehyde** (230 mg, 1.25 mmol) in THF (20 mL), and potassium hydroxide (280 mg, 5.0 mmol) in EtOH (15 mL) and water (2 mL). After addition, the mixture was cooled to r.t. and the precipitate was filtered, washed with water, and dried. The target quinone was obtained as an intense yellow fluorescent powder.
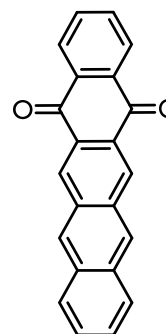
Yield: 80% (310 mg, 1.0 mmol).

^{1}H NMR (CDCl$_3$, 400 MHz): δ = 9.10 (s, 2 H), 8.73 (s, 2 H), 8.41 – 8.48 (m, 2 H), 8.07 – 8.14 (m, 2 H), 7.81 – 7.88 (m, 2 H), 7.58 – 7.65 (m, 2 H) ppm.

Spectral data is consistent with reported data [82]. Because of the poor solubility, a ^{13}C NMR spectrum could not be recorded.

2,6-Bis(m-di-tert-butylphenyl)anthraquinone

Under an inert atmosphere, 2,6-dibromoantraquinone (250 mg, 683 μmol), 2,4-di-tert-butylphenylboronic acid (352 mg, 1502 μmol, 2.2 eq.) and Pd(PPh$_3$)$_4$ (39 mg, 34 μmol, 5 mol%) were suspended in EtOH (5 mL) and PhMe (30 mL). An aqueous potassium carbonate solution (5 mL, 2 M) was added, and the mixture was heated to 100 °C for 20 h. During this time, the suspension became a brown solution, which was then washed with water. The organic phase was dried over sodium sulfate and subjected to column chromatography (SiO$_2$, Hx:DCM 3:1 → Hx:DCM 1:1). The solvent was removed to give a pale yellow, crystalline powder.
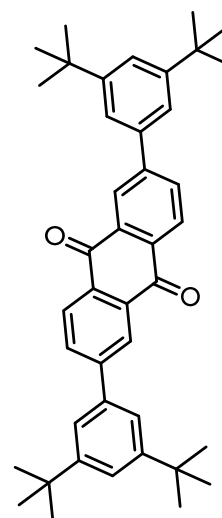
Yield: 288.8 mg (494 μmol, 72 %)

R$_f$ = 0.65 (Hx:DCM 1:1, UV$_{265}$ yellow).

^{1}H NMR (CDCl$_3$, 400 MHz): δ = 8.56 (s, 2 H, J = 8.0 Hz, anthra), 8.41 (d, 2 H, J = 8.0 Hz, anthra), 8.03 (d, 2 H, anthra), 7.54 (s, 6 H, 2 × Ph), 1.42 (s, 36 H, 4 × t-Bu) ppm.

^{13}C{^{1}H} NMR (CDCl$_3$, 101 MHz): δ = 183.4 (2 C, CO), 151.9 (4 C, m-Ph), 149.0 (4 C, C-C), 132.9 (2 C, $\underline{C}$CO), 132.3 (2 C, $\underline{C}$CO), 128.1 (2 C, C-C$\underline{C}$), 126.0 (2 C, C-C$\underline{C}$), 123.2 (2 C, CtBu$_2\underline{C}$), 121.9 (4 C, C-C$\underline{C}$CtBu), 35.2 (4 C, $\underline{C}$Me$_3$), 31.7 (12 C, C$\underline{Me}_3$) ppm.

FT-IR: $\tilde{\nu}$ = 2961, 2927, 2867, 1675, 1594, 1461, 1394, 1363, 1329, 1306, 1287 cm^{-1}.

HRMS (ESI+): m/z, calculated for [M+H]$^+$ (C$_{42}$H$_{49}$O$_2$): 585.3727, found: 585.3722.

Solubility: DCM (good), EA (insoluble), acetone (insoluble).

3.7.3. HWE couplings

dmdtiPr[EtCN]

A solution of **dmdtP[EtCN]** (75 mg, 196 µmol) in THF (4 mL) was ultrasonicated for 5 min and degassed by passing an argon stream through for another 5 min. This solution was then cooled to -78 °C and butyllithium (1.6 M in Hx, 135 µL, 216 µmol) was added dropwise whereupon the solution turned green and the solution was stirred for 20 min. Then, acetone (81 µg, 85 µL, 255 µmol, 1.3 eq.) was added dropwise to the mixture. After 20 min, the solution was warmed up to 0 °C, and after another 20 min to r.t. and the solvent was evaporated, the residue was dissolved in DCM (60 mL), washed with water (20 mL) and then the organic phase was dried with sodium sulfate. Subsequent column chromatography (Hx:EtOAc 2:1, SiO_2) gave an off-white semisolid of pure product.
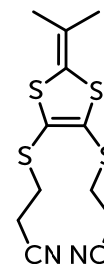
Yield: 92% (65 mg, 182 µmol).

R_f = 0.33 (Hx:EtOAc 2:1), 0.80 (DCM:EtOAc 1:1).

^{1}H NMR (CDCl$_3$, 400 MHz): δ = 3.06 (t, J = 7.1 Hz, 4 H, SCH$_2$), 2.74 (t, J = 7.1 Hz, 4 H, CH$_2$CN), 1.71 (s, 6 H, 2 × Me) ppm.

^{13}C{^{1}H} NMR (CDCl$_3$, 101 MHz): δ = 126.5, 120.9, 119.4, 117.7, 31.0, 22.8, 19.0 ppm.

HRMS (ESI+): *m/z*, calculated for [M+H]$^+$ (C$_{12}$H$_{15}$N$_2$S$_4$): 315.0113, found: 315.0103.

dmdtAd[EtCN]

A solution of **dmdtP[EtCN]** (1.0 g, 2.6 mmol, 1.5 eq.) in THF (40 mL) was cooled to –78 °C. n-Butyllithium (2.5 M in Hx, 1.05 mL, 2.6 mmol, 1.5 eq.) was added dropwise after which the solution changed its color from yellow to green. The solution was stirred for 1 h. Adamantanone (262 mg, 1.74 mmol, 1 eq.) in THF (20 mL) was added dropwise. The resulting suspension was stirred for 20 h while warming back to r.t. The reaction mixture was extracted with DCM (200 mL), brine (100 mL), and water (100 mL) until the aqueous phase turned purple. The resulting organic phases were combined and dried with sodium sulfate. After column chromatography (SiO$_2$, Hx:EE 2:1) an orange powder was obtained.
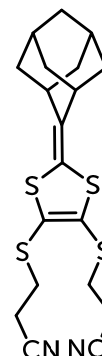
Yield: 59% (420 mg, 1.03 mmol).

R$_f$ = 0.45 (Hx:EtOAc 2:1, yellow, UV$_{265}$ visible)

^{1}H NMR (CDCl$_3$, 400 MHz): δ = 3.04 (t, J = 7.2 Hz, 4 H, SCH$_2$), 2.75 (t, J = 7.2 Hz, 4 H, CH$_2$CN), 2.47 (br s, 2 H, 2 × C=CH), 1.96 (br s, 2 H, Ad) 1.70 – 1.90 (m, 10 H, Ad) ppm.

^{13}C{^{1}H} NMR (CDCl$_3$, 101 MHz): δ = 137.0, 125.7, 117.8, 111.0, 38.0, 37.7, 36.7, 30.9, 28.0, 19.1 ppm.

FT-IR: $\tilde{v}$ = 2909, 2849, 1719, 1700, 1448, 1418, 1098, 1059, 956, 891, 797 cm^{-1}.

HRMS (ESI+): m/z, calculated for [M+Na]$^+$ (C$_{19}$H$_{22}$N$_2$S$_4$Na): 429.0558, found: 429.0545.

dmdt₂Ad[EtCN]

A solution of **dmdtP[EtCN]** (689 mg, 1.8 mmol, 3 eq.) in THF (20 mL) was cooled to –78 °C. n-Butyllithium (2.5 M in Hx, 0.72 mL, 1.8 mmol) was added dropwise whereupon the solution changed its color from yellow to green. The solution was stirred for 1 h. A solution of 2,6-adamantanedione (99 mg, 0.6 mmol, 1 eq.) in THF (20 mL) was added dropwise. The mixture was stirred for another 2 h at –78 °C after which the cooling dewar was topped up with dry ice and stirred overnight. The reaction was quenched with NH_4Cl solution (10 mL). Water (10 mL) and brine (10 mL) were added, and the aqueous phase was extracted with DCM (3 × 20 mL). The organic phase was separated and dried with sodium sulfate. After removal of the solvent the crude product was dissolved in a minimal amount of DCM and layered with Hx. Overnight a precipitate formed in the freezer. The product was isolated as a yellowish-gray powder. Recrystallization from $CDCl_3$ in an NMR tube yielded yellow crystals suitable for single crystal analysis.

Yield: 91% (370 mg, 547 µmol).

R_f = 0.4 (Hx:EtOAc 1:1, yellow, UV_{265} visible).

^{1}H NMR (CDCl₃, 400 MHz): δ = 3.06 (t, J = 7.1 Hz, 8 H, SCH₂), 2.76 (t, J = 7.1 Hz, 8 H, CH₂CN), 2.55 (br, 4 H, Ad), 1.86 (br, 8 H, Ad) ppm.

^{13}C{^{1}H} NMR (DMSO-d₆, 101 MHz): δ = 131.7, 124.9, 118.9, 112.5, 38.1, 36.2, 30.3, 18.3 ppm.

FT-IR: $\tilde{\nu}$ = 2920, 2252, 1612, 1569, 1423, 1232, 1176, 944, 913, 890, 729 cm^{-1}.

HRMS (ESI+): m/z, calculated for [M+Na]$^+$ ($C_{28}H_{28}N_4S_8Na$): 698.9972, found: 698.9907.

dmdt₂Anthra[EtCN]

A solution of **dmdtP[EtCN]** (5.0 g, 13.07 mmol, 3 eq.) in dry THF (200 mL) was cooled to –78 °C and n-butyllithium (2.5 M in Hx, 5.3 mL, 13.07 mmol, 3 eq.) was added dropwise whereupon the solution changed to a greenish color. Stirring was continued for 1 h and then anthraquinone (907 mg, 4.36 mmol, 1 eq.) was added to the mixture over the course of 10 min. The dewar was topped up with dry ice and left stirring overnight. The solution was then extracted with DCM (4 × 200 mL) and washed again with water (100 mL). After drying with sodium sulfate the solvent was evaporated leaving a greenish-black product. Recrystallization from 5:1 EtOAc:Hx (250 mL) gave a yellow powder. Slow recrystallization from a DCE solution yielded crystals suitable for single crystal analysis.

As a byproduct, **dmdtAnthrene[EtCN]** was isolated.
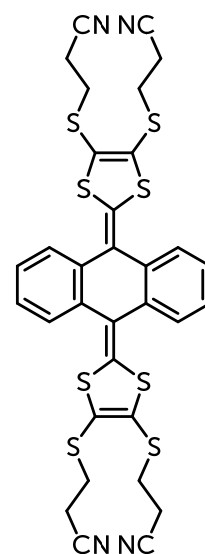
Yield: 46% (1.35 g, 2.0 mmol).

R_f = 0.4 (Hx:EtOAc 1:1, yellow, UV_{265} visible).

^{1}H NMR (CDCl₃, 500 MHz): δ = 7.55 (dd, 4 H, J=5.7, 3.3 Hz), 7.37 (dd, 4 H, J = 5.7, 3.3 Hz), 3.18 – 3.07 (m, 4 H), 3.07 – 2.96 (m, 4 H), 2.72 (t, 8 H, J = 6.7 Hz) ppm.

^{13}C{^{1}H} NMR (CDCl₃, 126 MHz): δ = 134.3 (4 C, arom.), 129.2 (2 C, SCS), 126.9 (4 C, CH), 126.3 (4 C, C=C), 125.4 (4 C, CH), 124.7 (2 C, arom.), 117.5 (4 C, CN), 31.1 (4 C, CH₂S), 19.0 (4 C, CH₂CN) ppm.

FT-IR: $\tilde{v}$ = 3061, 2928, 2250, 1723, 1535, 1495, 1456, 1446, 1416, 1282, 904, 782, 757, 730, 676, 644 cm^{-1}.

HRMS (ESI+): m/z, calculated for [M+H]$^+$ (C₃₂H₂₅N₄S₈): 720.9839, found: 720.9837.

dmdt₂Penta[EtCN]

A solution of **dmdtP[EtCN]** (1.0 g, 2.61 mmol, 3 eq.) in THF (40 mL) was reacted at -78 °C with n-butyllithium (2.5 M in Hx, 1.05 mL, 2.61 mmol, 3 eq.) for 1 h. Then the asymmetric **pentacene-5,14-dione** (269 mg, 0.87 mmol, 1 eq.) was added over the course of 10 min. The resulting reddish-brown suspension was stirred for 20 h while warming back to r.t. The reaction mixture was extracted with DCM (500 mL) until TLC showed no further extraction of unreacted pentaquinone. The resulting organic phases were combined and dried with sodium sulfate. After column chromatography (SiO₂, Hx:EtOAc 1:1) an orange powder was obtained.
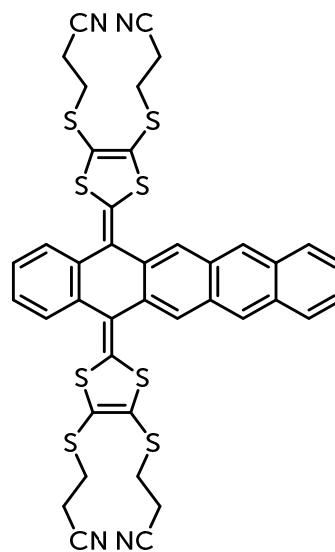
Yield: 37% (271 mg, 329 µmol)

R_f = 0.4 (Hx:EtOAc 1:1, yellow, UV_{265} visible).

^{1}H NMR (CDCl₃, 400 MHz): δ = 8.45 (s, 2 H, central anthracene), 8.03 (dd, 2 H, J=6.5, 3.3 Hz, outer anthracene), 7.97 (s, 2 H, inner anthracene), 7.58 (dd, 2 H, J = 5.7, 3.3 Hz, outer anthracene), 7.50 (dd, 2 H, J = 6.5, 3.2 Hz, isolated benzene), 7.40 (dd, 2 H, J = 5.7, 3.3 Hz, isolated benzene), 3.19 – 3.06 (m, 4 H, SCH₂), 3.06 – 2.93 (m, 4 H, SCH₂), 2.75 – 2.66 (m, 8 H, NCCH₂) ppm.

^{13}C{^{1}H} NMR (CDCl₃, 101 MHz): δ = 134.4, 132.9, 132.5, 130.2, 129.8, 128.3, 127.3, 126.6, 126.3, 126.1, 125.9, 125.1, 124.9, 117.7, 31.2, 19.5 ppm.

FT-IR: $\tilde{\nu}$ = 3050, 2924, 2854, 2250, 1532, 1492, 1453, 1441, 1415, 1284, 908, 728, 645 cm⁻¹.

HRMS (ESI+): m/z, calculated for [M+H]⁺ (C₄₀H₂₉N₄S₈): 821.0152, found: 821.0173.

dmdt$_2$Dtbpa[EtCN]

A solution of **dmidP[EtCN]** (300 mg, 784 µmol, 3 eq.) in THF (12 mL) was reacted at –78 °C with n-butyllithium (2.5 M in Hx, 314 µL, 784 mmol, 3 eq.) for 1 h. Soluble **2,6-bis(m-di-tert-butylphenyl) anthraquinone** (153 mg, 261 µmol, 1 eq.) was then added over the course of 10 min. The resulting reddish-brown suspension was stirred for 20 h while warming back to r.t. Extraction with DCM (250 mL) was carried out until the aqueous solution turned purple and no more color was absorbed into the organic phase. The resulting organic phases were combined and dried with sodium sulfate. After column chromatography (SiO$_2$, Hx:EtOAc 3:2) a brown-yellow powder was obtained.
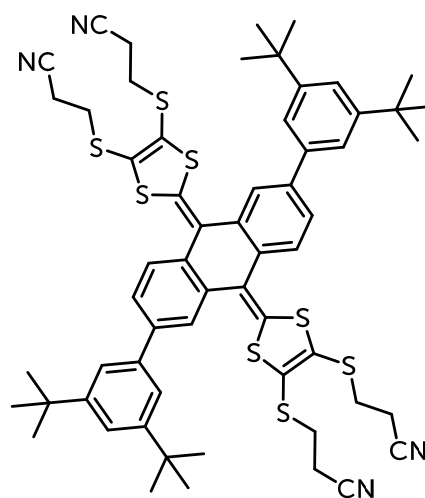
Yield: 49% (139 mg, 127 µmol)

R$_f$ = 0.4 (Hx:EtOAc 3:2, yellow, UV$_{265}$ visible).

^{1}H NMR (CDCl$_3$, 400 MHz): δ = 7.77 (s, 2 H, anthra), 7.63 (dd, 4 H, J= Hz, anthra), 7.51 (s, 4 H, o-Ph), 7.49 (s, 2 H, p-Ph), 2.95 – 3.22 (m, 8 H, SCH$_2$), 2.80 – 2.65 (m, 8 H, NCCH$_2$), 1.46 (s, 36 H, 12 × Me) ppm.

^{13}C{^{1}H} NMR (CDCl$_3$, 101 MHz): δ = 151.4, 141.0 , 139.6, 134.8, 132.9, 129.1, 127.0, 126.2, 125.8, 125.8, 124.7, 124.2, 122.0, 121.6, 117.5, 117.4, 35.1, 31.6, 31.2, 31.1, 19.1, 19.0 ppm.

FT-IR: $\tilde{\nu}$ = 2961, 2865, 2552, 1593, 1529, 1474, 1422, 1391, 1362, 1260, 1246, 1082, 1019, 906, 798, 728, 648 cm^{-1}.

4

PROPERTIES OF A FAMILY OF DMDT-BASED COMPLEXES

4. PROPERTIES OF A FAMILY OF **DMDT**-BASED COMPLEXES

The ligands prepared in Chapter 3 will be used to prepare functional compounds with different coordination environments for possible use in quantum computing and/or quantum sensing.

The first section of this chapter discusses the deprotection of the ligands. Section 4.2 describes the reaction of these ligands with different transition metal building blocks. The resulting complexes are investigated experimentally and theoretically in Section 4.3.

4.1. Deprotection of the Bridges

A number of deprotection strategies have been reported for propionitrile-protected thiolates [73],[83],[92]–[101],[84],[102]–[111],[85],[112],[86]–[91]. These strategies all involve a base, ranging from cesium carbonate to hydroxides, alkoxides, and lithium diisopropylamide (LDA). The most common deprotection strategy among these is using a methanolic cesium carbonate solution in solvents such as highly polar DMF or deprotection under the influence of tetraalkylammonium hydroxide in methanol.

Several different bases, solvents, and reaction temperatures were tried to find the optimal deprotection strategies. As the free tetrathiolates of **dmdt** are very sensitive to oxygen, they were trapped by complexation with titanocene dichloride and then analyzed. An overview of the conditions used is given in **Table 4.1**.

Table 4.1.   Screening of bases used to deprotect **dmdt$_2$Anthra[EtCN]** and subsequent capturing with titanocene dichloride.

	Base	Eq.	Solvent	Temperature	success[a]	Ref.
1	Bu$_4$NOH	4	MeOH/THF	r.t.	–	[100]
2	NaOMe	4	MeOH	r.t.	–	[113]
3	NaOEt	4	DCM	r.t.	–	[114]
4	KO^{t}Bu	4	THF	r.t.	–	[71]
5	CsOH	4	DMF/MeOH	r.t.	–	[115]
6	Cs$_2$CO$_3$	4	DMF/MeOH	r.t.	–[b]	[97]
7	Cs$_2$CO$_3$	5	H$_2$O/MeOH	r.t.	–	[114]
8	LDA	4	THF	−78 °C	✓	[97]
9	NaHDMS	4	THF	−78 °C	✓	–
10	LiHDMS	4	THF	−78 °C	✓	–

[a] success implies that a deprotection occurred and that the compound **dmdt$_2$Anthra[TiCp$_2$]** was detected by means of ESI-MS or ^{1}H NMR.
[b] Triply deprotected ligand could be identified by MS: **Cs(dmdt$_2$Anthra[TiCp, 1 EtCN])**.

For hydroxide, alkoxide, and carbonate bases, no conditions could be found for the clean removal of the four protecting groups, and mostly partial deprotection was observed by mass spectrometry and ^{1}H NMR. Although it cannot be clearly demonstrated, it is assumed that as the polarity of the solvent increases, the reaction tends to produce chains rather than isolated dimers of **dmdt**.

Deprotection was successful for both LDA and HDMS as bases in THF solution at low temperatures. Reproducibility tests showed that commercial solutions of HDMS, however, were of variable quality. In contrast, the in situ preparation of LDA always gave good and reproducible results, and this strategy was used in the following. The deprotection was investigated as a function of temperature and reaction time to further simplify and improve the LDA route. **Table 4.2** shows the results of this for the set of ligands available:

While the deprotection of the group of quinones proceeds fairly rapidly to give a red (for **dmdt₂Anthra[EtCN]** and **dmdt₂Dtbpa[EtCN]**) or purple (for **dmdt₂Penta[EtCN]**) solution, the deprotection of **dmdt₂Ad[EtCN]** appears to evolve slowly during the addition of LDA as the color of the solution first changes to green, then back to yellow and finally after some time to a deep green color. This suggests the presence of several isolated stages of deprotection in the reaction mixture.

The observed variety in deprotection environments suggests that the nature of the linker significantly influences the deprotection reaction. Indeed, highly variable deprotection conditions have been reported [97] in literature for dithiolenes differing in the protection groups.

From **Table 4.2**, it can be seen that the deprotection of the quinoid ligands **dmdt₂Anthra[EtCN]**, **dmdt₂Penta[EtCN],** and **dmdt₂Dtbpa[EtCN]** only proceeds smoothly at low temperatures of –78 °C. Deprotection can work at higher temperatures, although the yields obtained after complexation with titanocene dichloride appear lower than deprotection at lower temperatures.

Table 4.2. Screening of reaction conditions to deprotect various **dmdt** ligands with LDA in dry THF with yields of the corresponding **dmdt₂X[TiCp₂]**.

dmdt₂X[EtCN] → dmdt₂X⁴⁻
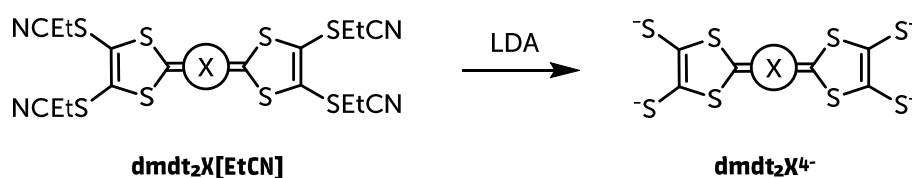
Temperature	Reaction time	dmdt₂Anthra[EtCN]	dmdt₂Ad[EtCN]	dmdt₂Penta[EtCN]	dmdt₂Dtbpa[EtCN]
−78 °C	1 h	35 %	20 %	—[a]	—[a]
−78 °C	2 h	51 %	24 %	62 %	53 %
r.t.	1 h	17 %	50 %	—[a]	—[a]
r.t.	2 h	15 %	63 %	—[a]	—[a]

[a] not screened.

In contrast to this, the adamantane-based ligand **dmdt₂Ad[EtCN]** is much more challenging to deprotect. Although it is possible to deprotect it under the same conditions as the quinoid structures, this deprotection only occurs at a reasonable rate at room temperature. This observation can be explained by the fact that the adamantane structure cannot accept electrons from the **dmdt** coordination site to weaken the protective bond of EtCN to the mercaptane, resulting in a more difficult deprotection. This may explain why higher temperatures are required for the deprotection.

With the above information, the selected reaction conditions of at least 2 h of reaction time with LDA at low temperatures for quinoid **dmdt** structures and room temperature for the alkyl **dmdt** structure were set.

4.2. Coordination Chemistry of **dmdt**

The complex chemistry of the **dmit** motif ligand and its chalcogen analogs has been extensively described in literature [116]. Most of the reported compounds are homoleptic. However, **dmdt** ligands possess two coordination sites, and homoleptic compounds are hardly realizable as they would immediately form unwanted coordination polymers. Therefore, heteroleptically coordinating metal precursors with **dmdt** ligands are preferred.

The design criteria mentioned in Section 2.1 are important to follow up not only for the ligands – which should have as few protons as possible and separate the unpaired electrons well – but also for the used metal center used as a qubit. Since metals such as vanadium in combination with **dmit** are exceptionally good for coherence applications [13],[117], compounds incorporating vanadium were sought. However, only a handful of results were found: Only simple derivatives of **dmit** and 1,2-dithioles were previously coordinated with vanadium, and the often-used vanadyl(IV) ion readily forms complexes of type **VO(dmit)$_2$**, suggesting that derivatives of it have an increased chance of forming chains.

In addition to this, it is generally difficult to make heteroleptic vanadyl(IV) complexes with one chelating and two labile monodentate ligands. The only reasonable coordinating metal precursor found in literature to support such a coordinating fashion was vanadocene(IV). Extending the search further to other metallocenes that should be chemically similar, a large number of additional complexes have been reported with titanocene(IV), as well as its heavier homologs such as hafnium, niobium, molybdenum, and zirconium [97],[109],[112],[114],[118]–[121].

This makes (light) metallocenes an excellent target for the coordination of the novel **dmdt** ligands. In particular, the occurrence of the heteroleptic vanadocene(IV) compound, as it is paramagnetic and stable in its default state, and the fact that often the diamagnetic titanocene(IV) analog is also known, which can serve as a diamagnetic equivalent and can help in the development of the synthesis, as it is more amenable to EPR studies.
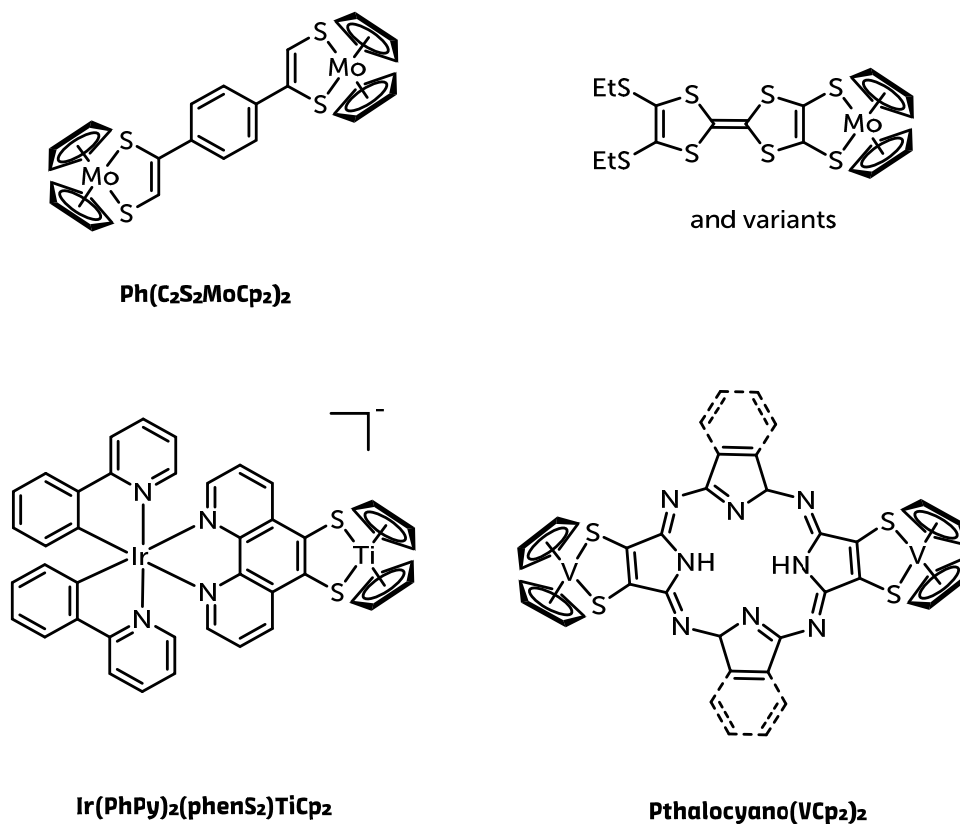
Ph(C₂S₂MoCp₂)₂

and variants

Ir(PhPy)₂(phenS₂)TiCp₂

Pthalocyano(VCp₂)₂

Figure 4.1. Metallocenes of dithiolenes found in literature, including the only example of a vanadocene dithiolene dimer [97],[109],[118],[119].

Besides the metallocenes, metal(II) ions have also been found to coordinate with **dmit**, including platinum(II), cobalt(II), and nickel(II) [68],[109],[122]–[125]. However, these ions are less suitable for qubit implementation, i.e., they are either not EPR-active in a default state or have too fast relaxation times due to their increased spin-orbit coupling (SOC), to name a few. Some of these examples mentioned in literature are listed below in **Figure 4.1**.

4.2.1. Titanium(IV) Complexes of **dmdt**-Ligands

We have chosen the following titanium complexes as target molecules to serve as diamagnetic models for the analogous paramagnetic vanadium complexes: **dmdt$_2$X[TiCp$^R_2$]** (X = **Anthra**, **Dtbpa**, **Penta**, **Ad**, R = **iPr, ***).

Preparation of dmdt-titanocenes(IV) with bare cyclopentadienyls

The preparation of the dimeric **dmdt**-titanium(IV) systems with titanocene was carried out immediately after the deprotection of the ligand under the appropriate conditions, stated in Section 4.1 since the free bis-thiols are very air-sensitive and is summarized in **Figure 4.2**.

The general reaction procedure was as follows: To a solution of the free tetrathiolate, 2 equivalents of TiCp$_2$Cl$_2$ dissolved in a small amount of dry THF were added very slowly. For the quinoid systems **dmdt$_2$Anthra**, **dmdt$_2$Penta**, and **dmdt$_2$Dtbpa,** the color changed to a dark neon green during the addition. For the adamantane system **dmdt$_2$Ad**, this color change to blue-green occurred overnight.
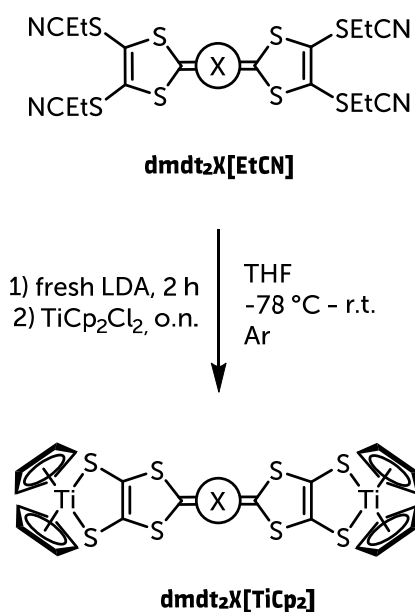

Figure 4.2.   Complexation reaction of titanocene(IV) to **dmdt$_2$X[EtCN]** ligands. X = **Anthra**, **Penta**, **Dtbpa**, **Ad**.

Table 4.3. Reaction conditions to yield the various titanocene(IV) complexes.

Compound	Temperature	Time	Yield
dmdt₂Anthra[TiCp₂]	−78 °C to r.t.	12 h	51 %
dmdt₂Penta[TiCp₂]	−78 °C to r.t.	12 h	62 %
dmdt₂Dtpba [TiCp₂]	−78 °C to r.t.	12 h	53 %
dmdt₂Ad[TiCp₂]	−78 °C to r.t. (12 h), r.t (12 h)	24 h	63 %

The compounds were purified through vacuum-assisted dry column chromatography [72] with DCM since the reaction was quite clean, and any unreacted free tetrathiole either decomposed or did not move through the stationary phase because of its high charge. Subsequent precipitation from DCM with Hx and further washing of the precipitate with hexanes afforded the pure coordination compound in satisfactory yields, as shown in **Table 4.3**.

All compounds were characterized by ^{1}H, mass spectrometry, UV-VIS, IR spectroscopy, and spectroelectrochemical (SEC) techniques, which are thoroughly described in Section 4.3. Due to the very low signal intensity and the small amount of sample available, it was not possible to record ^{13}C$\{^1$H$\}$ spectra. It was, however, found that the complexes are indefinitely stable in air in solid form but decompose over several weeks in solution.

Preparation of **dmdt**-titanocenes(IV) with substituted cyclopentadienyls

In addition to the regular, unsubstituted $TiCp_2Cl_2$, two additional, commercially available titanocenes were tested for their ability to coordinate to **dmdt₂Anthra**: These were $TiCp^{iPr}_2Cl_2$ and $TiCp^*_2Cl_2$, as their different steric influences on the titanium coordination site could change the exchange rate of the chloride to the **dmdt** ligand.
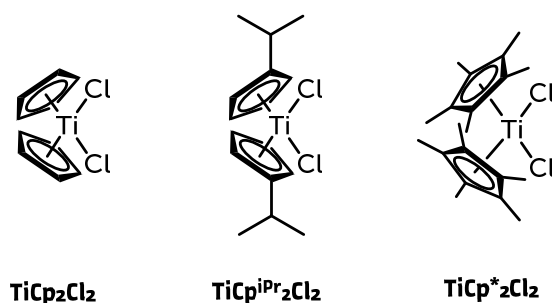
Figure 4.3. Titanocene(IV) dichlorides used for the complexation of **dmdt₂X**.

All three compounds were detected by means of mass spectrometry following the previously described reaction route. However, the observed reaction times became significantly longer with increasing steric bulk of the cyclopentadienyls. In fact, while the unsubstituted $TiCp_2Cl_2$ and **dmdt₂Anthra⁴⁻** react quite readily within a few hours, the $TiCp^*_2Cl_2$ requires reaction times of up to a week. Interestingly, heating the reaction mixture didn't significantly increase the reaction rate. As expected, the isopropyl-variant $TiCp^{iPr}_2Cl_2$ lies within the two extremes but still very much on the side of the unsubstituted titanocene derivative.

However, while the unsubstituted titanocene derivatives are easily purified as described, the isopropyl and decamethyl-substituted derivative is less stable. This did not allow for proper purification.

4.2.2. Vanadium(IV) Complexes of **dmdt**-Ligands

After successfully synthesizing the titanocene(IV) derivatives of the titanium dimers in Section 4.2.1, we attempted to apply the same procedures to obtain the vanadocene(IV) analogs.

Since literature described the vanadocene(IV) and titanocene(IV) variants of **dmit** to be accessible [114], this approach did not seem far-fetched. However, this was not the case for the novel **dmdt₂X** systems.

In fact, the synthetic procedures successfully used for the titanocene derivatives were not at all applicable to the vanadocene equivalent. Although a reaction appeared to occur because the deep red deprotected ligand solution of **dmdt₂Anthra⁴⁻** and the green deprotected ligand solution of **dmdt₂Ad⁴⁻** respectively turned carmine red upon addition of VCp₂Cl₂, isolation of a pure product was not successful.

Suspecting that the reaction occurs at low temperatures but decomposes upon warming to room temperature, the reaction was monitored by X-band EPR, resulting in the observation of the signal shown in **Figure 4.4**.
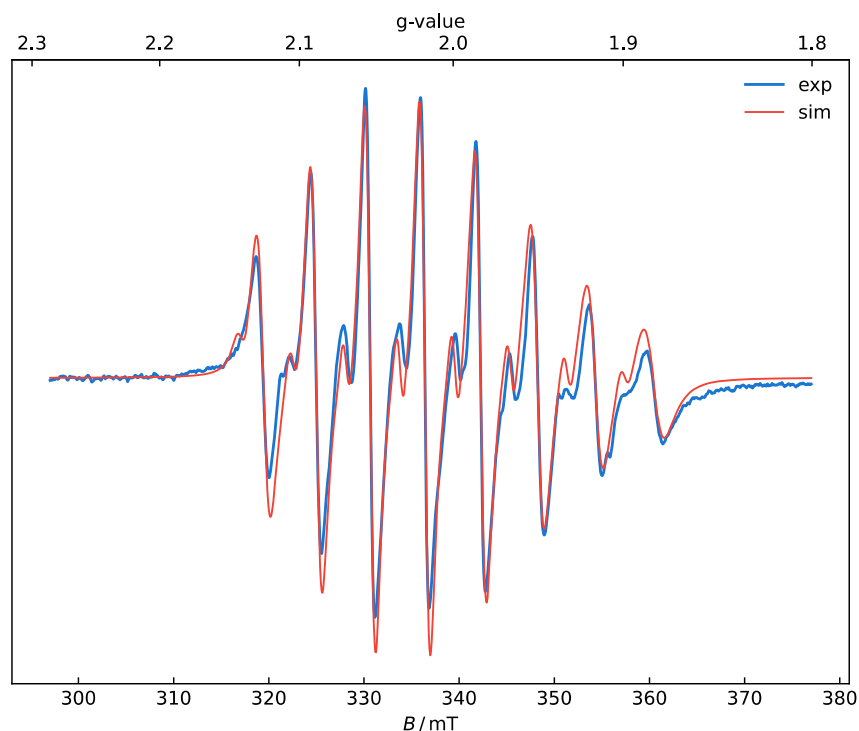

Figure 4.4.   (blue) CW X-Band EPR spectra of an observed vanadium species in the reaction mixture of the deprotected tetrathiolate **dmdt₂Anthra⁴⁻** with vanadocene(IV) dichloride in THF at lower than r.t. In addition to the main signal, another vanadium signal with an intensity of 6% can be observed. (red) Simulation with the following parameters for the vanadium species: $S = 1/2$, $g_1 = 1.977$, $g_2 = 1.974$, $g_3 = 2.016$, $A_1 = 110$ MHz, $A_2 = 381$ MHz, $A_3 = 0$ MHz, $t_{corr} = 40$ ps and $S = 1/2$, $g = 2.012$, $A_1 = 160$ MHz, $A_2 = 288$ MHz, $A_3 = 38$ MHz, $t_{corr} = 50$ ps.

Due to the interaction of the electrons with the nuclear spin of $I = 7/2$ of the ^{51}V isotope, a characteristic eight-lined hyperfine structure is expected. This is observed, but there are seven additional lines with much lower intensities visible. The distorted, unsymmetrical envelope of the signal suggests a strong tumbling motion in the solution state, which is not present in the EPR spectrum of the starting material VCp_2Cl_2. In addition, the observed spectrum is consistent with previously reported data of regular vanadium-**dmit** species [119],[127] from multiple sources regarding hyperfine couplings and g-values. Both these factors might result from a formed unsymmetrical vanadium-**dmit** species.

However, upon reaching room temperature, the signal slowly disappears within minutes while precipitates form. This disappearance may have several causes: Either the complex forms in the solution, but the product is very insoluble and precipitates when the solution warms up, or the reaction does not lead to the desired product, and the precipitate is an unwanted compound. To determine this, we followed the strategy shown in **Figure 4.16**:
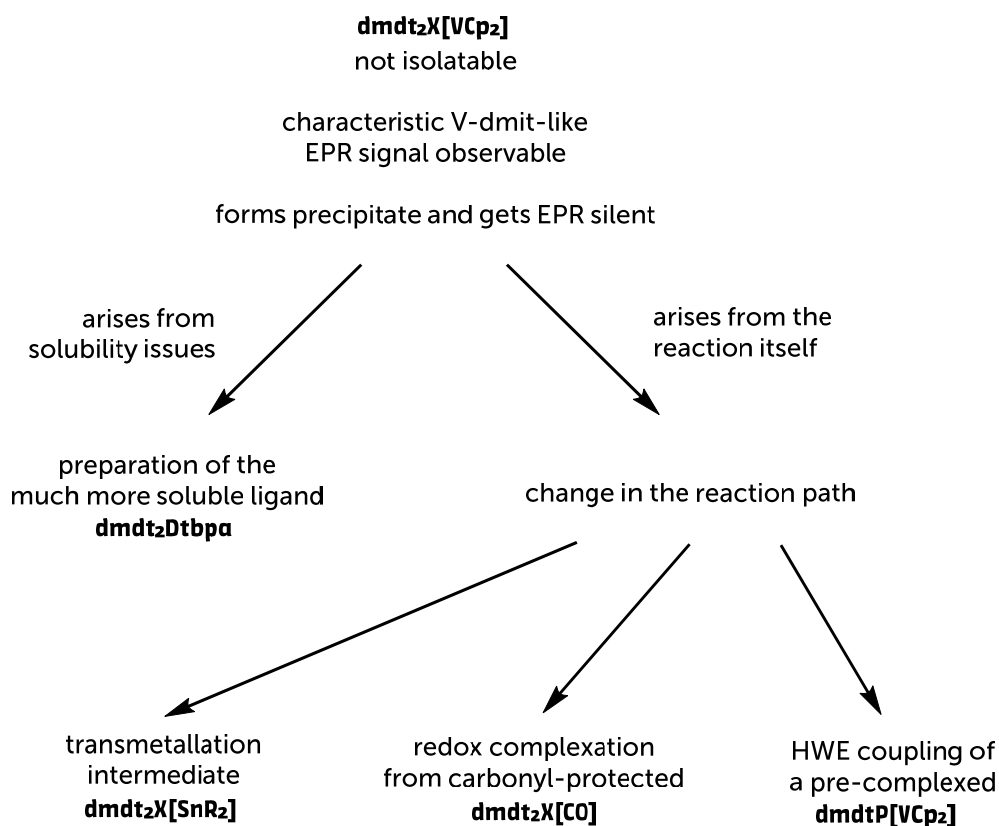
dmdt₂X[VCp₂]
not isolatable

characteristic V–dmit–like
EPR signal observable

forms precipitate and gets EPR silent

arises from
solubility issues

arises from the
reaction itself

preparation of the
much more soluble ligand
dmdt₂Dtbpa

change in the reaction path

transmetallation
intermediate
dmdt₂X[SnR₂]

redox complexation
from carbonyl-protected
dmdt₂X[CO]

HWE coupling of
a pre-complexed
dmdtP[VCp₂]

Figure 4.5.   Flow chart to resolve the challenges in isolating a **dmdt₂X[VCp₂]** species.

Lefthand Pathway: Potential Solubility Issues

Since the disappearance of the EPR signal was accompanied by the formation of a precipitate, the more soluble derivative of the bridging ligand **dmdt₂Dtbpa** was developed to rule out solubility problems as the cause of the failed product isolation. This compound was chosen because it was straightforward to prepare by a Suzuki reaction of 2,5-di-tertbutylphenylboronic acid with 2,6-dibromoanthraquinone and then applying the established HWE reaction to form the corresponding protected ligand.
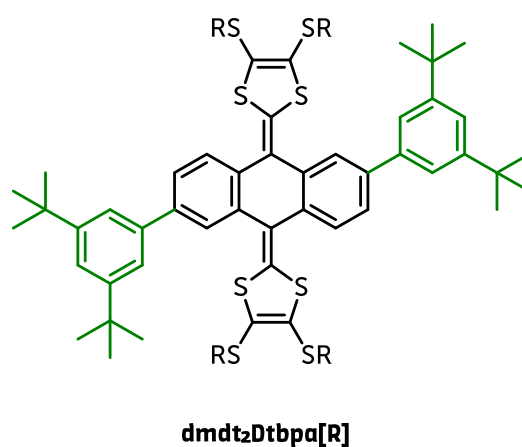

dmdt₂Dtbpa[R]

Figure 4.6.   Soluble **dmdt₂Dtbpa[R]** ligand. The solubility was immensely increased by the introduction of two di-tert-butylphenyl groups via a Suzuki coupling of the corresponding boronic acid with dibromoanthraquinone.

Indeed, the use of **dmdt₂Dtbpa** instead of **dmdt₂Anthra** prevented the formation of a precipitate after the addition of vanadocene dichloride and subsequent warming to room temperature. In addition, the brown-red reaction solution showed a vanadium **dmdt** EPR signal for a brief amount of time. Although this was a very encouraging result, it was still impossible to isolate this compound, nor could it be detected by mass spectrometry. Removing the solvent simply left an EPR inactive powder that was hard to redissolve behind.

Righthand Pathway: Potential Reaction Issues

The second possibility was that the reaction pathway prevented the product from being formed successfully. Therefore, several other routes which should theoretically lead to the target compound **dmdt₂X[VCp₂]** were evaluated:

- Introduction of tin as a transmetallation intermediate:

  As reported in literature, the direct metalation with some metallocenes can be troublesome and complicated by the formation of undefined byproducts. To avoid this, a possible route via a dialkyltin(IV) compound has been previously reported, which after successful isolation, can serve as a starting compound for a clean transmetallation. This has been previously successfully employed by several groups [97],[109],[126].

- Switch to a carbonyl protection group:

  An interesting alternative approach is to use of a carbonyl protecting group. This then provides a redox reaction path (see **Figure 4.7**): When metallocenes(II) such as vanadocene(II) are heated in toluene with the carbonyl-protected **dmdt₂X[CO]** ligands, they undergo a redox reaction forming the desired metallocene(IV) dmdt structure with the release of carbon monoxide, which drives the reaction to completion [127]–[129].

- Formation of the complex before coupling via HWE:

  As described in literature, HWE coupling of backend-phosphonated **dmit** compounds is possible after their complexation with titanocene(IV). Applying this procedure to the known isolatable and stable vanadium(IV) compounds could lead to the formation of the target compound **dmdt₂X[VCp₂]**. [130]

All three options were evaluated as they all appeared promising.

The procedure for replacing the propionitrile protecting group with dialkyltin(IV) is shown in the lefthand path of **Figure 4.7**. The reaction conditions for this reaction follow the general complexation routine established for titanium and **dmdt₂Anthra**. After the addition of

dibutyltin(IV) or dimethyltin(IV) dichloride to the reaction mixture, the dark red color of the free tetrathiolate **dmdt₂Anthra⁴⁻** immediately faded to a clear, transparent orange color, indicating that a reaction has taken place. Unfortunately, it was not possible to isolate a pure product from this mixture, nor did a mass spectrometric analysis of the reaction mixture did not indicate the presence of the ditin compound either.

Since it was not possible to isolate the tin compound despite numerous attempts, we turned to the second option – the redox reaction with a carbonyl-protected ligand, which is shown in the righthand path in **Figure 4.7**: The only concern with this reaction is the use of triphosgene as the carbonylation agent as it is particularly toxic in nature. Transprotection of the propionitrile ligands to the corresponding CO ligands was also unsuccessful.

To circumvent the problem of transprotection of propionitrile to carbonyl, the preparation of a carbonyl-protected **dmit** variant was pursued and is shown in **Figure 4.8**. A literature search also revealed that this variant had apparently already been prepared in 1992 by Misaki et al. [131]. Regrettably, the synthesis of the O-methylated compound **dmit[CHOMe]** could not be obtained, which led to another dead end.

Finally, an attempt was made to generate the dithiolene cyclopentadienyl vanadium complex first and to prepare the dinuclear complex in a second step by coupling two of the complexes with a suitable spacer: Hartke et al. reported an HWE reaction of a phosphonated titanocene [130]. The proposed reaction path is shown in **Figure 4.9**. Although the preparation of the phosphonated titanocene **dmdtP[TiCp₂]** was possible, albeit with a low yield of 6%, the preparation of the analogous vanadium compound was unfortunately not possible as only an undefined, non-separable oil was obtained.
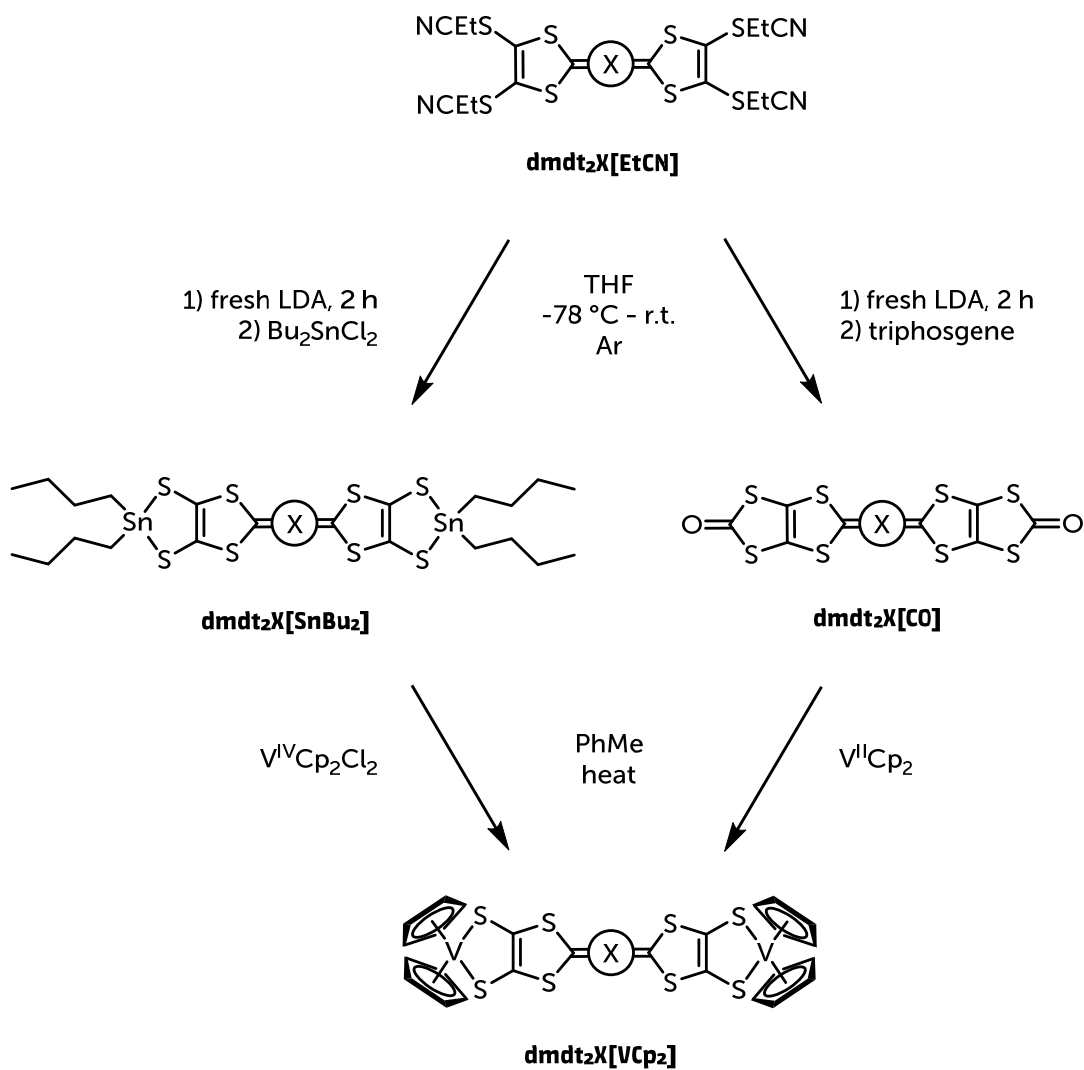
Figure 4.7. Synthetic approach to a (left route) tin-protected and (right route) carbonyl-protected **dmdt₂X** ligand to access **dmdt₂X[VCp₂]**. X = **Ad**, **Anthra**, **Penta** or **Dtbpa**.
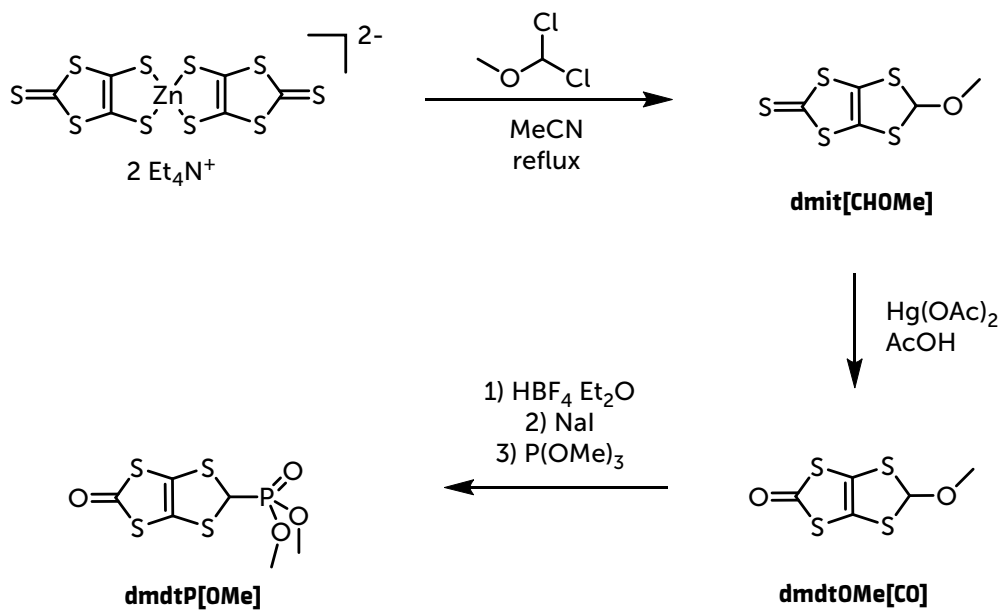
Figure 4.8. Preparation of a carbonyl-protected **dmdt** ligand by Misaki [131].
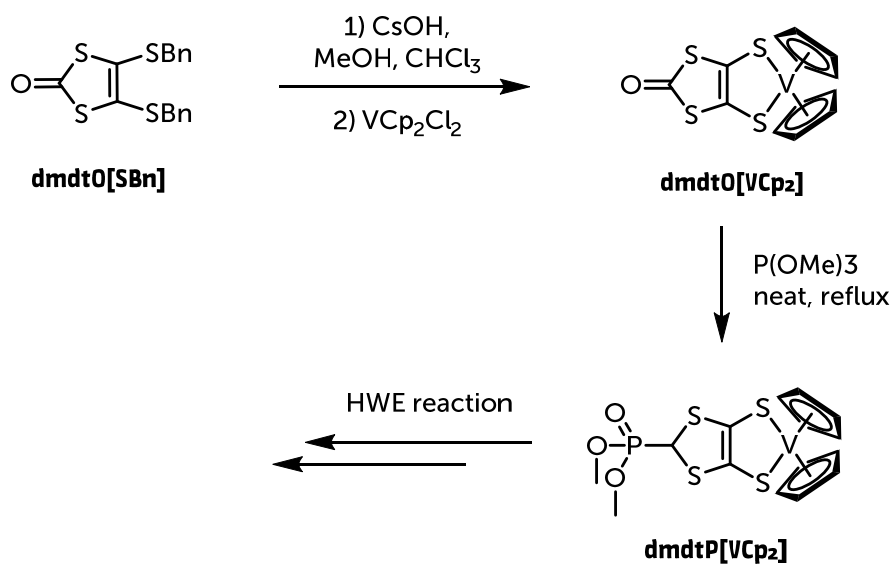

Figure 4.9. Possible synthetic route to a suitable already coordinated reagent for the HWE reaction. Created on the basis of [130].

In retrospect, none of the above routes yielded the target vanadocene. The suspected formation of chains may be an explanation for this observation, although it does not provide a sufficient answer as to why the use of the highly soluble **dmdt₂Dtbpa** ligand did not yield any precipitate.

To gain some more insight into whether the presence of two coordination sites in one molecule might be the problem, one of the initially prepared ligands to optimize the HWE reaction in Section 3.5.1 – **dmdtAd[EtCN]** – was used to prepare the corresponding **dmdtAd[TiCp₂]** and **dmdtAd[VCp₂]**. In the case of the vanadium monomer **dmdtAd[VCp₂]**, it was directly determined by X-band EPR in the reaction solution (see **Figure 4.10**), which looked different from the vanadocene dichloride used as a reagent. This clearly supports the notion that two coordination sites in one molecule are the main problem in isolating a dimeric vanadocene species.
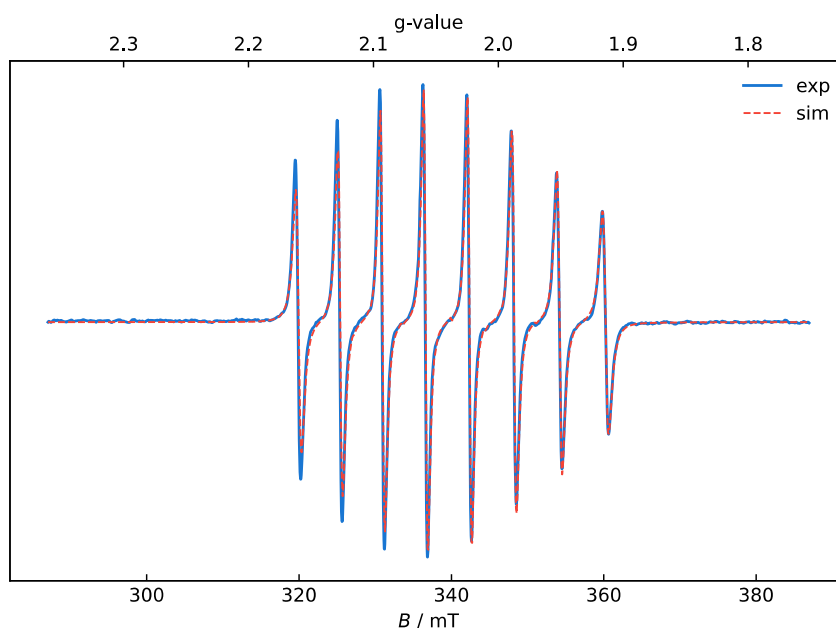

Figure 4.10. (blue) CW X-Band EPR spectra of the THF reaction solution of most likely **dmdtAd[VCp₂]** at room temperature. (red) Simulation with the following parameters for the vanadium species: $S = 1/2$, $g_\perp = 1.978$, $g_\parallel = 1.990$, $A_1 = 53$ MHz, $A_2 = 426$ MHz, $A_3 = 0$ MHz, $t_{corr} = 10$ ps.

In conclusion, it was unfortunately not possible to obtain the dimeric vanadium(IV) complexes of the prepared ligands. Nevertheless, it should be clearly mentioned that this does not mean that these compounds are inaccessible, but rather that during this work, no way was found to isolate them.

4.3. Physical Properties of **dmdt**-Titanocene(IV) Dimers

Since the reaction screening for the optimal conditions to deprotect the ligands to form tetrathiolates already used titanocene as the transition metal to form a coordination compound, these were characterized. However, only **dmdt₂Anthra[TiCp₂]** and **dmdt₂Ad[TiCp₂]** will be compared throughout this chapter as they represent the two main types of ligands used. More data on the other two compounds **dmdt₂Penta[TiCp₂]** and **dmdt₂Dtbpa[TiCp₂]**, can be found in the appendix, all of which are very similar to the data obtained for **dmdt₂Anthra[TiCp₂]**.
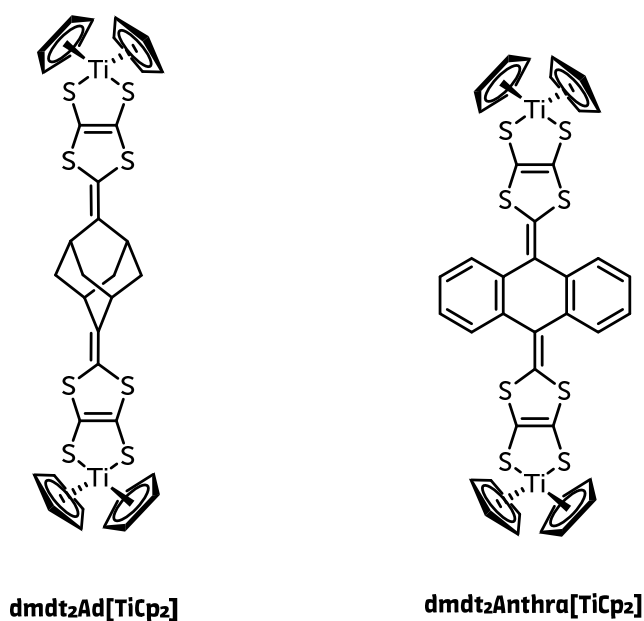

dmdt₂Ad[TiCp₂]   **dmdt₂Anthra[TiCp₂]**

Figure 4.11.   Structures of **dmdt₂Anthra[TiCp₂]** and **dmdt₂Ad[TiCp₂]**.

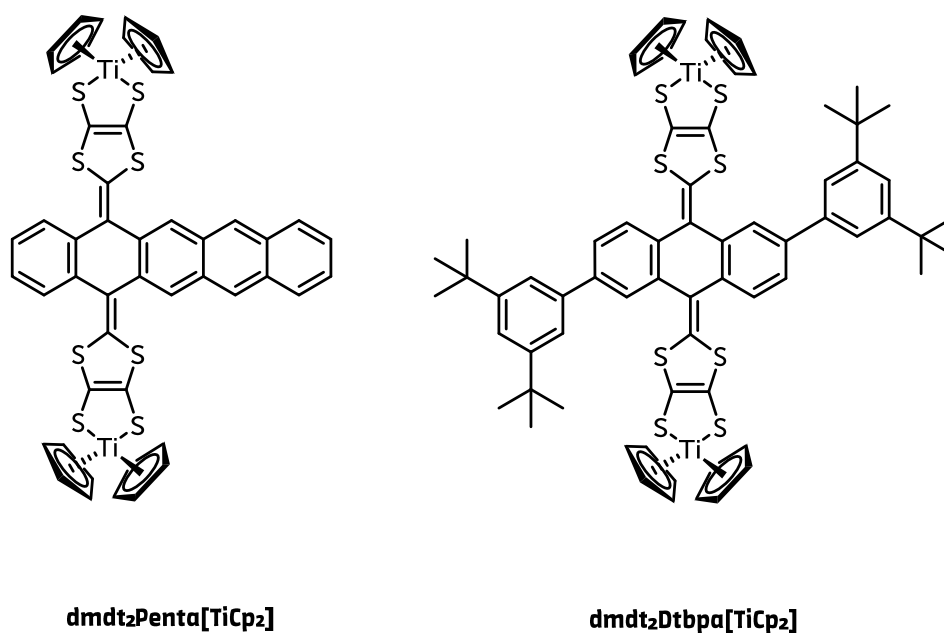**dmdt₂Penta[TiCp₂]**   **dmdt₂Dtbpa[TiCp₂]**

Figure 4.12.   Structures of **dmdt₂Penta[TiCp₂]** and **dmdt₂Dtbpa[TiCp₂]**.

4.3.1. Cyclic Voltammetry

Cyclovoltammetric measurements were performed under an argon atmosphere in a 0.1 M, argon-purged solution of Bu_4NPF_6 in dry DCM at room temperature. A platinum electrode was used as the working and counter electrodes. The reference electrode was a silver wire. All potentials were referenced to the ferrocene/ferrocenium redox pair as an internal standard.

Figure 4.13 shows the cyclic voltammograms of compounds **dmdt₂Anthra[TiCp₂],** and **dmdt₂Ad[TiCp₂],** and a summary of the electrochemical data is given in **Table 4.4**. All complexes show one distinct reversible reduction wave as well as one broad, mostly irreversible oxidation wave within the potential window of the solvent. The reversible reduction wave at a half-wave potential of about −1.6 V vs. Fc/Fc⁺ and with a peak separation of 80–100 mV implies a one-electron redox process since the ideal potential is 90 mV per transferred electron [132]. The oxidation wave is irreversible or poorly reversible, depending on the ligand system. While the oxidation in **dmdt₂Ad[TiCp₂]** is very much irreversible, it seems to become more reversible towards the quinoid systems such as **dmdt₂Anthra[TiCp₂]**.
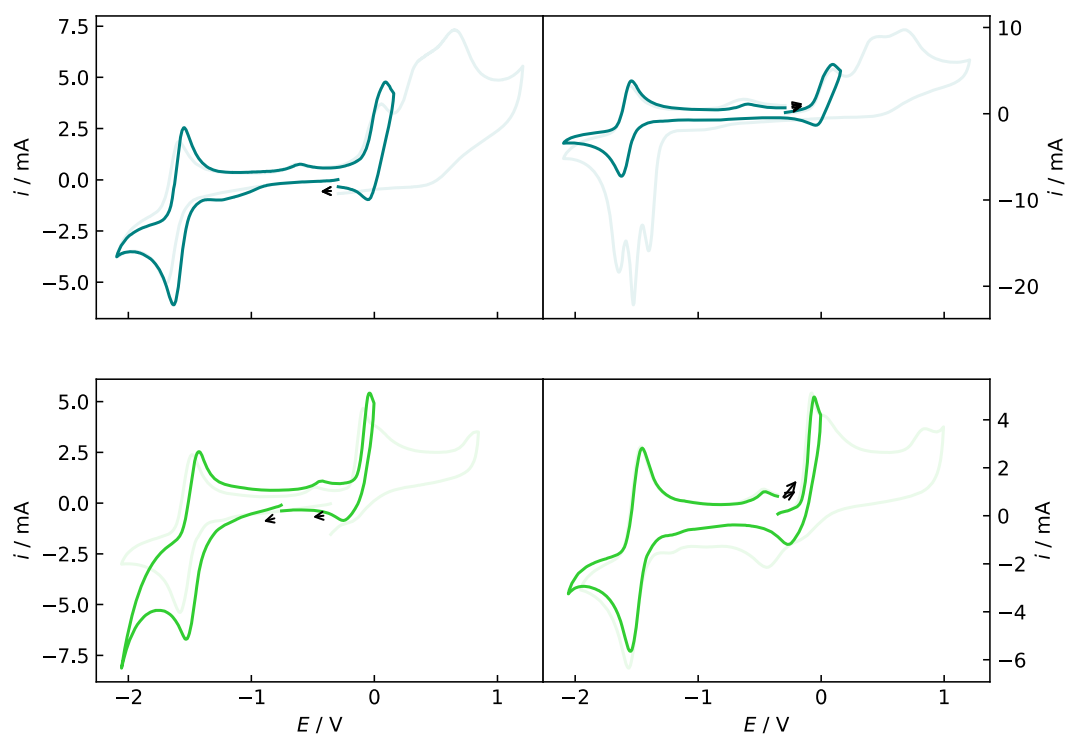
Figure 4.13. Cyclic voltammogram of (top) **dmdt₂Ad[TiCp₂]** and (bottom) **dmdt₂Anthra[TiCp₂]**, in DCM / 0.1 M [NBu₄][PF₆] at 100 mV s⁻¹. The left column represents a sweep into the reduction, while the right represents a sweep into the oxidation first. Less opaque cyclic voltammograms are representing full sweeps, while solid colors represent only the first waves.

Compared to literature data on **Cp*₂Ti(dmit)** [133], the reversible reduction wave can be attributed to a metal-centered reduction from titanium(IV) to titanium(III). It is interesting to note that literature [135] reported reduction potentials that correlate with the S-S hinge angle of the coordination site (either obtained by DFT or reported in literature). While **dmit[TiCp₂],** with its thione backbone and a tilt angle of 47.4(3)° is already reduced at a mere -1.185 V, a larger tilt angle of 49.2(1)° as in **dddt[TiCp₂]**, decreases the reduction potential to -1.525 V . Fitting to this trend are also the reduction potentials of the **dmdt₂X[TiCp₂]** family as shown in **Table 4.4**.
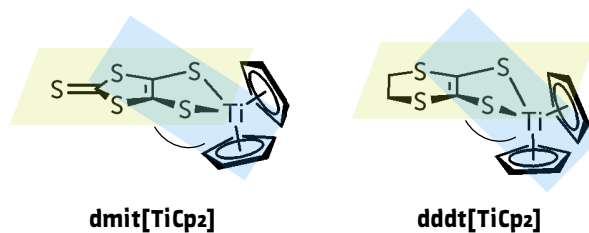
dmit[TiCp₂]   **dddt[TiCp₂]**

Figure 4.14. Structure of the compounds listed in literature in **Table 4.4** with indicated tilt angles between the dithiolene and the coordinating metal.

Table 4.4. Electrochemical data[a] for **dmdt₂X[TiCp₂]** and reported analogous complexes.

		$E^0_{298}/\mathrm{V}(\Delta E_p/\mathrm{mV})$ [b]			
Complex	Solvent	Red1	Ox1	hinge angle	Ref
dmdt₂Anthra[TiCp₂]	DCM	−1.479 (104)	− [c]	49.7 [e]	this work
dmdt₂Penta[TiCp₂]	DCM	−1.505 (80)	− [c]	49.7 [e]	this work
dmdt₂Btpba [TiCp₂]	DCM	−1.557 (81)	− [c]	49.7 [e]	this work [f]
dmdt₂Ad[TiCp₂]	DCM	−1.589 (81)	− [c]	50.1 [e]	this work [f]
TiCp₂Cl₂	THF	−1.3	−	−	[134]
TiCp₂Br₂	THF	−1.1	−	−	[134]
dmit[TiCp₂]	MeCN	−1.185 [d]	+0.525 [d]	47.4(3)	[133]
dddt[TiCp₂]	MeCN	−1.525 [d]	+0.245 [d]	49.2(1)	[133]
dmit[TiCp*₂]	MeCN	−1.415 [d]	+0.255 [d]	38.3(9)	[133]
dddt[TiCp*₂]	MeCN	−1.665 [d]	+0.045 [d]	−	[133]

[a] From cyclic voltammetry with 0.1 M [Bu₄N][PF₆] in DCM at a scan rate of 100 mV s⁻¹.
[b] Potential in V versus SCE; peak potential differences (in parentheses).
[c] Irreversible process.
[d] Measured against Ag/Ag⁺, corrected to match Fc/Fc⁺.
[e] calculated by DFT.
[f] cyclic voltammograms can be found in the appendix.

Since no other reversible waves are present, and other metal-centered electron transfers are unlikely, modified **dmdt** quinoid ligands can be considered innocent and do not promote any electron exchange between the two **dmdt** sites.

Although the shape of the voltammogram and the reversibility of the oxidation process varies from quinone-based to adamantyl-based ligands, it is evident that initial oxidation of the ligand results in an irreversible chemical process in which the coordination sphere of the titanium is oxidized: Sweeping past the reduction wave afterward, the CV now exhibits multiple waves of possibly different titanium environments. This decomposition of the thiolene was previously described in literature [111] but could not be confirmed in this case.

4.3.2. UV/VIS-Spectroelectrochemistry and Time-Dependent DFT

Absorption spectra of the various complexes and their respective reduced species were collected with an optically transparent thin-layer electrochemical (OTTLE) cell [135] at room temperature in a 0.1 M [Bu$_4$N][PF$_6$] / DCM solution and are shown in **Figure 4.15**, and the corresponding spectroelectrochemical data are listed in **Table 4.5**. As indicated by cyclic voltammetry, the first electrochemically accessible reduction is reversible, as evident by the recovery of the initial spectrum upon reoxidation.

The titanium dimers **dmdt$_2$Ad[TiCp$_2$]** and **dmdt$_2$Anthra[TiCp$_2$]** exhibit a broad absorption band between 600 nm and 800 nm in their neutral state. In addition, the quinoid-based dimers show additional features below 500 nm, while **dmdt$_2$Ad[TiCp$_2$]** shows no prominent features in this region.

TD-DFT calculations were performed to assign the low energy absorption band: Since no single crystals could be grown from the compounds themselves, existing crystal data of **dmit[TiCp$_2$]** resembling the coordination sphere, as well as data from crystal structures of the bridging units, were used to construct a structure corresponding to the expected geometry. In fact, three structural isomers are possible for all quinoid-like molecules. **Figure 4.16** lists all the conformers schematically. These were then geometry-optimized utilizing DFT using the B3LYP functional in a def2-tvzp basis set. The resulting geometry

was then fed into a TD-DFT calculation using the PBE0 functional in the same basis set, accompanied by a COSMO solvent model.

The calculated transition energies and oscillator strengths visualized in **Figure 4.17** to **Figure 4.23** show surprisingly good agreement with the experimental spectra, suggesting that the calculated geometry corresponds well to that of the real compounds. Since the calculations show little difference between the isomers, only the most prevalent isomers were used to assign bands from UV/Vis spectroscopy.

Based on these calculations, we generally assign the long wavelength band in the UV/Vis spectra of the complexes to an LMCT transition from the bridge to the metal center. A more thorough comparison of the TD-DFT results for both types of systems follows.
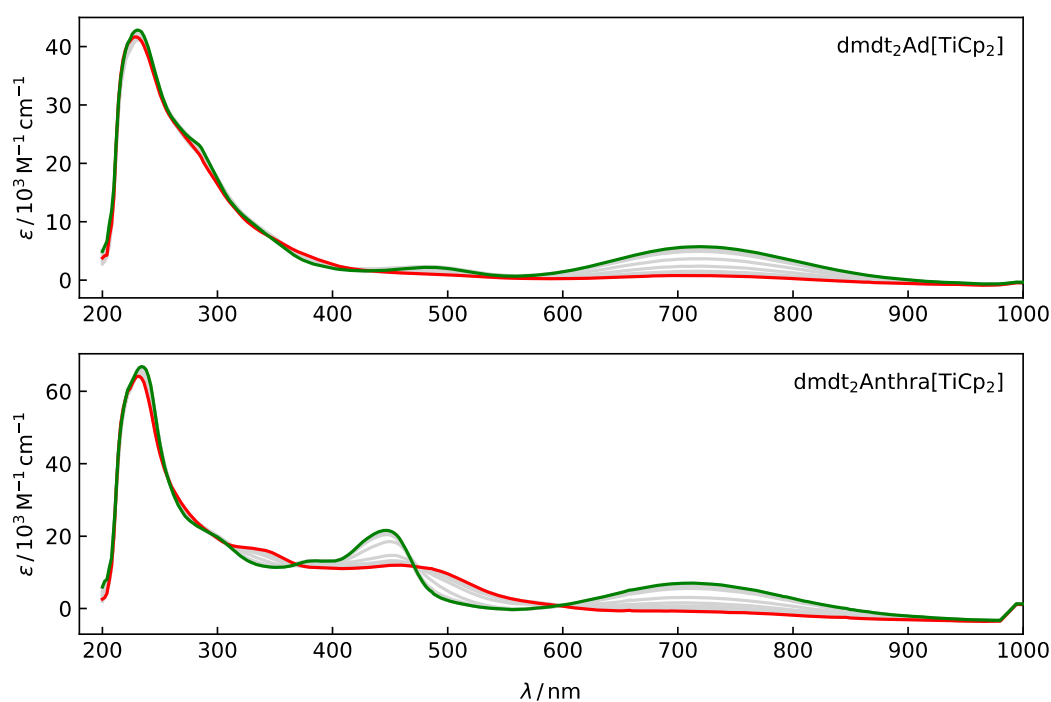
Figure 4.15. UV/VIS spectroelectrochemical response upon reduction of **dmdt$_2$Anthra[TiCp$_2$]** and **dmdt$_2$Ad[TiCp$_2$]** (from top to bottom) in DCM / 0.1 M [NBu$_4$][PF$_6$]. Green spectra represent the initial species, red the final reduced species. Measurement performed together with Marc Schnierle.

Table 4.5. Spectroelectrochemical data of titanium dimers **dmdt₂Ad[TiCp₂]** and **dmdt₂Anthra[TiCp₂]** at r.t. in an OTTLE cell in 0.1 M [Bu₄N][PF₆] / DCM and their pure ligands.

Compound	Ti(n)	$\lambda_{max}/nm(\varepsilon/10^3 M^{-1}cm^{-1})$
dmdt₂Ad[TiCp₂]	IV	236 (66.9), 291 (20.2), 377 (13.7), 446 (22.2), 717 (7.5)
	III	232 (63.8), 292 (21.0), 341 (16.0), 464 (12.2)
dmdt₂Anthra[TiCp₂]	IV	230 (42.9), 281 (23.7), 347 (7.5), 487 (2.5), 722 (5.8)
	III	228 (41.4), 275 (23.3)
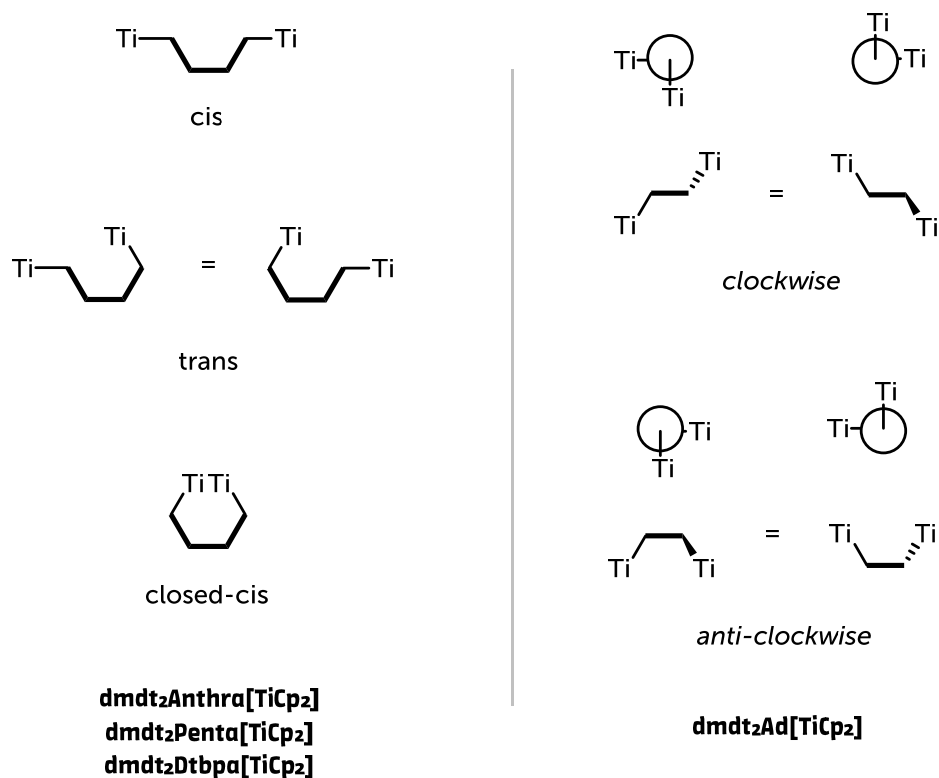
Figure 4.16. Schematic structural isomers of **dmdt₂X[TiCp₂]**. Newman projections viewed from the side of the molecule depicted underneath it.

dmdt$_2$Anthra[TiCp$_2$]

Figure 4.17 shows the calculated UV/VIS spectrum of **dmdt$_2$Anthra[TiCp$_2$]** and its reduced counterpart **dmdt$_2$Anthra[Ti(III)Cp$_2$]** in its most likely cis-variant, compared to the experimentally measured spectra of the complex. With the help of the calculations, the experimental absorption bands can be assigned.
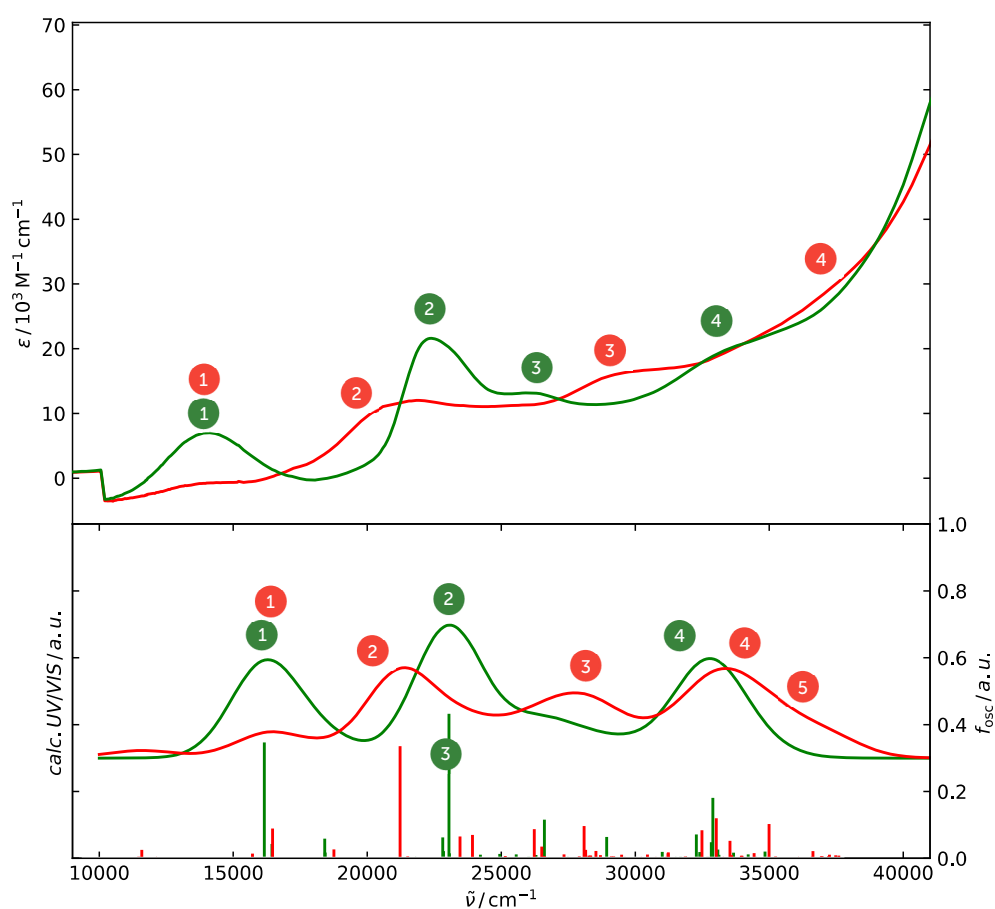
Figure 4.17. TD-DFT calculated (bottom) and (top) experimental UV/VIS spectra in DCM of (green) **dmdt$_2$Anthra[TiCp$_2$]** and (red) **dmdt$_2$Anthra[Ti(III)Cp$_2$]**.

Transition 4, ❶

$\tilde{v}_{DFT} = 16155\ cm^{-1}, f_{osc} = 0.347$

Transition 23, ❷

$\tilde{v}_{DFT} = 23046\ cm^{-1}, f_{osc} = 0.433$

Transition 42, ❸

$\tilde{v}_{DFT} = 26608\ cm^{-1}, f_{osc} = 0.116$

Transition 117, ❹

$\tilde{v}_{DFT} = 32897\ cm^{-1}, f_{osc} = 0.181$
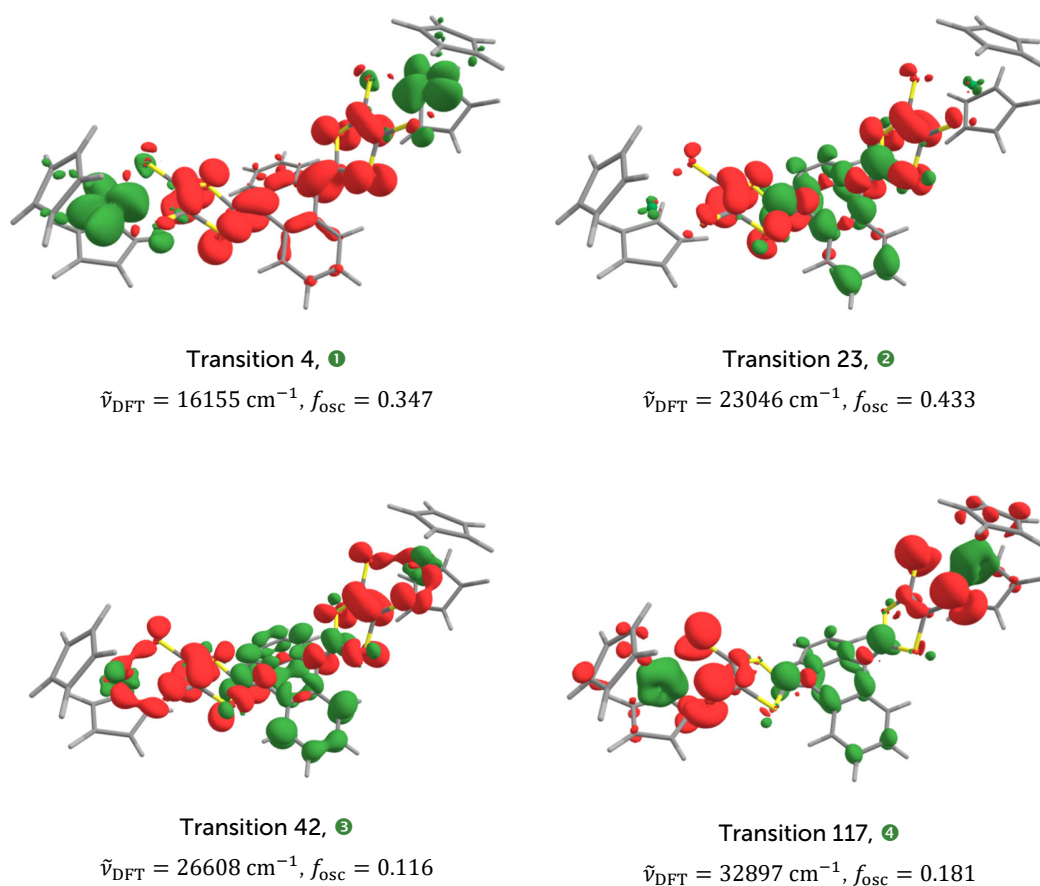
Figure 4.18. Difference densities obtained by TD-DFT (PBE0/def2-tvp/COSMO) representing selected UV/Vis transitions calculated for **dmdt₂Anthra[TiCp₂]**. Red areas indicate decreasing electron density, while green areas indicate increasing electron density. Contour value $H = 0.001$.

The lowest energy absorption band of the UV/Vis spectrum of **dmdt₂Anthra[TiCp₂]**, which is the transition in the experimentally observed transition at $\tilde{v}_{exp} \approx 14000\ cm^{-1}$ ($\tilde{v}_{DFT} = 16155\ cm^{-1}, f_{osc} = 0.347$, ❶) is dominated by a change in electron density from the bridge in its HOMO state to the LUMO, which is centered on the titanium atoms, i.e., an LMCT transition.

The second most prominent feature is located at $\tilde{v}_{exp} \approx 22390\ cm^{-1}$ ($\tilde{v}_{DFT} = 23046\ cm^{-1}$, $f_{osc} = 0.433$, ❷) Unlike the first transition, this one is mostly of intraligand (IL) nature and corresponds to intraligand charge transfer from the **dmdt** to the anthracene parts of the ligand.

Furthermore, the transition at $\tilde{\nu}_{\mathrm{exp}} \approx 26120\,\mathrm{cm}^{-1}$ ($\tilde{\nu}_{\mathrm{DFT}} = 26608\,\mathrm{cm}^{-1}$, $f_{\mathrm{osc}} = 0.116$, ❸) exhibits a mixed IL/MLCT character, as 44% of the electron density shifts towards the cyclopentadienyl rings and 22% shifts away from the titanium towards the central ligand. Overall, the density around the titanium is reduced.

In the area $\tilde{\nu}_{\mathrm{DFT}} > 30000\,\mathrm{cm}^{-1}$ several transitions have been calculated. They are represented by the last denoted transition at $\tilde{\nu}_{\mathrm{exp}} \approx 33920\,\mathrm{cm}^{-1}$ ($\tilde{\nu}_{\mathrm{DFT}} = 32897\,\mathrm{cm}^{-1}$, $f_{\mathrm{osc}} = 0.181$, ❹). It shifts the electron density away from the **dmdt** units toward both the anthraquinone and titanium atoms, giving it a partial LMCT and IL character.

In contrast to the neutral compound, **dmdt₂Anthra[Ti(III)Cp₂]** shows quite different absorptions in the low-energy regions of $\tilde{\nu}_{\mathrm{exp}} < 20000\,\mathrm{cm}^{-1}$. The first two prominent transitions are shown in **Figure 4.17** at $\tilde{\nu}_{\mathrm{exp}} \approx 14000\,\mathrm{cm}^{-1}$ ($\tilde{\nu}_{\mathrm{DFT}} = 16468\,\mathrm{cm}^{-1}$, $f_{\mathrm{osc}} = 0.089$, ❶) and $\tilde{\nu}_{\mathrm{exp}} \approx 20700\,\mathrm{cm}^{-1}$ ($\tilde{\nu}_{\mathrm{DFT}} = 21227\,\mathrm{cm}^{-1}$, $f_{\mathrm{osc}} = 0.336$, ❷) and appear to be identical in character. **Figure 4.20** shows that they are mostly MLCT in character. The electron density is shifted from the coordination sphere of the titanium atoms to the central ligand part. This is consistent with the fact that in the reduced variant, most of the spin density is located on the titanium(III) centers, as can be seen in **Figure 4.19**.
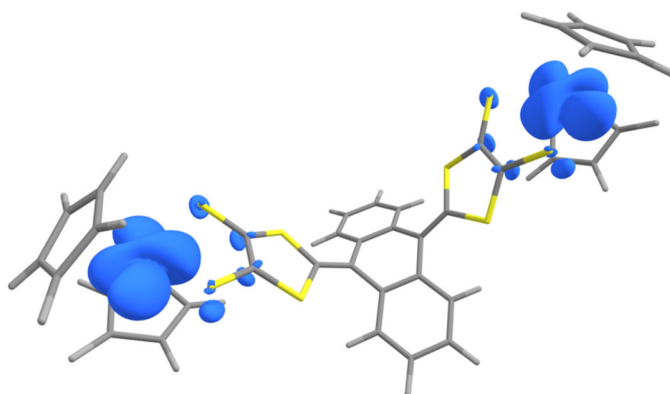

Figure 4.19.   Spin density of **dmdt₂Anthra[Ti(III)Cp₂]** calculated by DFT (PBE0/def2-tzvp). Contour value $H = 0.003$.

All other features at $\tilde{\nu}_{\mathrm{exp}} \approx 29340$ cm^{-1} ($\tilde{\nu}_{\mathrm{DFT}} = 28092$ cm^{-1} , $f_{\mathrm{osc}} = 0.097$, ❸), $\tilde{\nu}_{\mathrm{exp}} \approx 37030$ cm^{-1} ($\tilde{\nu}_{\mathrm{DFT}} = 33029$ cm^{-1}, $f_{\mathrm{osc}} = 0.120$, ❹) can also be classified as MLCT with some ILCT character which reduce the electron density on the cyclopentadienyl ligands.
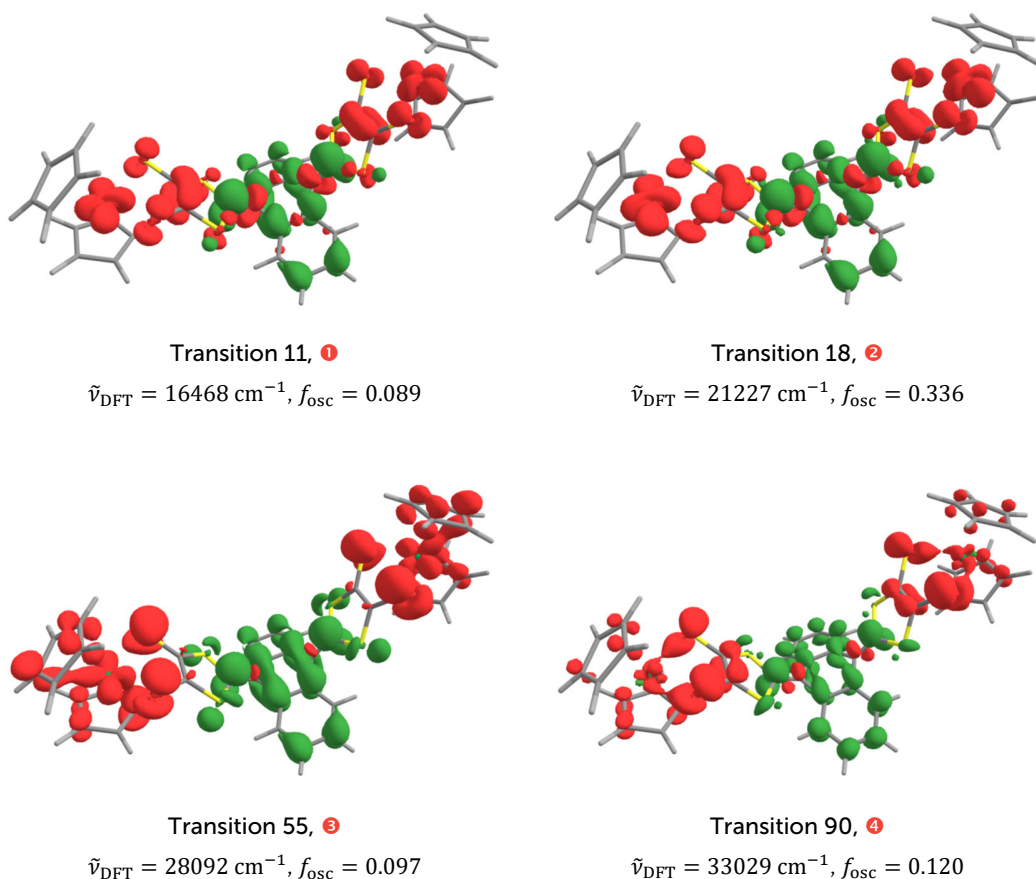

Transition 11, ❶

$\tilde{\nu}_{\mathrm{DFT}} = 16468$ cm^{-1}, $f_{\mathrm{osc}} = 0.089$

Transition 18, ❷

$\tilde{\nu}_{\mathrm{DFT}} = 21227$ cm^{-1}, $f_{\mathrm{osc}} = 0.336$

Transition 55, ❸

$\tilde{\nu}_{\mathrm{DFT}} = 28092$ cm^{-1}, $f_{\mathrm{osc}} = 0.097$

Transition 90, ❹

$\tilde{\nu}_{\mathrm{DFT}} = 33029$ cm^{-1}, $f_{\mathrm{osc}} = 0.120$

Figure 4.20. Difference densities obtained by TD-DFT (PBE0/def2-tvp/COSMO) representing selected UV/Vis transitions calculated for **dmdt$_2$Anthra[Ti(III)Cp$_2$]**. Red areas indicate decreasing electron density, while green areas indicate increasing electron density. Contour value $H = 0.001$.

dmdt₂Ad[TiCp₂]

In analogy to **dmdt₂Anthra[TiCp₂], Figure 4.21** shows the calculated UV/VIS spectrum of **dmdt₂Ad[TiCp₂]** and its reduced analog **dmdt₂Ad[Ti(III)Cp₂]**, compared to the experimentally acquired spectra of the of the complex.
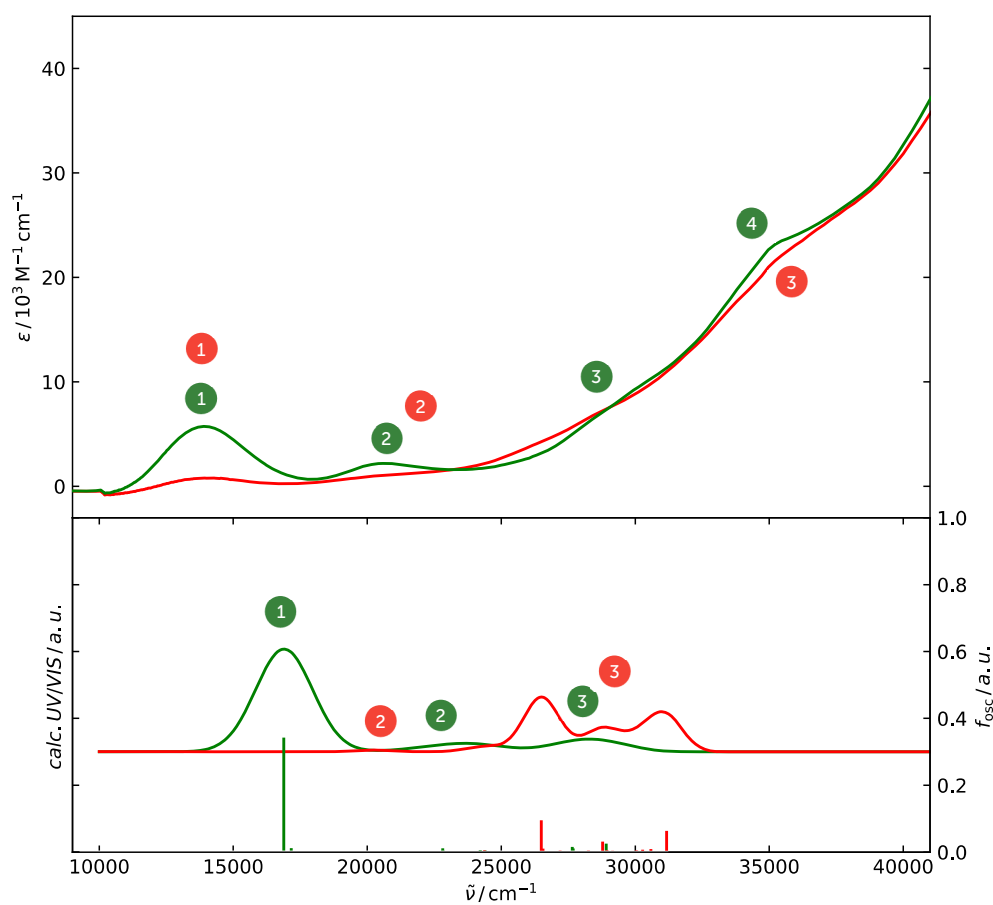
Figure 4.21. TD-DFT calculated (bottom) and (top) experimental UV/VIS spectra in DCM of (green) **dmdt₂Ad[TiCp₂]** and (red) **dmdt₂Ad[Ti(III)Cp₂]**. Greyed area represents solvent cutoff of DCM.
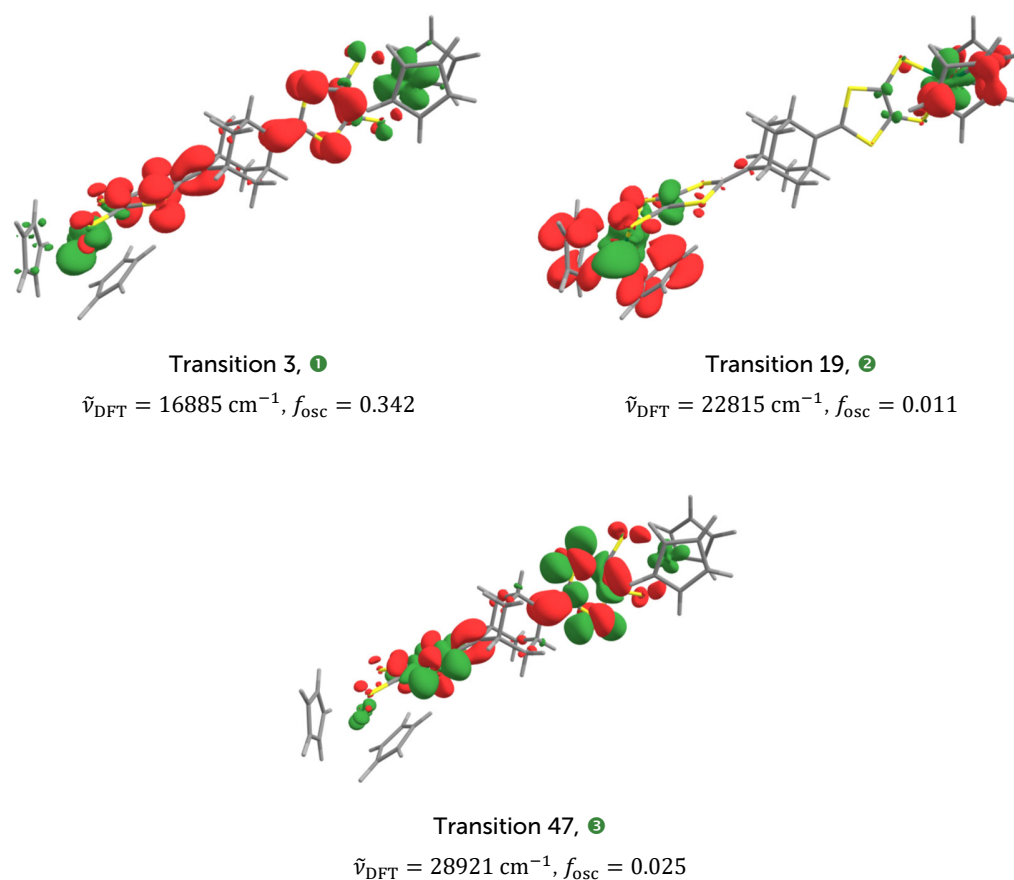
Transition 3, ❶

$\tilde{v}_{\text{DFT}} = 16885 \text{ cm}^{-1}, f_{\text{osc}} = 0.342$

Transition 19, ❷

$\tilde{v}_{\text{DFT}} = 22815 \text{ cm}^{-1}, f_{\text{osc}} = 0.011$

Transition 47, ❸

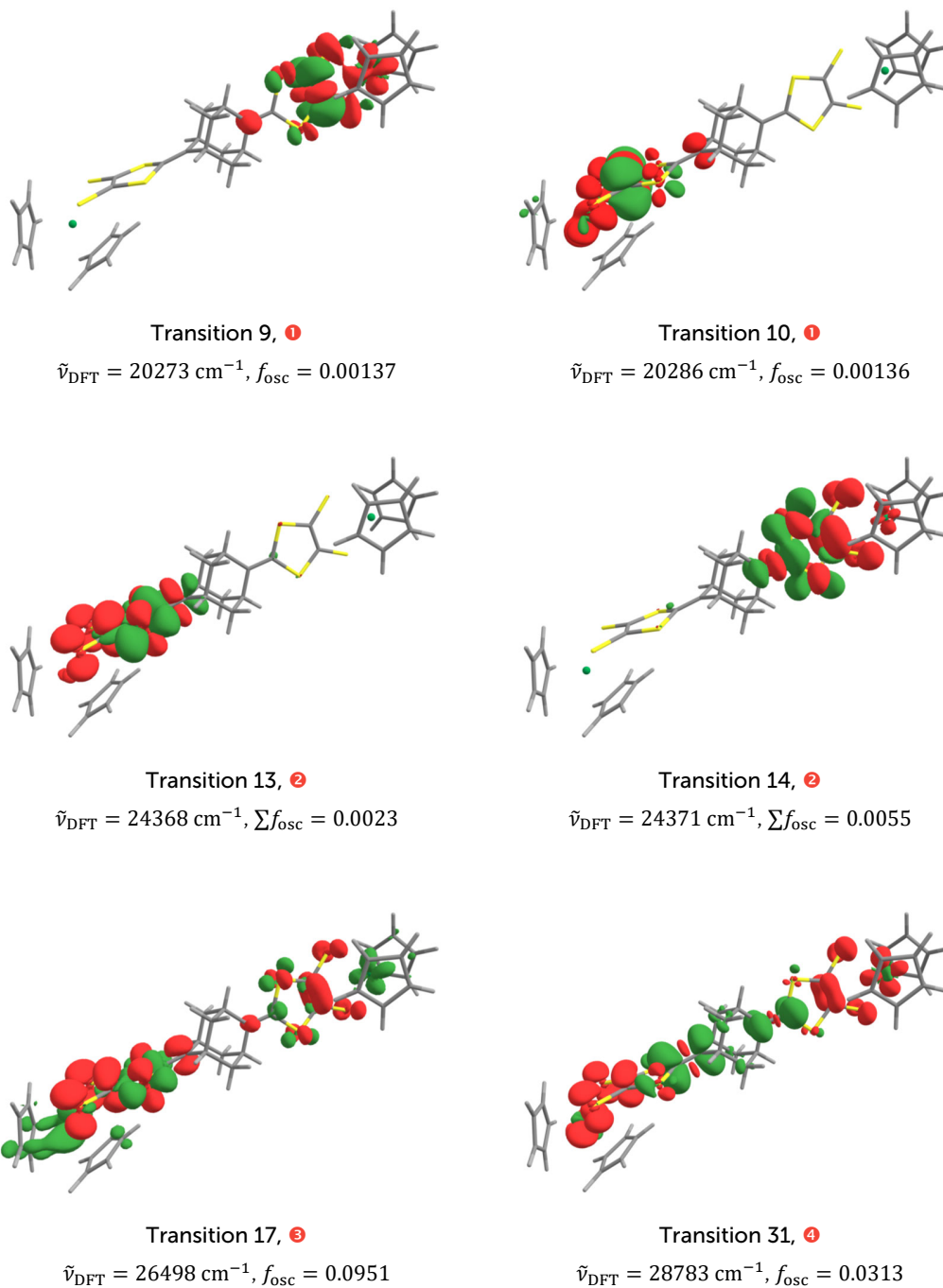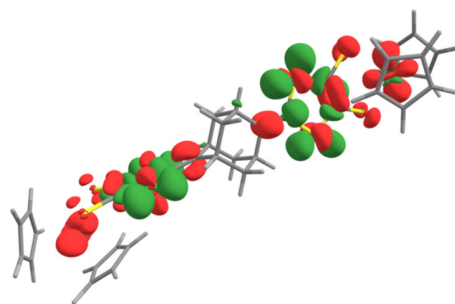$\tilde{v}_{\text{DFT}} = 28921 \text{ cm}^{-1}, f_{\text{osc}} = 0.025$

Figure 4.22. Difference densities obtained by TD-DFT (PBE0/def2-tvp/COSMO) representing selected UV/Vis transitions calculated for **dmdt₂Ad[Ti(IV)Cp₂]**. Red areas indicate decreasing electron density, while green areas indicate increasing electron ensity. Contour value $H = 0.001$.

As for **dmdt₂Anthra[TiCp₂]**, the UV/Vis data of **dmdt₂Ad[TiCp₂]** show a prominent feature corresponding to an LMCT from the dithiolene coordination site **dmdt** towards the titanium atoms. It is visible at $\tilde{v}_{\text{exp}} \approx 13840 \text{ cm}^{-1}$ ($\tilde{v}_{\text{DFT}} = 16885 \text{ cm}^{-1}$, $f_{\text{osc}} = 0.342$, ❶). This is very close to the observed and calculated values for **dmdt₂Anthra[TiCp₂]**.

The second visible feature is located at $\tilde{v}_{\text{exp}} \approx 20520 \text{ cm}^{-1}$ ($\tilde{v}_{\text{DFT}} = 22815 \text{ cm}^{-1}$, $f_{\text{osc}} = 0.011$, ❶). It has a much lower intensity in both experimental and theoretical data and can be attributed to an LMCT transition. In contrast to the first described band, this one involves the cyclopentadienyl rings instead of the **dmdt** site.

Figure 4.23. Difference densities obtained by TD-DFT (PBE0/def2-tvp/COSMO) representing selected UV/Vis transitions calculated for **dmdt₂Ad[Ti(III)Cp₂]**. Red areas indicate decreasing electron density, while green areas indicate increasing electron density. Contour value $H = 0.001$.

Transition 47, ⑤

$\tilde{\nu}_{\mathrm{DFT}} = 31168 \ \mathrm{cm}^{-1}, f_{\mathrm{osc}} = 0.0636$

Figure 4.23 continued.

Above $\tilde{\nu}_{\mathrm{exp}} = 14000 \ \mathrm{cm}^{-1}$ two more features are visible, but only one is described by TD-DFT. The feature at $\tilde{\nu}_{\mathrm{exp}} \approx 30220 \ \mathrm{cm}^{-1}$ ($\tilde{\nu}_{\mathrm{DFT}} = 28921 \ \mathrm{cm}^{-1}$, $f_{\mathrm{osc}} = 0.025$, ❸) is dominated by an IL ($\pi \rightarrow \pi^*$) on the dithiolenes.

Except for the first observed and calculated transitions, all others are weak. The calculations also give a good insight into the electron barrier properties. As shown in **Figure 4.18**, the adamantyl spacer readily separates the electrons between the two metal coordination sites. In the corresponding **dmdt₂Anthra[TiCp₂]**, this separation was not visible.

In addition to the unreduced compound, the experimental UV/Vis data of the reduced species **dmdt₂Ad[Ti(III)Cp₂]** can be compared with the calculated data. Here the independence of the electronic environments of the two metals is even more pronounced. However, the assignments from the calculation are more difficult to correlate. The representative transitions observed at $\tilde{\nu}_{\mathrm{exp}} \approx 13960 \ \mathrm{cm}^{-1}$ do not have calculated corresponding transitions and may be a remnant of non-reduced Ti(IV). The first calculated transition lies at $\tilde{\nu}_{\mathrm{exp}} \approx 20580 \ \mathrm{cm}^{-1}$ ($\tilde{\nu}_{\mathrm{DFT}} \approx 20273 \ \mathrm{cm}^{-1}$, $\sum f_{\mathrm{osc}} = 0.00272$, ❶). However, a second transition at $\tilde{\nu}_{\mathrm{DFT}} \approx 24368 \ \mathrm{cm}^{-1}$ ($\sum f_{\mathrm{osc}} = 0.0078$, ❷) is also shown by TD-DFT. Both observed transitions consist of two separate transitions by TD-DFT but with the same energy and almost the same oscillator strength, as shown in **Figure 4.23** (transitions 9+10 and 13+14).

Other than these bands, more very weak bands are visible above 25000 cm^{-1}. Comparing these with some selected calculated transitions (in **Figure 4.23**, transitions 17, 31, 47), it can be seen that they consist mostly of ILCTs.

4.3.3. CW-EPR spectroscopy on Titanium(III)

Although very sensitive, titanium(III) species are interesting for qubit applications. A titanium(III) complex has just recently been proposed as a molecular spin qubit by Sessoli and coworkers [136]. They investigated a Ti(III) complex with both a cyclopentadienyl and a cyclooctatetraene (cot) ligand.

With reference to the cyclovoltammetry performed in Section 4.3.1, which determined the reduction potential of the titanium dimers to be around -1.6 V (in DCM), only a handful of reducing agents are suitable for reducing the systems discussed in this section from titanium(IV) to titanium(III): Besides decamethylcobaltocene with a reduction potential of -1.94 V vs. Fc/Fc$^+$, only reducing agents such as sodium naphthalide (NaNAP), potassium graphite (KC$_8$) or alkaline (earth) metals are suitable.

Upon further literature research, Guyon et al. [133] found that a Ti(III) species of a silicon-bridged titanocene was generated in situ by the reaction of sodium naphthalide in THF at a lowered temperature of -20 °C.

As a moonshot to check the feasibility of this approach, a small amount of **dmit$_2$Anthra[TiCp$_2$]** was reduced with KC$_8$. This resulted in the observation[1] of a strong signal, very similar in both g-value, *A*-value, and shape to the Ti(III) species reported by Sessoli and very similar isotropic g-value reported by Guyon. As a result, this approach was pursued further.

---

[1] unfortunately, the measurement data got corrupted as a result of a software fault.

Table 4.6.   Reduction agents with their corresponding reduction potentials.

Reduction agent	solvent	approx. reduction potential vs. Fc/Fc$^+$	Ref.
FeCp$_2^*$	DCM	−0.59 V	[137]
CoCp$_2$	DCM	−1.33 V	[137]
CoCp$_2^*$	DCM	−1.94 V	[137]
KC$_8$	−	−2.49 V	[138]
FeCpCp*	glyme	−2.09 V	[137]
BPA[b]	THF	−2.30 V	[137]
Na	THF	−3.04 V	[137]
NAP[a]	THF	−3.10 V	[137]

[a] Naphthalide ion   [b] Benzophenone anion radical

In Situ Electrochemical Reduction of Titanium(IV) to Titanium(III)

Inspired by the results of the chemical reduction, a more thorough EPR SEC study was performed on all titanium compounds. The titanium(IV) species were electrochemically reduced in situ in DCM in an EPR tube at 0 °C. The counter and working electrode were made from platinum, while the reference electrode was a silver wire.

The EPR spectrum of the compound **dmdt$_2$Anthra[Ti(III)Cp$_2$]** at 293 K is shown in **Figure 4.24**. The other three compounds behave in the same way and the corresponding EPR spectra and simulations are shown in the appendix and will not be discussed separately.

The spectra show a strong isotropic signal at $g_{iso} = 1.985(2)$ with a shoulder towards higher fields and hyperfine splitting with signal intensities much smaller than the central signal at room temperature. These are only clearly visible towards lower fields and broaden significantly upon higher fields.

The deviation of this signal from the electron's g-value of the central signal and the presence of small hyperfine satellites indicate a titanium(III) centered radical. The isotropic g-value is significantly different from 2, indicating that the electron is placed in an orbital with metallic character due to its spin-orbit coupling [139]. This is also consistent with the spin

density calculated by DFT: The already previously shown **Figure 4.19** shows an almost purely metal-centered spin density for **dmdt₂Anthra[Ti(III)Cp₂]**, with a very small contribution on the **dmdt** ligand.

The hyperfine splitting itself results from the interactions with the nuclear spins of the two stable titanium isotopes with $I > 0$. These are ^{47}Ti (7.4 %, $I = 5/2$) and ^{49}Ti (5.4%, $I = 7/2$). Both the observed hyperfine pattern and the low g-value resulting from a less than half-full d-shell are described in literature [139]. Note the strong broadening of the hyperfine lines towards higher fields. This is consistent with the geometry of the titanium dimers. Their rod-like appearance causes them to tumble in the fast-motion regime.
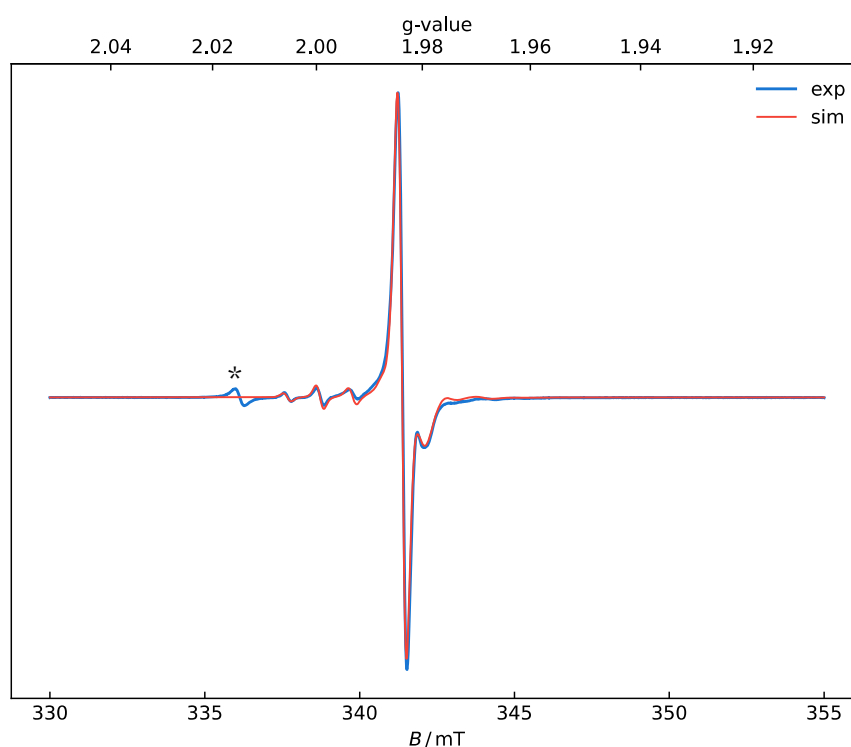
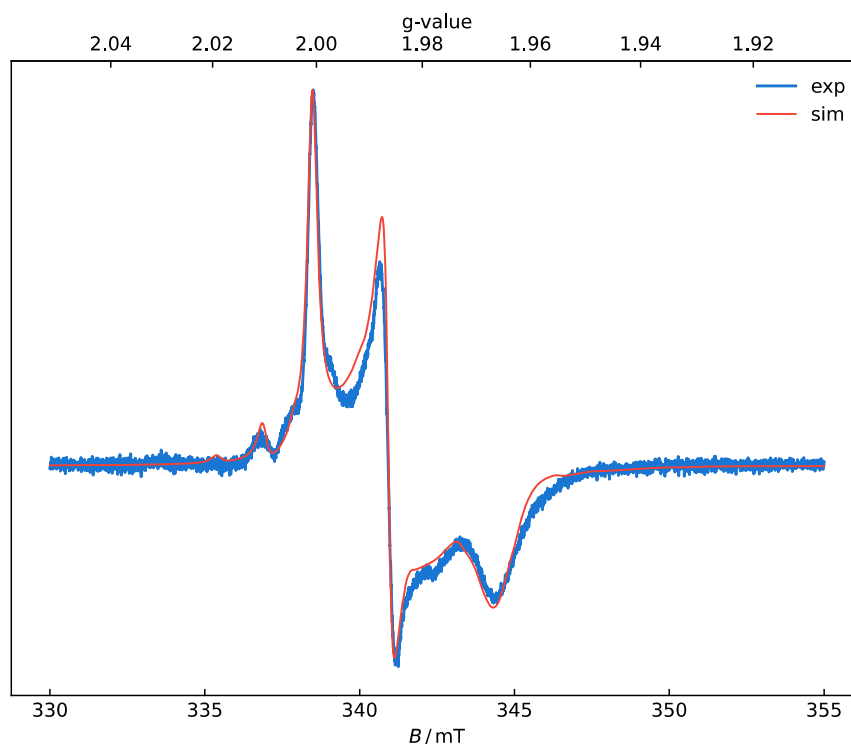**Figure 4.24.** EPR spectra of the in situ SEC EPR reduction of **dmdt₂Anthra[TiCp₂]** to **dmdt₂Anthra[Ti(III)Cp₂]** in THF / 0.1 M [NBu₄][PF₆] at 293 K. Simulation in red with parameters taken from **Table 4.7** and a second underlying $S = 1/2$ species with $g = 1.982(2)$ and a weight of 20%. * impurity on the platinum electrode.

Though, the shoulder of the main titanium-centered signal is unrelated to the titanium species. Upon cooling, its intensity does not change proportionally to that of titanium. In addition, the ratio of these signals is not consistent when the measurement is repeated. It varies from 9% to 20% and is probably a competing process on the ligand. The fact that directly applying the voltage to reduce Ti(IV) to Ti(III) (determined in Section 4.3.1) results in a less pronounced shoulder also supports that this signal is indeed coming from the ligand.

Table 4.7. Important EPR parameters of **dmdt$_2$X[Ti(III)Cp$_2$]** acquired by simulation of the data by in situ reduction in THF / 0.1 M [NBu$_4$][PF$_6$] as well as data from literature.

	X =				Ti(SiRCp$_2$)Cl$_2$	TiCp(cot)
	Ad	**Anthra**	**Penta**	**Dtbpa**		
g_{iso} [ac]	1.985(2)	1.985(2)	1.985(2)	1.984(2)	1.981(1)	–
g_x	1.967(2)	1.967(2)	1.966(2)	1.965(2)	–	1.972(3)
g_y	1.987(2)	1.987(2)	1.987(2)	1.987(2)	–	1.972(3)
g_z	2.001(2)	2.001(2)	2.001(2)	2.001(2)	–	2.001(1)
$A_{iso}(^{47}\text{Ti})$/ MHz [bc]	29.3	29.3	29.3	29.3	12(1)	–
$A_x(^{47}\text{Ti})$ / MHz	42	44	44	44	–	52.4(8)
$A_y(^{47}\text{Ti})$ / MHz	46	44	44	44	–	52.4(8)
$A_z(^{47}\text{Ti})$ / MHz	ca. 0	ca. 0	ca. 0	ca. 0	–	ca. 5
t_{corr} / ps [c]	316(30)	316(30)	316(30)	316(30)	–	–
ref.	this work				[139]	[136]

[a] $g_{iso} \approx \sum g_i /3$
[b] $A_{iso} \approx \sum A_i /3$
[c] in solution

The frozen solution spectrum of **dmdt₂Anthra[Ti(III)Cp₂]** at 100 K shows an anisotropic, rhombic signal. This is also characteristic of the observed titanium(III) species. Besides the strong broadening of the titanium signal, the shoulders broaden over-proportionally. In addition, the line shape changed from Gaussian in solution to Lorentzian in frozen state.

The important extracted EPR parameters of the four titanium dimers are listed in **Table 4.7**, including a comparison with literature Ti(III) species.

Although two isomers are present in the compound, their coordination environment does not affect the second titanium atom in any significant way, as no duplication of the EPR signals is observed.

Figure 4.25.   EPR spectra of the in situ SEC EPR reduction of **dmdt₂Anthra[TiCp₂]** to **dmdt₂Anthra[Ti(III)Cp₂]** in THF / 0.1 M [NBu₄][PF₆] at 100 K. Simulation in red with parameters taken from **Table 4.7** and a second underlying $S = 1/2$ species with $g = 1.982(2)$ and a weight of 20%.

4.3.4. Pulsed EPR spectroscopy on Titanium(III)

To observe the relaxation behavior of the Ti(III) species, it was not possible to use the in situ generated species discussed in the previous section. Instead, a more careful approach was taken with the chemically reduced species.

In the cold and under inert gas in a glove box, it was possible to prepare a deep red solution of the doubly reduced Ti(III) species by reducing the Ti(IV) species with decamethylcobaltocene (see **Figure 4.26**). Great care was taken not to add excessive amounts of decamethylcobaltocene, although the small sample amount of sample used made this difficult. Excess solids in the reaction mixture were removed immediately after a minute into the reaction using syringe filters. The reaction was scaled so that the resulting reaction solution contained a 2 mM solution of the target Ti(III) species.
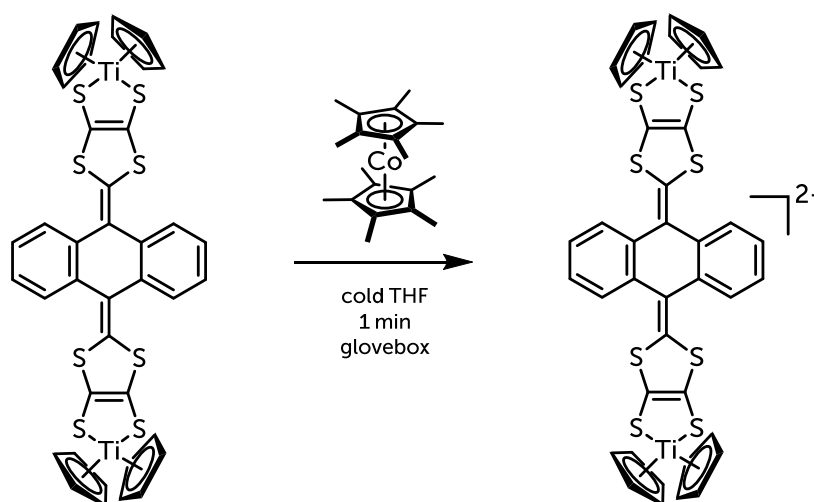
Figure 4.26. Chemical reduction of **dmdt₂Anthra[TiCp₂]** with decamethylcobaltocene to form **(CoCp*₂)₂(dmdt₂Anthra[Ti(III)Cp₂])**.

The solution was then transferred into a Q-band EPR tube, which was then placed in a sealable X-band tube. Before performing the pulsed EPR experiments, the solution was checked for consistency with the in-situ results by measuring a room temperature X-band EPR spectrum. Interestingly, no additional underlying radical species were observed in the chemically reduced sample.

Following this verification, ESE detected spectra, as well as phase memory and spin-lattice relaxation times, were measured from 5 K to 80 K in both regular THF and deuterated THF, using the Hahn echo and the inversion recovery pulse sequence, respectively.

The field-swept electron spin echo (ESE) spectrum shows a relatively narrow signal over a field range of less than 40 mT. The signal is composed of three lines resulting from a rhombic g-tensor. Based on the parameters obtained from in-situ X-band measurements (**Table 4.7**), its simulation agrees well with the observed spectrum. The spectra recorded in regular and deuterated THF are the same.
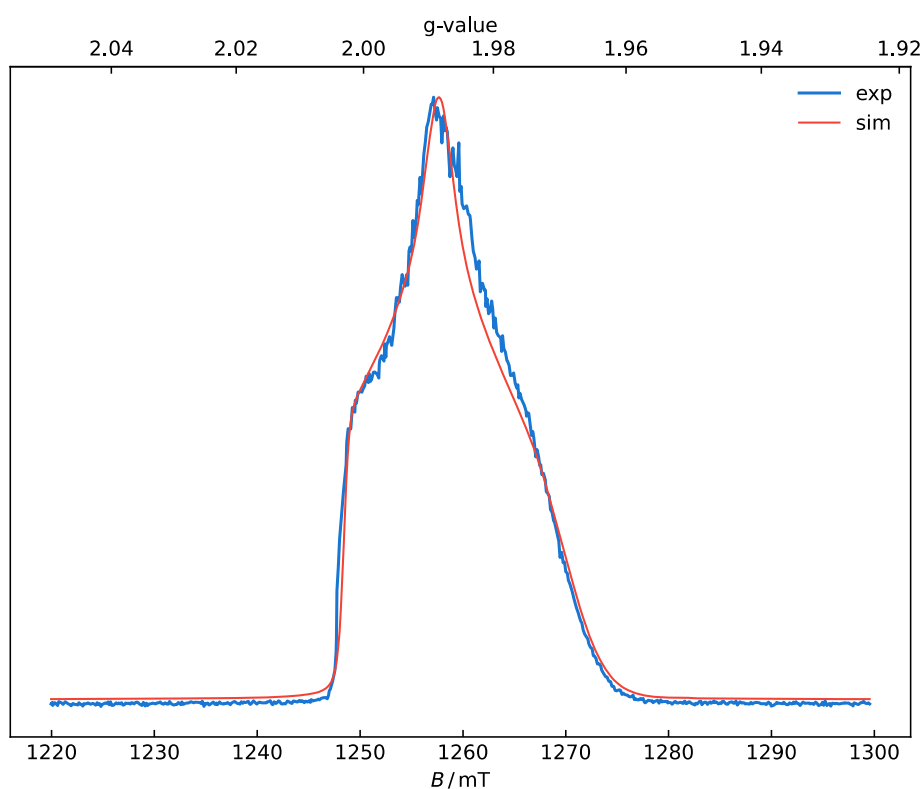
Figure 4.27. ESE-detected Q-band EPR spectrum of the chemically reduced **(CoCp*₂)₂(dmdt₂Anthra[Ti(III)Cp₂])** in THF at 7 K. Simulation in red with parameters taken from **Table 4.7**.

The spin-lattice relaxation times T_1 were obtained by fitting the experimental data with a biexponential function (see **Equation (11))**. The phase memory times T_m were fitted were a monoexponential function (see **Equation (12)**). The extracted values are summarized in **Table 4.8** and visualized in **Figure 4.28** and **Figure 4.29**.

In the sin-lattice relaxation measurements, two relaxation processes could be observed, indicated by the biexponential fit (see **Figure 4.28**). For the slow process, the observed spin-lattice relaxation times are very similar, regardless of the deuteration of the solvent. at low temperatures of 5 K, they are 115(14) ms for the regular THF and 126(16) ms for the deuterated THF, respectively. This value decreases rapidly to 62(7) ms (protonated) and 51(6) ms (deuterated) at 7 K. At 40 K, the values are only a mere 0.6(2) ms (protonated) and 0.32(5) ms (deuterated). For the fast process, there is a difference at low temperatures visible with 11(2) ms for the protonated solvent and 7(1) ms for the deuterated solvent. However, they become very similar as the temperature is increased. These similar relaxation times are to be expected since nuclear spins in the solvent should only have a visible effect on the phase memory time but not on the spin-lattice relaxation time.
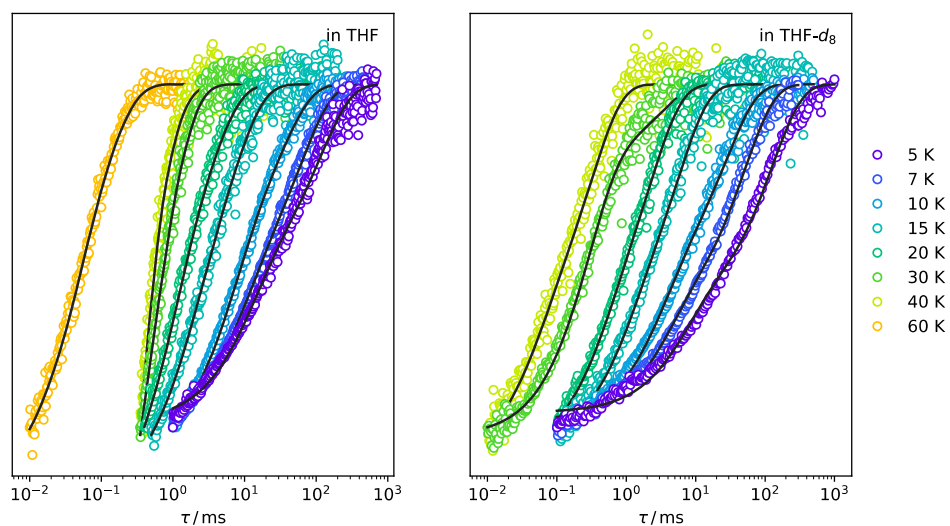
Figure 4.28.   Inversion recoveries of a 2 mM solution of **(CoCp*$_2$)$_2$(dmdt$_2$Anthra[Ti(III)Cp$_2$])** in THF (left) and THF-d$_8$ (right) at 1257.5 mT and 35 GHz. Solid lines represent fits with parameters from **Table 4.8**.
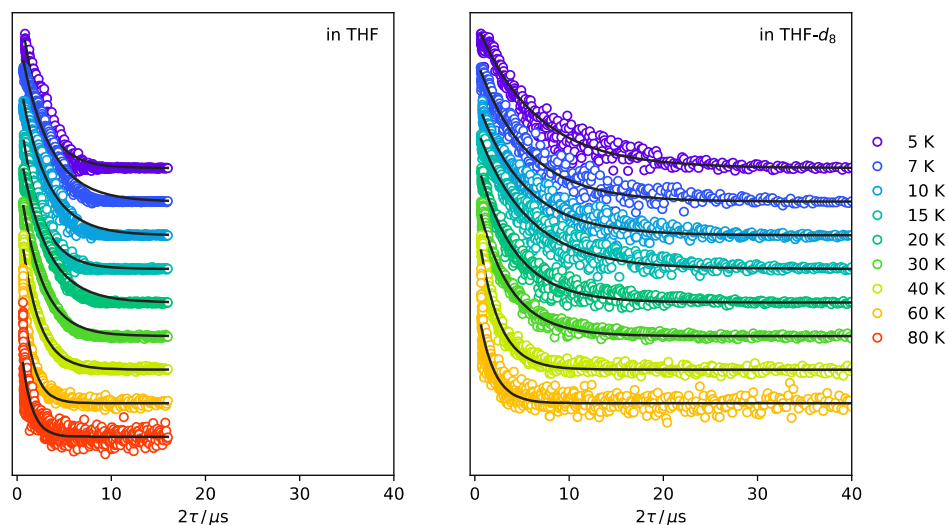
Figure 4.29. Hahn-echo decays of 2 mM solution of **(CoCp*$_2$)$_2$(dmdt$_2$Anthra[Ti(III)Cp$_2$])** in THF (left) and THF-d$_8$ (right) at 1257.5 mT and 35 GHz. Solid lines represent fits according to **Table 4.8**.

The results of the Hahn echo experiments tell a different story. As expected, the deuteration of the solvent does indeed have a very positive effect on the relaxation times: At 5 K, while T_m is only 2.2(3) µs for the non-deuterated solvent, it almost triples to 6.3(7) µs for the deuterated solvent. However, this factor decreases to around 2 starting from 7 K, where the molecule has a relaxation time of 3.0(3) µs in the non-deuterated solvent and 5.2(6) µs in the deuterated solvent. After that, the relaxation times remain mostly constant and decrease only after 40 K.

The comparison of the obtained values with literature is quite tricky since there are not many titanium(III) relaxation times to be found at all. In 2020, Sessoli [136] published a paper on the aforementioned **Ti(III)Cp(cot)** molecule, including some relaxation data. In this publication, long T_m values of more than 10 µs are observed below 20 K and although only available in a graph, can be extracted to be around 20 µs at 10 K for **Ti(III)Cp(cot)** in deuterated toluene. The figures included in the publication also show T_1 to be about 20 ms at 10 K, again decreasing rapidly with increasing temperature to about 0.02 ms at 140 K.

Table 4.8. (left) Spin-lattice relaxation times $T_{1,s}$ and $T_{1,f}$ and their contributions A extracted from fitting the measured inversion recovery decays with a biexponential fit function and (right) Spin-spin relaxation times T_m extracted from fitting the measured Hahn echo decays with a monoexponential fit function including standard deviations of 2 mM **(CoCp*$_2$)$_2$(dmdt$_2$Anthra[Ti(III)Cp$_2$])** in regular and deuterated THF at various temperatures.

T / K	in THF				in THF-d$_8$			
	A_s	A_f	$T_{1,s}$ / ms	$T_{1,f}$ / ms	A_s	$T_{1,s}$ / ms	A_f	$T_{1,f}$ / ms
5	−1.15(9)	−0.82(6)	115(14)	11(2)	−1.3(1)	126(16)	−0.61(4)	7(1)
7	−1.2(1)	−0.80(6)	62(7)	7(1)	−1.4(1)	51(6)	−0.61(5)	3.6(5)
10	−1.08(8)	−1.09(8)	33(4)	6.0(8)	−1.18(9)	28(4)	−0.80(6)	3.0(4)
15	−1.43(3)	−0.99(1)	7(1)	1.5(4)	−1.44(8)	5.7(8)	−0.67(1)	0.9(2)
20	−1.280(2)	−1.36(4)	3.5(6)	0.8(2)	−1.45(8)	2.4(3)	−0.71(1)	0.4(1)
30	−2.4(3)	−1.7(2)	0.8(2)	0.3(1)	−0.468(5)	3.0(7)	−1.6(1)	0.29(4)
40	−2.0(8)	−5.0(4)	0.6(2)	0.2(4)	−1.49(8)	0.32(5)	−0.73(2)	0.04(1)
60	−1.24(5)	−1.13(4)	0.12(1)	0.04(4)	–	–	–	–
80	–	–	–	–	–	–	–	–

T / K	in THF		in THF-d$_8$	
	A	T_m / μs	A	T_m / μs
5	1.4(2)	2.2(3)	1.1(1)	6.3(7)
7	1.3(1)	3.0(3)	1.1(1)	5.2(6)
10	1.3(1)	2.8(3)	1.0(1)	5.0(6)
15	1.3(1)	2.1(2)	1.1(1)	5.4(6)
20	1.3(1)	2.8(3)	1.1(1)	4.0(5)
30	1.3(1)	2.3(2)	1.1(1)	3.4(4)
40	1.3(1)	1.9(2)	1.2(1)	2.1(2)
60	1.3(2)	1.2(1)	0.9(1)	1.6(2)
80	1.0(1)	1.0(1)	–	–

Although these times are not the record times of the vanadium(IV) dmit qubits [10] and lag behind the reported monomeric Ti(III) species, the observed relaxation times are promising for a novel, dimeric titanium(III) species and make these compounds of interest for use in qubit and ultimately qugate applications, with their fairly high spin-lattice relaxation times as well as decent spin-spin relaxation times.

4.4. Conclusion

In this chapter, the coordination chemistry of the ligands of type **dmdt₂X[EtCN]** was explored. This involved establishing the deprotection requirements of the ligands to then subsequently be able to coordinate metals to them.

It was found that these ligands behave quite differently from the unmodified dmit ligand. The deprotection requirements and especially the way they coordinate with metals were significantly different, and the results are shown in **Figure 4.30**.

While the titanocene(IV) dimers **dmdt₂X[TiCp₂]** are readily and consistently accessible in good yields, the transfer to an EPR-active vanadocene(IV) species was not possible. Although a vanadium **dmdt** species was detected by recording an X-band EPR spectrum of the reaction solution, this signal rapidly disappeared as the solution warmed to room temperature. It is most likely that the coordination compound reacts further to form chains of an unknown EPR silent vanadium species, although this could not be fully confirmed due to the insolubility of the precipitate formed. An indication that this is still the case is that it was possible to access the monomeric **dmdtAd[TiCp₂]** and **dmdtAd[VCp₂]** compounds without them showing signs of decomposition or complexation problems. Attempts to use other synthetic routes, such as transmetallation based on tin(IV) or redox complexation, were also unsuccessful. The necessary intermediates could not be isolated and were not detectable by spectroscopy.

Furthermore, four diamagnetic titanium(IV) dimers could be isolated: **dmdt₂Ad[TiCp₂]**, **dmdt₂Anthra[TiCp₂]**, **dmdt₂Penta[TiCp₂]** and **dmdt₂Dtbpa[TiCp₂]**. They could be characterized by NMR and mass spectrometry and additionally partially by CV, cw-EPR, p-EPR and UV/Vis SEC.

In electrochemical studies, all titanium(IV) dimers exhibit only one reversible reduction to Ti(III) as well as a mostly irreversible oxidation of the ligand. This observed reduction is also consistent with literature reports of Ti(III) species and, therefore, can be considered metal-based. UV/VIS SEC provided additional insight into the reduction process. In all compounds, the long wavelength VIS band was attributed to an LMCT. In addition, further transitions observed in the neutral Ti(IV) compounds as well as in the reduced Ti(III) compounds, could be assigned to the results of the TD-DFT calculations. For the **dmdt₂Ad[Ti(III)Cp₂]**, it was even possible to support the electronic independence of the two coordination spheres by TD-DFT.

It was also possible to observe the reduced Ti(III) dimers by in situ EPR spectroscopy from room temperature down to 100 K. This further confirmed the titanium-based reduction even more as for all, a strong titanium(III) signal was observed at $g = 1.985(2)$, characteristic of a $S = 1/2$ titanium system, including titanium isotopic satellites. However, there was a secondary, smaller signal underlying the central titanium(III) signal, most likely from a concurrent process on the ligand or an impurity. The spin density calculated from DFT is mainly on the titanium, but a small amount is located on the **dmdt** coordination site. Upon freezing the solution, this isotropic signal changed into a rhombic signal, which is also consistent with literature for Ti(III).

Interestingly, the additional smaller signal was not observed when the compounds were chemically reduced with decamethylcobaltocene. The chemical reduction also allowed the acquisition of pulsed EPR data of the **dmdt₂Anthra[TiCp₂]**, providing insight into the relaxation behavior of a **dmit**-like paramagnetic titanium dimer. It was found that the relaxation times are good for such a system. At 5 K, T_m was determined to be 2.2(3) µs for the non-deuterated solvent and 6.3(7) µs in deuterated THF. T_1 reached just over 100 ms, with 115(14) ms for the non-deuterated and 126(16) ms for the deuterated variant.

Relating the measured phase-memory times to QIP applications, the observed Ti(III) dimeric "qugate" offers potential as a future qubit and qugate. The observation makes these titanium compounds in their reduced state worth exploring more in their property as potential qugates. At the same time, however, an air-stable or even shelf-stable alternative should be developed.
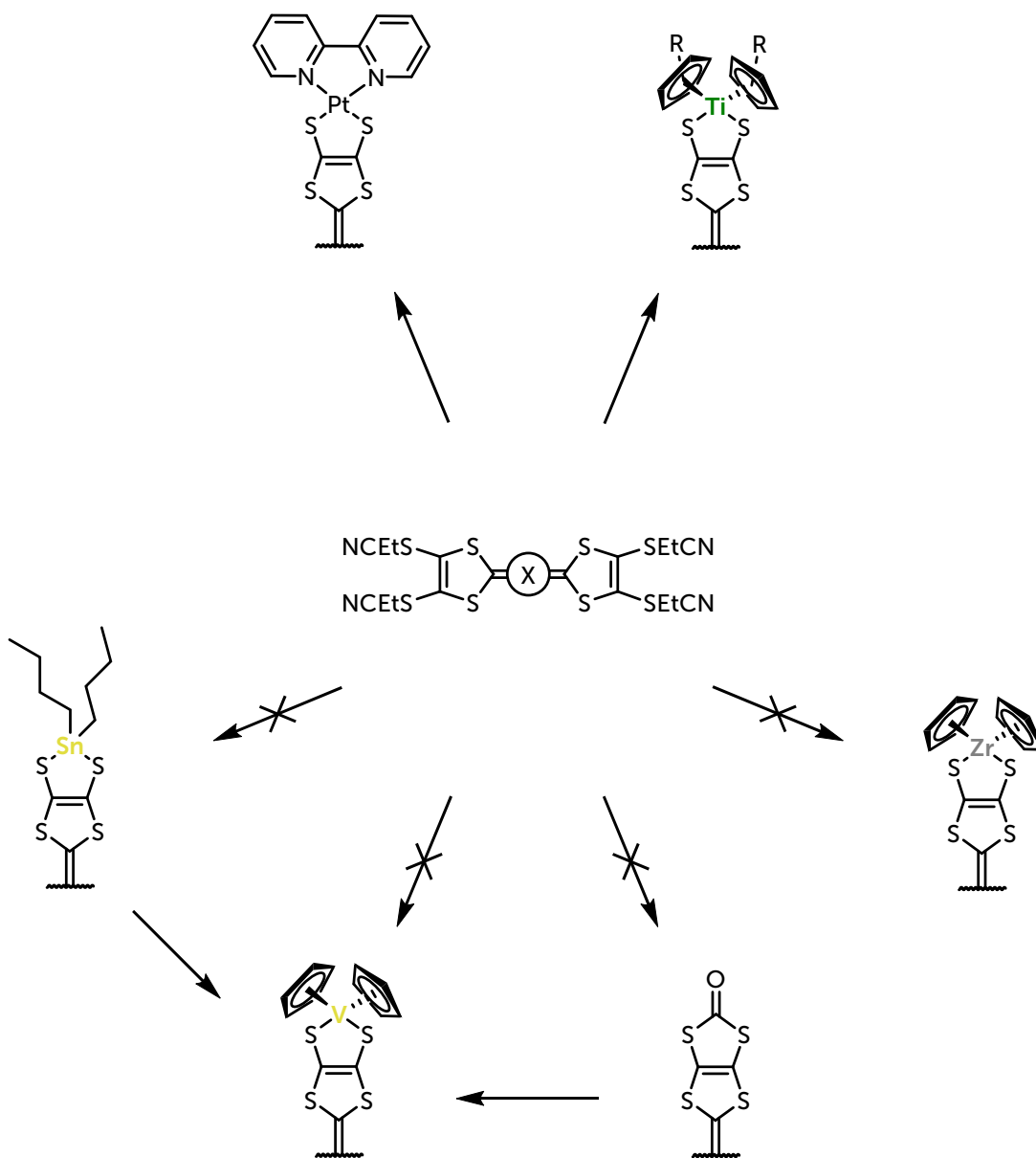
Figure 4.30. Explored routes towards different metal complexes based on **dmdt** dimers. Besides the similarities of titanocene(IV) and vanadocene(IV), the vanadocene(IV) was not accessible via several routes, including redox-routes. X = **Anthra**, **Penta**, **Dtbpa**, **Ad**; R = alkyl.

4.5. Experimental Section

All manipulations were carried out under an atmosphere of argon or nitrogen using standard Schlenk line techniques if not stated otherwise. Dry solvents were purchased from Acros Organics in AcroSeal bottles or dried using standard techniques. Commercially available chemicals listed in the supporting information were used as received unless otherwise stated. For known compounds, spectral data were compared to literature to confirm identity, and if possible, new data was acquired, or changes in the synthetic approach were denoted.

Chromatography was performed on silica 60 (diameter 0.040 – 0.063 mm). Reaction control was performed with thin-layer chromatography plates (TLC) made from Silica 60 impregnated with F_{254} by Macherey-Nagel.

Solution NMR spectra were recorded on either a Bruker Avance AV250 (^1H 250 MHz), Bruker Avance AV300 (^1H 300 MHz; ^{13}C 63 MHz), a Bruker Ascend 400 (^1H 400 MHz; ^{13}C 101 MHz), a Bruker Avance AV500 (^1H 500 MHz) or a Bruker Ascend 700 (^1H 700 MHz) at 303 K. Spectra are always referenced against residual solvent signals.

IR spectra were recorded on a Bruker Vektor 22 FT-IR spectrometer in ATR mode by the analytics division of the Institute of Organic Chemistry, University of Stuttgart.

ESI mass spectra were recorded on a Bruker Daltonics Micro-TOF Q spectrometer and **EI mass spectra** on a Finnigan MAT95 at 70 eV by the analytics division of the Institute of Organic Chemistry, University of Stuttgart.

Elemental analyses (C, H, N, S) were determined on an Elemental Micro Cube analyzer by Barbara Förtsch, Institute of Inorganic Chemistry, University of Stuttgart.

X-Band EPR spectra were recorded on a MagnetTech MiniScope MS 400 spectrometer. The magnetic field shift was corrected using a DPPH standard sample. If not otherwise indicated, measurements were conducted at room temperature.

Cyclic voltammetry was either performed on a Methrom Autolab B.V. potentiostat or a Keithley 2450 SourceMeter source measure unit. A three-electrode configuration consisting of platinum working and counter electrodes, as well as a silver reference electrode, was used. The measurements were performed under argon in 0.1 M $[Bu_4N][PF_6]$ solution.

Potentials are referenced against ferrocene/ferrocenium as the internal standard. Measurements conducted on the Methrom device were performed together with Marc Schnierle from the Institute of Inorganic Chemistry, University of Stuttgart.

UV-vis-NIR spectroelectrochemical measurements were performed in 0.1 M $[Bu_4N][PF_6]$ solution using an optically transparent thin-layer electrochemical (OTTLE) cell in tandem with a TIDAS diode array spectrometer from J&M Analytik AG. Measurements were performed together with Marc Schnierle, M.Sc.

EPR spectroelectrochemical measurements were performed in 0.1 M $[Bu_4N][PF_6]$ solution using platinum as a counter and working electrode as well as a silver reference directly in an EPR tube. Measurements were recorded on a MagnetTech ESR5000 together with Simon Suhr from the Institute of Inorganic Chemistry, University of Stuttgart.

Pulsed electron paramagnetic resonance (pEPR) was recorded on a homebuilt Q-band spectrometer [140], and spectra were simulated with Easyspin 5.2.30 [141]. The microwave frequency was 35.000 GHz. Samples were prepared by dissolving the corresponding diamagnetic compound in cold, dry THF in a glovebox and adding a pre-weighted reduction agent. The sample was afterward transferred through a syringe filter directly into a Q-band EPR tube and was always freeze-quenched by directly inserting it into the already cold resonator chamber to prevent precipitation of the compound when cooling down. The cavity was always tuned to the third mode of a TE_{011}-resonator. For the determination of spin-lattice relaxation times, the inversion-recovery pulse sequence was used, while the determination of the spin-spin relaxation times was conducted using the Hahn-echo pulse sequence. The experimental error of the setup is quantified as 10%, as determined by Dominik Dengler [40], in addition to the statistical error arising from the fitting procedure.

Density functional theory (DFT) calculations were performed with the ORCA 4.0.1 package [142]. Starting structure files were generated with Avogadro. Geometry optimization and frequency analysis was carried out with the B3LYP functional and the def2-TZVP basis set. Atom-pairwise dispersion correction was done with the Becke-Johnson dampening scheme (D3BJ) [143],[144]. For time-dependent DFT, the PBE0 functional accompanied by the def2-TZVP basis set was used. 150 roots were generated per run. The calculated UV/Vis spectra were obtained by applying a Gaussian broadening similar to the experimentally observed broadening to the transitions obtained in the TD-DFT calculation.

4.5.1. Coordination Compounds

dmdt₂Anthra[TiCp₂]

dmdt₂Anthra[EtCN] (40 mg, 55 µmol, 1 eq.) in dry THF (3 mL) was cooled to –78 °C and lithium diisopropylamide (freshly prepared 250 mM solution in THF, 1 mL, 221 µmol, 4 eq.) was added, whereupon the orange solution immediately turned dark red. Stirring was continued for 2 h at low temperature. Titanocene dichloride (28 mg, 110 µmol, 2 eq.), dissolved in dry THF (2 mL) was added dropwise and slowly over 5 min. The dark red solution turned bright neon green and was stirred overnight. The resulting solution was filtered over silica and evaporated under reduced pressure to give a dark green, almost black powder. To further purify this, it was dissolved in a minimal amount of DCM and precipitated with twice the amount of Hx.
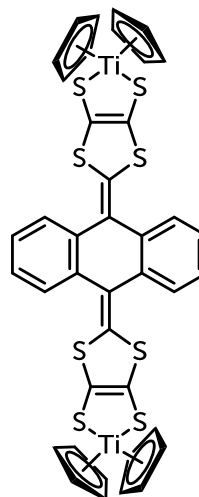
Yield: 51% (23 mg, 28 µmol).

R_f = 0.5 (Hx:EtOAc 1:1, green spot).

^{1}H NMR (CDCl₃, 400 MHz): δ = 7.75 (br, 4 H, anthra, conformer B), 7.57 (m, 4 H, anthra, conformer A), 7.28 (m, 4 H, anthra, conformers A+B), 6.02 (br, 10 H per conformer, 2 × Cp, conformers A+B), 5.81 (br, 10 H per conformer, 2 × Cp, conformer A), 5.66 (br, 10 H per conformer, 2 × Cp, conformer B) ppm.

^{1}H NMR (DMSO-d₆, 400 MHz): δ = 7.70 (m/br, 4 H, anthra, conformer B), 7.58 (m, 4 H, anthra, conformer A), 7.40 (m, 4 H, anthra, conformers A+B), 6.25 (br, 10 H per conformer, 2 × Cp, conformers A+B), 5.97 (br, 10 H per conformer, 2 × Cp, conformer A), 5.77 (br, 10 H per conformer, 2 × Cp, conformer B) ppm.

^{13}C{^{1}H} NMR: Signal intensity was too low to acquire a spectrum.

FT-IR: $\tilde{\nu}$ = 3111, 2927, 1734, 1526, 1445, 1384, 1282, 1017, 908, 820, 754, 730, 643 cm^{-1}.

HRMS (ESI+): m/z, calculated for [M+H]$^+$ ($C_{40}H_{29}S_8Ti_2$): 860.8998, found: 860.8895.

dmdt$_2$Ad[TiCp$_2$]

To **dmdt$_2$Ad[EtCN]** (20 mg, 30 µmol, 1 eq.) in dry THF (6 mL) lithium diisopropylamide (freshly prepared 250 mM solution in THF, 0.5 mL, 117 µmol, 4 eq.) was slowly added at r.t., whereupon the beige solution immediately turned pale green. Towards the end of the addition the solution changed to yellow, which faded to green again over the course of stirring for 2 h at r.t. Titanocene dichloride (15 mg, 59 µmol, 2 eq.) dissolved in dry THF (1 mL) was added dropwise and slowly over 5 min. The dark red solution turned blueish-green and was stirred overnight. The resulting blue solution was filtered over silica and evaporated under reduced pressure to yield a dark teal, almost black powder. To further purify this, it was dissolved it a minimal amount of DCM and precipitated with twice the amount of Hx.
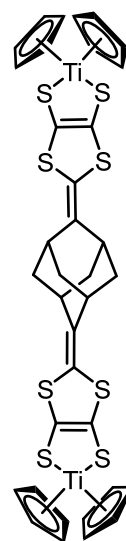
Yield: 63% (15 mg, 18 µmol).

R$_f$ = 0.6 (Hx:EtOAc 1:1, green spot).

^{1}H NMR (DCM-d$_2$, 400 MHz): δ = 5.79 (br, 10 H, 2 × Cp), 5.52 (br, 10 H, 2 × Cp), 2.34 (br, 4 H, Ad), 1.60 (br, 8 H, Ad) ppm.

^{1}H NMR (DMSO-d$_6$, 400 MHz): δ = 6.17 (br, 10 H, 2 × Cp), 5.83 (br, 10 H, 2 × Cp), 3.6 (br, 4 H, Ad), 1.76 (br, 8 H, Ad) ppm.

^{13}C{^{1}H} NMR: Signal intensity was too low to acquire a spectrum.

FT-IR: $\tilde{v}$ = 2920, 2850, 1611, 1443, 1374, 1351, 1096, 1019, 944, 909, 820, 731 cm^{-1}.

HRMS (ESI+): m/z, calculated for [M+H]$^+$ (C$_{36}$H$_{33}$S$_8$Ti$_2$): 816.9310, found: 816.9303.

dmdt$_2$Penta[TiCp$_2$]

dmdt$_2$Penta[EtCN] (24 mg, 28 μmol, 1 eq.) in dry THF (2 mL) was cooled to −78 °C and lithium diisopropylamide (freshly prepared 250 mM solution in THF, 0.5 mL, 111 μmol, 4 eq.) was added, whereupon the orange solution immediately turned dark purple. Stirring was continued for 2 h at low temperature. Titanocene dichloride (14 mg, 55 μmol, 2 eq.), dissolved in dry THF (1 mL) was added dropwise and slowly over 5 min. The dark purple solution turned bright green and was stirred overnight. The resulting solution was filtered over silica and evaporated under reduced pressure to give a dark green, almost black powder. To further purify this, it was dissolved in a minimal amount of DCM and precipitated with twice the amount of Hx.
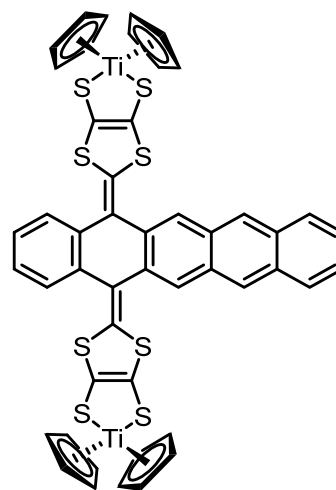
Yield: 62% (17 mg, 17 μmol).

R$_f$ = 0.6 (Hx:EtOAc 1:1, green spot).

^{1}H NMR (THF-d$_6$, 400 MHz): δ = 8.37 (s, 2 H, anthra), 7.92 (s, 2 H, anthra), 7.92 (d, 2 H, anthra), 7.51 (br, 2 H, isolated Ph), 7.32–7.34 (m, 2 H, anthra), 7.21 (br, 2 H, isolated Ph), 6.00 (br, 10 H per conformer, 2 × Cp, conformers A+B), 5.79 (br, 10 H per conformer, 2 × Cp, conformer A), 5.56 (br, 10 H per conformer, 2 × Cp, conformer B) ppm.

^{13}C{^{1}H} NMR: Signal intensity was too low to acquire a spectrum.

FT-IR: $\tilde{v}$ = 2922, 1734, 1525, 1440, 1384, 1019, 909, 820, 747, 644 cm^{-1}.

HRMS (ESI+): m/z, calculated for [M+H]$^+$ (C$_{48}$H$_{33}$S$_8$Ti$_2$): 960.9313, found: 960.9311.

dmdt$_2$Dtbpa[TiCp$_2$]

dmdt$_2$Dtbpa[EtCN] (30 mg, 28 µmol, 1 eq.) in dry THF (1 mL) was cooled to −78 °C and lithium diisopropylamide (freshly prepared 250 mM solution in THF, 0.5 mL, 111 µmol, 4 eq.) was added, whereupon the yellow solution immediately turned dark red. Stirring was continued for 2 h at low temperature. Titanocene dichloride (14 mg, 55 µmol, 2 eq.), dissolved in dry THF (1.5 mL) was added dropwise and slowly over 5 min. The dark purple solution turned bright green and was stirred overnight. The resulting solution was filtered over silica and evaporated under reduced pressure to give a dark green, almost black powder. To further purify this, it was dissolved in a minimal amount of DCM and precipitated with twice the amount of Hx.
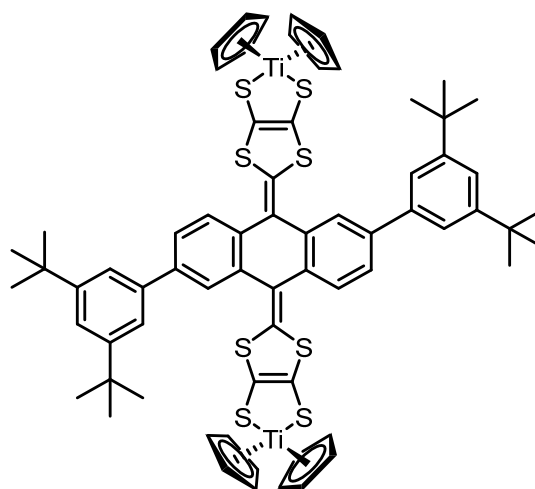
Yield: 53% (23 mg, 19 µmol).

R$_f$ = 0.3 (Hx:EtOAc 1:2, green spot).

^{1}H NMR (CDCl$_3$, 400 MHz): δ = 7.86–7.80 (m, 2 H, anthra), 7.70–7.64 (m, 2 H, anthra), 7.58–7.51 (m, 6 H, dtbpa-H), 7.50–7.47 (br, 2 H, dtbpa), 6.05 (br, 10 H per conformer, 2 × Cp, conformers A+B), 5.84 (br, 10 H per conformer, 2 × Cp, conformer A), 5.68 (br, 10 H per conformer, 2 × Cp, conformer B), 1.41 (s, 36 H, Me) ppm.

^{13}C{^{1}H} NMR: Signal intensity was too low to acquire a spectrum.

dmdtAd[TiCp]

dmdtAd[EtCN] (20 mg, 49 µmol, 1 eq.) in dry THF (3 mL) was cooled to −78 °C and lithium diisopropylamide (freshly prepared 235 mM solution in THF, 0.4 mL, 98 µmol, 2 eq.) was added, whereupon the yellow solution immediately turned dark red. Stirring was continued for 2 h at low temperature. Titanocene dichloride (12 mg, 49 µmol, 2 eq.), dissolved in dry THF (3 mL) was added dropwise and slowly over 5 min. The dark red solution turned bright green and was stirred overnight. The resulting solution was filtered over silica and evaporated under reduced pressure to give a dark green, almost black powder. To further purify this, it was dissolved in a minimal amount of DCM and precipitated with twice the amount of Hx.
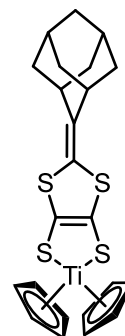
Yield: 61% (14 mg, 29 µmol).

R_f = 0.6 (Hx:EtOAc 2:1, blue-green spot).

^{1}H NMR (CDCl$_3$, 400 MHz): δ = 5.99 (s, 5 H, Cp), 5.72 (s, 5 H, Cp), 2.51 (br s, 2 H, Ad), 1.75–1.97 (m, 12 H, Ad) ppm.

^{13}C{^{1}H} NMR: Signal intensity was too low to acquire a spectrum.

HRMS (ESI+): m/z, calculated for [M+H]$^+$ (C$_{23}$H$_{25}$S$_2$Ti): 477.0313, found: 477.0310.

5

ORGANOBASED MULTI-QUBIT-SYSTEMS WITH PTM RADICALS

5. ORGANOBASED MULTI-QUBIT-SYSTEMS WITH PTM RADICALS

To evaluate whether perchlorinated trityl (**PTM**) radicals are useful candidates for 2-qubit systems, such radicals were provided by the group of Dr. Núria Crivillers of the Institute of Sciences and Materials, University of Barcelona, Spain. Synthesis and structural characterization were performed by Jesús Alejandro De Sousa. This chapter deals with the relaxation behavior and the inter-qubit interaction in the diradical system as studied by means of dipolar EPR spectroscopy. These measurements were carried out in the group of Dr. Floriana Tuna at the University of Manchester, United Kingdom. First, a brief overview of the compound class is presented. Then, the Q-band EPR data acquired in Stuttgart together with Jonathan Wischnat, including the coherence properties of both T_1 and T_m are determined for all compounds, and finally, the results of the three different dipolar spectroscopy methods employed were compared to each other.

5.1. About Trityl Radicals

Triphenylmethyl – or short trityl – radicals themselves are already widely used in EPR as distance rulers or markers in biochemical applications [145],[146]. The mother of all trityl compounds was prepared by Gomberg as early as 1900 [147].
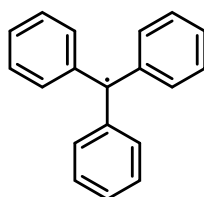
**Gomberg's
Trityl Radical**

Figure 5.1.   Structure of the first trityl radical by Gomberg [147].

It is the first radical ever described as a stable compound in organic chemistry. It was discovered by Gomberg while attempting to prepare hexaphenylethane. Due to their narrow EPR linewidths and long coherence times, trityl radicals have played a crucial role in the development of modern EPR techniques and have become the precursor of the much more stable variants described below.

5.1.1. Finland Trityl Radical

In 1996, the company Nycomed Innovations AB published a series of tri(tetrathiaaryl)methyl (TAM) radicals designed exclusively for stability in biological media and non-toxicity, as well as having a single, sharp EPR line [148]. One of the most prominent of these is the so-called Finland trityl radical (**FTR**).

FTR
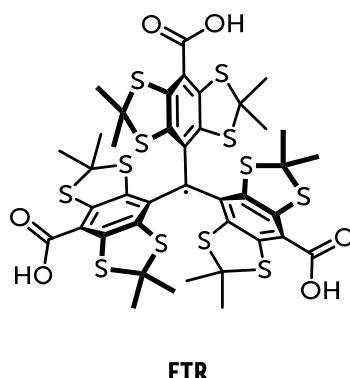
Figure 5.2.   Structure of the Finland trityl radical developed by Nycomed Innovations AB [148].

It contains thioketal groups which, due to their steric bulk, protect the central radical and make it chemically inert. This inertness, especially towards reduction, proved to be very useful for applications in biological media and in the presence of oxygen. In addition, the broadening of the EPR signal due to hyperfine coupling to hydrogen nuclear spins is not pronounced since none are present in the immediate vicinity. This absence also contributes to the long phase memory times of the radical center (see Chapter 2.4) [149]–[151].

5.1.2. Perchlorinated Trityl Radicals

In addition to FTRs, chemists have made progress in creating new organic radicals that are stable under a wide range of conditions. Perchlorinated trityl radicals, also known as polychlorotriphenylmethyl (**PTM**) radicals, are, in this respect, perfect candidates. Their chlorinated environment sterically protects the central radical, making them thermally and chemically stable. The chloro-substituents also force the phenyl rings into a propeller-like formation. As a result, these radicals are inert not only to oxygen but also to chemicals. This makes them perfect building blocks for larger, more complex radical systems. Recent research applications of trityl radicals include but are not limited to molecular electronic junctions, optical devices, and molecular switches [152].

5.2. The Compounds

The perchlorinated trityl radicals studied are shown in **Figure 5.3**. Their synthesis is described in [153]. In this chapter, both the non-functionalized PTM monomer **PTM-mono** and its modified **PTM-tail** counterpart, which can subsequently be coupled to form a **PTM-di** dimer, were investigated. All three are highly soluble in a wide range of solvents, including PhMe, DCM, and CS$_2$. However, they are light-sensitive and should be handled in a dark environment.

PTM-mono   **PTM-tail**
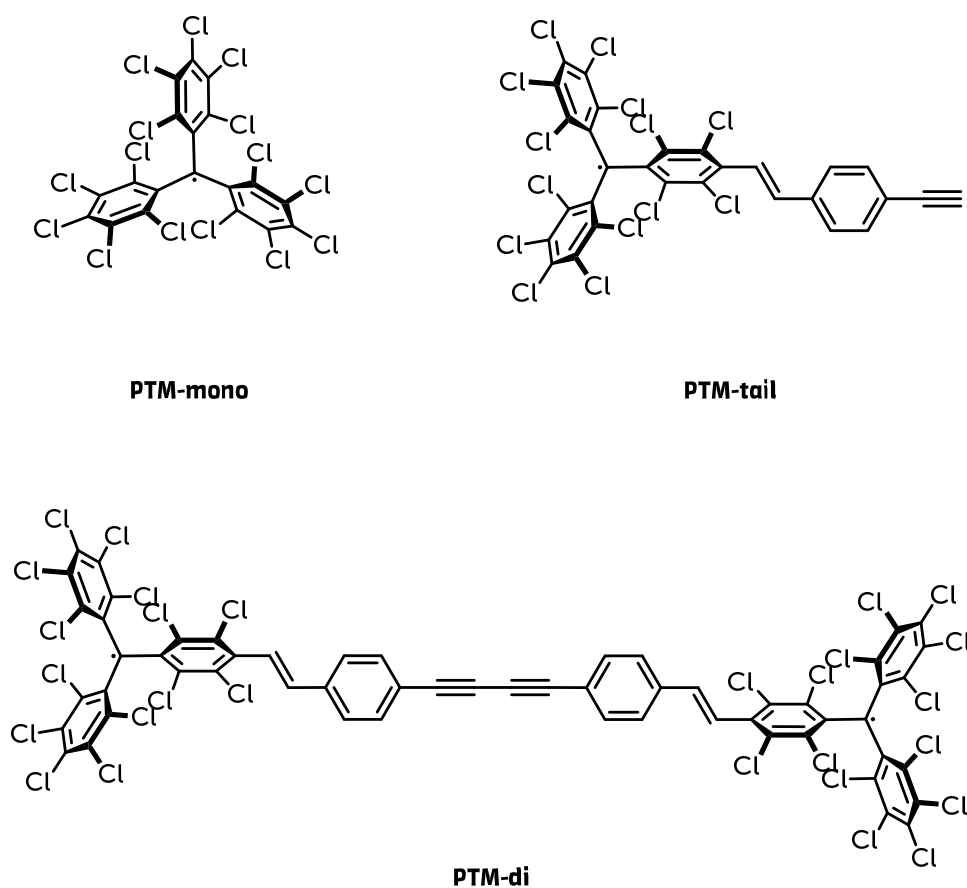
PTM-di

Figure 5.3.   Structures of the investigated **PTM** radicals provided by the Crivillers group in Barcelona, Spain.

5.3. EPR Spectra and Relaxation Times

The three PTM compounds, **PTM-mono**, **PTM-tail**, and **PTM-di**, were investigated in a 200 µM carbon disulfide solution over a wide temperature range by pulsed EPR at Q-band frequencies. Phase memory and spin-lattice relaxation times were measured using the Hahn echo pulse sequence and the inversion recovery pulse sequence, respectively. Carbon disulfide was chosen because of its excellent solvent properties and the absence of nuclear spins in the solvent itself.

5.3.1. ESE spectra

The Q-band echo detected EPR spectra of the three PTM compounds **PTM-mono**, **PTM-tail,** and **PTM-di** at 7 K are shown in **Figure 5.4**. All three compounds exhibit a single, very narrow resonance line with a width of only 3 to 5 mT, just around the g-value of the free electron. The relative field shift of the spectra can mainly be attributed to offsets in the teslameters of the spectrometer as it reaches its precision limits. While the **PTM-di** exhibits almost no visible anisotropy as the spectrum is highly symmetrical, the **PTM-mono** and especially the **PTM-tail** show a strong visible anisotropy.

The anisotropy observed in all three systems is consistent with their chemical structure. While **PTM-mono** is highly symmetric, **PTM-tail** is less symmetric as one of the phenyl rings is modified to make the molecule usable in chemical transformations. The **PTM-di** was expected to have a similar asymmetric g-tensor, but this was not observed.

In addition, no hyperfine interactions between the electron spins and the chlorine nuclear spins are resolved. This is likely because the spin densities of the free radicals are well located on the carbon atom, resulting in a weak hyperfine in any case. Also, as mentioned already in 2.1.2, the quadrupole nuclei of chlorine relax very fast, and the interactions with the radicals are averaged to zero [24].

The simulation of all spectra is possible with slight modifications of literature g-tensor parameters [23]. However, these deviations can be attributed to magnetic field deviations of the spectrometer. The simulation parameters for **PTM-mono**, **PTM-tail**, and **PTM-di** are given in **Table 5.1**. These g-values are typical for isolated organic radicals.
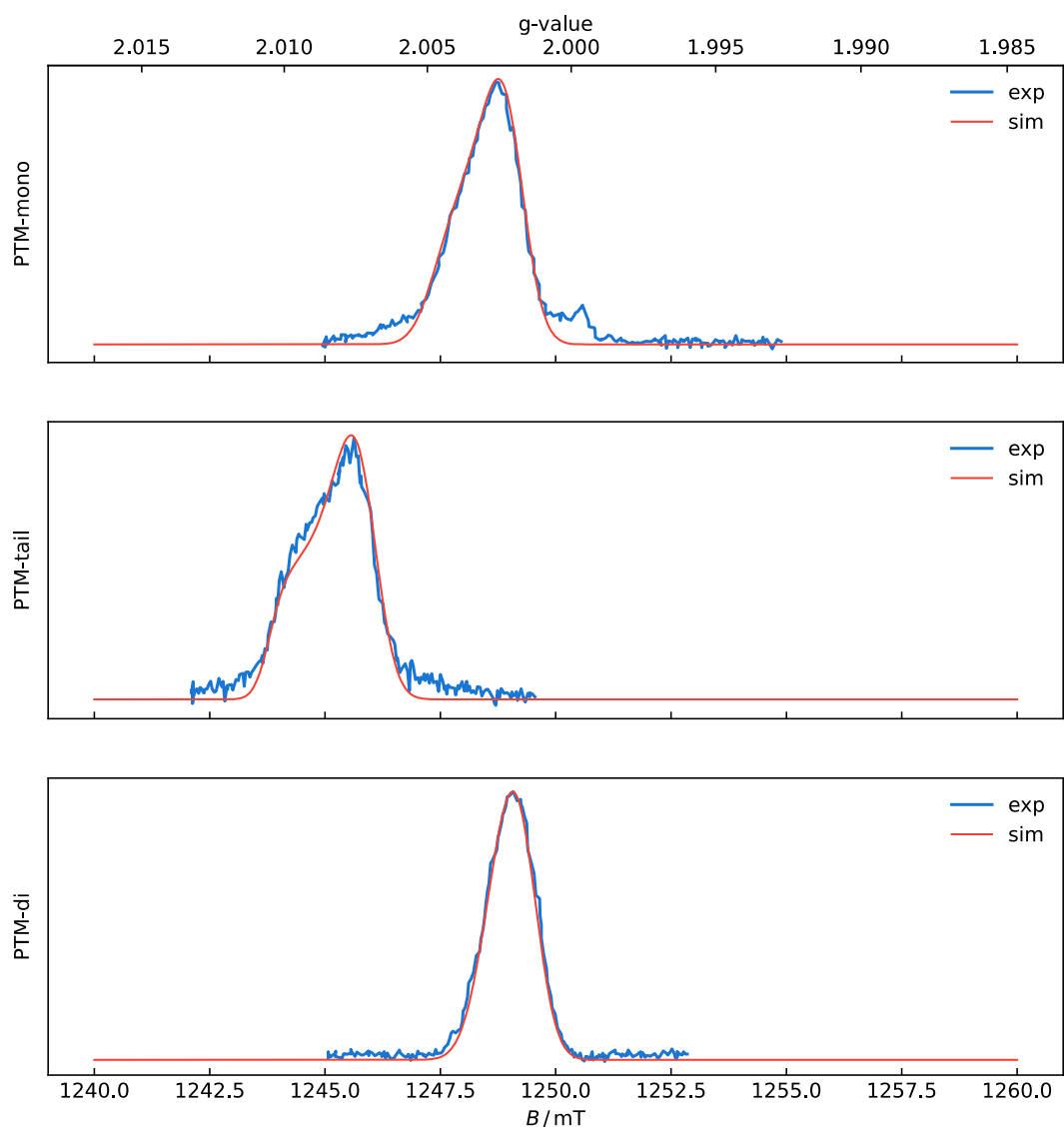
Figure 5.4. Q-Band ESE-detected spectrum of a 200 µM solution of the three PTM radicals **PTM-mono**, **PTM-tail** and **PTM-di** in CS$_2$ at 7 K. Simulation in red with parameters taken from **Table 5.1**.

Table 5.1. Important EPR parameters of **PTM-mono, PTM-tail** and **PTM-di** determined by simulation of the spectra recorded on 200 µM solutions in CS_2 as well as literature data. g-Strains are in the order of 0.0015. Due to the very narrow line width and field offset of the magnet used, rather big uncertainties in the g-values arise.

	PTM-mono	PTM-tail	PTM-di	PTM-mono	PTM-tri(p-COO)[b]
S	½	½	½[a]	½	½
g_1	2.002(3)	2.002(3)	2.007(3)		2.0013
g_2	2.002(3)	2.002(3)	2.007(3)		2.0016
g_3	2.005(3)	2.003(3)	2.011(3)		2.0042
g_{iso}				2.0026	2.0024
ref.	this work			[154]	[23]

[a] two isolated $S = 1/2$ PTM radicals.
[b] ^{13}C enriched PTM radical with all three p-Cl substituted with p-COO⁻

5.3.2. Relaxation Times T_1 and T_m

Temperature-dependent measurements of the spin-lattice relaxation times T_1 and phase memory times T_m were performed in a temperature range of 7 K to 150 K at the field setting corresponding to the maximum spectral intensity. The recorded inversion recovery curves are shown in **Figure 5.5**, and Hahn echo curves are shown in **Figure 5.6**.

The spin-lattice relaxation times T_1 were obtained by fitting the measured data with a monoexponential fit function (see **Equation (10)**). The phase memory times T_m were fitted with a biexponential function (see **Equation (14)**). The extracted values are summarized in **Figure 5.7** and listed in **Table 5.3** and **Table 5.2**.

T_1 Relaxation Times
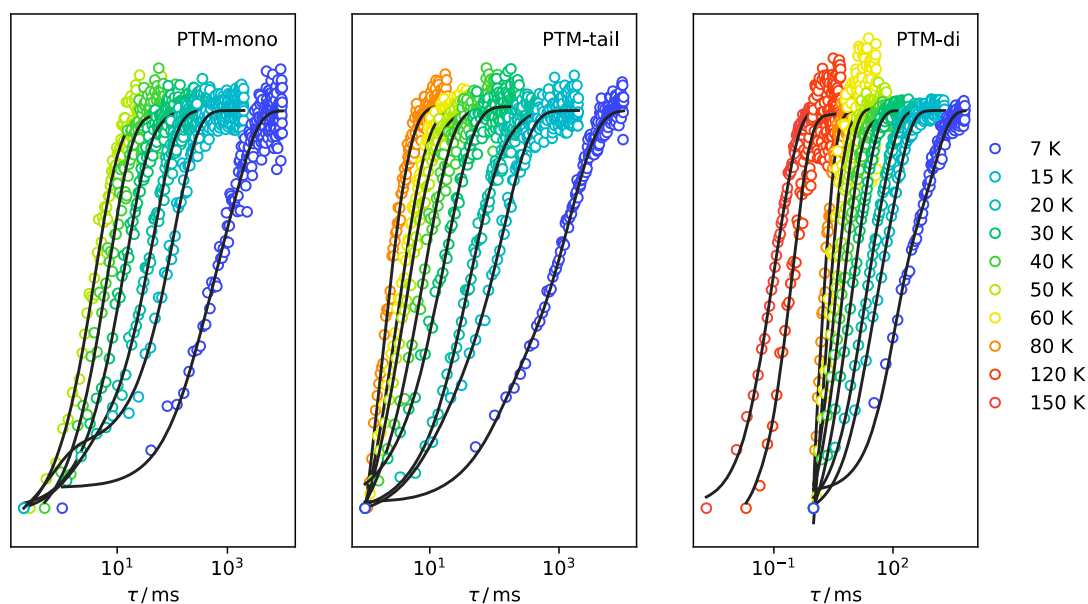
Figure 5.5.   Inversion recovery curves recorded on 200 µM solutions of **PTM-mono**, **PTM-tail,** and **PTM-di** in CS_2 at 1249.0 mT and 35.000 GHz and different temperatures, as indicated in the figure. Solid lines represent fits according to **Table 5.2**.

All three compounds have very similar spin-lattice relaxation times (see **Figure 5.7**). At low temperatures of 7 K, they are very long. Within the margin of error, the two monomeric radicals **PTM-mono** and **PTM-tail** exhibit T_1 times of over 1 s, while the relaxation time of **PTM-di** is significantly shorter with 607(81) ms. These values decrease sharply upon increasing the temperature, with all three compounds exhibiting a relaxation time of around 7 ms at 40 K. This sharp decrease, in combination with a plot of $\log(T_1)$ versus $\log(T)$, showing a very linear dependence, suggests a Raman-like relaxation process. This behavior is also often found to be the dominant T_1 relaxation mechanism for spin-1/2-systems in frozen solutions [155]–[157]. This decreasing trend continues to the highest measurement temperature, beyond which the signal-to-noise ratio did not allow further measurements of the spin-lattice times. This was the case at 80 K, 150 K, and 60 K for **PTM-mono**, **PTM-di,** and **PTM-tail,** respectively.

T_m Relaxation Times
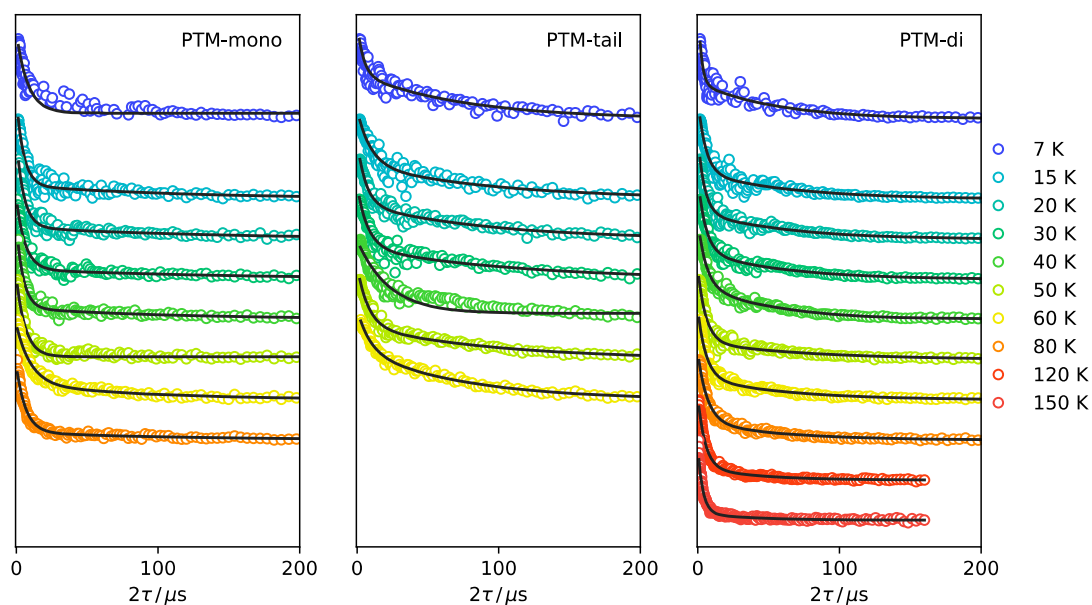
Figure 5.6. Hahn-echo decays of a 200 µM solution of **PTM-mono**, **PTM-tail**, and **PTM-di** at 1249.0 mT in CS_2 and at 35.000 GHz. Solid lines represent fits according to **Table 5.3**. Curves have been offset for clarity.

For the phase memory times T_m, all recorded measurements (see **Figure 5.6**) can be described with good agreement with a biexponential decay function, indicating two different processes or two different environments. In all cases, the slower observed relaxation process contributes less to the fit than the fast one. In **PTM-mono**, this slow contribution is, on average, about 10%, in **PTM-tail** about 30%, and in **PTM-di** about 30%. The length of the fast process is quite similar and temperature-stable throughout the three compounds, with $T_{m,f} \approx 6$ µs and can be attributed to the spectral diffusion due to local concentration differences [158]. However, the slow process differs significantly across the molecules. At 7 K, **PTM-mono** exhibits a slow relaxation process with a $T_{m,s}$ of 249(140) µs, while **PTM-tail** only has $T_{m,s}$ of 103(37) µs and finally **PTM-di** only with $T_{m,s}$ of 80(30) µs. For all three compounds these relaxation times remain fairly stable over a wide temperature range.

These extracted phase memory times at 7 K are very long, in fact, the phase memory times of **PTM-mono** and **PTM-tail** are much longer than other trityl radicals as described in the introduction of this chapter. In fact, at low temperatures, Finland trityl radicals have only

T_m times of around 5 μs and partially chlorinated radicals up to 13 μs (see Appendix 7.9 for more information). Going beyond related molecules, these PTM radicals can even compete with those with the slowest relaxation times – **V(dbddto)$_3$$^{2-}$** ($T_m$ = 675 μs in CS$_2$) and **N@C$_{60}$** (T_m = 230 μs in CS$_2$).

It is very likely that this improvement is the result of applying methods to remove nuclear spins from the molecules as well as from the solvent (see 2.1.2). Considering the difference between the three systems, it can be said that while **PTM-mono** is the unmodified perchlorinated trityl radical, which has no significant influence from nuclear spins in the vicinity, the amount of influence of nuclear spins on the radical increases in **PTM-tail**, which has an ethylene-phenyl-ethyne backbone integrated. The largest perturbation is expected and observed in **PTM-di**, which not only has a significant number of hydrogens with nuclear spins in the vicinity, but also contributions from dipolar coupling, which leads to instantaneous diffusion, and, thus, decreases T_m.

Table 5.2. Spin-lattice relaxation times T_1 extracted from fitting the measured inversion recovery decays with a monoexponential fit function including standard deviations of 200 μM **PTM-mono**, **PTM-tail** and **PTM-di** in CS$_2$ at various temperatures.

T_1 / ms

T / K	PTM-mono	PTM-di	PTM-tail
7	1071(139)	607(81)	1341(160)
15	102(12)	80(10)	126(16)
20	43(5)	39(5)	56(7)
30	16(2)	13(1)	17(2)
40	7.3(9)	6.6(8)	8(1)
50	4.6(6)	3.7(4)	4.8(6)
60	–	2.1(4)	3.3(4)
80	–	1.2(1)	1.7(2)
120	–	0.32(5)	–
150	–	0.14(2)	–

Figure 5.7. Temperature dependency of the extracted phase memory times T_{m} and spin-lattice relaxation times T_1 of all investigated PTM compounds. For T_{m}, the size of the marker correlates with the overall contribution of the relaxation process to the fit. The data of this table is found in **Table 5.2** and **Table 5.3**.

Table 5.3. Spin-spin relaxation times $T_{m,s}$ and $T_{m,f}$ and their contributions A extracted from fitting the measured Hahn-echo decays with a biexponential fit function including standard deviations of 200 μM **PTM-mono**, **PTM-di**, **PTM-tail** and **PTM-di** in CS_2 at various temperatures.

T / K	PTM-mono				PTM-di				PTM-tail			
	A_s	$T_{m,s}$ / μs	A_f	$T_{m,f}$ / μs	A_s	$T_{m,s}$ / μs	A_f	$T_{m,f}$ / μs	A_s	$T_{m,s}$ / μs	A_f	$T_{m,f}$ / μs
7	0.11	249(140)	1.16	5.2(9)	0.23	80(30)	1.06	3.9(9)	0.35	103(37)	0.84	6(2)
15	0.17	129(36)	1.07	5.2(8)	0.34	65(13)	0.91	5.4(9)	0.44	95(19)	0.67	9(2)
20	0.15	145(38)	1.08	5.3(8)	0.34	62(11)	0.94	4.7(7)	0.45	90(15)	0.79	6(1)
30	0.13	163(49)	0.88	6.2(9)	0.36	59(10)	0.90	5.5(8)	0.41	108(19)	0.76	8(1)
40	0.14	120(27)	1.04	5.0(7)	0.44	51(8)	0.79	5.8(9)	–	–	–	–
50	–	–	–	–	0.22	78(18)	0.91	5.8(8)	0.42	97(14)	0.74	8(1)
60	0.20	93(26)	0.74	10(2)	0.28	60(11)	0.83	5.9(8)	0.63	74(10)	0.51	9(2)
80	0.10	114(37)	0.82	6.6(9)	0.24	55(13)	0.84	7(1)	–	–	–	–
120	–	–	–	–	0.16	40(10)	0.86	5.3(7)	–	–	–	–
150	–	–	–	–	0.09	39(13)	0.81	3.6(5)	–	–	–	–

5.4. Dipolar Spectroscopy on **PTM-di**

Considering the very intense, sharp line of the **PTM-di** diradical, its use as a molecular ruler and 2-qubit system is possible. To further investigate the dipolar influences in the molecule, more advanced pulsed EPR techniques are used in this chapter. The basics of these methods are summarized in the theoretical section 2.5, so this chapter is dedicated to the results only.

The **PTM-di** molecule could be used in dipolar spectroscopy. Three different methods were used to determine the best method for this particular system and to independently confirm the results obtained. These three methods were Double Electron Electron Resonance (DEER) spectroscopy, Single-Frequency Technique for Refocusing Dipolar Couplings Spectroscopy (SIFTER) spectroscopy, and finally double quantum coherence (DQC) spectroscopy.

Since the relaxation times of the **PTM-di** radical is very long, measurements were performed in a 200 µM solution in a 1:1 mixture of toluene and DCM at an elevated temperature of 50 K. This increased the amount of measurement data that could be recorded without sacrificing signal intensity. The results of these measurements are shown in **Figure 5.8**.

5.4.1. DEER

First, DEER experiments were performed on the sample. These proved to be quite challenging because the complete EPR signal at Q-band spans only 3 mT (84 MHz), and the observer and pump pulse must be far enough apart to avoid overlapping. This problem could be circumvented in the future by using higher frequencies to stretch the signal components out.

To apply a 4-pulse DEER sequence to the **PTM-di** sample, a pump and observer position had to be chosen. The best ones that were used are shown in **Figure 5.9**. In addition to the one shown, several other pump and observer positions were evaluated, including varying the pulse width and pulse shape using an arbitrary waveform generator (AWG), but with little success, resulting in the use of traditional rectangular pulses.

Figure 5.8. 4-pulse DEER (blue), SIFTER (magenta, background oscillation is a measurement artifact), and DQC (green) experiments performed on 200 µM solution of **PTM-di** in PhMe:DCM 1:1. (left) Background corrected time traces (full lines) and simulations thereof (dotted lines) retrieved using DeerAnalysis, (top right) Fourier transforms of the time traces, (bottom right) distance distributions.

Figure 5.9.   ESE spectrum of a 200 µM solution of the **PTM-di** in PhMe:DCM 1:1 at 34.035 GHz and 50 K with the pulse positions of the pump and observer pulse for the 4-pulse DEER measurement.

A faint DEER oscillation was recorded at these positions, as visible in **Figure 5.8** (blue traces). After Fourier transform and analysis with DeerAnalysis, the distance between the two radicals was determined to be 2.4(1) nm.

5.4.2. SIFTER and DQC

Since the dipolar oscillation signals obtained by DEER were quite weak, two other pulse sequences used in dipolar spectroscopy were applied to the sample as they have been shown to work better for systems similar to **PTM-di** [159]. Both SIFTER and DQC do not use two different microwave frequencies but rather different detection channels and are highly advantageous for measuring dipolar oscillations in compounds with narrow spectra (see 2.6).

The results of these single-frequency methods are also shown in **Figure 5.8** as the magenta and green traces for the SIFTER and DQC measurements, respectively. During data processing, it was not possible to completely remove the oscillations caused by background

crossing echoes in the SIFTER measurement, as can be seen by the remaining regular additional oscillation. This is a well-known problem because SIFTER does not use any phase cycling to remove other coherence paths, such as Hahn echoes (see 2.6.3). However, the traces show clear dipolar oscillations.

Overall, the time traces are basically identical, and the results are consistent with the DEER experiment performed on **PTM-di.** The distance distributions of both DQC and SIFTER measurements are centered at 2.4 nm, the same as obtained by the DEER measurement.

In general, it can be said that both the DQC and SIFTER measurements are much more suited for sharp-lined PTM radicals. Not only are these methods much easier to apply to the PTM radicals since they can excite the whole EPR signal and use it for observation, instead of only small parts of it as DEER permits on these types of samples, but also the observed oscillations are much clearer and more reliable to analyze.

5.5. Conclusion

In this chapter, the relaxation behavior of a series of PTM radicals – two monomers and one dimer – has been studied. In addition, dipolar spectroscopy was applied to the dimer **PTM-di** to investigate the dipolar interactions of the two intermolecular spins with three different pulse sequences: 4-pulse DEER, SIFTER, and DQC.

It was found that all radicals exhibit very similar relaxation behavior both in terms of spin-lattice relaxation T_1 and phase memory time T_m. The data could be collected in a temperature range of up to 60 K, 80 K, and 150 K for **PTM-mono**, **PTM-tail**, and **PTM-di**, respectively. **PTM-di** has reduced coherence times compared to the two monomers. However, PTM radicals show extremely long spin-lattice relaxation times of about 1 s in carbon disulfide at low temperatures of 7 K. The spin-lattice relaxation decreases rapidly by orders of magnitude as the measurement temperature doubles.

For the phase memory time T_m, the Hahn echo decay curve was found to be biexponential. All three compounds exhibit very slow phase memory times. While **PTM-mono** and **PTM-tail** have phase memory times of over 100 µs, **PTM-di** has only about 70 µs. These values are

much larger than similar reported trityl radicals and also very competitive with the reported best of the best, ranking third just behind **V(dbddto)$_3$$^{2-}$** and **N@C$_{60}$**.

The multi-frequency DEER and single-frequency SIFTER and DQC measurements at Q-band frequencies on the PTM radical dimer **PTM-di** consistently gave an inter-spin distance of 2.4 nm across all measurement techniques. However, DEER measurements were challenging because both the observer and the pump pulse must be placed on such narrow signals signal without interfering with each other.

However, this is inconsistent with the distance suggested by the structure obtained by force field optimization of the molecule. Although no crystal structure of the **PTM-di** radical or the **PTM-di** radical precursor has been obtained, ^{1}H NMR data of the double bonds suggests that the radical is present in an all-trans-form, as shown in **Figure 7.78**. From force-field approximations (UFF), the distance of the radicals is therefore given to be about 2.76 nm (see appendix for a force-field optimized molecular structure). Unfortunately, what exactly causes this difference of 0.36 nm is not yet known.

Considering the obtained relaxation times and the fact that they are among the best-known so far, all compounds show immense qubit potential. Their qubit figure of merit Q_m is on the order of 10^4, which is competitive with other qubit systems. For the dimer, although the inter-spin distance of 2.4 nm is not the most favorable distance for a good dipolar coupling between the two electrons, it's well-definedness and possibility to quantify the spin-spin coupling and thus potentially individually addressing the two radical centers is very charming and could be a good first candidate for a reliable 2-qubit gate.

5.6. Experimental Section

Samples were synthesized and analyzed to be pure compounds by Jesús Alejandro De Sousa, Molecular Nanoscience and Organic Materials Department, Institut de Ciència de Materials de Barcelona, and were used as received.

Pulsed electron paramagnetic resonance was recorded on a homebuilt Q-band spectrometer [140], and spectra were simulated with Easyspin 5.2.30 [141]. The dataset for extracting spin-lattice relaxation times was recorded by Jonathan Wischnat. The microwave frequency was 35.000 GHz unless stated otherwise. Samples were prepared by dissolving the corresponding compound in the appropriate dry solvent. The sample was always freeze-quenched by directly inserting it into the already cold resonator chamber to prevent precipitation of the compound when cooling down. The cavity was always tuned to the third mode of a TE_{011}-resonator. For the determination of spin-lattice relaxation times, the inversion-recovery pulse sequence was used, while the determination of the spin-spin relaxation times was conducted using the Hahn-echo pulse sequence. The experimental error of the setup is quantified as 10%, as determined by Dengler [40], in addition to the statistical error arising from the fitting procedure. Experimental errors for this spectrometer were generally estimated to be $\Delta g = 0.003$, $\Delta A = 0.3$ MHz for microwave frequencies of 35.000 GHz on the basis of repeated measurements of the same sample.

Data analysis of the relaxation data was done with the help of a self-written library in Python 3.8.

Pulsed dipolar electron paramagnetic resonance was recorded on a Bruker Elexsys E580 system, equipped with an AWG pulse shaping unit, during a Short-Term Scientific Mission to the group of Dr. Floriana Tuna at the University of Manchester, United Kingdom. The measurements were carried out by Edmund Little. Sample preparation was conducted by preparing a solution of the corresponding compound in the appropriate dry solvent. The sample was freeze quenched by directly inserting it into the already cold resonator chamber to prevent precipitation of the compound when cooling down. Data acquired was processed with the DeerAnalysis 2021b toolbox [160].

6

SPIN DYNAMICS OF GROUP 11 PORPHYRIN MONO- & DIMERS

6. SPIN DYNAMICS OF GROUP 11 PORPHYRIN MONO- & DIMERS

In order to investigate the influence of spin-orbit coupling (SOC) on the coherence properties within a group of the periodic table, a series of group 11 porphyrin mono- and dimers are studied in this chapter. These porphyrins were provided by the group of Prof. Dr. Biprajit Sarkar at the Institute of Inorganic Chemistry, University of Stuttgart. The synthesis, electrochemical and structural characterization were carried out by Shubhadeep Chandra. In this chapter, the relaxation behavior will be investigated. First, a brief overview of the compounds and the molecular structure data obtained by Chandra et al. is presented. Then, Q-band EPR data, including the coherence properties of both T_1 and T_m are determined for all compounds. Finally, these data are compared between the different metal compounds.

6.1. About Metalloporphyrins

Similar to phthalocyanines, which have been previously explored in the field of molecular quantum bits [161]–[164] because of their flexible synthetic properties as well as their wide commercial availability, porphyrins exhibit a very strong tendency to bind a wide range of metals [165].

Due to their structural similarity to heme and occurrence in the cytochrome P450 enzyme family, metalloporphyrins and their derivatives are paramount in biology and, indeed, for life itself [166]. They also have important applications in molecular electronics [167] and catalysis [166],[168],[169]. In contrast to metalloporphyrins, which have been extensively studied in this context, metalloporphyrins have not been extensively studied in QIP. In literature, there are pulsed EPR studies of iron porphyrins [170],[171], cobalt porphyrins [172], and others. In addition, porphyrins are sometimes used in EPR ruler applications [173].

However, none of these studies have been directly focused on possible qubit applications – only copper porphyrins have been investigated for their spin properties: For example, in 2018, Roubeau et al. studied a copper porphyrin in 2D nanosheets [174], and in 2019, Freedman et al. published the use of an array of copper porphyrins in a metal-organic framework (MOF) as a candidate qubit [175]. The main benefit behind their approach lies in the very regular placement of the potential qubit within the framework. They also studied the spin-dynamics within this MOF (shown in **Figure 6.1**) and proposed a spatial limit of 50 Å within which spin-spin interactions significantly contribute to decoherence.

Besides the study of porphyrins in frameworks, a thorough study of the qubit properties with more metals in MOFs is not known. However, there is a rather large variety of metalloporphyrins with paramagnetic metals, making them ideal candidates to investigate the spin dynamics throughout a whole group in the periodic table as one can more thoroughly observe trends and possibly new candidates for qubits not thought of previously. The influence of spin-orbit coupling on the decoherence of metal complexes has already been investigated by Freedman et al. on the group 8 metals iron, ruthenium, and osmium [176]. But up until now and to the best of our knowledge, there is no such comparison in literature for the behavior of the relaxation times of all three group 11 metals. Only in the late 1990s Eaton and Eaton investigated the phase memory T_m and spin-lattice T_1 relaxation

times of monomeric copper(II) and silver(II) porphyrins in glassy solvents and doped solids [177]. The compounds studied in this chapter are shown in **Figure 6.2**.
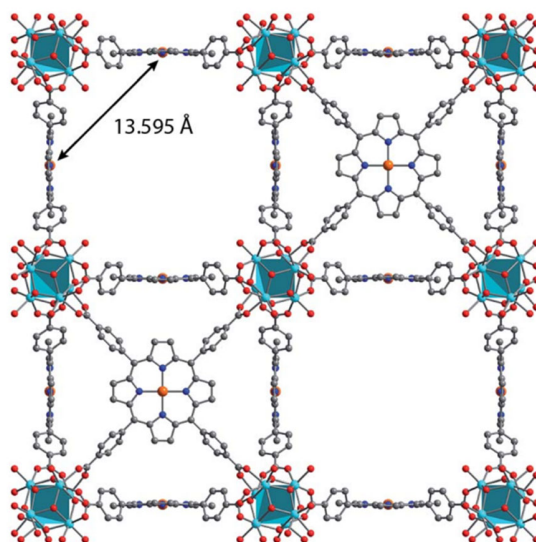
Figure 6.1.   Crystal structure of the copper porphyrin MOF created by Freedman et al. [175]. Reproduced from [175] with permission from the Royal Society of Chemistry.
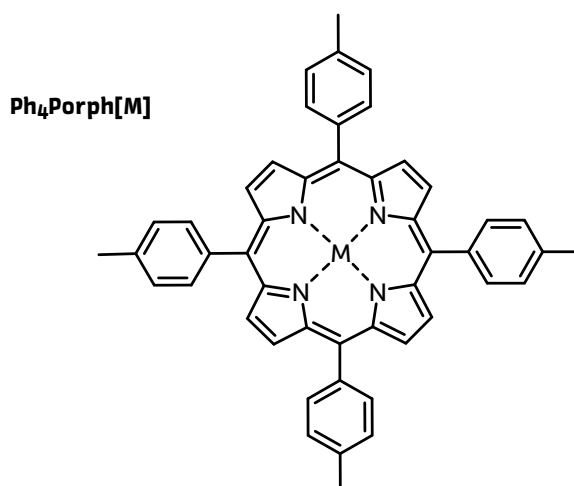
Figure 6.2.   Mono-porphyrins **Ph₄Porph[M]** (with M = **VO**, **Cu**, **Ag**) investigated by pulsed EPR by Eaton and Eaton [177].

6.2. The Compounds

The porphyrins studied in the following are shown in **Figure 6.3**. A detailed description of their synthesis can be found in Chandra's Ph.D. thesis [169]. To briefly summarize their preparation: They were condensed by a Rothemund reaction of the corresponding aryl aldehyde with dipyrromethene. The resulting symmetrical porphyrin structure can then be arylated at the CH_2 bridgeheads to yield a separable mixture of the mono- and disubstituted variants. The isolated monosubstituted variant can then be used to form the meso-meso dimeric porphyrin by treatment with the hypervalent iodo-compounds (bis(trifluoroacetoxyl)iodo) benzene (PIFA). If desired, the metal can be inserted directly after the porphyrin formation or later by transmetallation.

The three types of porphyrin systems studied in this chapter are the monomeric species **monoPorph[M]** and its dimeric meso-meso counterpart **mmPorph[M]**, where **M** is either Cu, Ag, or Au. Since the fused compounds were quite insoluble, a much more soluble version was used, which will be referred to as **fsPorph[M]**.

monoPorph[M]
monomer
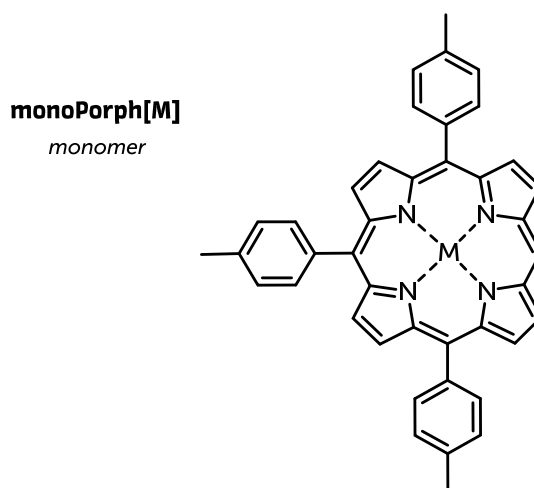
Figure 6.3.   Structures of the investigated porphyrins. M = **Cu**, **Ag**, **Au**.

mmPorph[M]
meso-meso
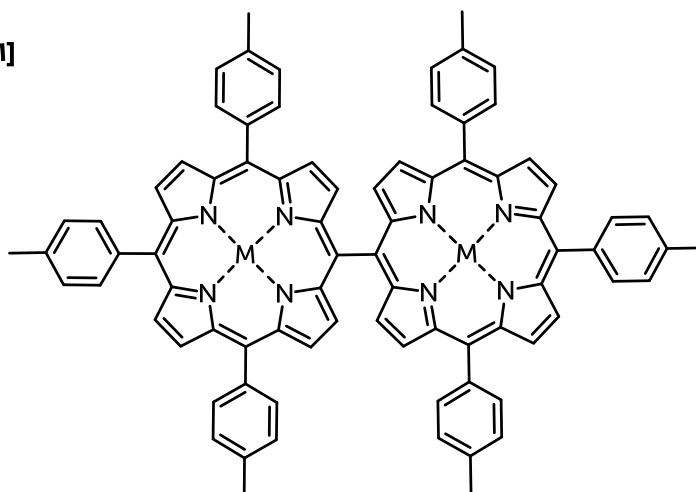
fsPorph[M]
fused soluble
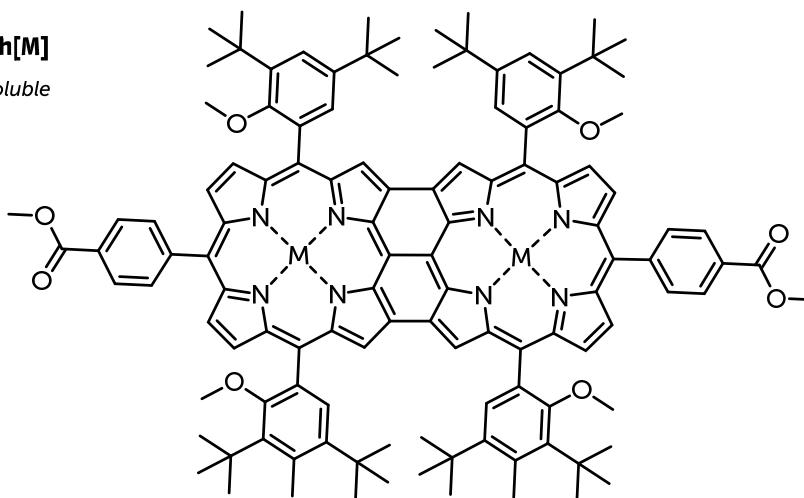
Figure 6.3   continued.

First, the molecular structure of the studied complexes is described using the crystallographic data provided by Chandra [169]. Since the monomeric structure of **monoPorph[M]** is very similar to half of the structure of the meso-meso dimer and no crystallographic data are available for it, it will be described here in the section on the structure of **mmPorph[M]**.
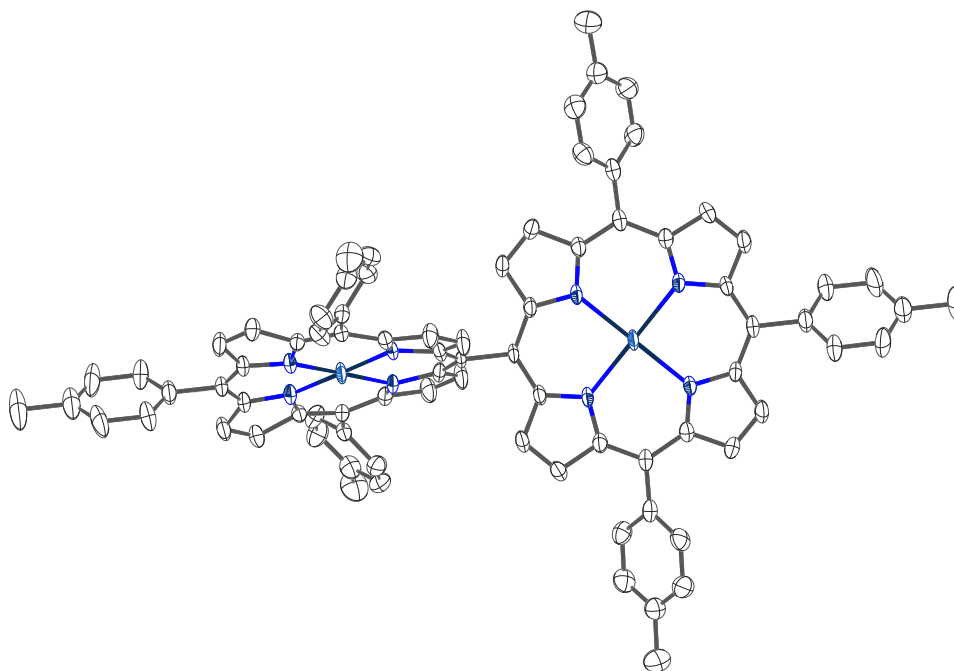
Figure 6.4. Molecular structure of **mmPorph[Ag]** determined by X-ray crystallography. Hydrogens and additional solvent molecules are omitted for clarity, and thermal ellipsoids are drawn at 50% probability level. Color code: Carbon (white), Nitrogen (blue), Silver (teal).

To represent the meso-meso family of porphyrins **mmPorph[M]**, **Figure 6.4** shows the silver(II) derivative. The silver atoms are in a slightly distorted square planar environment. The corresponding bite angles for the two sets of N-Ag-N are 89° and 91°. This, as well as the Ag-N distances of 2.090(7) Å are within the reported range of analogous complexes [178]. More importantly, from a spin dynamics point of view is that the crystal structure also shows that the two porphyrin units are tilted with respect to each other with a dihedral angle of 63° and that the two silver(II) atoms are 8.396(2) Å apart. This also suggests that the magnetic axes of the two metals are tilted with respect to each other. In solution, however, free rotation around the single bond connecting the two porphyrins is probably possible.
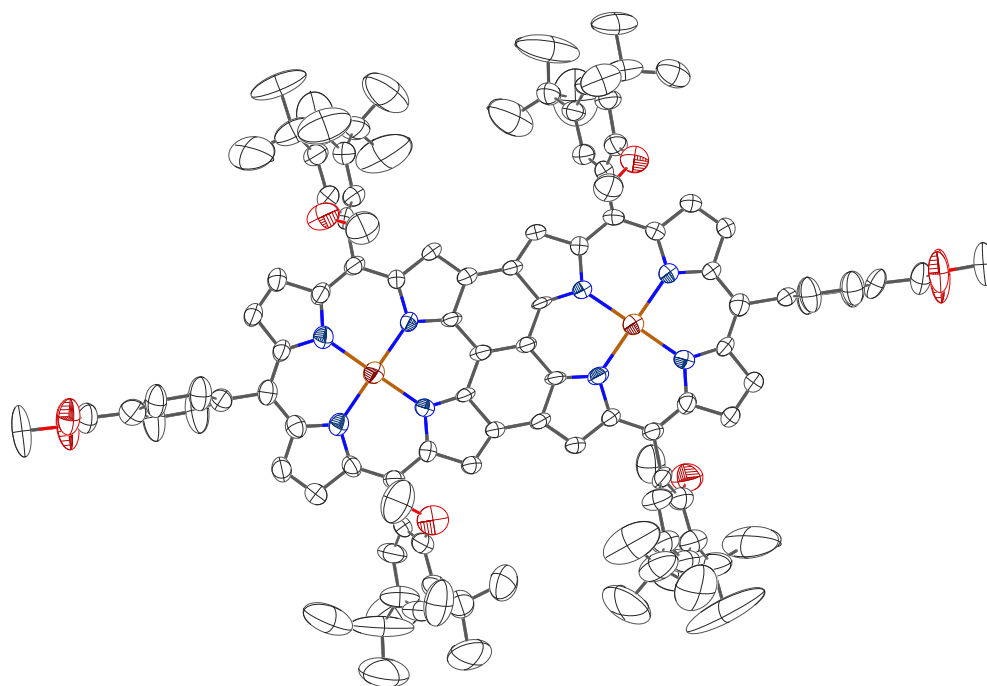
Figure 6.5.   Representation of the molecular structure of **fsPorph[Cu]** in the crystal. Hydrogens and additional solvent molecules are omitted for clarity, and thermal ellipsoids are drawn at 50% probability level. Color code: Carbon (white), Copper (brown), Nitrogen (blue), Oxygen (red).

Chandra et al. also succeeded in obtaining a crystal structure for the fused-soluble variant **fsPorph[Cu]** by slow vapor diffusion of benzene into an ethanol solution of the compound. The porphyrin core shows good structural resolution: The planes defined by the copper(II) atoms and their surrounding coordinating nitrogen atoms are nearly identical. The distance between the two copper centers is 8.3096(12) Å and the N-Cu-N angles are between 90.08(18)° and 89.99(18)°. The average bond length of the copper to the coordinating nitrogen atoms is 1.953(4) Å. No structural parameters are extracted for the surrounding substituted phenyl rings due to the poor resolution of the crystal in this region.

6.3. EPR Spectra and Relaxation Times

Pulsed EPR measurements were performed to investigate the relaxation behavior of all the Group 11 metalloporphyrins studied here. For all compounds, the ESE detected spectra, and the phase memory and spin-lattice relaxation times were measured between 5 K and 80 K with the Hahn echo pulse sequence and the inversion recovery pulse sequence, respectively. All samples were 2 mM solutions in PhMe. In the following, each metal is discussed separately and a final comparison between the metals is made in the last section.

6.3.1. Copper(II) Porphyrins

The field-swept electron spin echo (ESE) spectra of the three copper compounds investigated, **monoPorph[Cu]**, **mmPorph[Cu]**, and **fsPorph[Cu]**, including their numerical derivatives, are shown in **Figure 6.6**. All three spectra show a series of four positive features at low fields and one intense derivative-shaped feature at high fields. Such features are typical for copper(II). All three compounds have no resolved nitrogen hyperfine couplings and their single $g_\perp$ component is centred around 1217 mT. While the four steps resulting from the hyperfine coupling in the $g_\parallel$ component of **monoPorph[Cu]**, **mmPorph[Cu]** are clearly visible, the spectrum of **fsPorph[Cu]** is heavily washed out, but at least 5 steps are vaguely visible.

For **monoPorph[Cu]**, **mmPorph[Cu]** there are four $g_\parallel$ features corresponding to the hyperfine splitting to one nucleus with $I = 3/2$, i.e., a copper ion. Although less resolved, the more complex pattern found in the fused **fsPorph[Cu]** spectrum suggests that the two copper hyperfine interactions are not of equal strength.
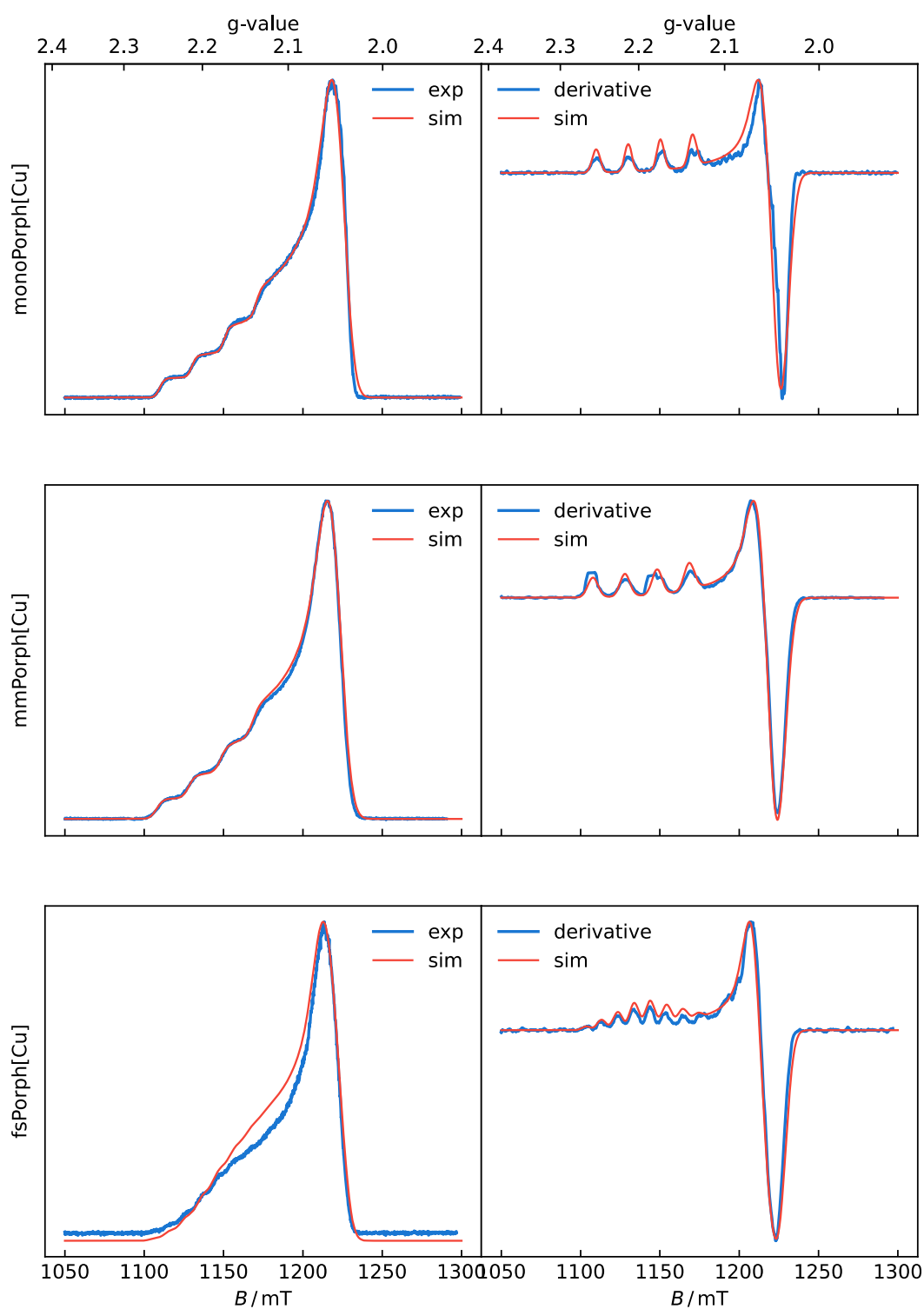
Figure 6.6. (left) Field-swept Q-Band ESE spectra and (right) pseudomodulated spectra of 2 mM solutions of **monoPorph[Cu]**, **mmPorph[Cu],** and **fsPorph[Cu]** in PhMe at 7 K (blue). Simulated in red with parameters taken from **Table 6.1**.

A good simulation of the spectra was obtained by using g-values of $g_\perp = 2.048(6)$ and $g_\parallel = 2.193(6)$ as well as $A_\perp(\text{Cu}) \approx 70\,\text{MHz}$ and $A_\parallel(\text{Cu}) \approx 610\,\text{MHz}$ for **monoPorph[Cu]** and **mmPorph[Cu]** as simulation parameters, which are mostly based on Wili et al. [179], who investigated very similar silylated fused copper(II) porphyrin dimers (hereafter referred to as **silylPorph[Cu]** and **f-silylPorph[Cu]**) thoroughly.

Since Chandra [169] and Wili et al. presented reasons to treat the fused copper(II) porphyrin as an $S = 1$ system and the complex pattern also suggests this, this approach was followed for **fsPorph[Cu]**: The g- and A-values were only slightly changed to accompany field shifts of the spectrometer throughout all three porphyrins. A zero-field splitting of $|D| = 240$ MHz, introduced by Wili for **silylPorph[Cu]** and **f-silylPorph[Cu]**, was included to reproduce the eight steps visible in the numerical derivation of the spectrum. Although this value should be smaller according to the point-dipole approximation, it is not possible to match the splittings in the spectra with a smaller $|D|$.

No half-field transition was observed – while Wili does indeed see a half-field transition. However, the absence of a half-field transition may be due to a poor signal-to-noise ratio.

Temperature-dependent measurements of the spin-spin relaxation times of **monoPorph[Cu]**, **mmPorph[Cu],** and **fsPorph[Cu]** were obtained at the peak maximum of the $g_\perp$ line. For all three compounds, this corresponded to about 1217 mT.

To extract the relaxation times from the gathered data, the Hahn-echo decays were fitted with a pure monoexponential fit function (see **Equation (12)**, **Figure 6.8**). The inversion recovery measurements were also fitted by also using a monoexponential fit function (see **Equation (10)**, **Figure 6.7**). All measured relaxation times are listed in **Table 6.4** and **Table 6.5**

Although the monomer **monoPorph[Cu]** has a spin-lattice relaxation time of 7.5(9)ms at 7 K, in **mmPorph[Cu]** it drops to 3.8(4)ms and to only 2.0(2)ms in the **fsPorph[Cu]**. **Figure 6.7** shows that all three compounds' spin-lattice relaxation times decrease rapidly from increasing temperature up to 80 K, where they are in the single-digit microsecond range. At temperatures above 80 K (60 K for the fused sample), the signal-to-noise ratio was insufficient to fit the data or detect an echo reliably.

Table 6.1. Important EPR parameters of **monoPorph[Cu]**, **mmPorph[Cu]** and **fsPorph[Cu]** determined by simulation of the spectra recorded on 2 mM solutions in PhMe. Additionally, literature data of similar compounds are shown.

	monoPorph[Cu]	mmPorph[Cu]	fsPorph[Cu]	silylPorph[Cu]	f-silylPorph[Cu]
S	½	½	1[b]	½	1[b]
$g_\perp$	2.048(3)	2.052(3)	2.048(3)	2.048	
$g_\parallel$	2.193(3)	2.197(3)	2.190(3)	2.19	
$A_\perp$ / MHz		70(1)		−80	−40
$A_\parallel$ / MHz		630(1)		−613	−306
D / MHz		−	240[a]	−	−240[a]
ref.		this work		[179]	

[a] D-tensor is rotated 90° around y with respect to g- and A-tensors ($D_{\mathrm{Frame}} = [0\pi/20]$), see [179].
[b] Two copper(II) centers.

.

Comparing **monoPorph[Cu]**, **mmPorph[Cu],** and **fsPorph[Cu]**, it seems that the drastic reduction of the spin-lattice relaxation correlates with the introduction of a second copper(II) ion and thus possible dipole-dipole interactions in the molecule. This interaction is particularly pronounced in the fused **fsPorph[Cu]** sample, as their magnetic axes are parallel to each other.
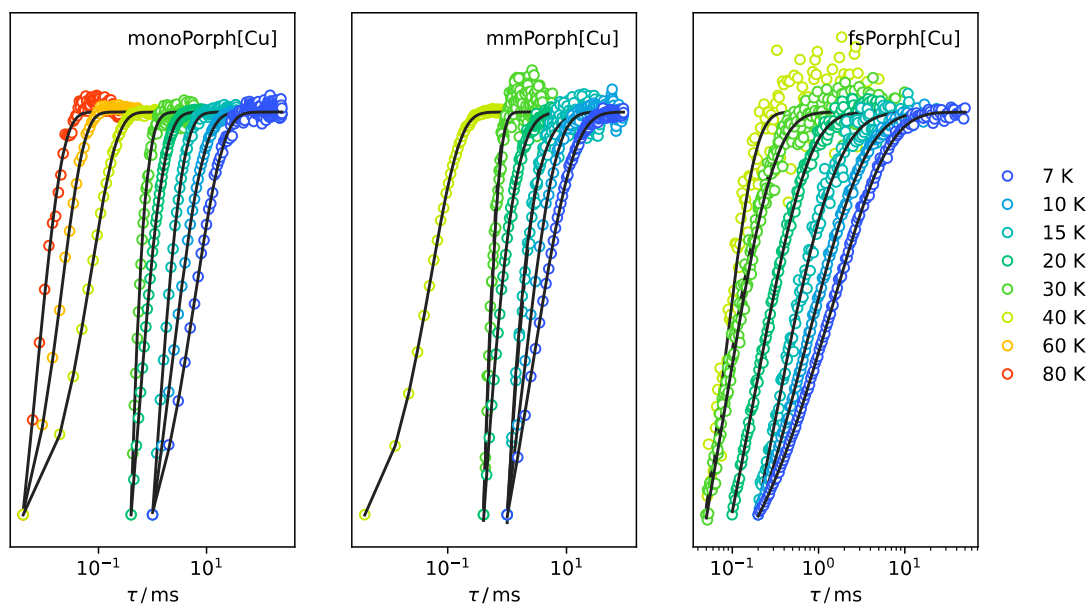
Figure 6.7. Inversion recoveries recorded on 2 mM solutions of **monoPorph[Cu]**, **mmPorph[Cu],** and **fsPorph[Cu]** in PhMe at 1217.9 mT and 35.000 GHz and different temperatures, as indicated in the figure. Solid lines represent fits according to **Table 6.4**. Curves have been offset for clarity.
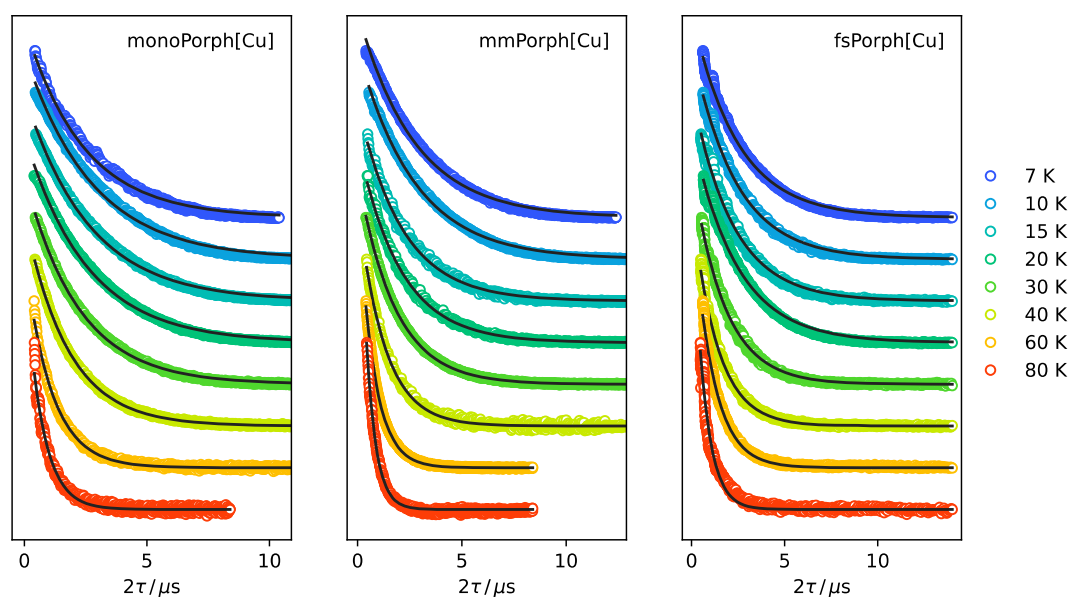
Figure 6.8. Hahn-echo decays recorded on 2 mM solutions of **monoPorph[Cu]**, **mmPorph[Cu],** and **fsPorph[Cu]** in PhMe at 1217.9 mT and 35.000 GHz and different temperatures as indicated. Solid lines represent fits according to **Table 6.4**. Curves have been offset for clarity.

For all three compounds, the Hahn echo decay measurements are shown in **Figure 6.12**. It can be seen that the phase memory times T_m of all three compounds behave very similarly. At 7 K, the phase memory times of the three porphyrins **monoPorph[Cu]**, **mmPorph[Cu],** and **fsPorph[Cu]** are 2.4(2) µs, 2.1(2) µs and 2.4(3) µs respectively. They remain stable up to 20 K, after which they decrease rapidly to 0.68(7) µs, 0.30(3) µs and 0.65(7) µs at 80 K.

The only major visible difference in the data is that the phase memory time of the monomeric species **monoPorph[Cu]** decreases more slowly than the corresponding dimeric forms. This is likely due to the absence of a second copper(II) ion in the molecule and cannot be attributed to an experimental error as the deviation is larger than the typical experimental error of about 10% [40] in the setup used.

6.3.2. Silver(II) Porphyrins

The corresponding porphyrin complexes of the second of the group 11 metals – silver – were also investigated for their relaxation properties. For **monoPorph[Ag]** and **mmPorph[Ag]**, the detected ESE spectra are shown in **Figure 6.9**. However, the **fsPorph[Ag]** did not show any ESE-EPR signal at 7 K. A reason for this could be an even stronger interaction than in the analogous **fsPorph[Cu]**, which shortens the relaxation times and thus increases the line width to be undetectable for the used EPR instrumentation.

The two spectra are very different in shape and form. Both show an axial system, which is expected for these types of silver compounds. However, the **monoPorph[Ag]** shows a very complex hyperfine pattern resulting from the four nitrogen nuclei around the silver atom in the porphyrin. Since the structure is not symmetric, there are two sets of different nitrogen nuclei present, highlighted in **Figure 6.10**.
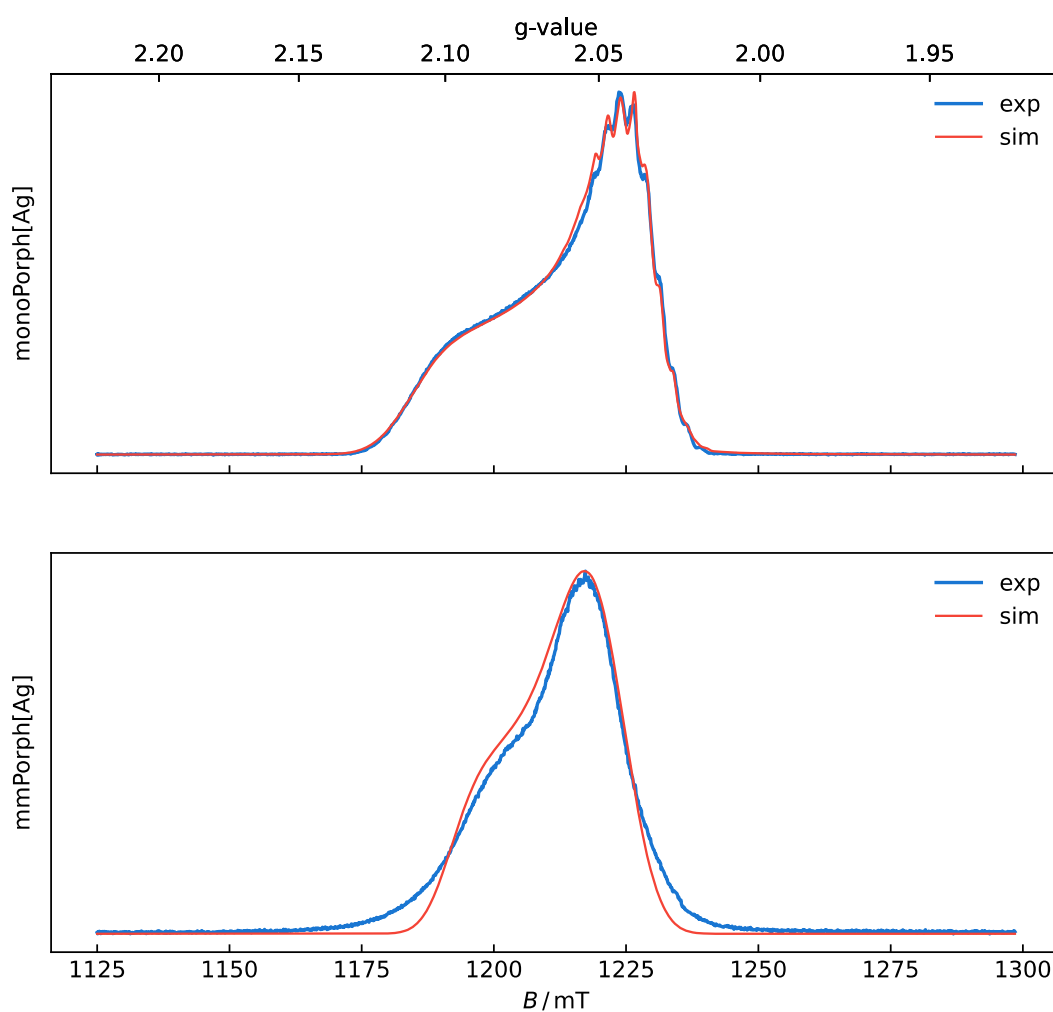
Figure 6.9. Q-Band ESE spectrum of a 2 mM solution of both **monoPorph[Ag]** and **mmPorph[Ag]** in PhMe at 7 K. Simulation in red with parameters taken from **Table 6.2**.
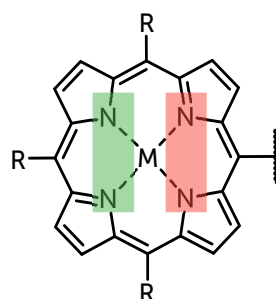
Figure 6.10. Electronically different sets of nitrogen nuclei in the investigated porphyrins.

The g-values of $g_\perp = 2.0385$ and $g_\parallel = 2.112$ were used for the simulation of the central silver atom. In addition, it showed a hyperfine coupling of $A_\perp = 176\,\text{MHz}$ and $A_\parallel = 86\,\text{MHz}$. The additional nitrogen atoms were simulated with the two pairs of equivalent nitrogen atoms mentioned above: The N_α atoms were simulated with a hyperfine coupling of $A_\perp = 94\,\text{MHz}$ and $A_\parallel = 49\,\text{MHz}$, while the N_β atoms were simulated with $A_\perp = 80\,\text{MHz}$ and $A_\parallel = 56\,\text{MHz}$, respectively.

However, to further refine the simulation, it was necessary to introduce a second organic spin system with a g-value of 2.0370 and with a weight of 8%. The simulation of **mmPorph[Ag]** is challenging, as the large strain in the spectrum makes it difficult to determine the simulation parameters reliably. Therefore, only an approximate fit was performed using the **monoPorph[Ag]** parameters as a basis. For the simulation, only the g-values were changed to be $g_\perp = 2.047$ and $g_\parallel = 2.098$. Since a similar spectrum can easily be obtained with very different hyperfine parameters, no interpretation of them is given.

Moving to the relaxation measurements, like for the copper(II) analogs in 6.3.1, inversion recovery and Hahn echo experiments were performed at the field position of maximum intensity, corresponding to $g_\perp$. For **monoPorph[Ag]** this was at $B = 1225.0\,\text{mT}$ and for **mmPorph[Ag]**, at 1218.6 mT. To fit the relaxation experiments and to be able to compare the results with the other group 11 metals, the inversion recovery experiments were fitted in the same way as for their copper counterparts.

Figure 6.11 shows the recorded inversion recovery experiments of a 2 mM solution of **monoPorph[Ag]** and **mmPorph[Ag]** in toluene. They were processed in analogy to the copper(II) variant. Compared to the copper(II) analogs in 6.3.1, the signal-to-noise was already too low at 40 K to fit the data reliably.

The same trend in coherence times as for the copper(II) between the two compounds is visible. Due to the influence of the neighboring Ag(II)-centered electron in **mmPorph[Ag]**, the coherence times are almost a factor of two smaller than its monomeric counterpart **monoPorph[Ag]**: The observed spin-lattice relaxation time T_1 for the dimer is only 9(1) ms, while for the monomers, it is 14(2) ms at 7 K. With increasing temperature, however, these

values become more and more similar and are identical within the error at 39 K, with 0.30(3) ms for **monoPorph[Ag]** and 0.26(3) ms for **mmPorph[Ag]**.

Table 6.2. Important EPR parameters of **monoPorph[Ag]** and **mmPorph[Ag]** acquired by simulation of the data of a 2 mM solution in PhMe. For more simulation parameters see appendix.

	monoPorph[Ag]		mmPorph[Ag][a]
	Silver radical	*Porphyrin radical*	
S	½	½	½
$g_\perp$	2.039(3)	2.037(3)	2.047
$g_\parallel$	2.112(3)	2.037(3)	2.098
$A_{\perp,\text{Ag}}$ / MHz	176.0(3)	–	176
$A_{\parallel,\text{Ag}}$ / MHz	86.0(3)	–	86
$A_{\perp,\text{N}_\alpha}$ / MHz	94.0(3)	–	94
$A_{\parallel,\text{N}_\alpha}$ / MHz	49.0(3)	–	49
$A_{\perp,\text{N}_\beta}$ / MHz	80.0(3)	–	80
$A_{\parallel,\text{N}_\beta}$ / MHz	56.0(3)	–	56
weight	–	8%	–

[a] Values are based on the simulation for the monomer. However, they must be treated with caution as the applied strains are hard to verify. This is also the reason no errors are indicated.
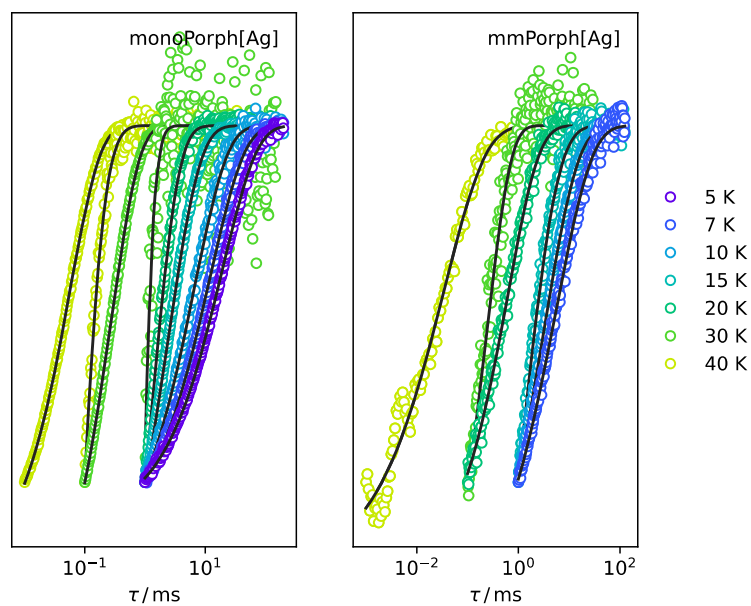
Figure 6.11. Inversion recoveries of a 2 mM solution of **monoPorph[Ag]** at 1225.0 mT and **mmPorph[Ag]** at 1218.6 mT in PhMe and at 35.000 GHz. Solid lines represent fits according to **Table 6.4**.
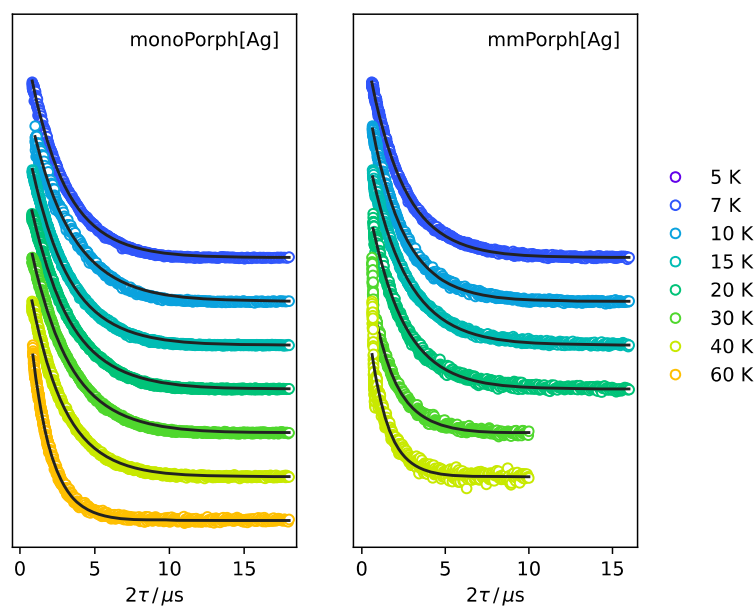
Figure 6.12. Hahn-echo decays of a 2 mM solution of **monoPorph[Ag]** at 1225.0 mT and **mmPorph[Ag]** at 1218.6 mT in PhMe and at 35.000 GHz. Solid lines represent fits according to **Table 6.4**. Curves have been offset for clarity.

The Hahn-echo decays are shown in **Figure 6.12**, and their extracted phase memory times T_m are listed in **Table 6.4**. For the monomer **monoPorph[Ag]**, the phase memory times T_m vary between ≈ 2.5 μs in the temperature range from 7 K to 40 K and 1.3(1)μs at 60 K. This stability is also observed for **mmPorph[Ag]**. Although the relaxation is generally faster, it remains stable throughout the whole temperature series measured from 7 K to 20 K, with $T_\mathrm{m} \approx 2$ μs, after which it drops to 1.1 μs at 40 K.

A comparison of the relaxation data for **monoPorph[Ag]** with those reported by Eaton and Eaton for **Ph₄Porph[Ag]** [177] shows that they are essentially the same over the temperature ranges measured. For example, at 15 K in PhMe:CHCl$_3$, T_m of **Ph₄Porph[Ag]** has been reported at $\sim$2.7 μs and has been measured to be 2.5(3) μs for **monoPorph[Ag]** in PhMe. Similarly, at 30 K, T_1 is about 0.5 ms for **Ph₄Porph[Ag]** and about 0.30(3) ms for **monoPorph[Ag]**. This is to be expected since the two molecules are very similar in their free electron environment.

6.3.3. Gold(II) Porphyrin

In addition to the stable copper and silver porphyrins, a meso-meso-linked gold porphyrin **mmPorph[Au]** was investigated. Due to its unstable nature, the sample preparation of this compound had to be carried out under an inert atmosphere, and the concentration of the sample solution could only be approximated to 2 mM.

Figure 6.13 shows the ESE-detected EPR spectra of **mmPorph[Au]**. It consists of a symmetric, 200 mT broad, single peak centered at 1220.1 mT. The spectrum was simulated by using the simulation parameters shown in **Table 6.3**. A cw X-band spectrum similar to the numerical derivative of the acquired Q-band spectrum has been reported for a very similar porphyrin system by Heinze et al. [180]. In addition to this, another very sharp feature is observed at 1249.1 mT. The sharpness suggests that this is an organic radical; indeed, this signal evolves from a dynamic equilibrium between a gold-centered radical system and a free organic porphyrin radical and has been described previously in literature [180],[181]. Upon recording ESE detected spectra at several temperatures, as shown in

Figure 6.13, it becomes clear that this really is an equilibrium as the ratio of porphyrin and gold signal changes.

Figure 6.14 shows the relaxation measurements, which were fitted in analogy to the previous copper(II) and silver(II) variants. The left side of **Figure 6.14** shows the recorded inversion recovery experiments for **mmPorph[Au]**. These could be reliably measured from 5 K to 20 K. As for the lighter group 11 metals, the spin-lattice relaxation time was extracted from a monoexponential fir function. It is immediately apparent that **mmPorph[Au]** exhibits a vastly different relaxation behavior than its lighter counterparts. The spin-lattice relaxation times T_1 are already at 7 K orders of magnitude smaller at 0.17(2) µs. Not only is this quite a drastic change, but so is its temperature dependence, as a temperature increase to 10 K drops this relaxation time to a mere 0.04(1) µs.

The right side of **Figure 6.14** shows the recorded Hahn echo experiments at low temperatures. To ensure compatibility with the results from Cu and Ag, these were also fitted with a monoexponential fit function with good agreement. The extracted relaxation times are quite consistent from 5 K to 15 K, with $T_m \approx 1.7$ ms, then drops sharply to only 1.2(1)ms at 20 K, after which the signal-to-noise is too low to extract data reliably.

Table 6.3. Important EPR parameters of **mmPorph[Au]** and the porphyrin radical system acquired by simulation of the data of a 2 mM solution in PhMe as well as literature values for a similar system.

| | mmPorph[Au] | | Ph$_4$Porph[Au] |
	Gold radical	*Porphyrin radical*	
S	½	½	½
g_1	2.155(3)	2.021(3)	2.182
g_2	2.060(3)	2.021(3)	2.056
g_3	1.970(3)	2.021(3)	1.982
A_1 / MHz	48(1)	48(1)	43
A_2 / MHz	20(1)	20(1)	20
A_2 / MHz	20(1)	20(1)	20
weight	–	0.3%	–
ref.	this work		[180]
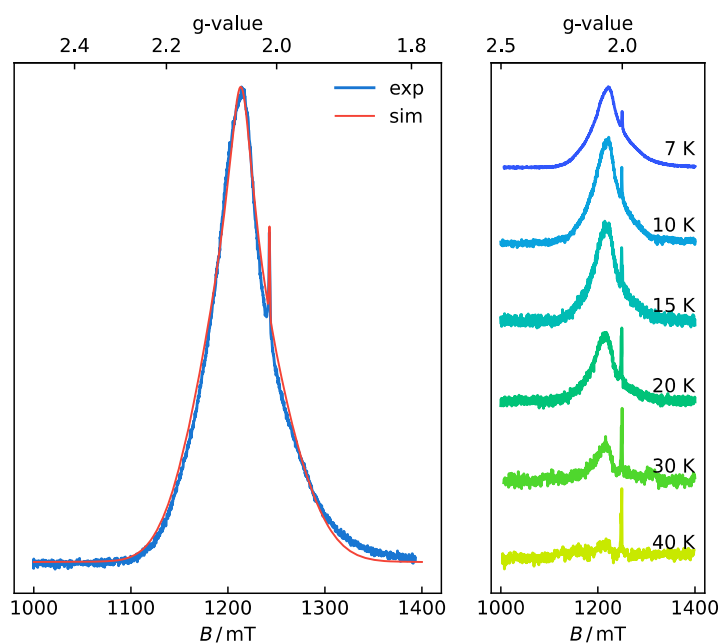
Figure 6.13. (left) Q-Band ESE spectrum of a 2 mM solution of **mmPorph[Au]** in PhMe at 7 K. Sharp signal at B = 1249.1 mT (g = 2.012) represents a porphyrin radical, with which the main gold signal is in equilibrium and is weighted at 0.3%. (right) Temperature evolution from 7 K to 40 K of the Q-band ESE spectra of the same solution normalized on the radical signal. Simulation in red with parameters taken from **Table 6.3**.
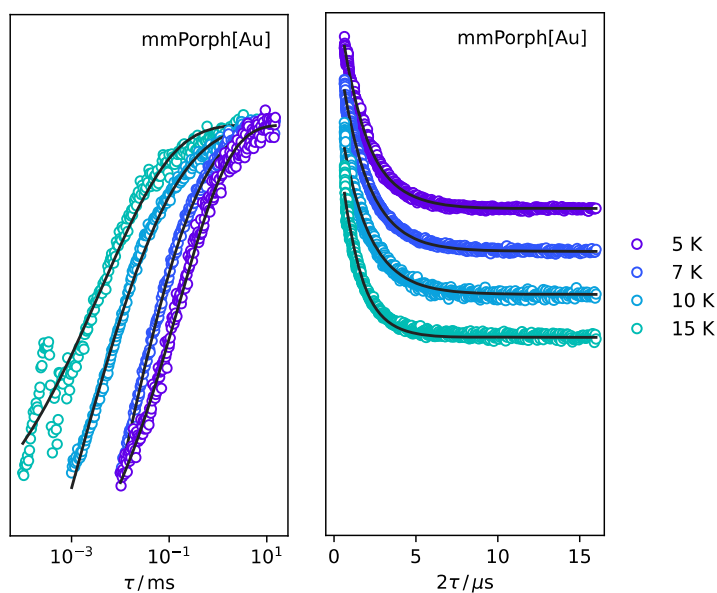
Figure 6.14. Inversion recoveries (left) and Hahn-echo decays (right) of a 2 mM solution of **mmPorph[Au]** in PhMe at 1220.1 mT and 35.000 GHz. Solid lines represent fits according to **Table 6.4**. Curves for the Hahn-echo decays have been offset for clarity.

Table 6.4. Spin-spin relaxation times T_m extracted from fitting the measured Hahn-echo decays with a monoexponential fit function including standard deviations of 2mM **monoPorph[Cu]**, **mmPorph[Cu]**, **monoPorph[Cu]**, **mmPorph[Ag]**, **mmPorph[Ag]**, **fsPorph[Ag]**, **mmPorph[Au]** in PhMe at various temperatures. Relaxation times are given in μs.

T / K	monoPorph[Cu]	mmPorph[Cu]	fsPorph[Cu]	monoPorph[Ag]	mmPorph[Ag]	fsPorph[Ag]	mmPorph[Au]
5	–	–	–	2.1(2)	–	–	1.6(2)
7	2.4(2)	2.1(2)	2.4(3)	2.4(2)	2.1(2)	–ᵃ	1.7(2)
10	2.7(3)	2.5(3)	2.3(2)	2.7(3)	2.0(2)	–ᵃ	1.7(2)
15	2.6(3)	2.8(3)	2.2(2)	2.5(3)	2.2(2)	–ᵃ	1.2(1)
20	2.5(3)	2.0(2)	2.4(3)	2.6(3)	2.0(2)	–ᵃ	–
30	2.2(2)	1.6(2)	1.7(2)	2.6(3)	1.5(2)	–ᵃ	–
40	1.7(2)	1.2(1)	1.3(1)	2.3(2)	1.1(1)	–ᵃ	–
60	1.1(1)	0.55(6)	1.1(1)	1.3(1)	–	–ᵃ	–
80	0.68(7)	0.30(3)	0.65(7)	–	–	–ᵃ	–

ᵃ no signal observable.

Table 6.5. Spin-lattice relaxation times T_1 extracted from fitting the measured inversion recovery with a monoexponential fit function including standard deviations of 2mM **monoPorph[Cu]**, **mmPorph[Cu]**, **monoPorph[Ag]**, **mmPorph[Ag]**, **fsPorph[Ag]**, **mmPorph[Au]** in PhMe at various temperatures. Relaxation times are given in ms.

T / K	monoPorph[Cu]	mmPorph[Cu]	fsPorph[Cu]	monoPorph[Ag]	mmPorph[Ag]	fsPorph[Ag]	mmPorph[Au]
5	–	–	–	22(2)	–	–[a]	0.35(5)
7	7.5(9)	3.8(4)	–	14(2)	9(1)	–[a]	0.17(2)
10	3.4(4)	2.5(3)	2.0(2)	7.9(9)	5.2(6)	–[a]	0.04(1)
15	1.3(1)	1.4(2)	0.64(8)	3.0(3)	2.5(3)	–[a]	0.012(2)
20	0.60(6)	0.29(3)	0.29(3)	1.3(1)	0.8(1)	–[a]	–
30	0.22(3)	0.13(1)	0.12(1)	0.30(3)	0.26(3)	–[a]	–
40	0.078(8)	0.040(4)	0.063(9)	0.064(7)	0.051(7)	–[a]	–
60	0.020(2)	0.005(1)	–	–	–	–[a]	–
80	0.008(1)	0.002(1)	–	–	–	–[a]	–

[a] no signal observable.

6.3.4. Comparison Amongst the Different Metal Ions

After looking at the different metals individually, a comparison is made between the three metals and with literature. A complete overview of the temperature dependence of the phase memory times and spin-lattice relaxation times is given in **Figure 6.15**.
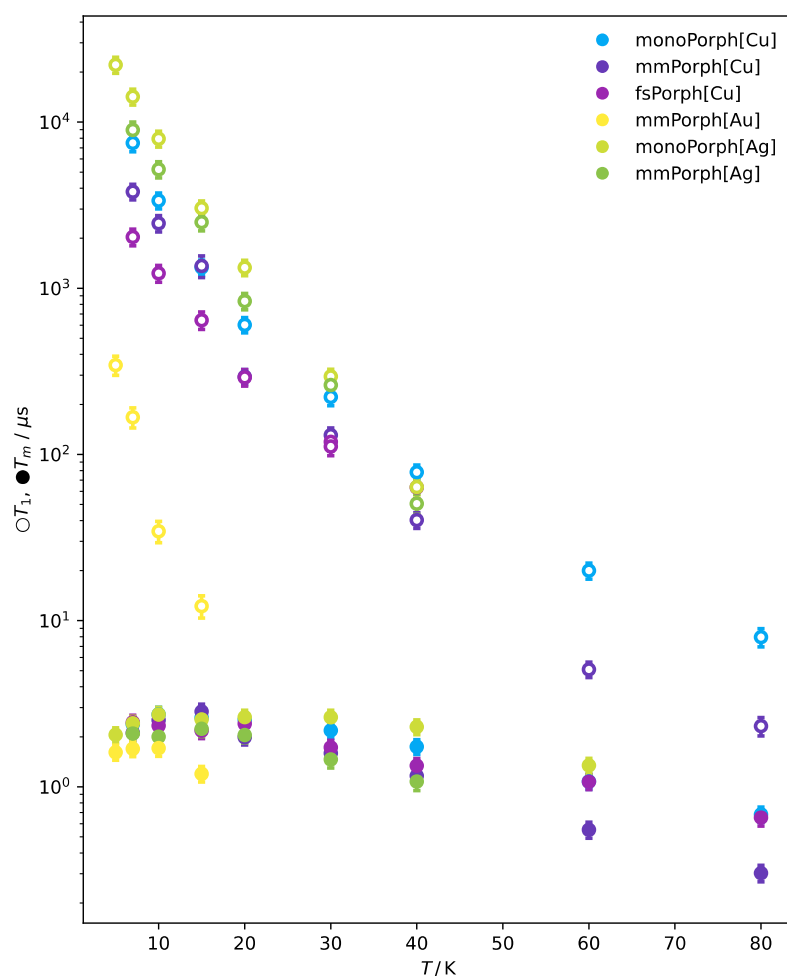
Figure 6.15. Temperature dependency of the extracted phase memory times T_m and spin-lattice relaxation times T_1 of all investigated compounds. The data of this table is found in **Table 6.4** and **Table 6.5**.

Phase-Memory Times T_m: Stable and Similar throughout Copper(II), Silver(II) and Gold(II)

Although the metals differ significantly, all five investigated compounds with an EPR signal share a common phase memory time in the range of $T_m = 2.0 \pm 0.6\,\mu s$ at 7 K. This relaxation time also remains quite stable up to around 30 K, after which they all drop off rapidly.

In fact, this is in agreement with the relaxation times recently reported by Ranieri et al. [182], who investigated similar porphyrins (with phenyl instead of tolyl substituents) with vanadyl ions as paramagnetic centers. They reported $T_m = 2.8\,\mu s$ for **monoPorph'[VO]** and $T_m = 3.5\,\mu s$ for **mmPorph'[VO]**, which are also very similar to the herein observed analogs and are also comparable to other reported dimers based on Cr_7Ni or lanthanides (see 7.9).

Spin-Lattice Relaxation Times T_1: A Strong Discrepancy between Expected and Observed

A striking difference between the copper and silver porphyrins is visible, however, in their spin-lattice relaxation. Contrary to the expectations, and based on the fact that SOC usually contributes significantly to decoherence [176],[183]–[187], the silver porphyrins all show much longer relaxation times than their copper counterparts, despite having a higher SOC. While T_1 at 7 K in **monoPorph[Cu]** is 7.5(9) ms , **monoPorph[Ag]** is almost twice at 14(2) ms.

This behavior was already described once by Eaton and Eaton in 1996 when they reported the spin relaxation of tetraphenyl copper(II) and silver(II) porphyrins **Ph₄Porph[Cu/Ag]** [177]. The relaxation times of these compounds were measured in toluene/chloroform mixtures of 2:1 between 20 and 120 K. In addition, they added a small amount of THF to reduce the chance of aggregation since the THF molecules act as an additional axial ligand on the porphyrin. Unfortunately, this paper also did not find an explanation for the quantitatively longer relaxation times of the silver analogs and only focuses on the temperature dependence, which is much more strongly pronounced in the silver variant than in the copper variant.

Comparing the acquired data for **monoPorph[Cu/Ag]** with those of Eaton and Eaton in [177], it can be seen that the observed relaxation times for **monoPorph[Cu]** are in the same range. While Eaton and Eaton reported a spin-lattice relaxation time of $T_1 \approx 800\,\mu s$ for their

Ph₄Porph[Cu] at 22 K, **monoPorph[Cu]** used in this study exhibits a $T_1 \approx 600$ μs at 20 K in pure toluene. The silver(II) analogues, **Ph₄Porph[Ag]** and **monoPorph[Ag]**, differ quite a bit as T_1 is reported to be around 1500 μs at ~30 K and 300 μs, respectively.

This unexpected trend does not continue for **mmPorph[Au]**. The detected relaxation times for this compound clearly follow the trend of faster decoherence with increasing SOC. While T_2 remains stable at 1.7(2) μs, T_m drops drastically to a mere 0.17(2) ms at 7 K.
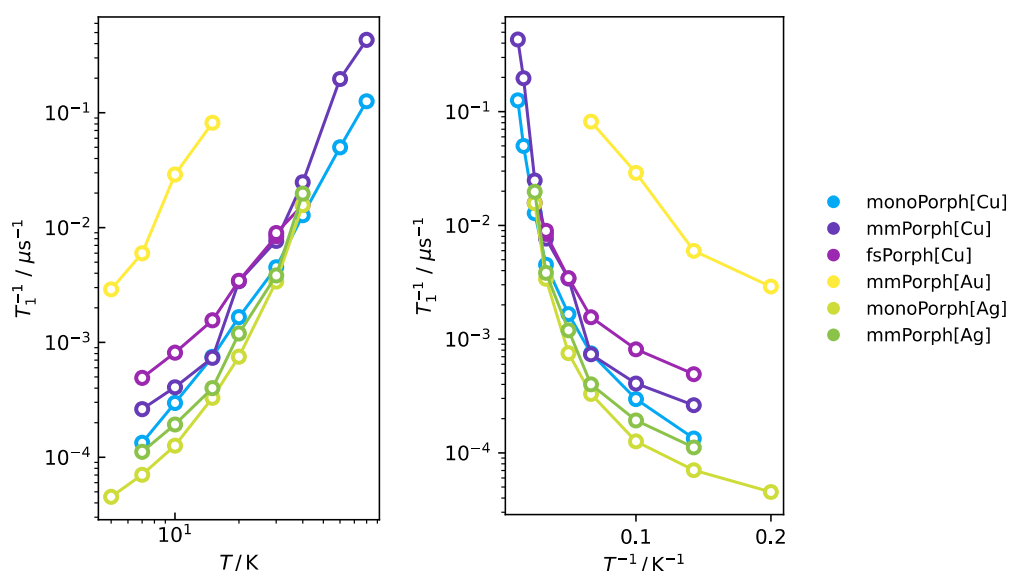
Figure 6.16. Spin-lattice relaxation times T_1 of the different porphyrins. (left) Raman processes should appear here as a linear dependency, as $T_1^{-1} = CT^n$. (right) Orbach processes should appear here as a linear dependency, as $T_1^{-1} \approx AE^3 \exp(-E/k_B T)$. Connections between data points should only provide a guide to the eye.

A quantitative assessment of which relaxation mechanisms – direct, Raman, or Orbach – are present from the data gathered is difficult. However, since an Orbach process requires a two-phonon process through an actual existing excited state, this seems unlikely for these types of porphyrins.

Much more likely is the relaxation by a Raman process, which requires a virtual excited state. This process (in addition to a direct process) should show a linear dependence when plotting $\log(T_1^{-1})$ versus $\log(T)$. An Orbach process, on the other hand, should be visible as a linear dependence of $\log(T_1^{-1})$ versus T^{-1}. Looking for these dependencies in **Figure 6.16**, no Orbach process is clearly visible, while a more or less linear dependence can be assumed with respect to the Raman process.

6.4. Conclusion

In this chapter, six porphyrin systems containing all three group 11 metals, copper, silver, and gold, have been investigated in different environments, from monomeric structures to loosely and rigidly linked dimeric structures in terms of their relaxation behavior. In all compounds, except the **fsPorph[Ag]**, quantum coherence could be observed by pulsed EPR measurements. For the first time, not only X-band cw-EPR but also the relaxation behavior of the heaviest analog, **mmPorph[Au]**, was observed by pulsed EPR spectroscopy.

When spin-lattice relaxation was studied, an intriguing and unexpected behavior was observed. While it is generally expected that the relaxation becomes faster with increasing spin-orbit coupling, this trend was not observed when transitioning from copper to silver. Surprisingly, the spin-lattice relaxation time at 7 K increased from about 7 ms to 14 ms, almost doubling. This phenomenon had previously been observed by Eaton and Eaton in a similar silver and copper porphyrin. However, the even heavier gold analog, **mmPorph[Au]**, conformed to the expected behavior, exhibiting rapid relaxation in the sub-millisecond range.

All the compounds investigated exhibited very similar phase memory times of around 2 µs at 7 K, falling in line with other vanadyl porphyrins reported in literature. These relaxation times remained primarily stable with increasing temperatures up to 30 K.

However, it is worth noting that these phase memory times, although stable, were not among the best reported. The Ti(III) dimer investigated in Section 4.3.4 has a similar (in protonated solvents) or triple (in deuterated solvents) relaxation time, and the PTM studied in Section 5.3.2 is far out of reach with phase memory times over 100 µs at 7 K. Nevertheless, these phase memory times do not exclude the possibility of their utilization as qubits since normal operations typically require only about 10 ns.

Determining the suitability of these compounds as a qugate with two qubits solely based on phase memory times is challenging. However, it can be concluded that the qubit distance is well-defined for their use as a qugate.

Finally, it is interesting to note that the influence of SOC on the phase memory time was not as significant as expected, except for the gold compound, which showed noticeable deviations from its lighter counterparts. Furthermore, the unexplained anomaly in the silver spin-lattice relaxation time underscores the need for further investigation to unravel the underlying reasons for these observed behaviors.

6.5. Experimental Section

Samples were synthesized and characterized by Shubhadeep Chandra, Institute of Inorganic Chemistry, University of Stuttgart and were used as received. The sample preparation of the gold porphyrin **mmPorph[Au]** was also done by Shubhadeep Chandra.

Pulsed electron paramagnetic resonance (pEPR) was recorded on a homebuilt Q-band spectrometer [140] and spectra were simulated with Easyspin 5.2.30 [141]. The microwave frequency was 35.000 GHz. Sample were prepared by dissolving the corresponding compound in the appropriate dry solvent. The sample was always freeze quenched by directly inserting it into the already cold resonator chamber to prevent precipitation of the compound when cooling down. The cavity was always tuned to the third mode of a TE_{011}-resonator. For the determination of spin-lattice relaxation times, the inversion-recovery pulse sequence was used, while the determination of the spin-spin relaxation times was conducted using the Hahn-echo pulse sequence. The experimental error of the setup is quantified as 10%, as determined by Dengler [40] in addition to the statistical error arising from the fitting procedure. Experimental errors for this spectrometer were generally estimated to be $\Delta g = 0.003$, $\Delta A = 0.3$ MHz for microwave frequencies of 35.000 GHz on the basis of repeated measurements of the same sample.

Data analysis of the relaxation data was carried out with the help of a self-written library in Python 3.8.

7

APPENDIX

7. APPENDIX

7.1. NMR Analytics

(dmdtSMe[EtCN])BF₄
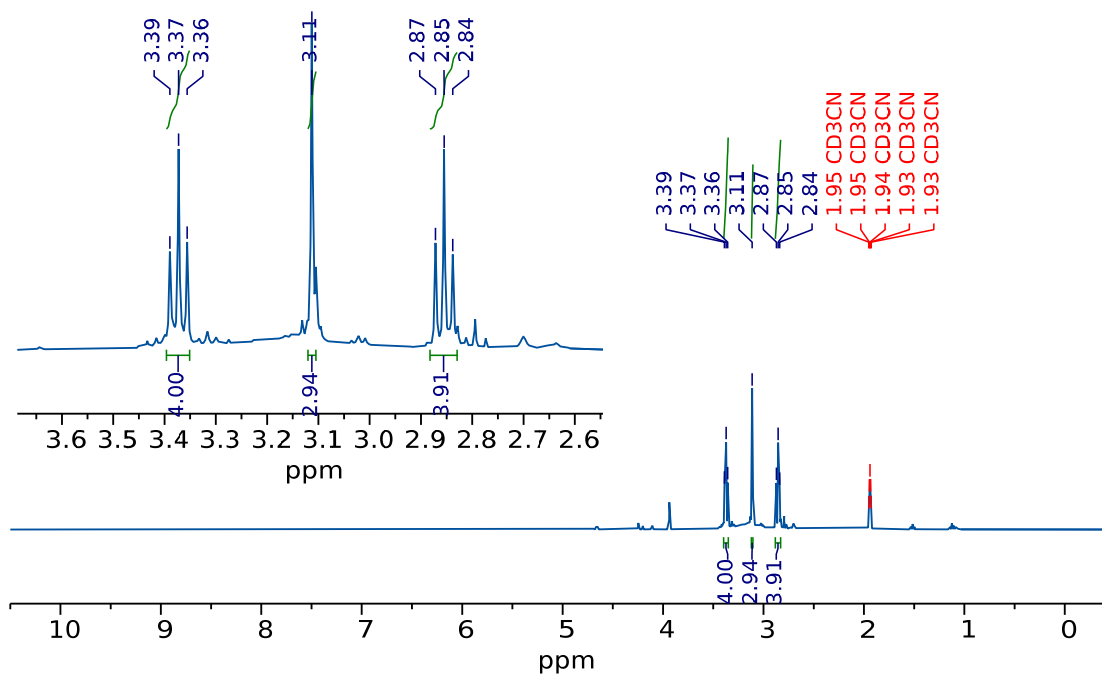
Figure 7.1. Crude ^{1}H NMR spectrum of **(dmdtSMe[EtCN])BF₄** (d$_3$-MeCN, 400 MHz).
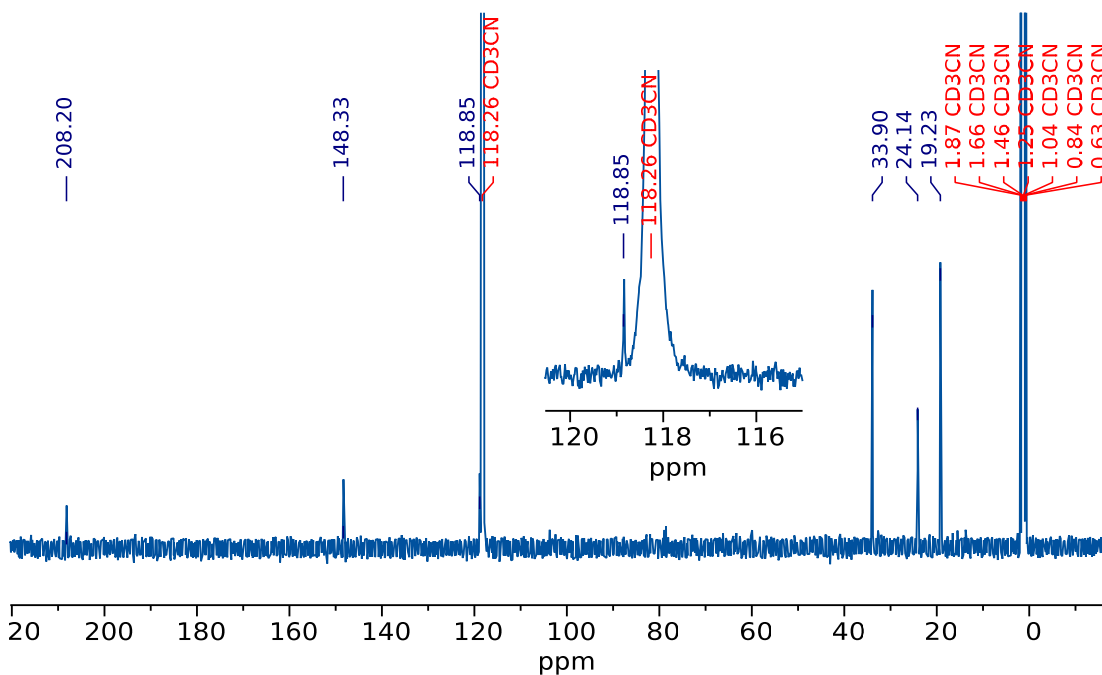
Figure 7.2. Crude ^{13}C{^{1}H} NMR spectrum of **(dmdtSMe[EtCN])BF₄** (d$_3$-MeCN, 101 MHz).

dmdtSMe[EtCN]
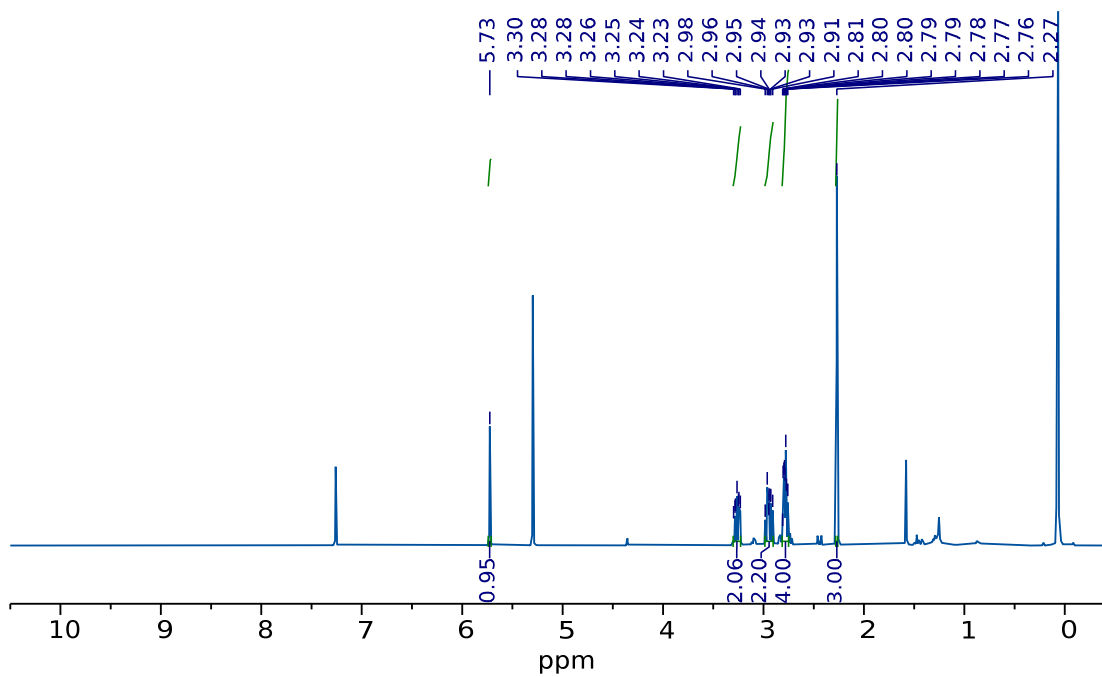
Figure 7.3.   ¹H NMR spectrum of **dmdtSMe[EtCN]** (CDCl$_3$, 400 MHz).
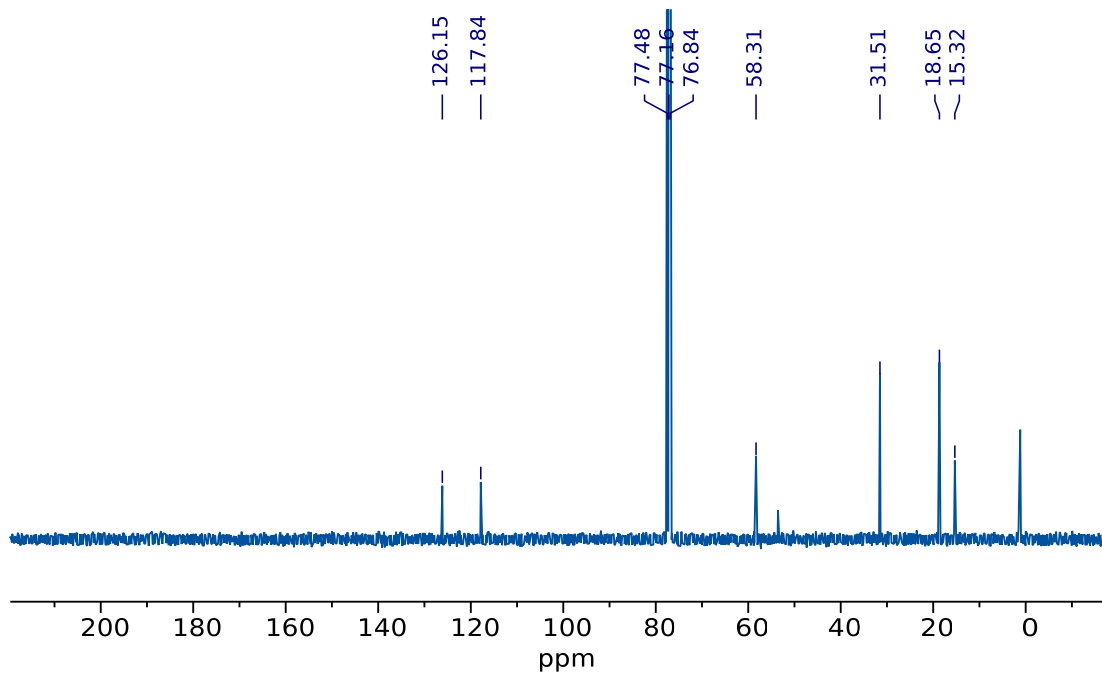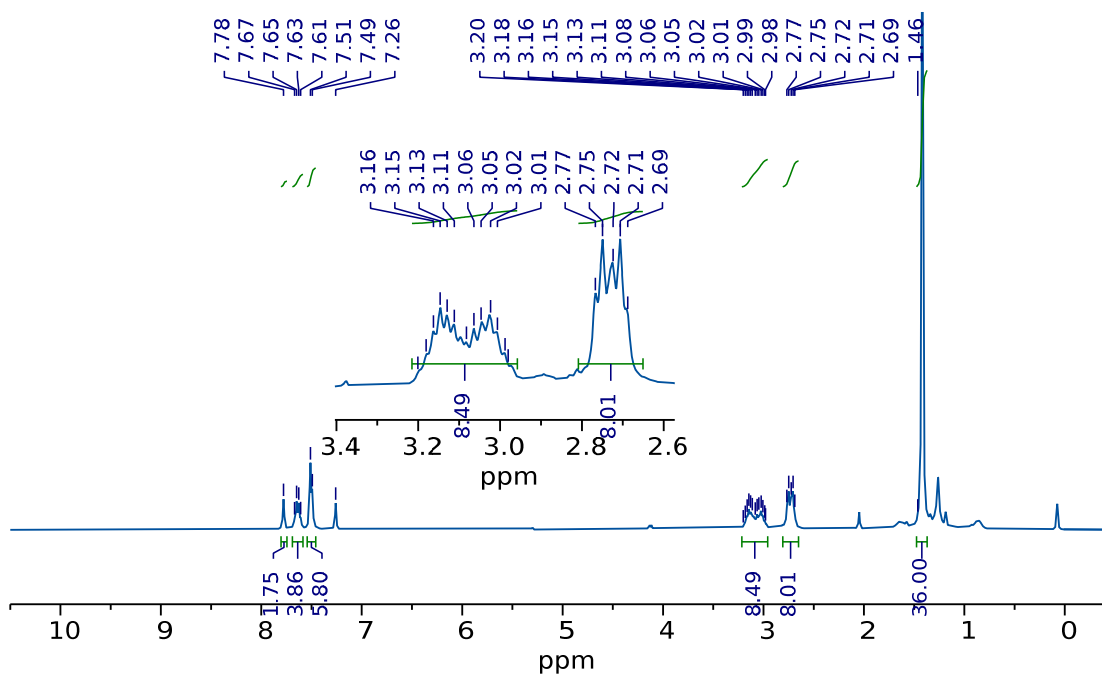

Figure 7.4.   ¹³C{¹H} NMR spectrum of **dmdtSMe[EtCN]** (CDCl$_3$, 101 MHz).
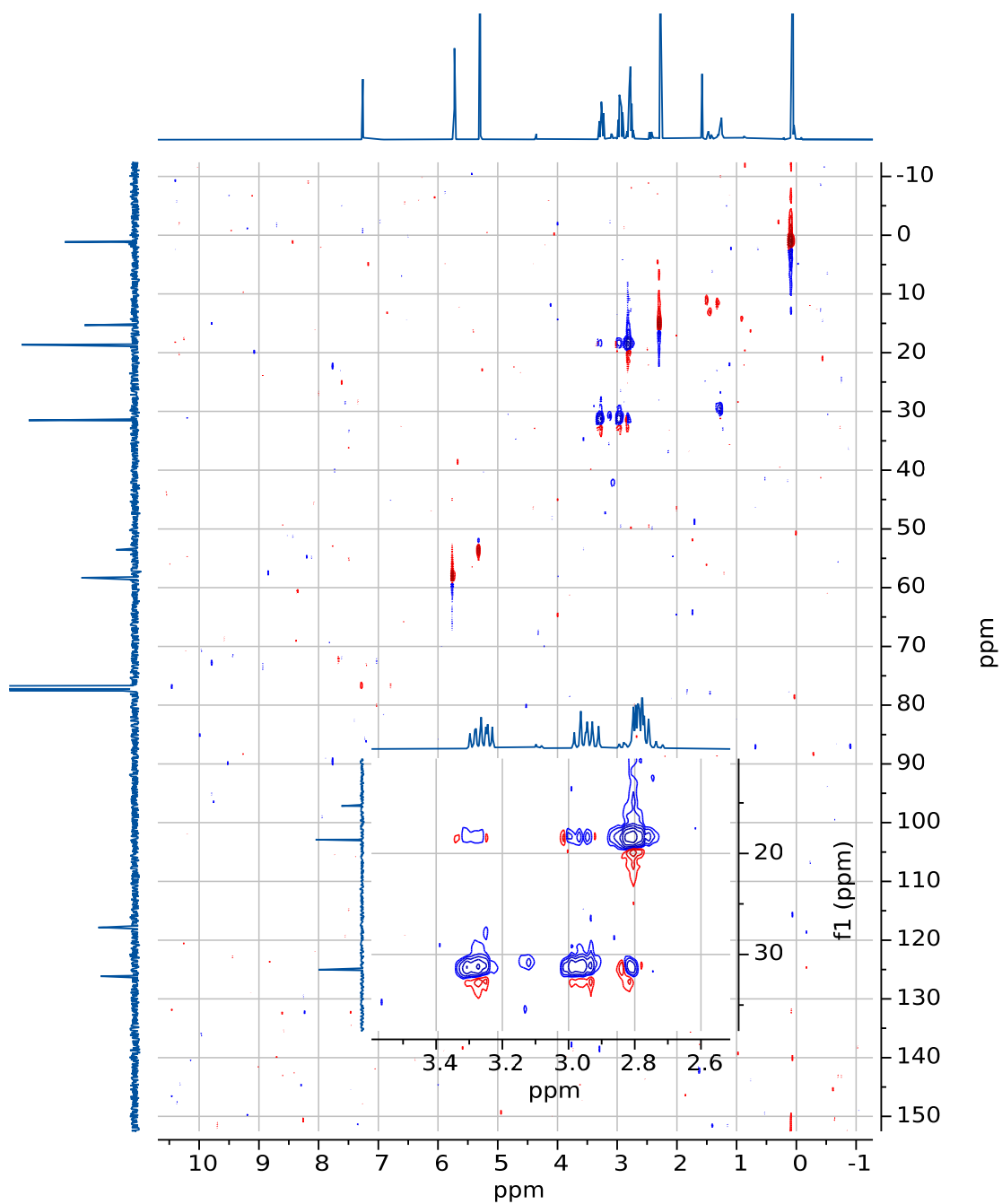
Figure 7.5. ^{1}H-^{13}C-HSQC NMR spectrum of **dmdtSMe[EtCN]** (CDCl$_3$, 101 MHz).

dmdtSEt[EtCN]
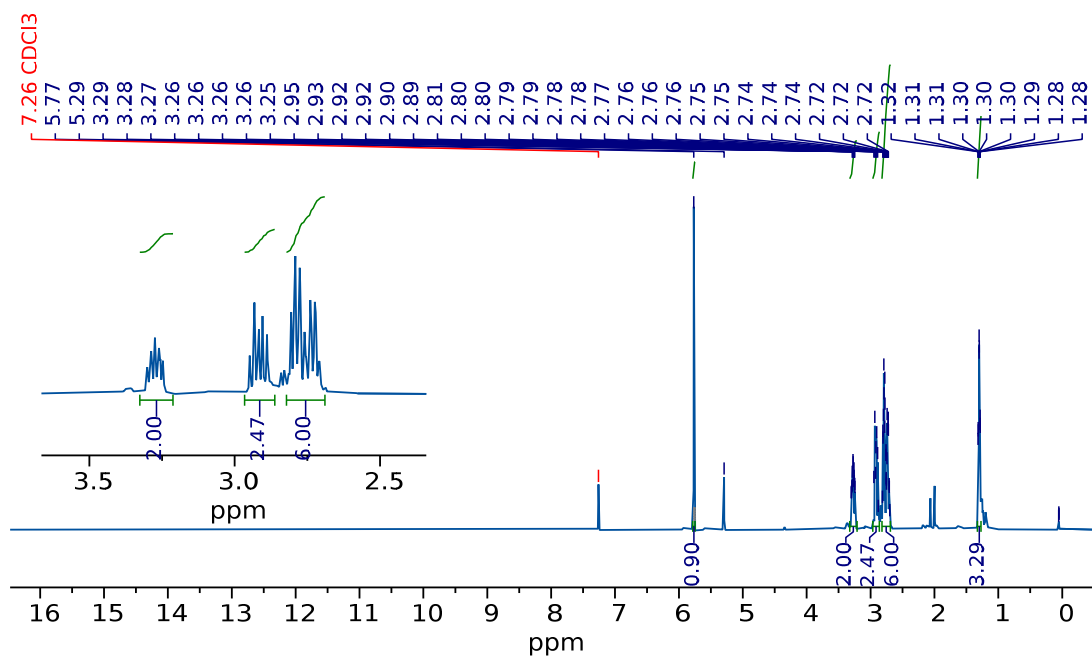
Figure 7.6.   ¹H NMR spectrum of **dmdtSEt[EtCN]** (CDCl₃, 500 MHz).
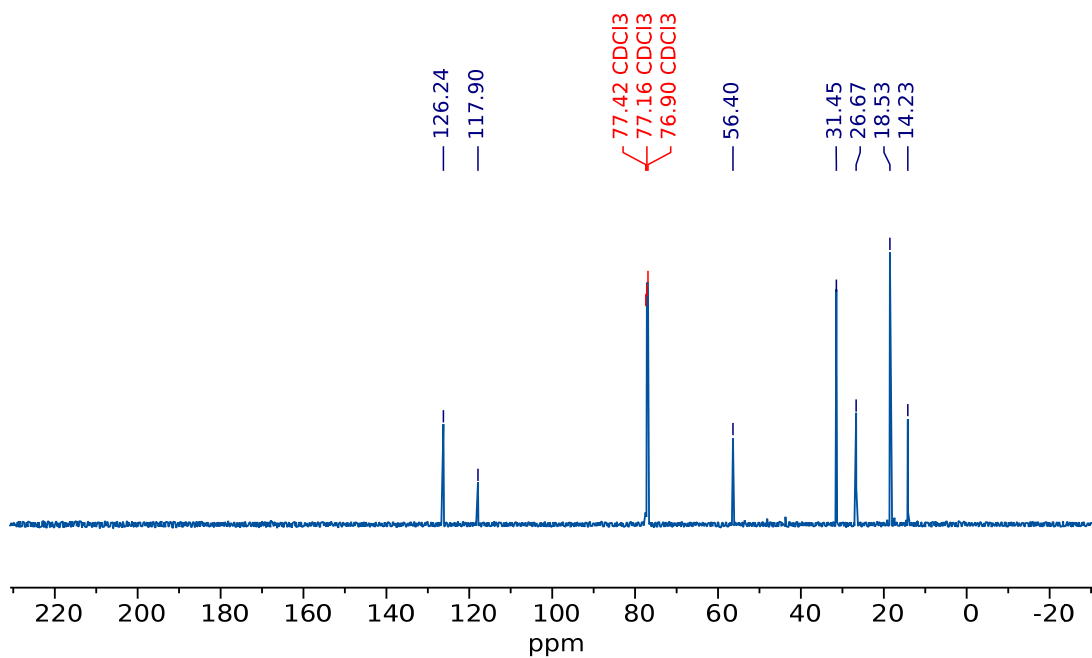
Figure 7.7.   ¹³C{¹H} NMR spectrum of **dmdtSEt[EtCN]** (CDCl₃, 126 MHz).

dmdtP[EtCN]
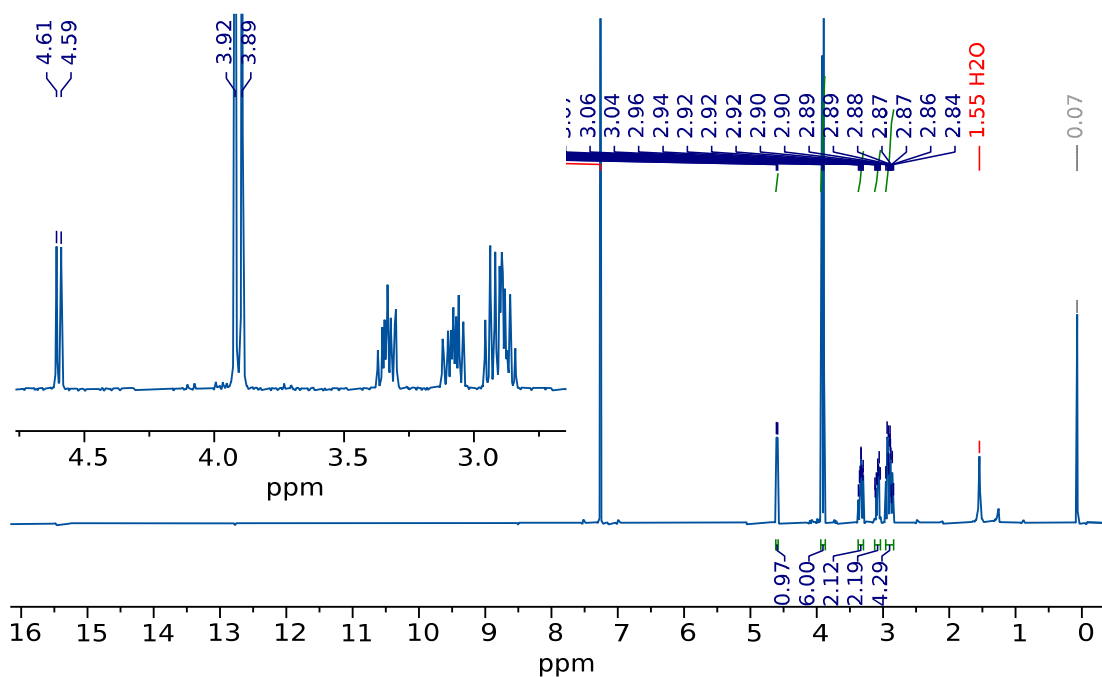
Figure 7.8. ¹H NMR spectrum of **dmdtP[EtCN]** (CDCl₃, 400 MHz).
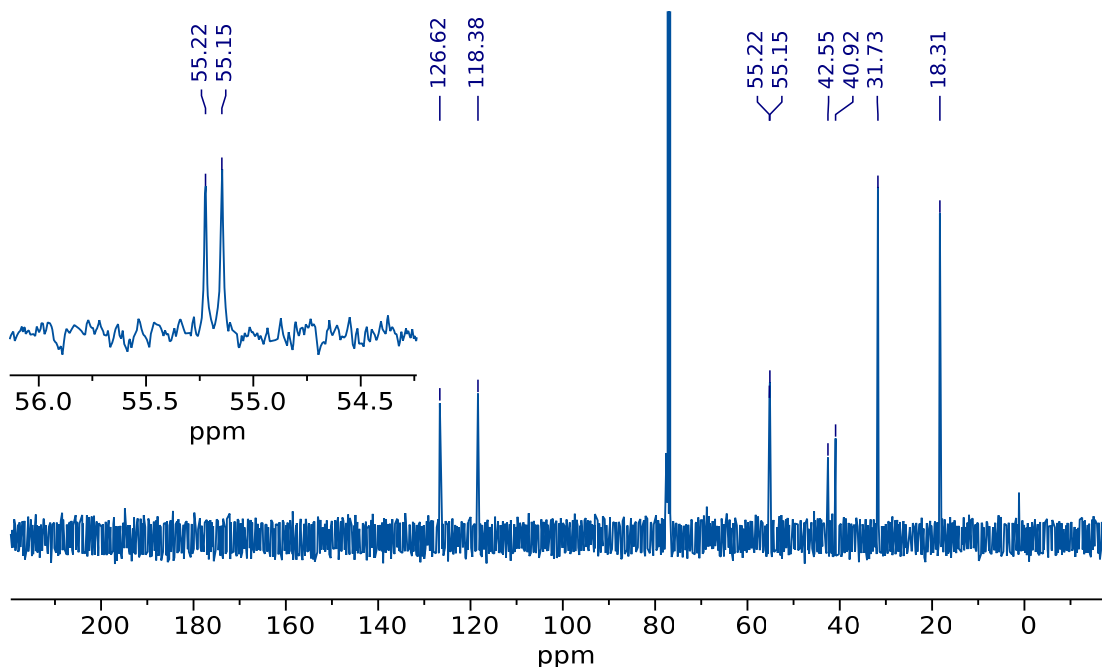
Figure 7.9. ¹³C{¹H} NMR spectrum of **dmdtP[EtCN]** (CDCl₃, 101 MHz).
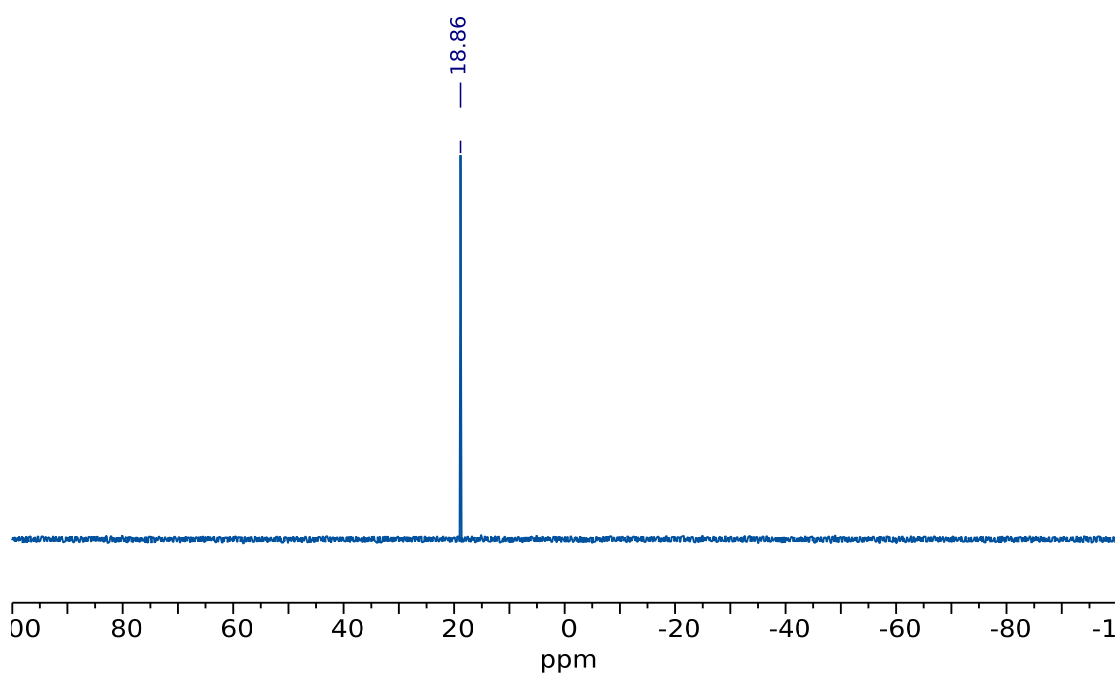
Figure 7.10. $^{31}P\{^1H\}$ NMR spectrum of **dmdtP[EtCN]** (CDCl$_3$, 162 MHz).
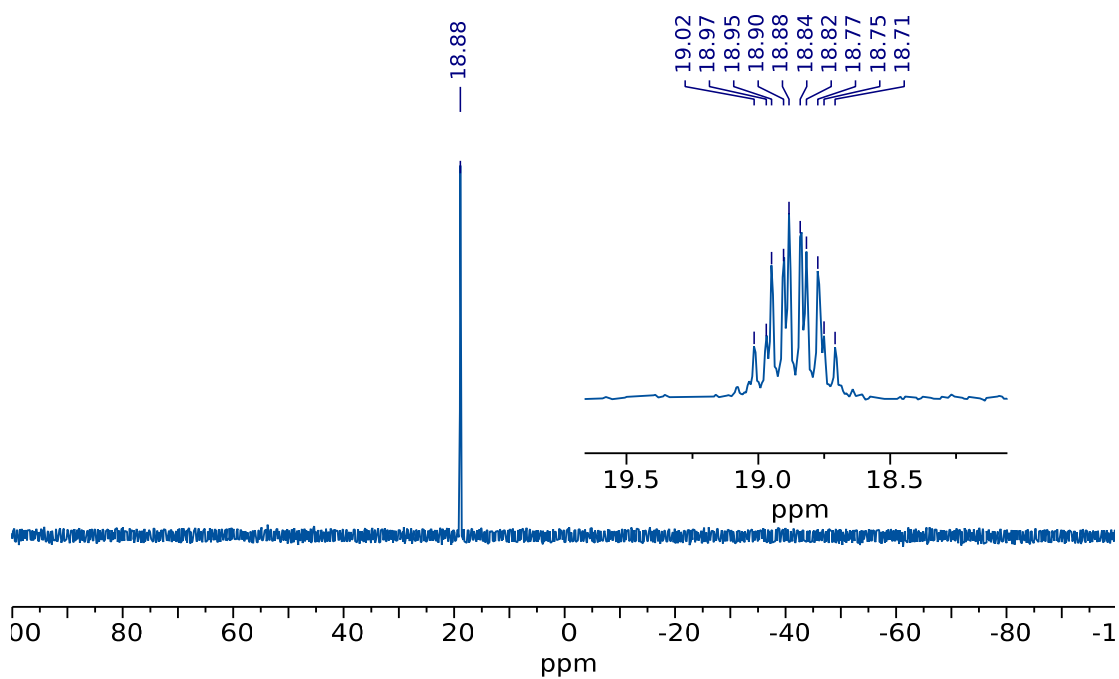
Figure 7.11. ^{31}P NMR spectrum of **dmdtP[EtCN]** (CDCl$_3$, 162 MHz).
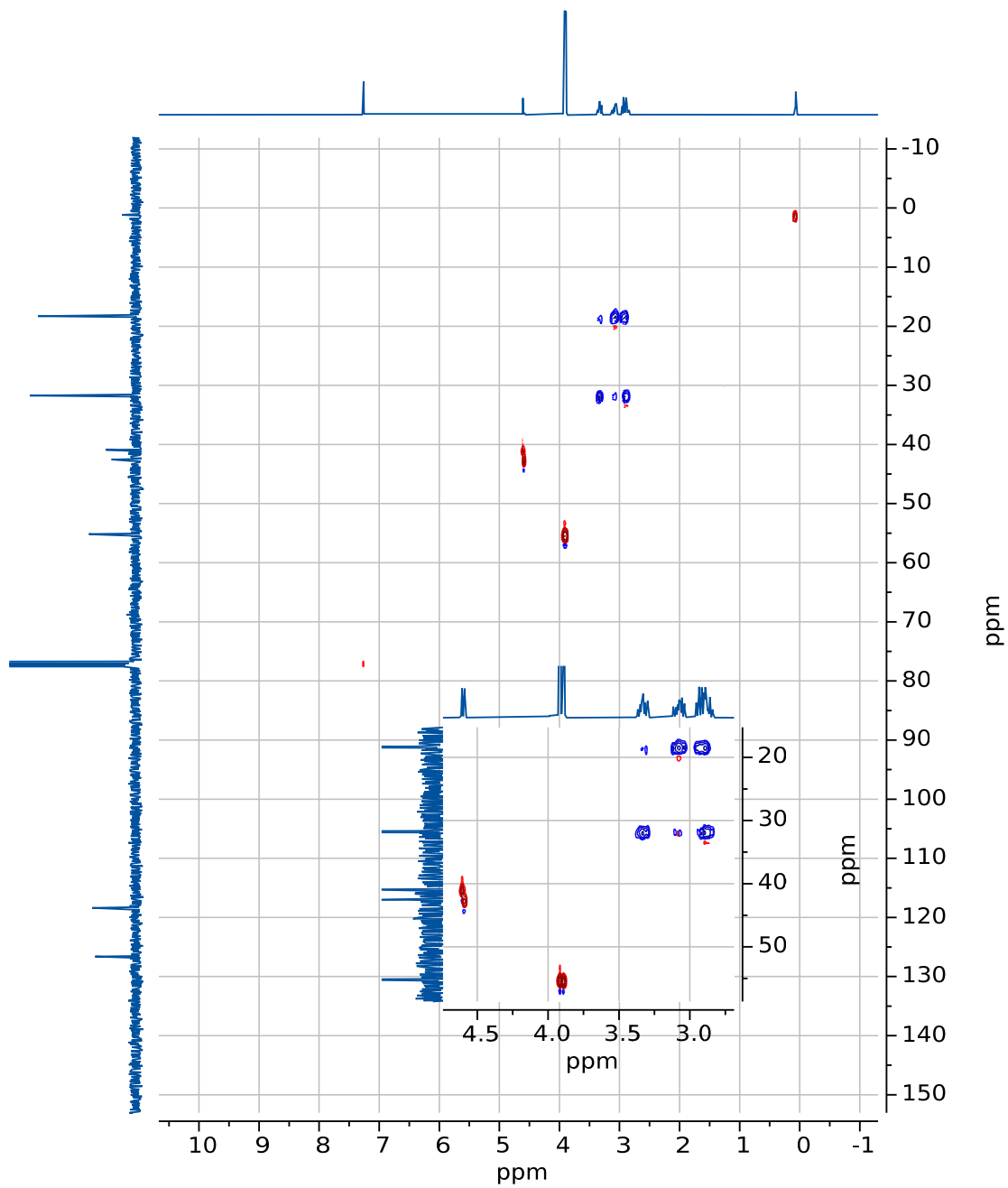
Figure 7.12. ^{1}H-^{13}C-HSQC NMR spectrum of **dmdtP[EtCN]** (CDCl$_3$).

2,6-Bis(m-di-tert-butylphenyl)anthraquinone
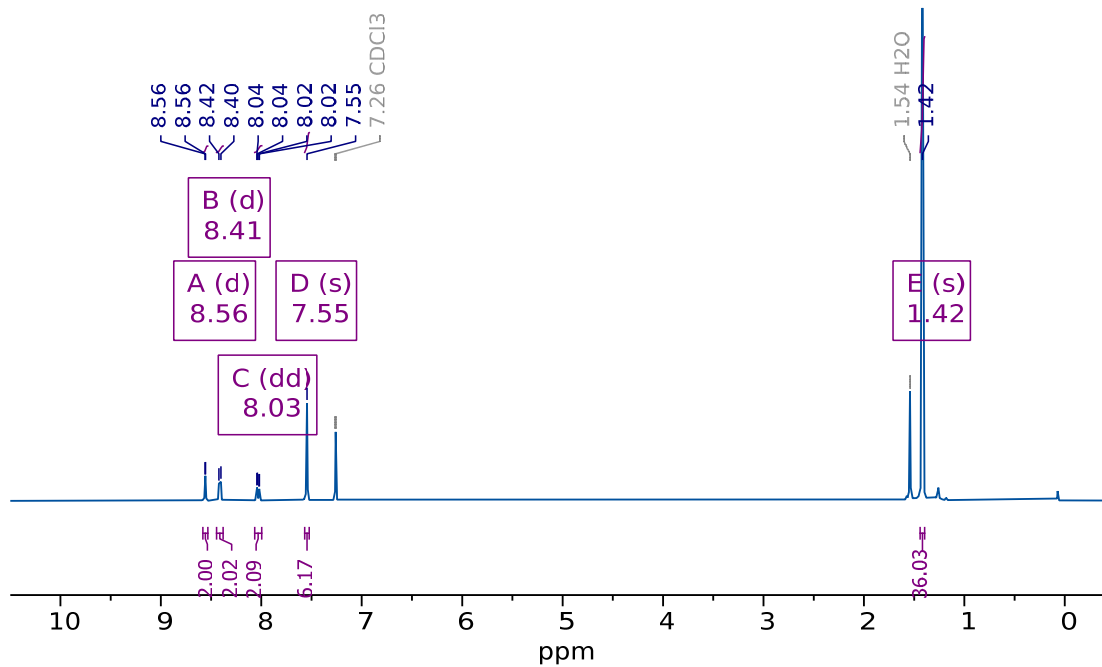
Figure 7.13. ^{1}H NMR spectrum of **2,6-bis(m-di-tert-butylphenyl)anthraquinone** (CDCl$_3$, 400 MHz).
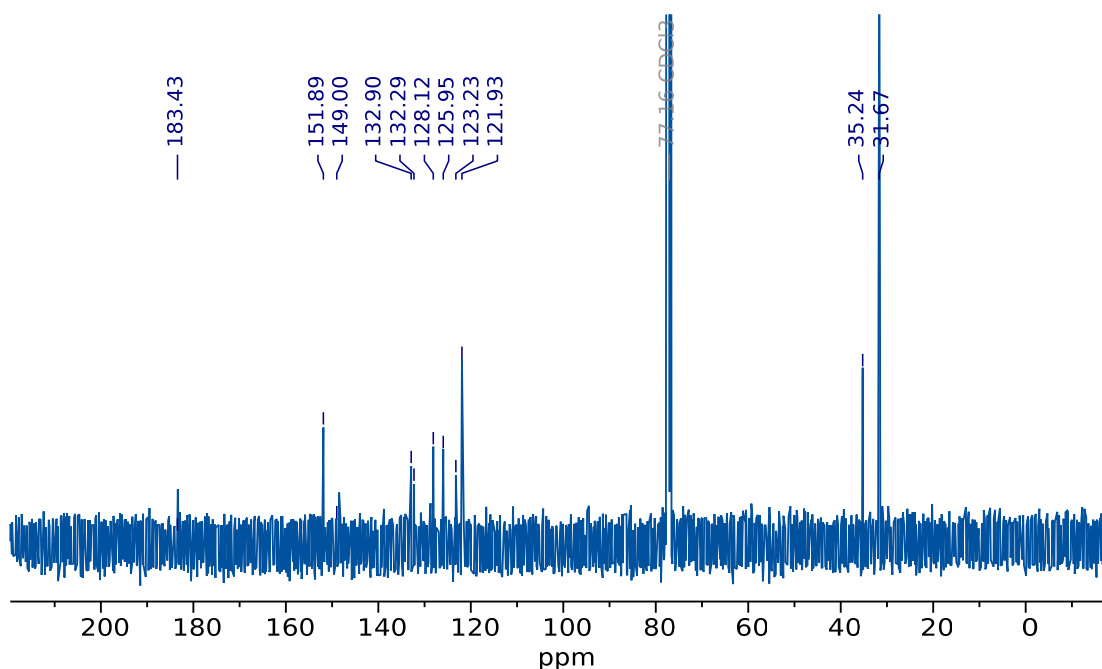
Figure 7.14. ^{13}C{^{1}H} NMR spectrum of **2,6-bis(m-di-tert-butylphenyl)anthraquinone** (CDCl$_3$, 101 MHz).

dmdtiPr[EtCN]
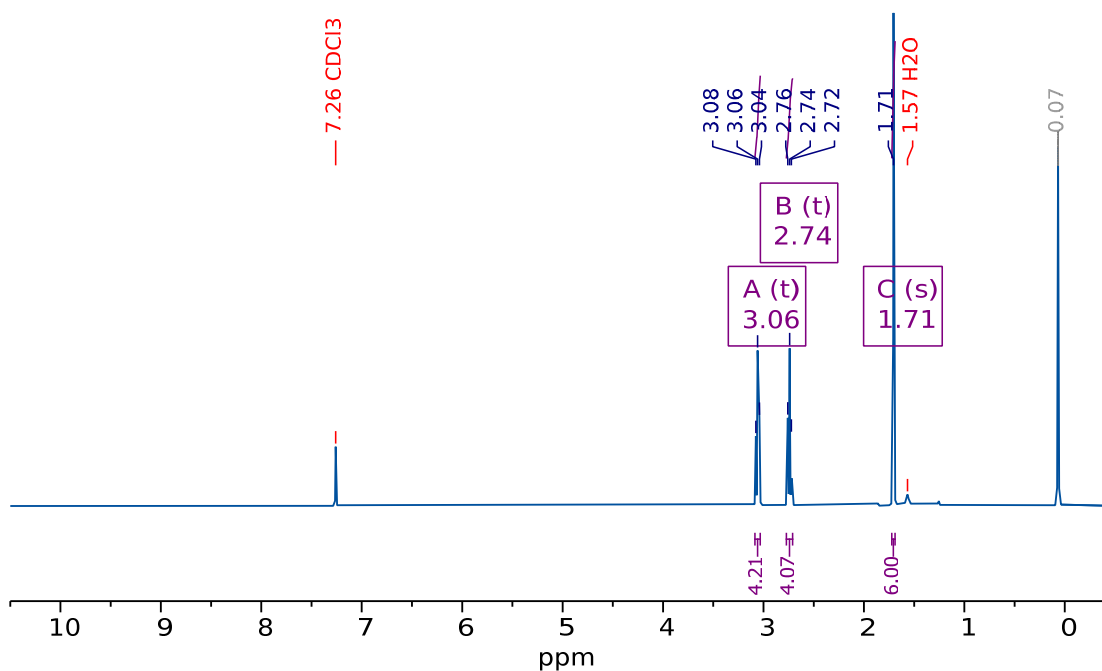
Figure 7.15. ^{1}H NMR spectrum of **dmdtiPr[EtCN]** (CDCl$_3$, 400 MHz).
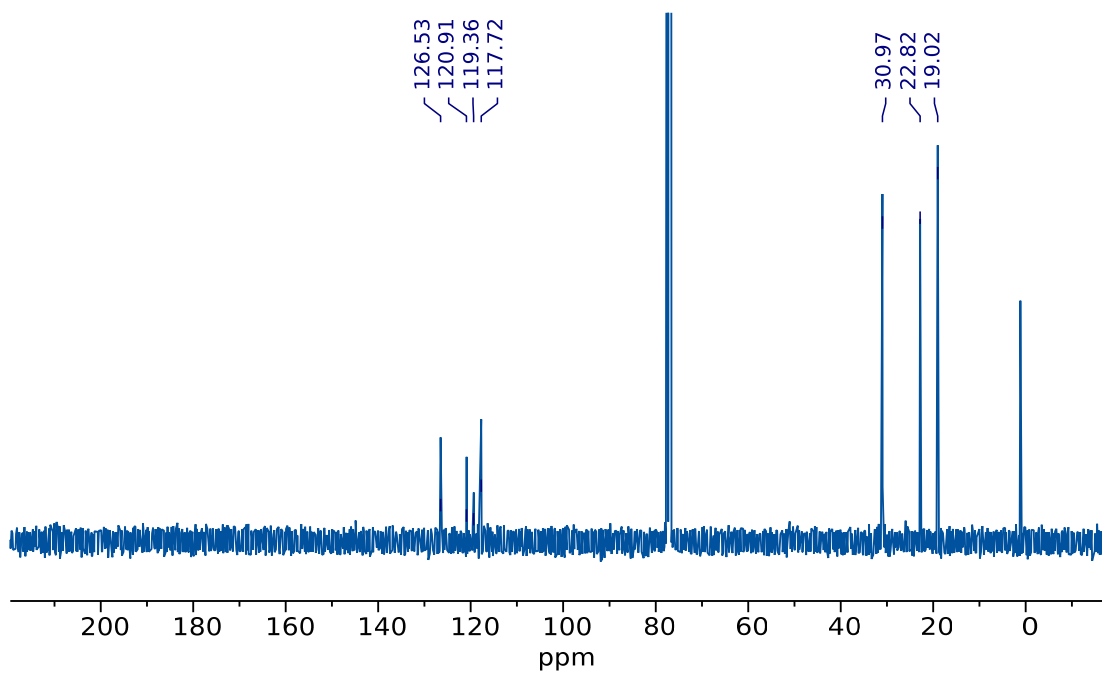
Figure 7.16. ^{13}C{^{1}H} NMR spectrum of **dmdtiPr[EtCN]** (CDCl$_3$, 101 MHz).

dmdtAd[EtCN]
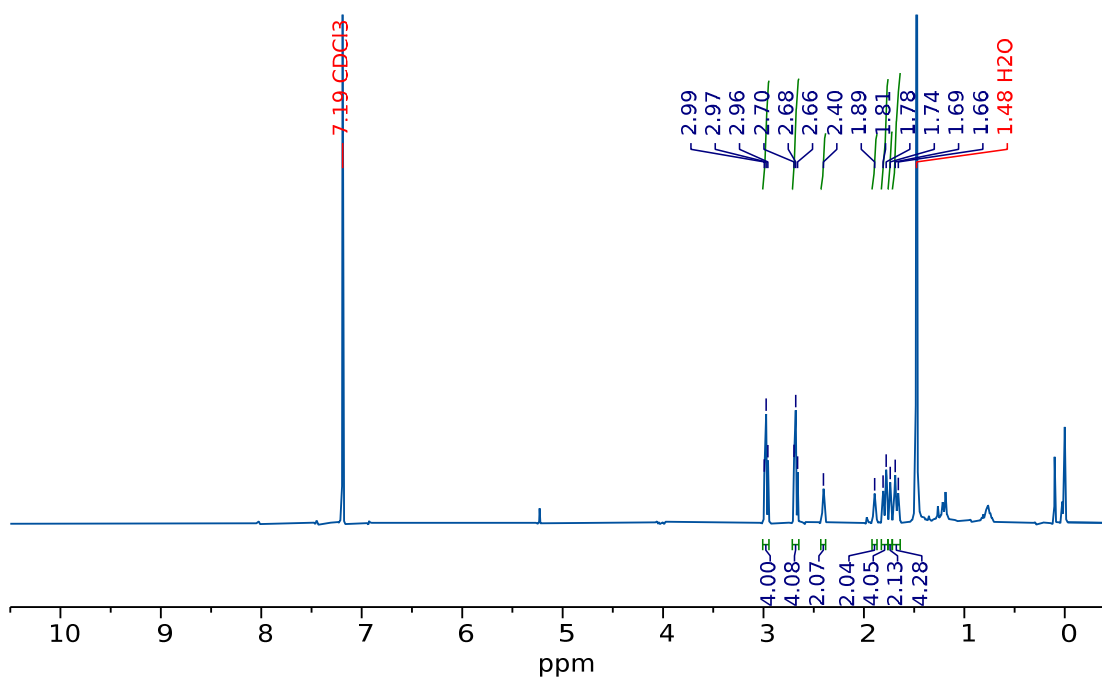
Figure 7.17. ¹H NMR spectrum of **dmdtAd[EtCN]** (CDCl₃, 400 MHz).
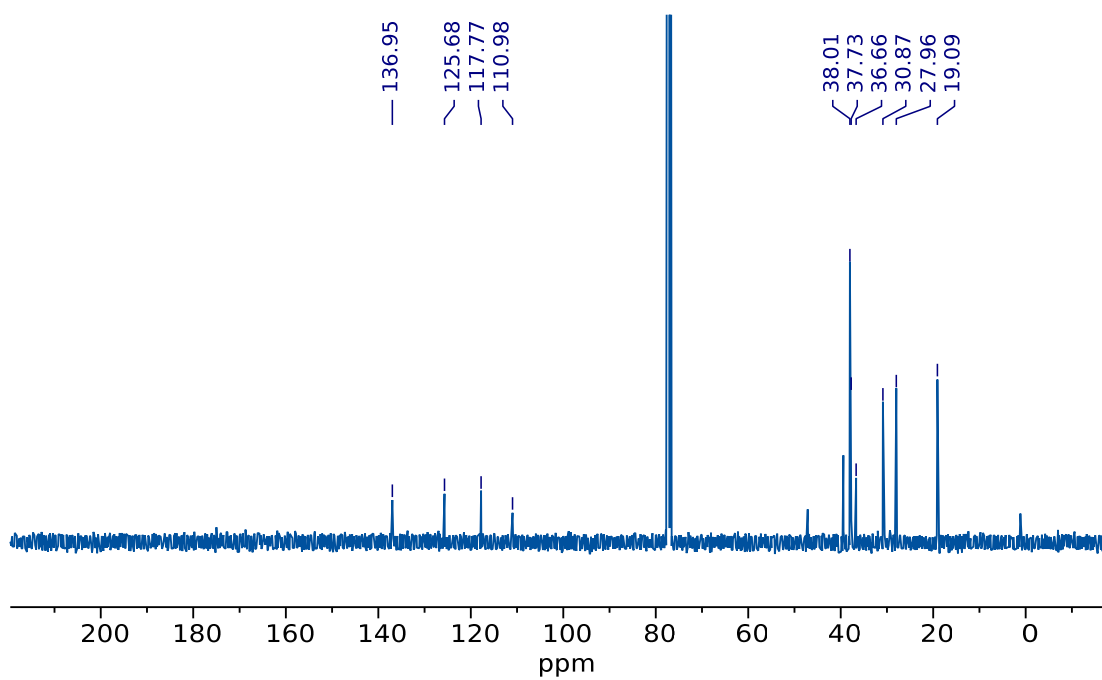
Figure 7.18. ¹³C{¹H} NMR spectrum of **dmdtAd[EtCN]** (CDCl₃, 101 MHz).

dmdt₂Ad[EtCN]
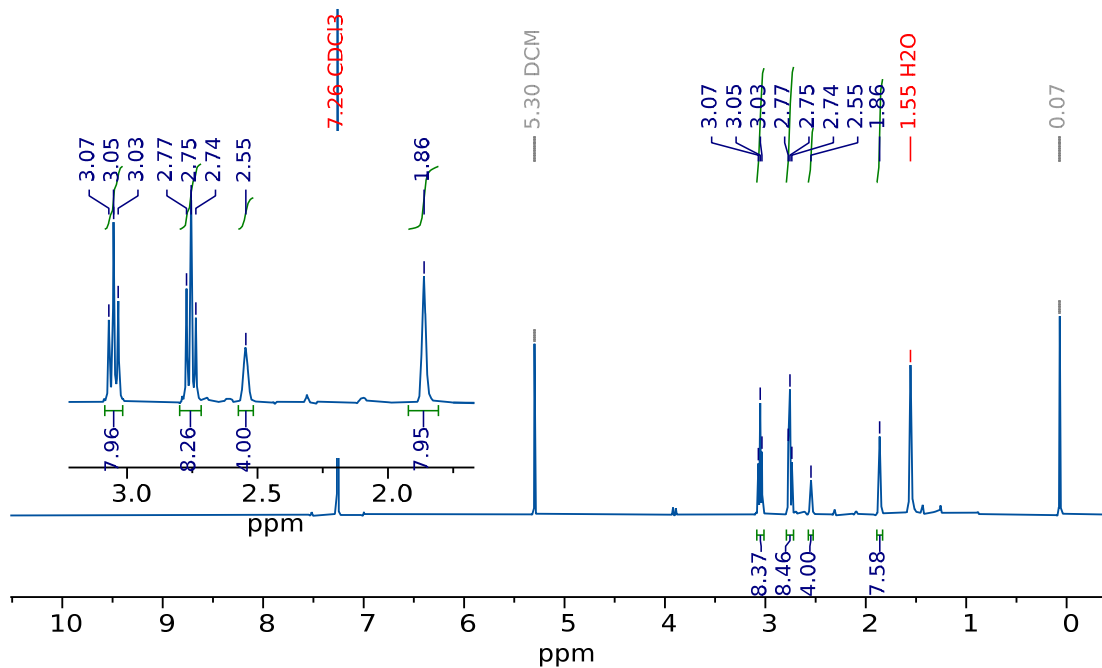
Figure 7.19. ¹H NMR spectrum of **dmdt₂Ad[EtCN]** (CDCl₃, 400 MHz).
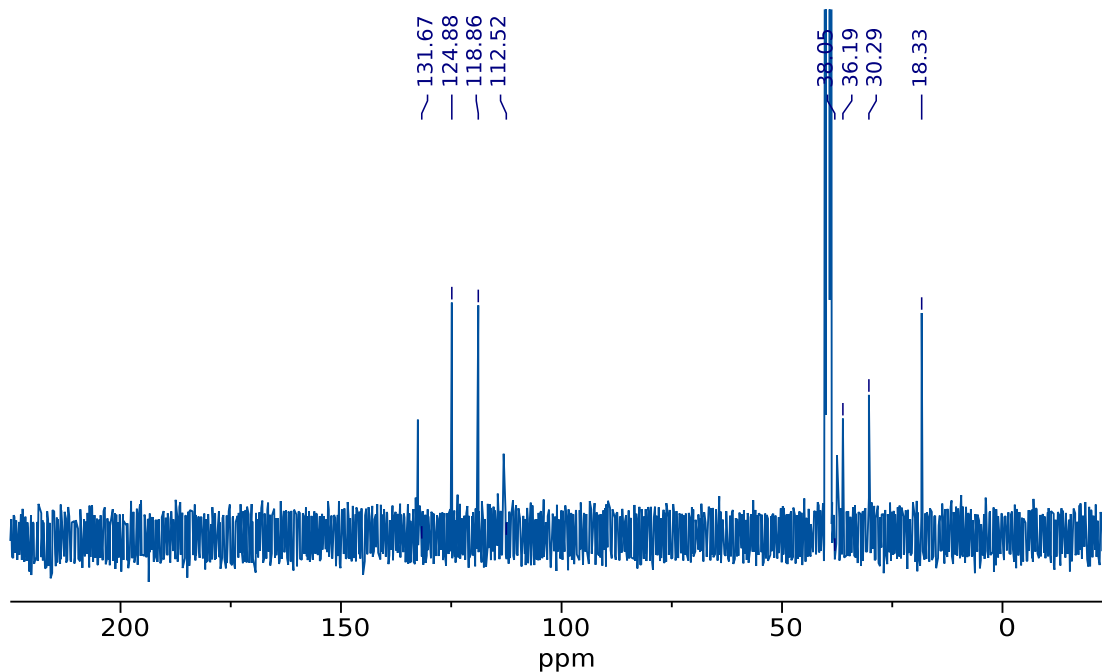
Figure 7.20. ¹³C{¹H} NMR spectrum of **dmdt₂Ad[EtCN]** (d₆-DMSO, 101 MHz).
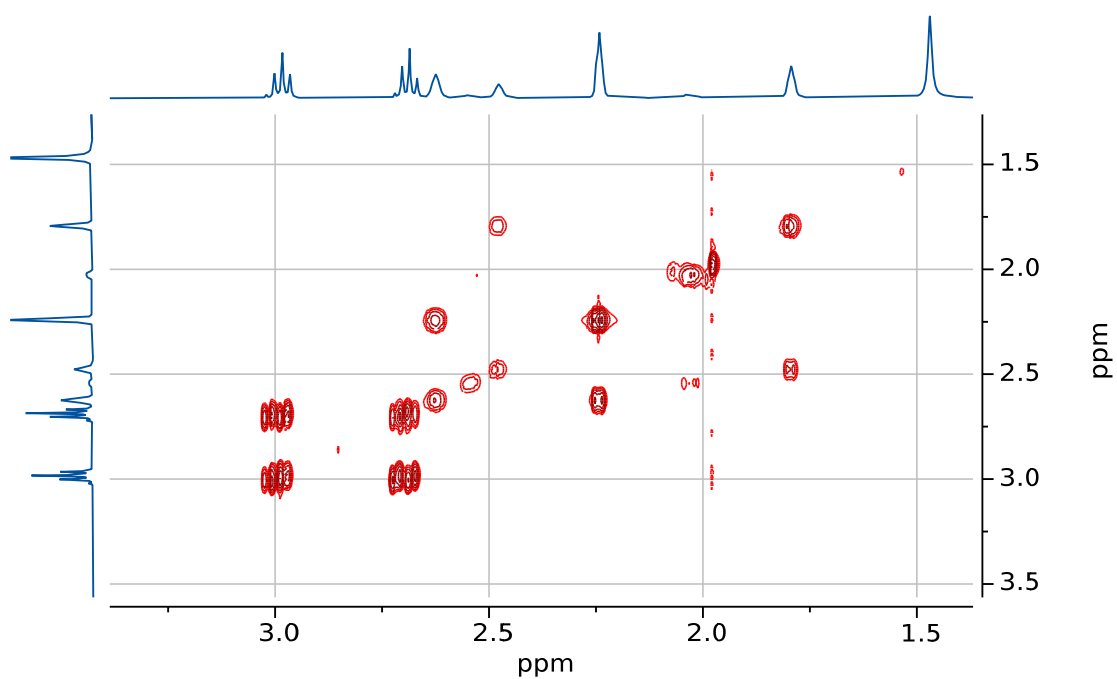
Figure 7.21. ^{1}H-^{1}H-COSY spectrum of **dmdt₂Ad[EtCN]** (CDCl₃, 400 MHz).
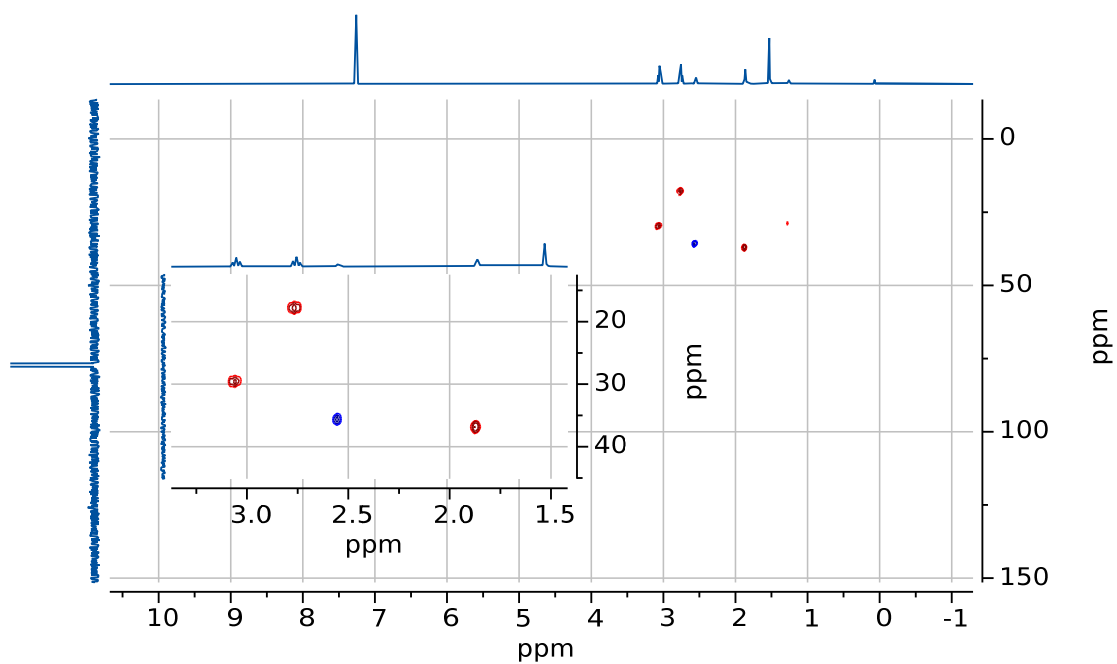
Figure 7.22. ^{1}H-^{13}C-HSQC spectrum of **dmdt₂Ad[EtCN]** (CDCl₃).

dmdt₂Anthra[EtCN]
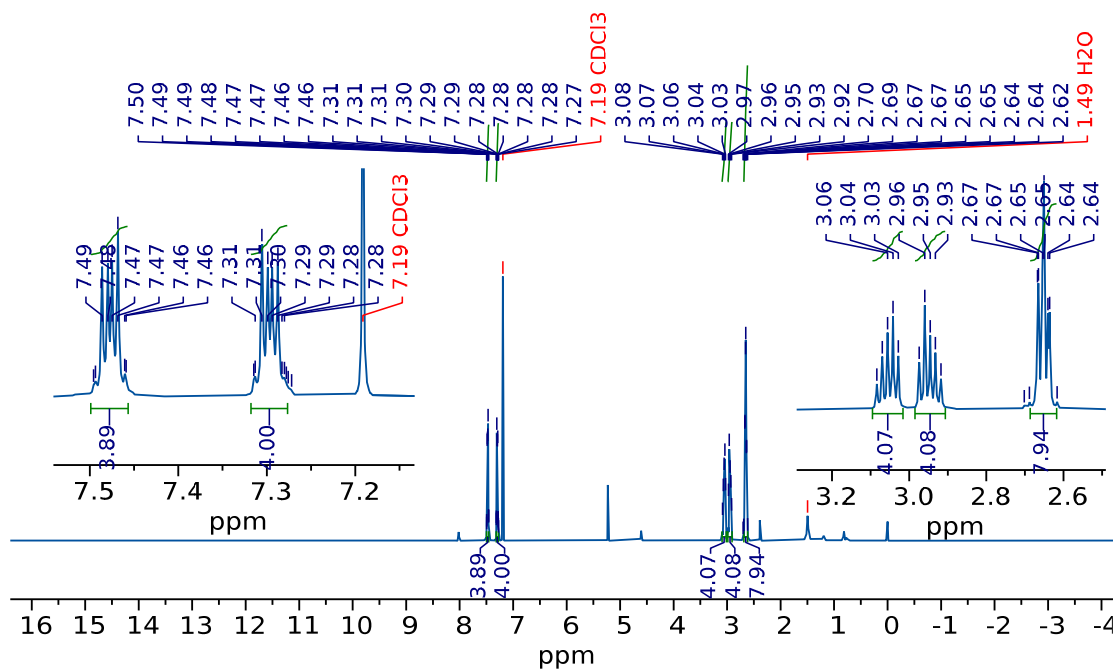
Figure 7.23. ¹H NMR spectrum of **dmdt₂Anthra[EtCN]** (CDCl₃, 500 MHz).
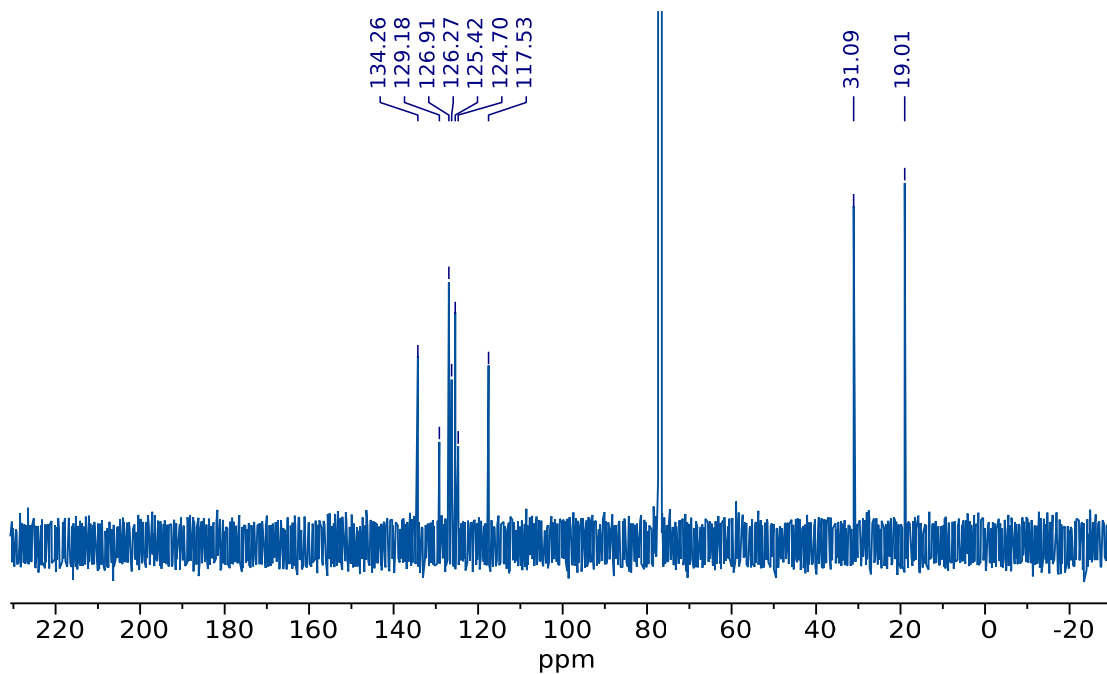
Figure 7.24. ¹³C{¹H} NMR spectrum of **dmdt₂Anthra[EtCN]** (CDCl₃, 126 MHz).
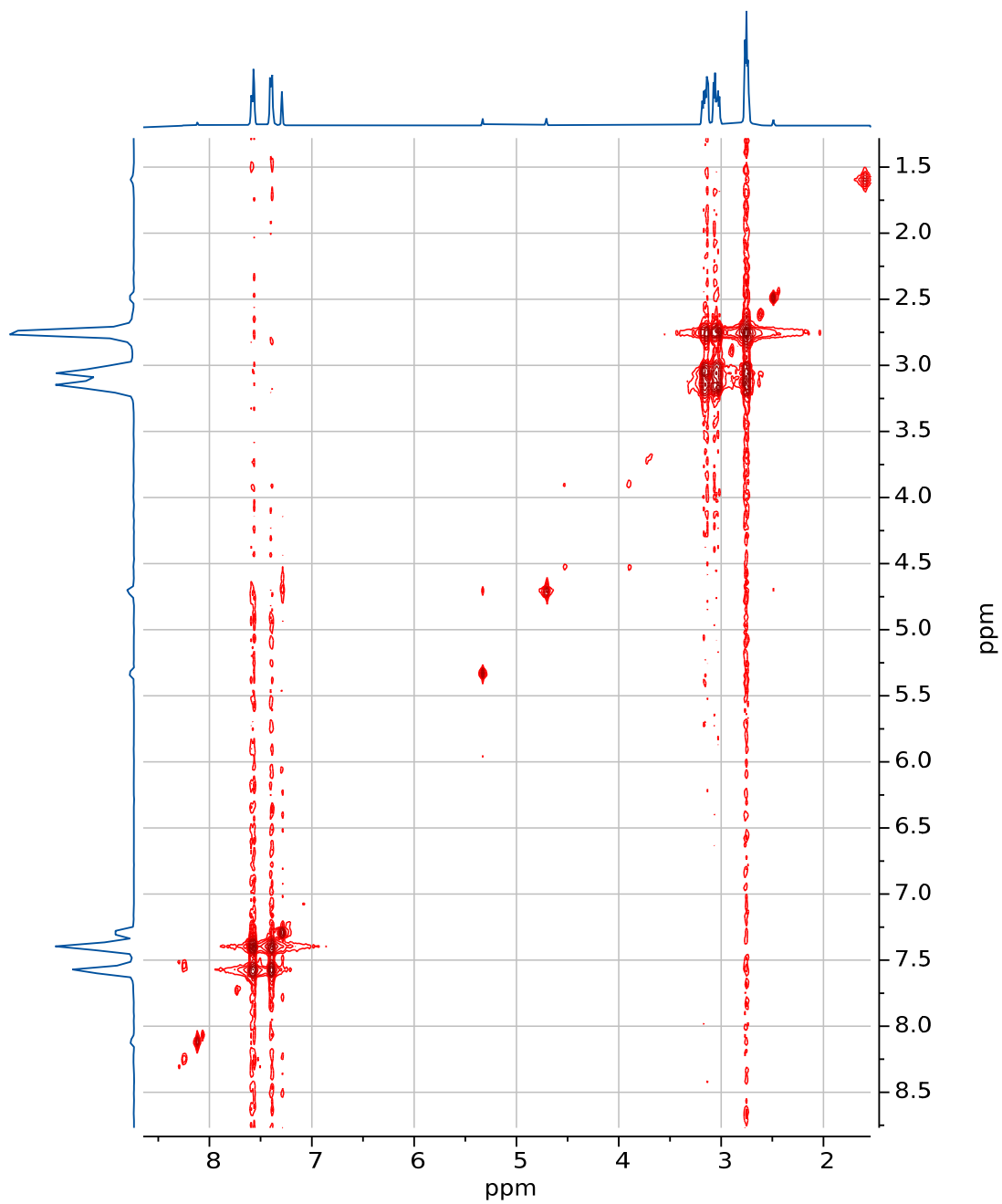
Figure 7.25. ¹H-¹H-COSY spectrum of **dmdt₂Anthra[EtCN]** (CDCl₃, 400 MHz).

dmdt₂Penta[EtCN]
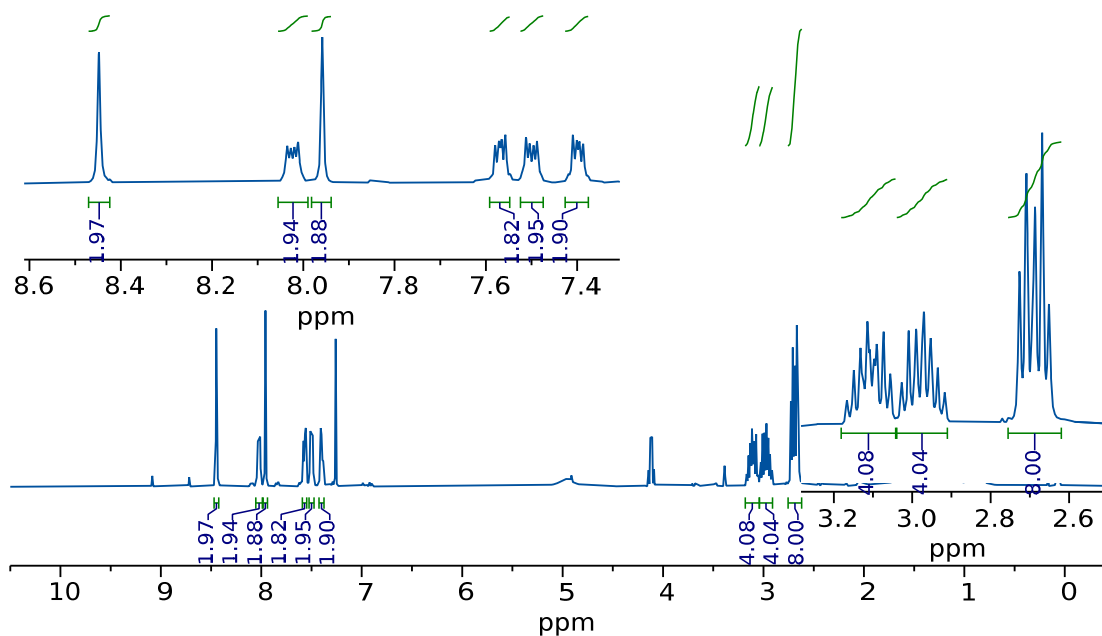
Figure 7.26. ¹H NMR spectrum of **dmdt₂Penta[EtCN]** (CDCl₃, 400 MHz).
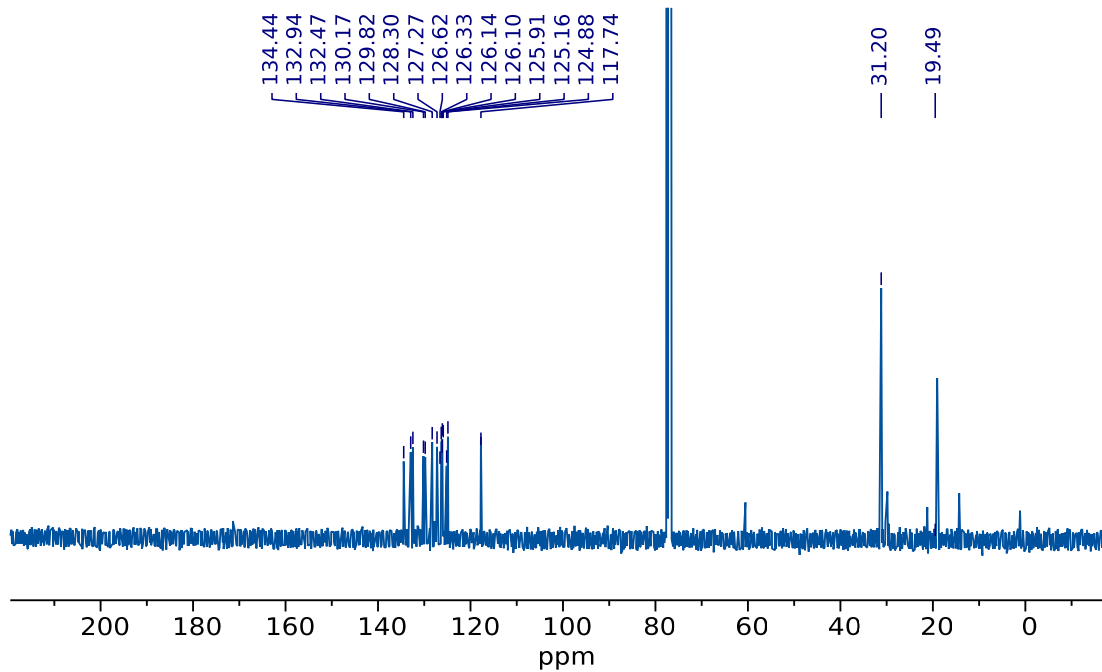
Figure 7.27. ¹³C{¹H} NMR spectrum of **dmdt₂Penta[EtCN]** (CDCl₃, 101 MHz).

dmdt₂Dtbpa[EtCN]

Figure 7.28.   ¹H NMR spectrum of **dmdt₂Dtbpa[EtCN]** (CDCl₃, 400 MHz).
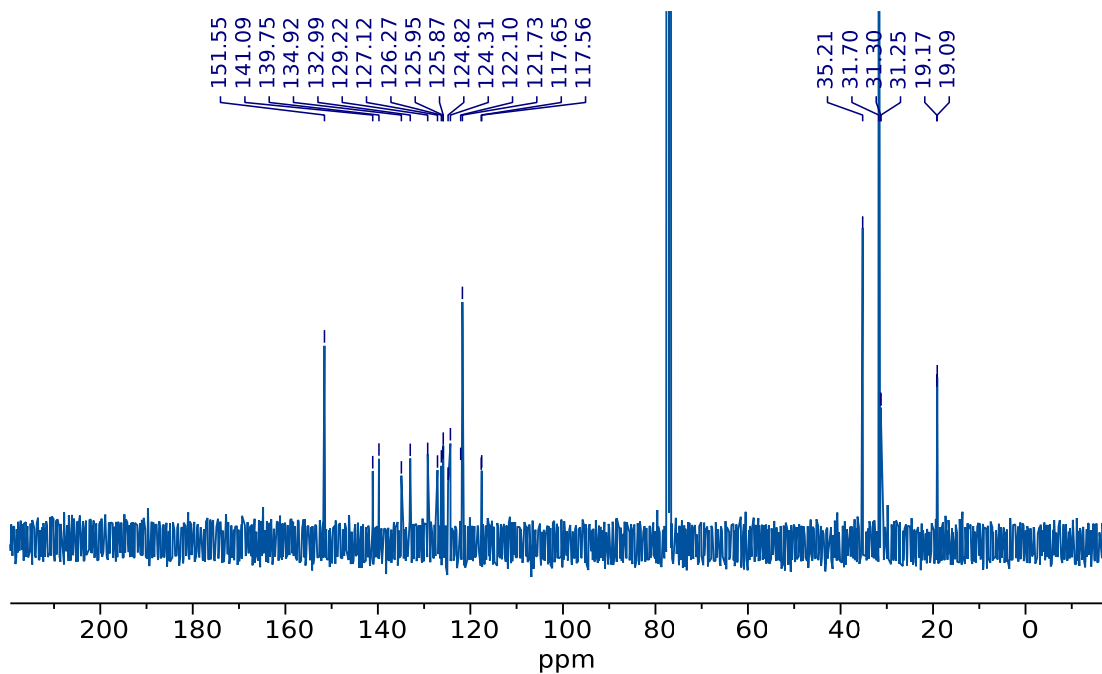
Figure 7.29.   ¹³C{¹H} NMR spectrum of **dmdt₂Dtbpa[EtCN]** (CDCl₃, 101 MHz).

dmdtAd[TiCp₂]
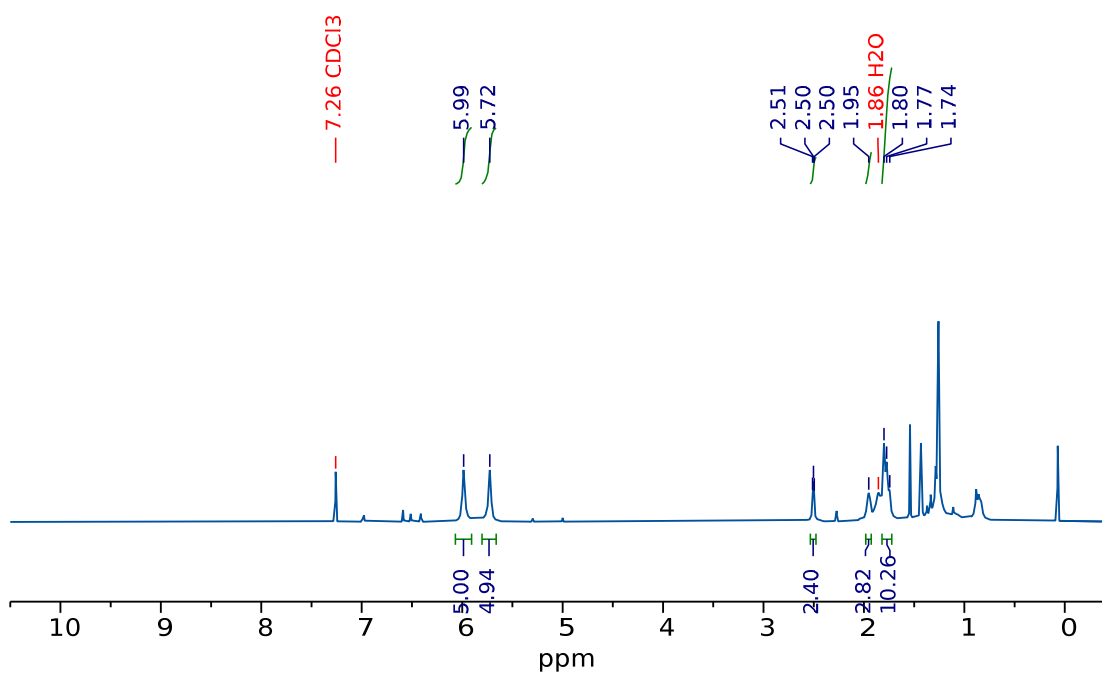
Figure 7.30. ¹H NMR spectrum of **dmdtAd[TiCp₂]** (CDCl₃, 400 MHz).

dmdt₂Ad[TiCp₂]
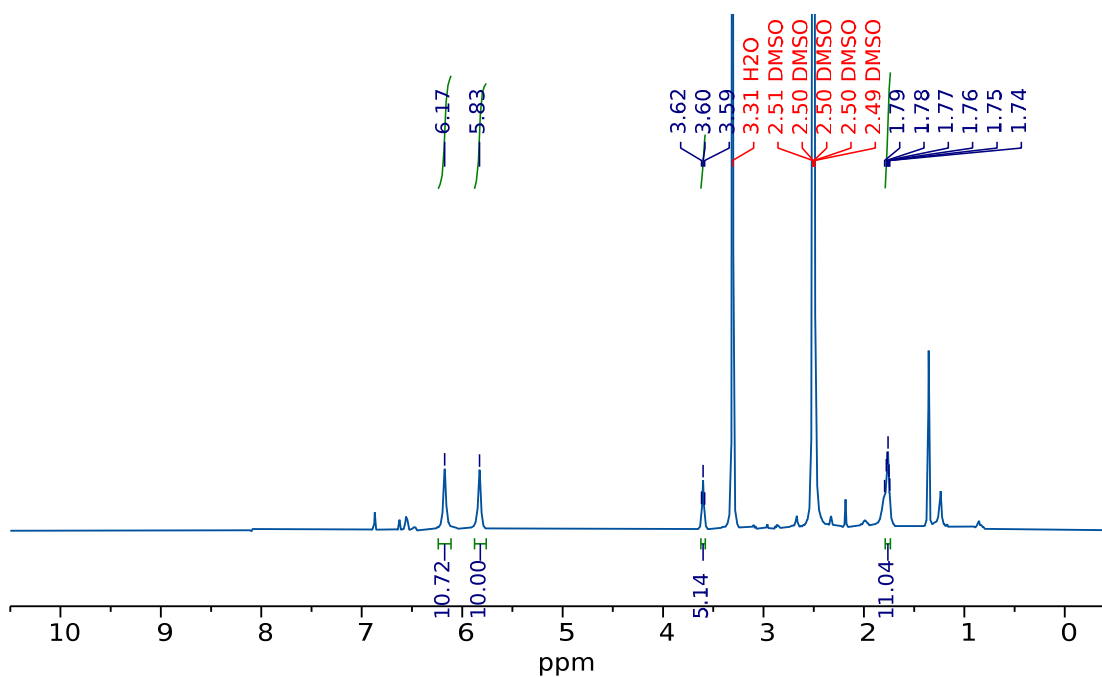
Figure 7.31. ¹H NMR spectrum of **dmdt₂Ad[TiCp₂]** (d₆-DMSO, 400 MHz).
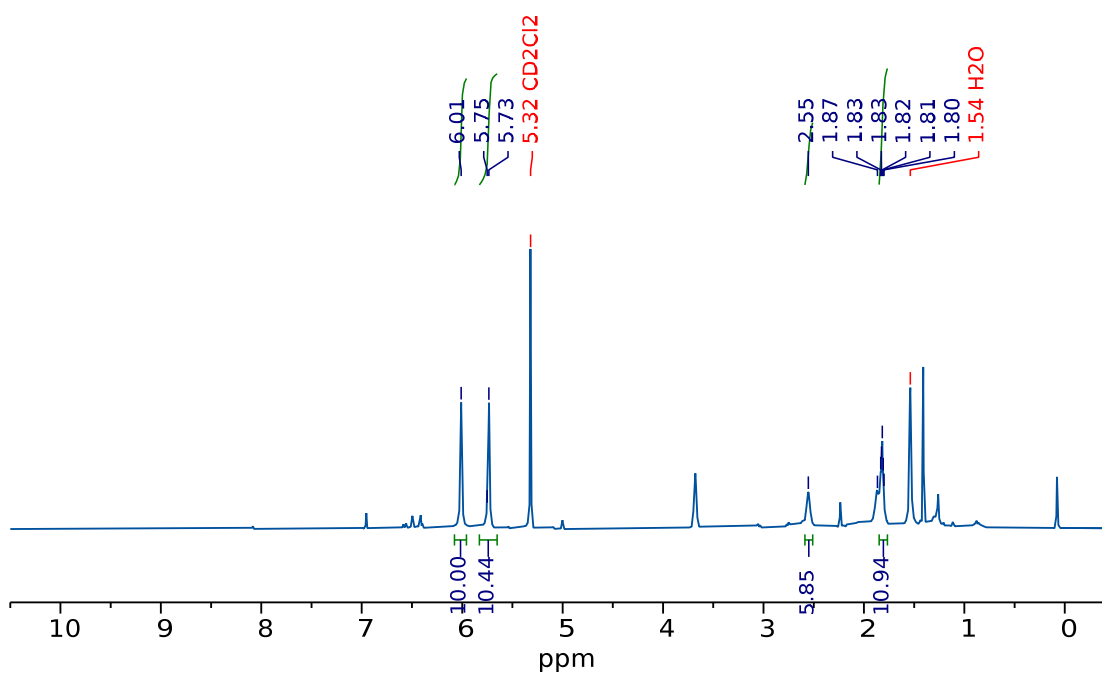
Figure 7.32. ¹H NMR spectrum of **dmdt₂Ad[TiCp₂]** (d₂-DCM, 400 MHz).

dmdt₂Anthra[TiCp₂]
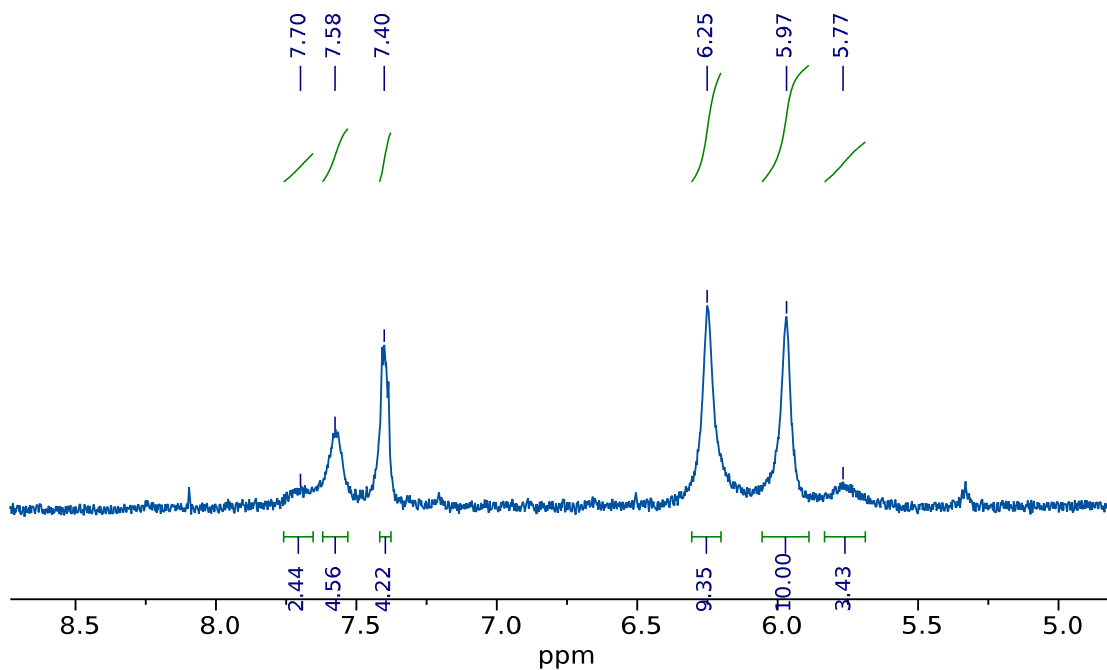
Figure 7.33.   ¹H NMR spectrum of **dmdt₂Anthra[TiCp₂]** (d₆-DMSO, 400 MHz).
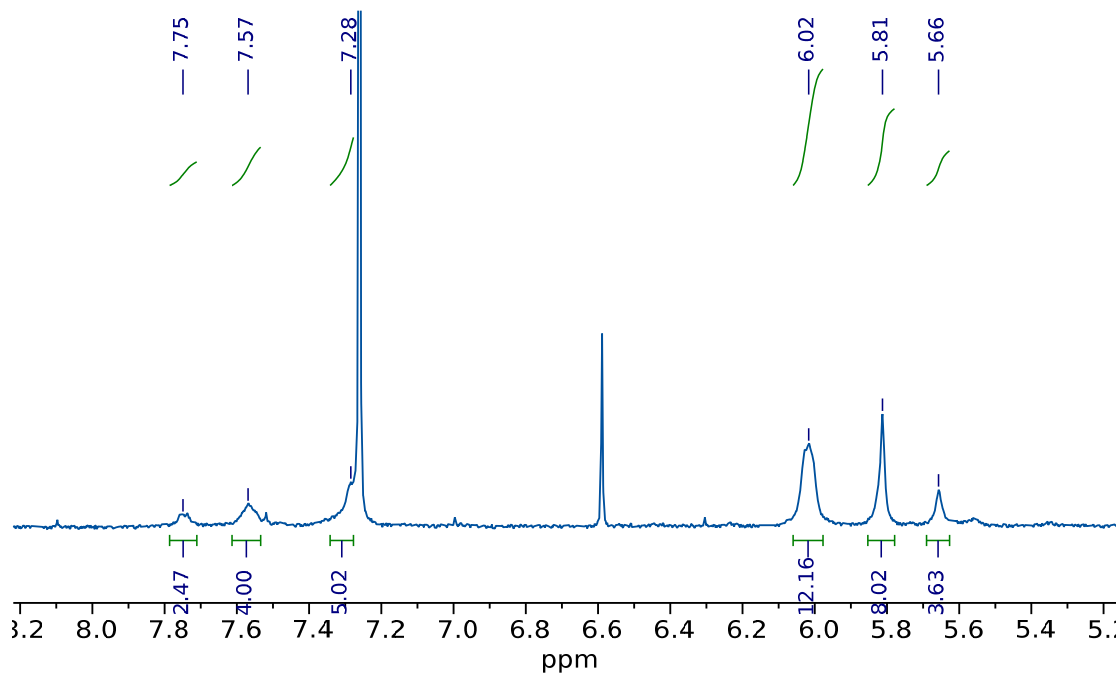
Figure 7.34.   ¹H NMR spectrum of **dmdt₂Anthra[TiCp₂]** (CDCl₃, 400 MHz).

dmdt₂Penta [TiCp₂]
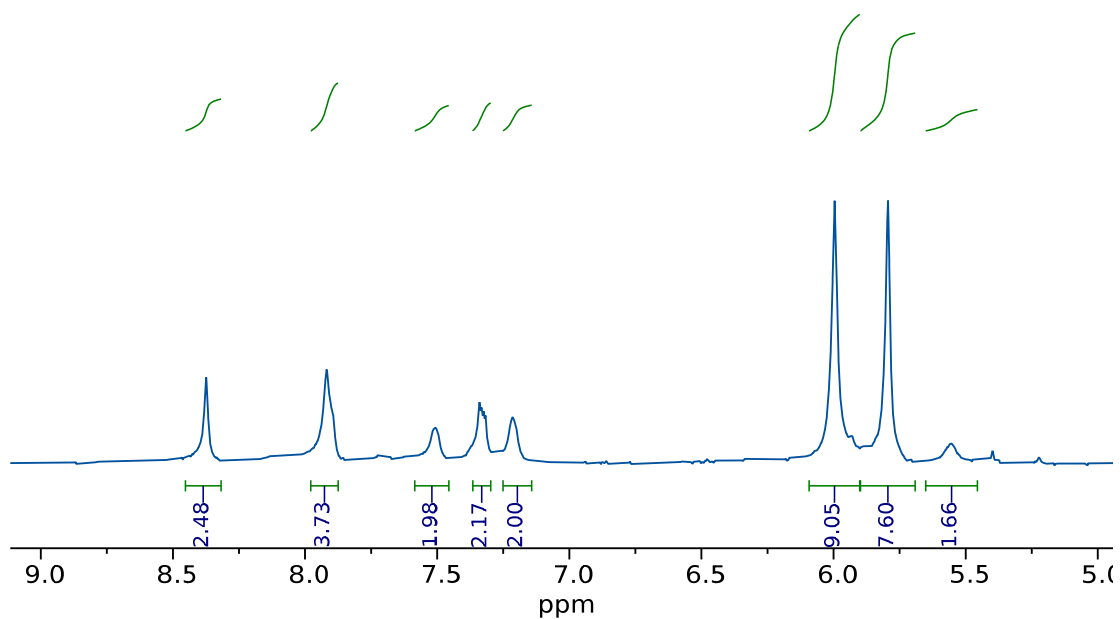
Figure 7.35.   ¹H NMR spectrum of **dmdt₂Penta[TiCp₂]** (d₈-THF, 400 MHz).
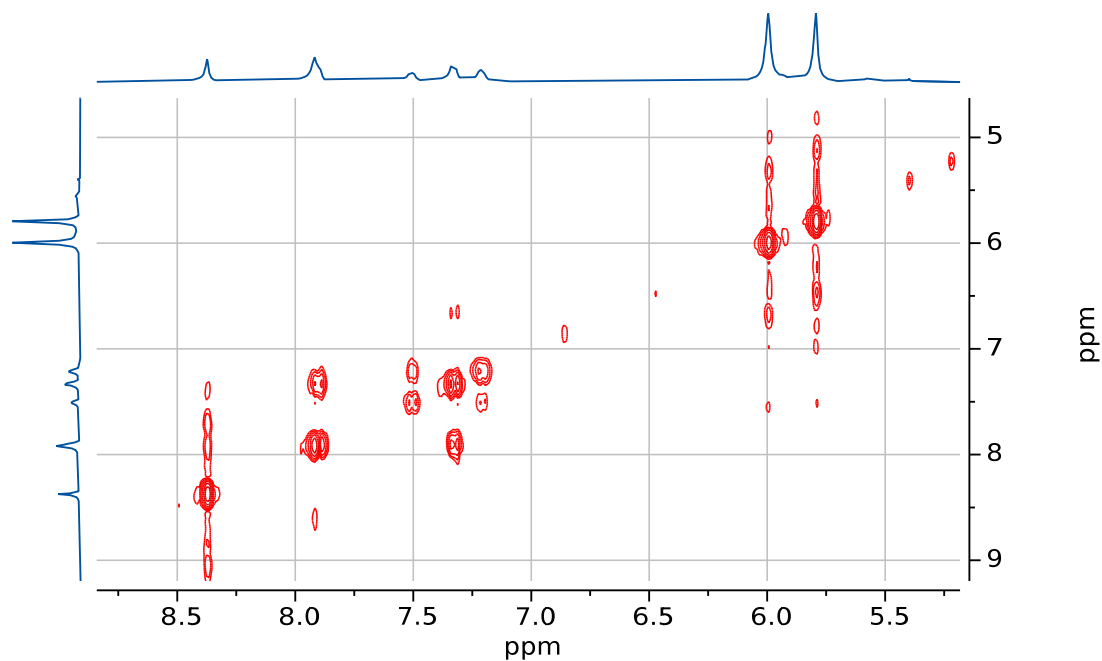
Figure 7.36.   ¹H-¹H-COSY spectrum of **dmdt₂Penta[TiCp₂]** (d₈-THF, 400 MHz).

dmdt₂Dtbpa [TiCp₂]
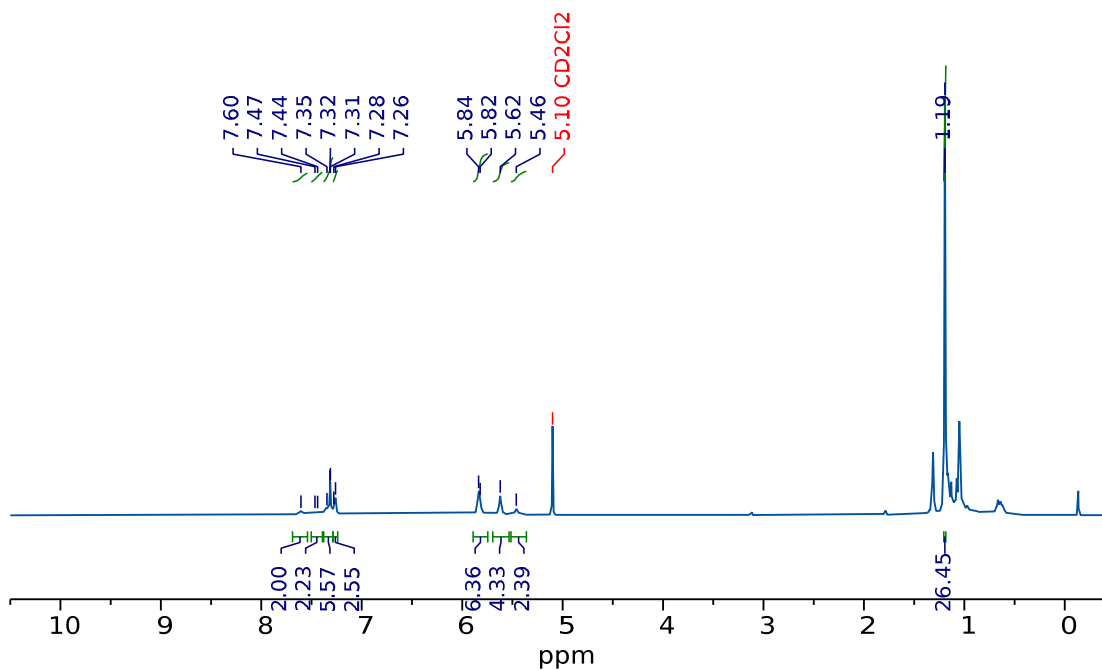
Figure 7.37.   ¹H NMR spectrum of **dmdt₂Dtbpa[TiCp₂]** (d₂-DCM, 400 MHz).

Non-Removable Residual Contamination in a Batch of Hexanes
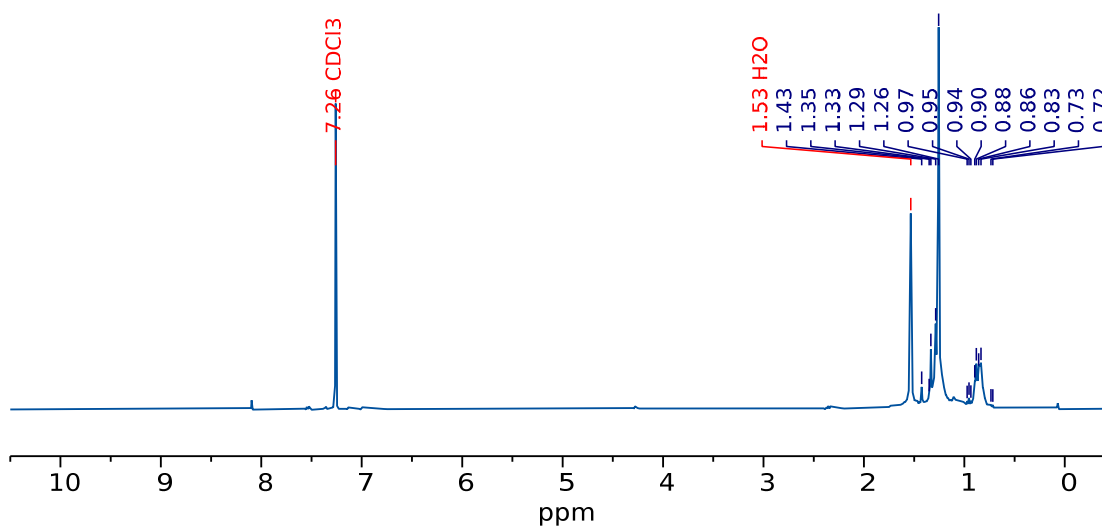
Figure 7.38.   ¹H NMR spectrum of the residues in a used batch of supposedly pure hexanes (CDCl₃, 400 MHz) which is present in several NMR spectra and could not be removed fully.

7.2. IR Analytics

dmdtSEt[EtCN]
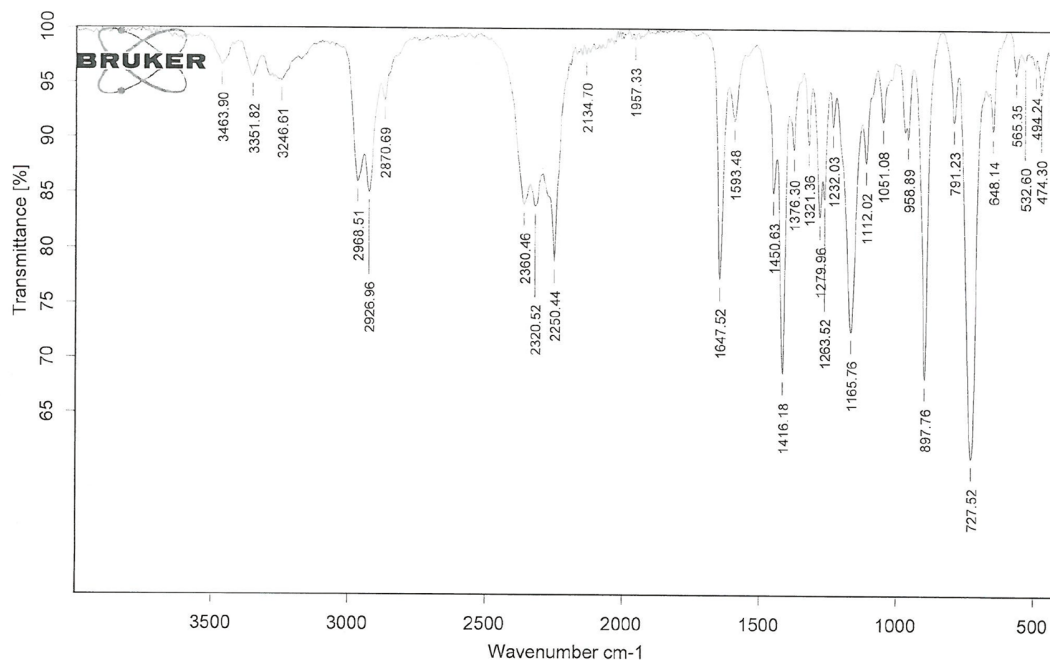
Figure 7.39. FT-IR spectrum of **dmdtSEt[EtCN]**.
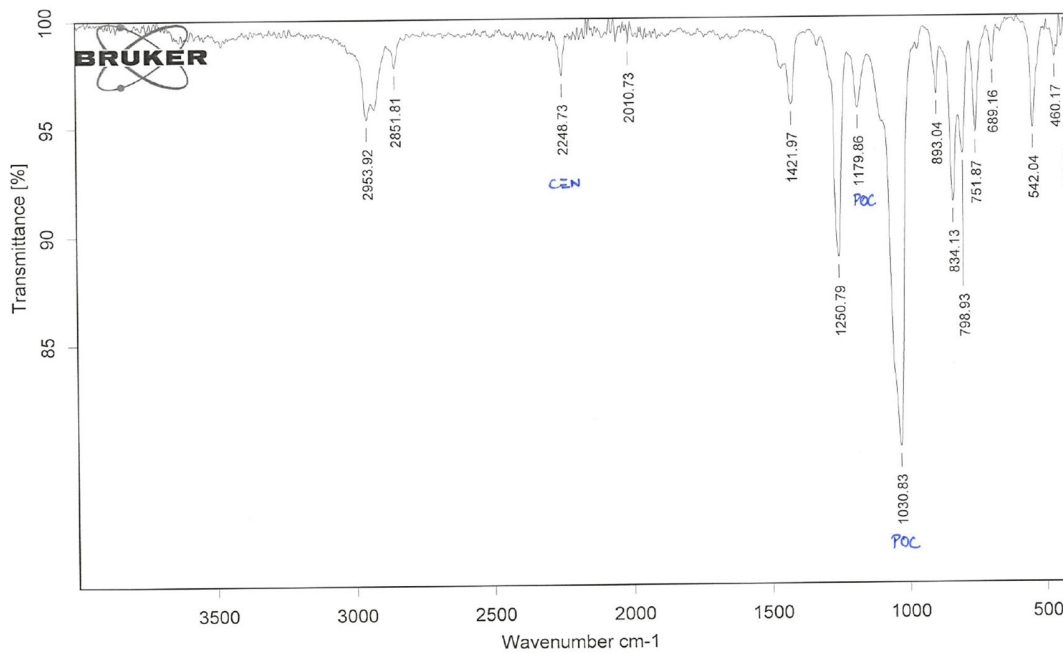
dmdtP[EtCN]

Figure 7.40. FT-IR spectrum of **dmdtP[EtCN]**.

2,6-Bis(m-di-tert-butylphenyl)anthraquinone
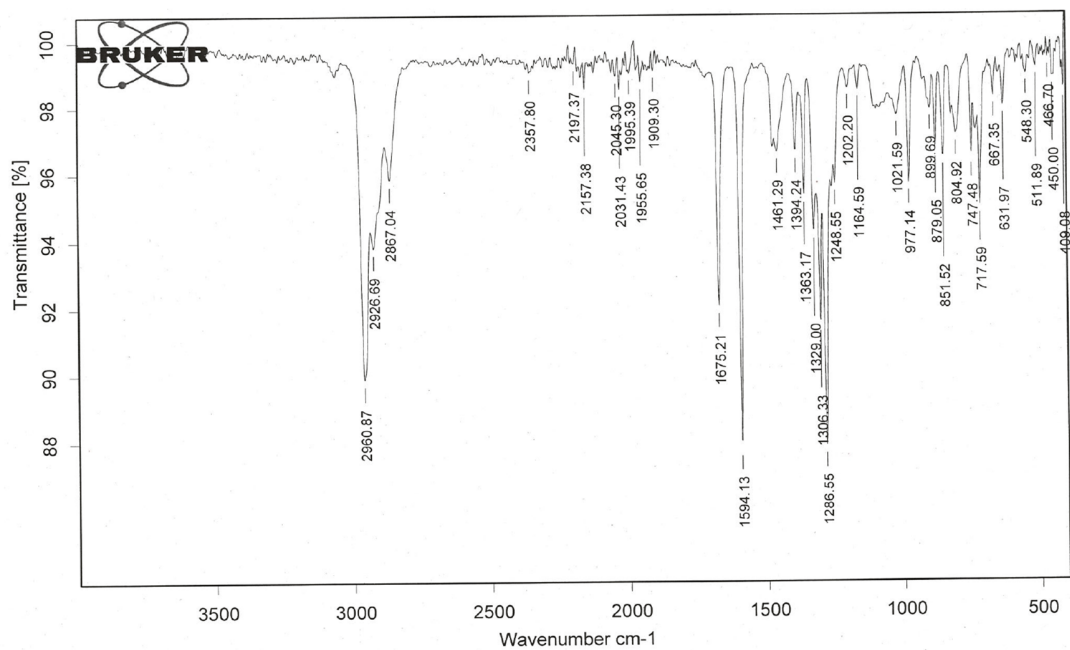
Figure 7.41. FT-IR spectrum of **2,6-bis(m-di-tert-butylphenyl)anthraquinone**.
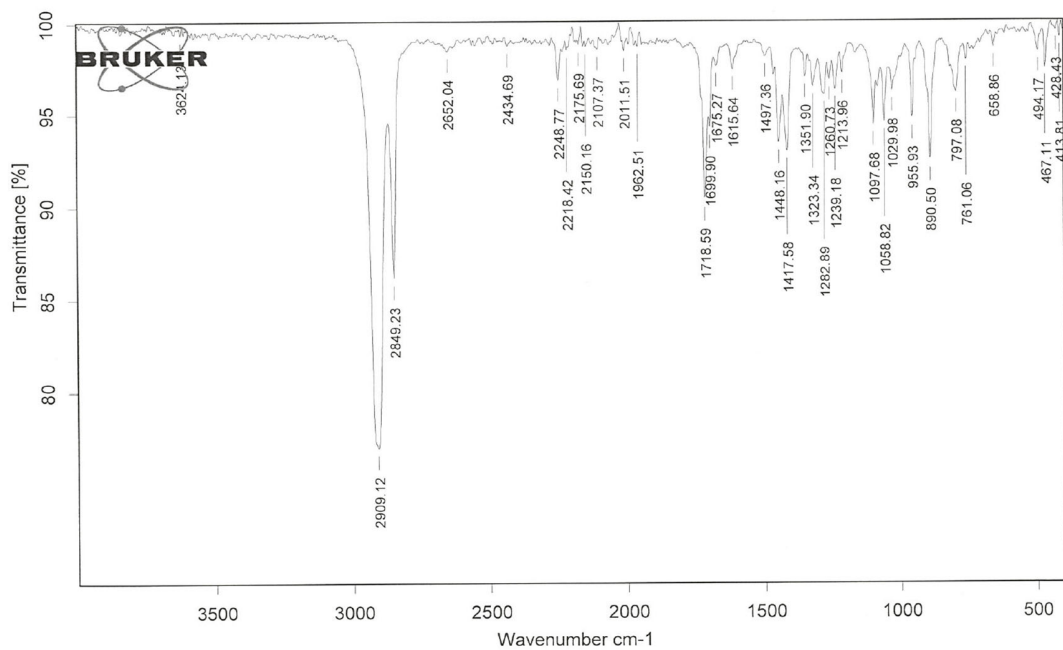
dmdtiPr[EtCN]

Figure 7.42. FT-IR spectrum of **dmdtAd[EtCN]**.
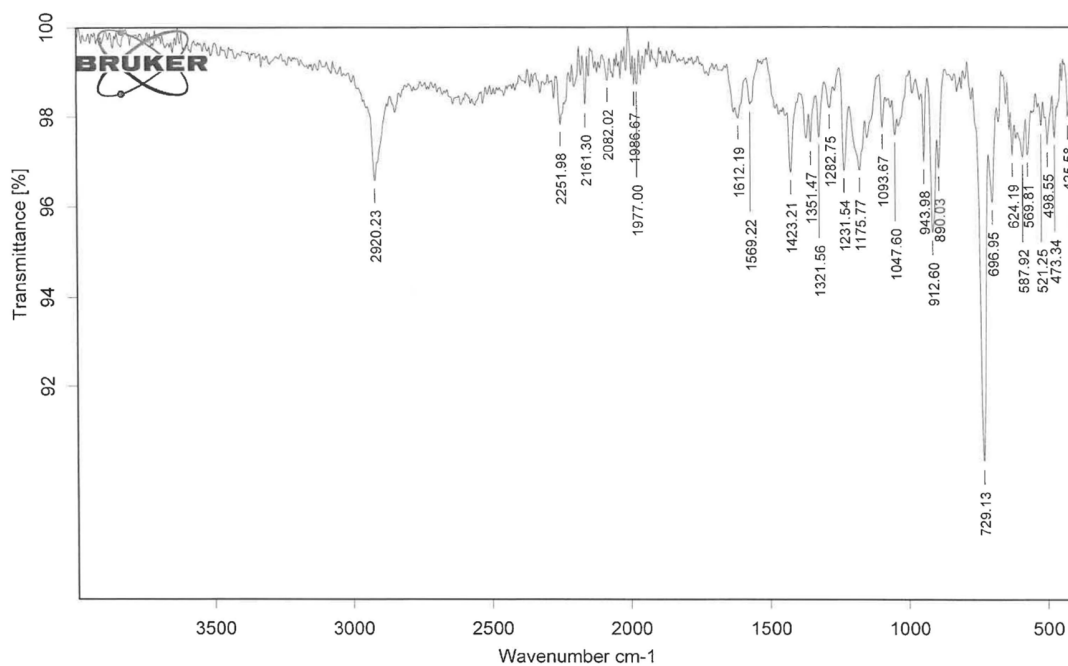
dmdt₂Ad[EtCN]

Figure 7.43. FT-IR spectrum of **dmdt₂Ad[EtCN]**.
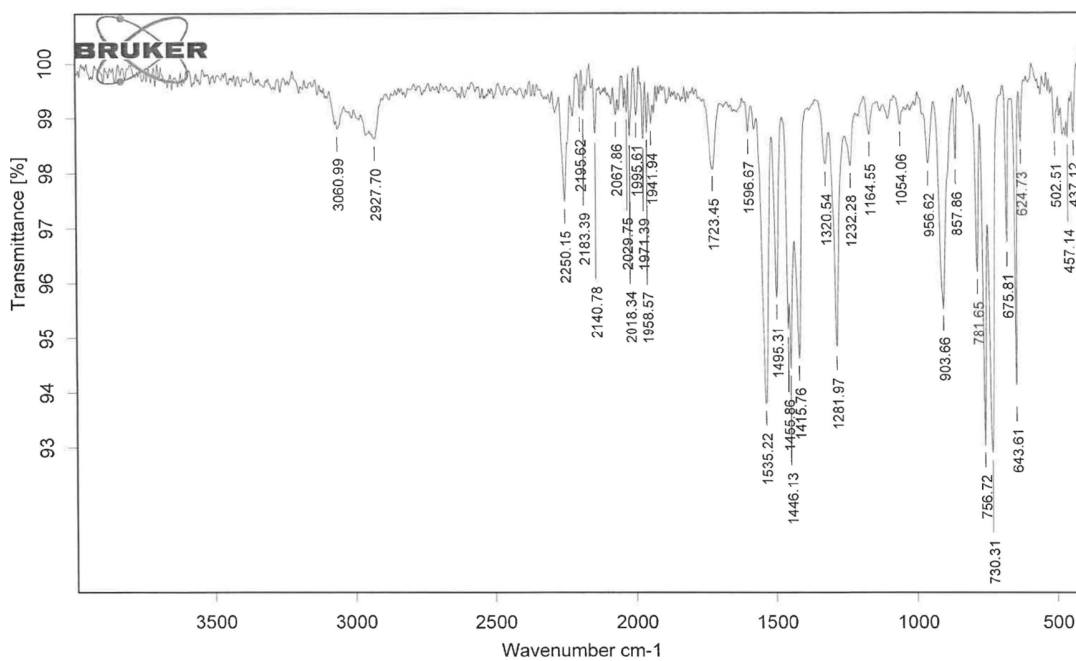
dmdt₂Anthra[EtCN]

Figure 7.44. FT-IR spectrum of **dmdt₂Anthra[EtCN]**.
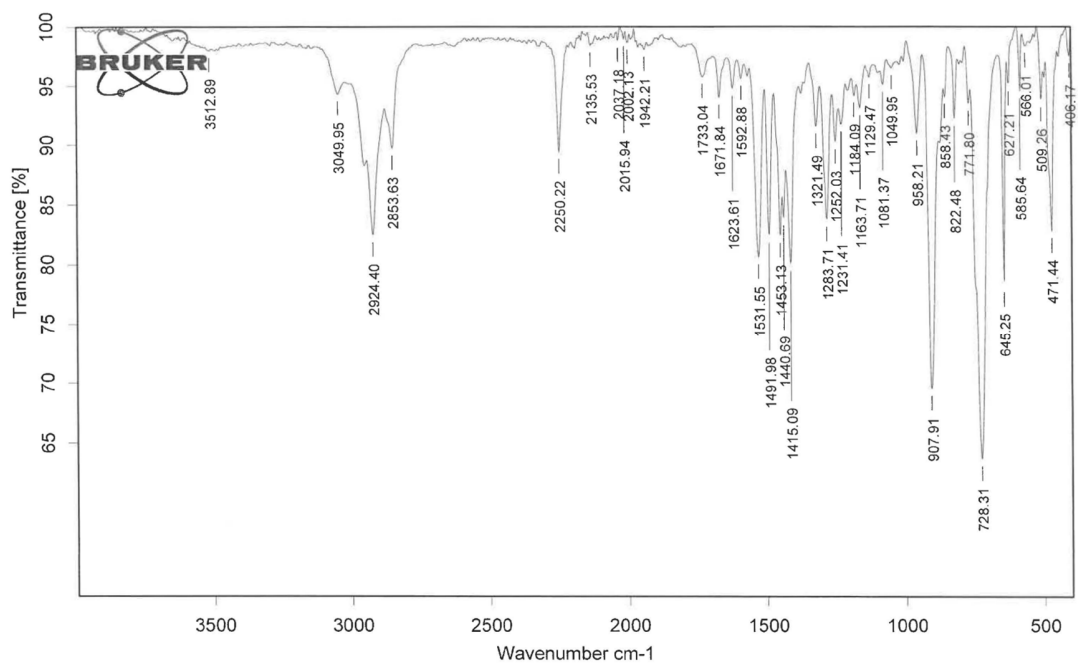
dmdt₂Penta[EtCN]

Figure 7.45.   FT-IR spectrum of **dmdt₂Penta[EtCN]**.

dmdt₂Dtbpa[EtCN]
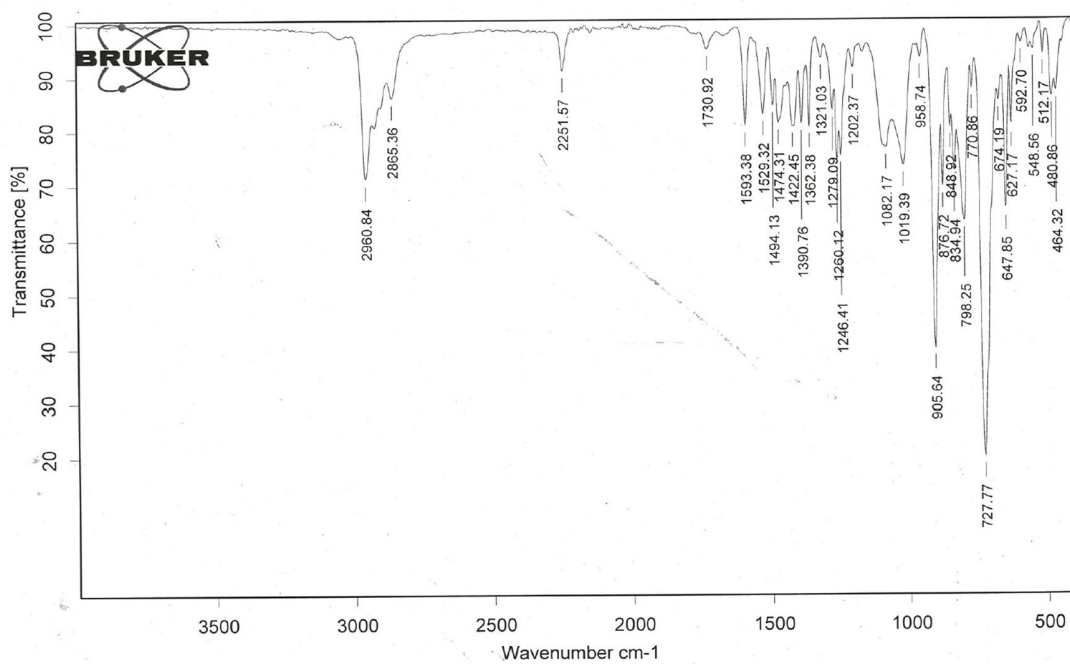
Figure 7.46.   FT-IR spectrum of **dmdt₂Dtpba[EtCN]**.

dmdt₂Ad[TiCp₂]
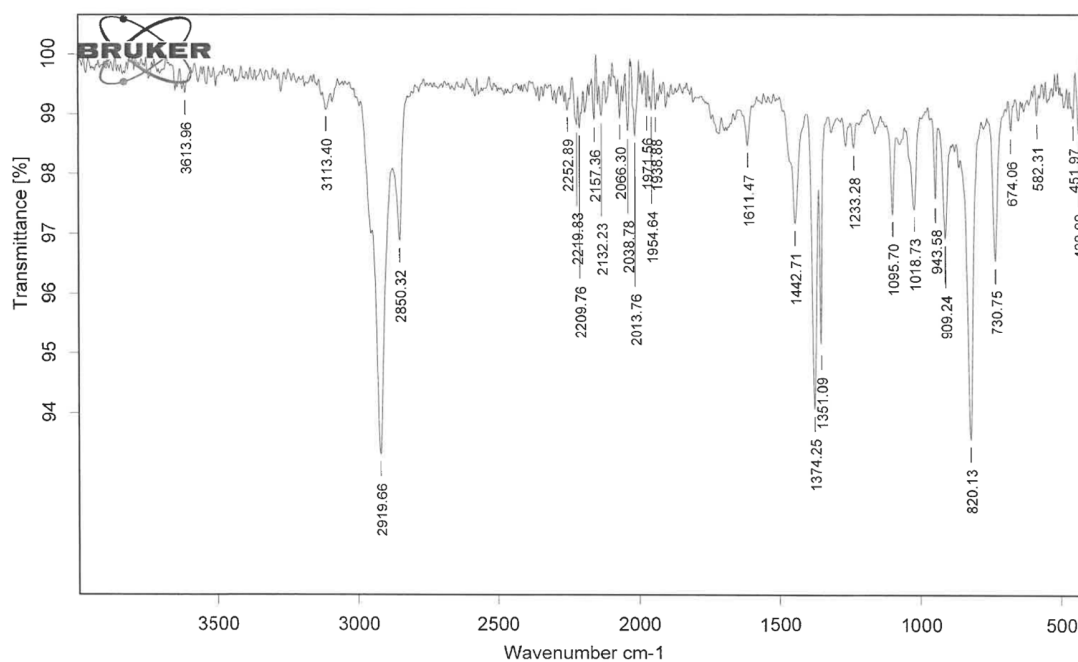
Figure 7.47.   FT-IR spectrum of **dmdt₂Ad[TiCp₂]₂**.
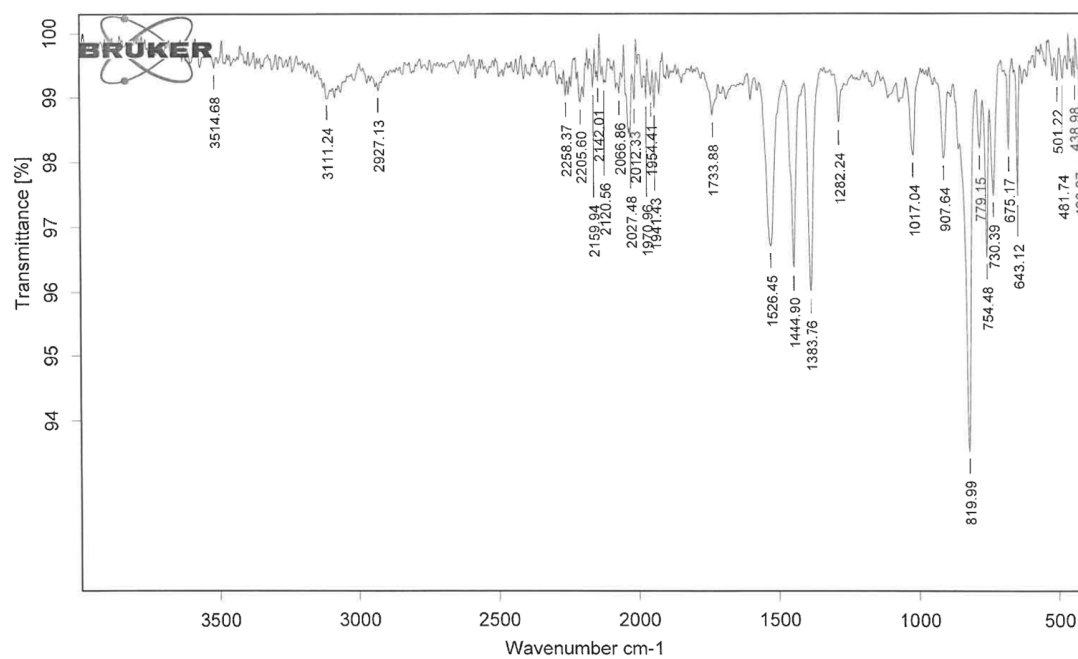
dmdt₂Anthra[TiCp₂]

Figure 7.48.   FT-IR spectrum of **dmdt₂Anthra[TiCp₂]₂**.
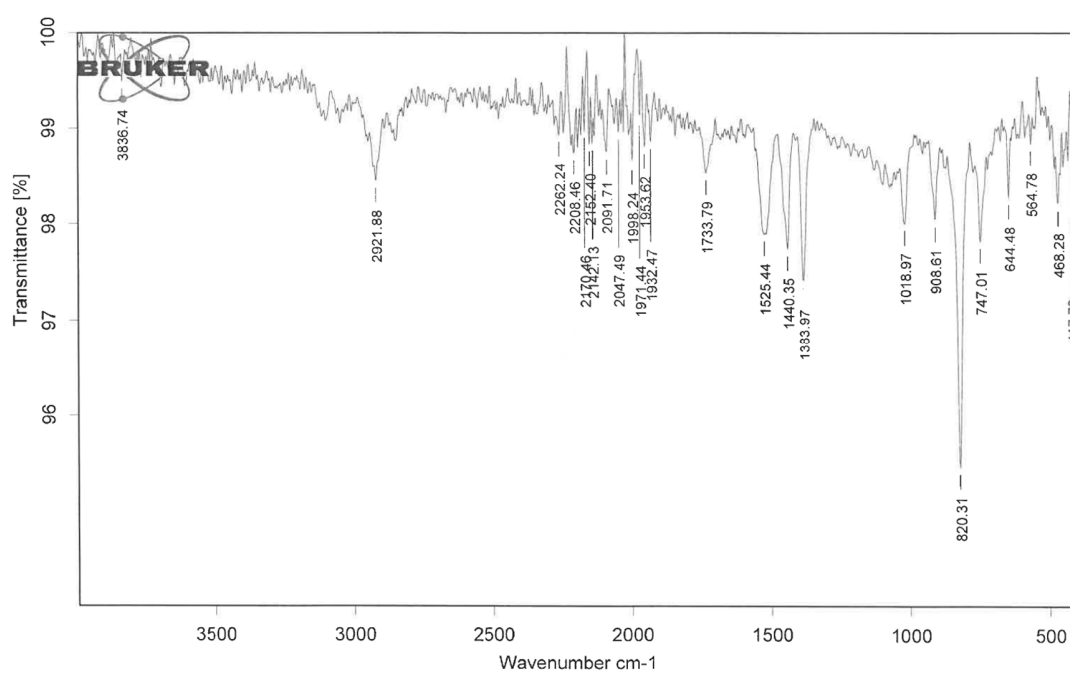
dmdt₂Penta [TiCp₂]

Figure 7.49.   FT-IR spectrum of **dmdt₂Penta[TiCp₂]₂**.

7.3. Mass Analytics

(dmdtSMe[EtCN])BF₄

Acquisition Parameter

Source Type	ESI	Ion Polarity	Positive	Set Nebulizer	1.3 Bar
Focus	Not active	Set Capillary	4500 V	Set Dry Heater	210 °C
Scan Begin	50 m/z	Set End Plate Offset	-500 V	Set Dry Gas	7.5 l/min
Scan End	1000 m/z	Set Collision Cell RF	180.0 Vpp	Set Divert Valve	Waste
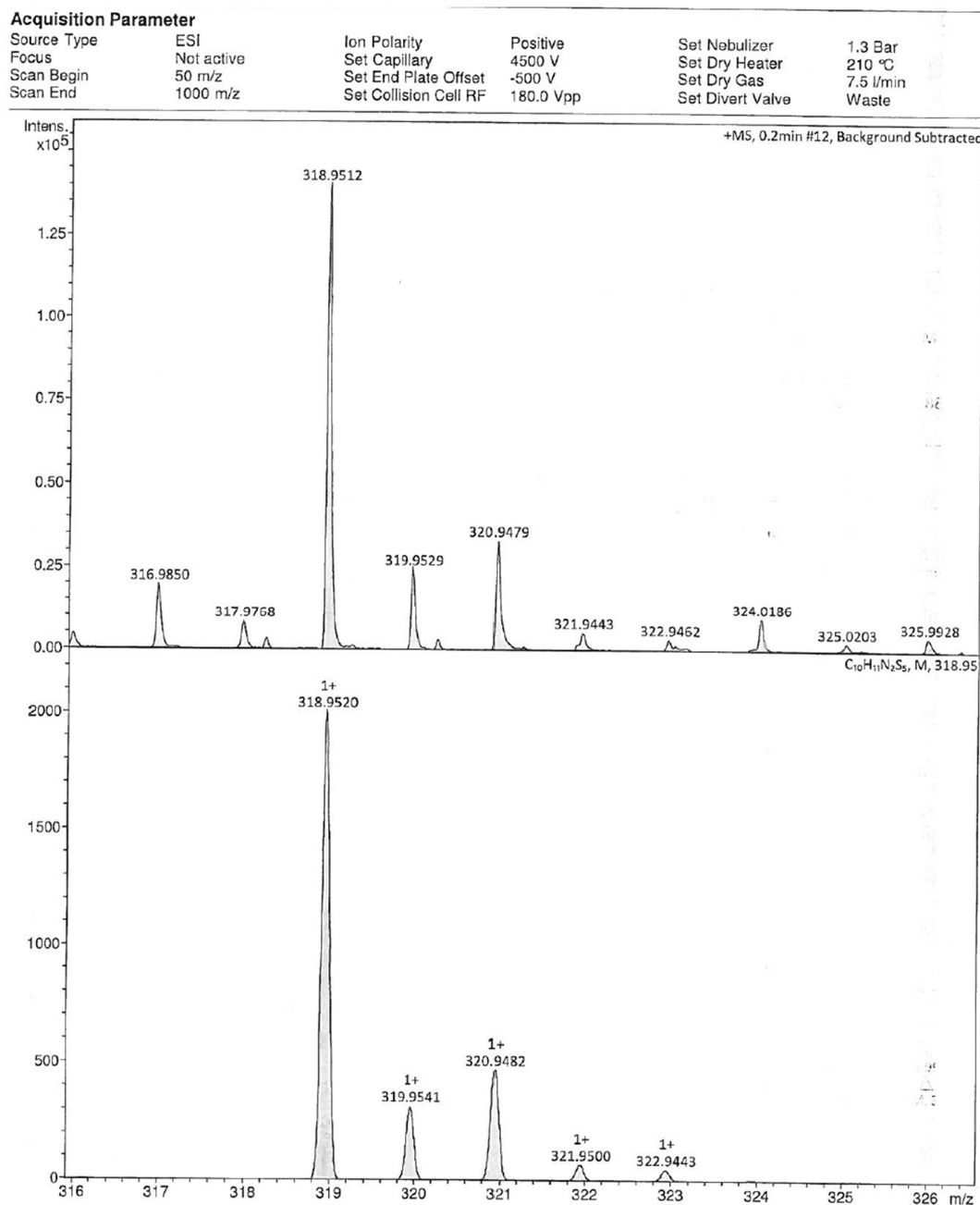
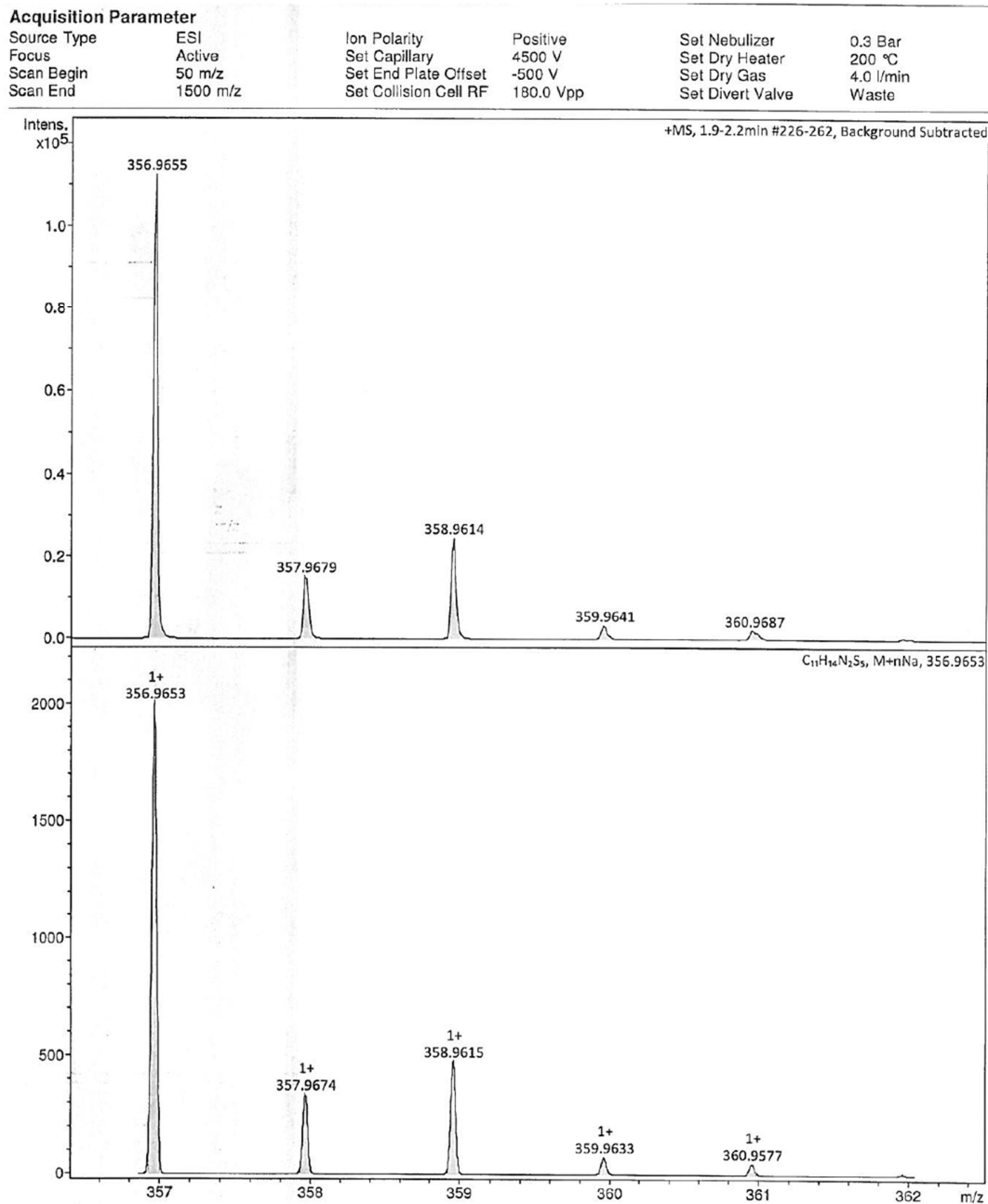**Figure 7.50.**   ESI(+)-HRMS spectrum of **(dmdtSMe[EtCN])BF₄**.
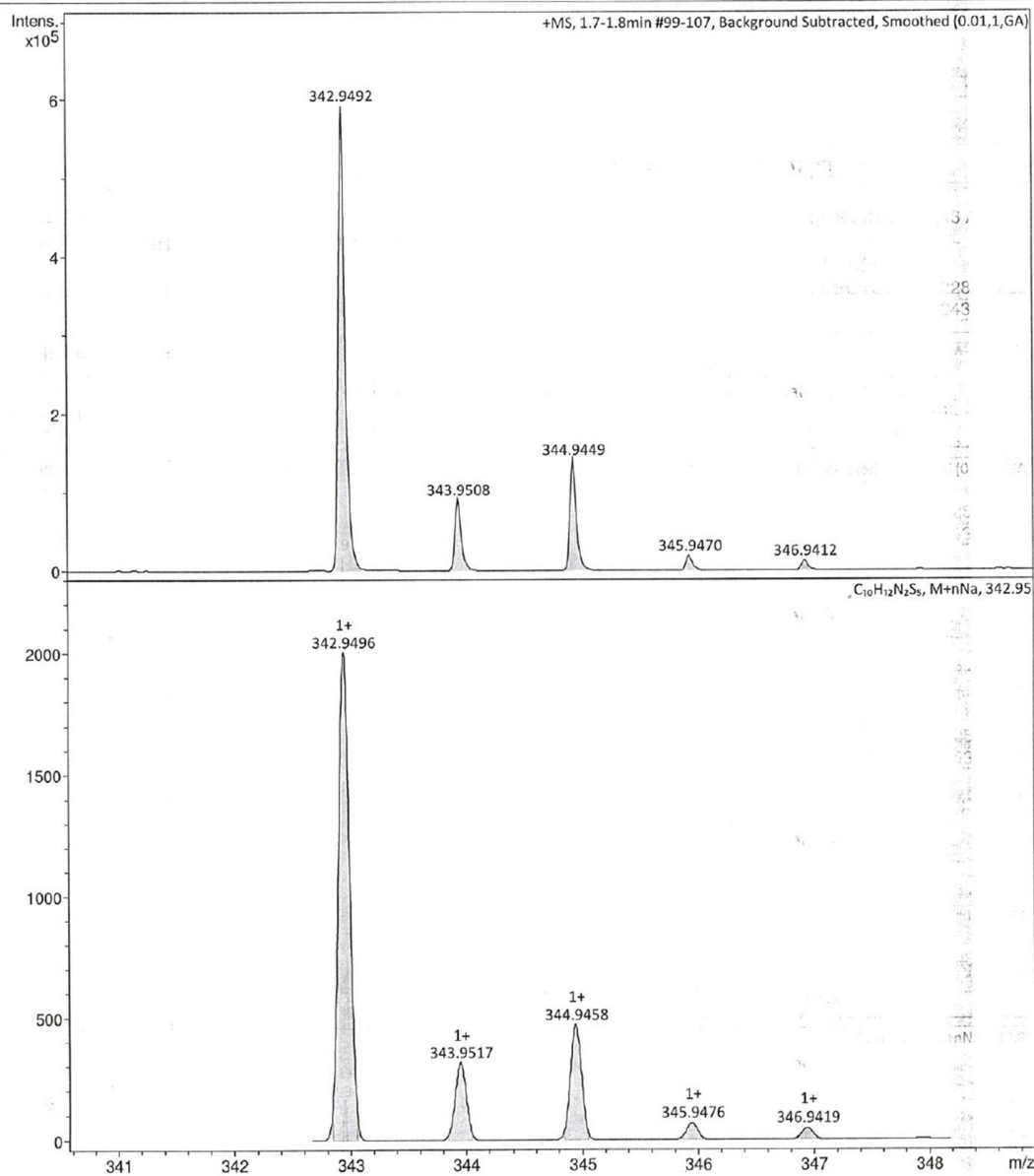
dmdtSMe[EtCN]

Figure 7.51.   ESI(+)-HRMS spectrum of **dmdtSMe[EtCN]**.

dmdtSEt[EtCN]

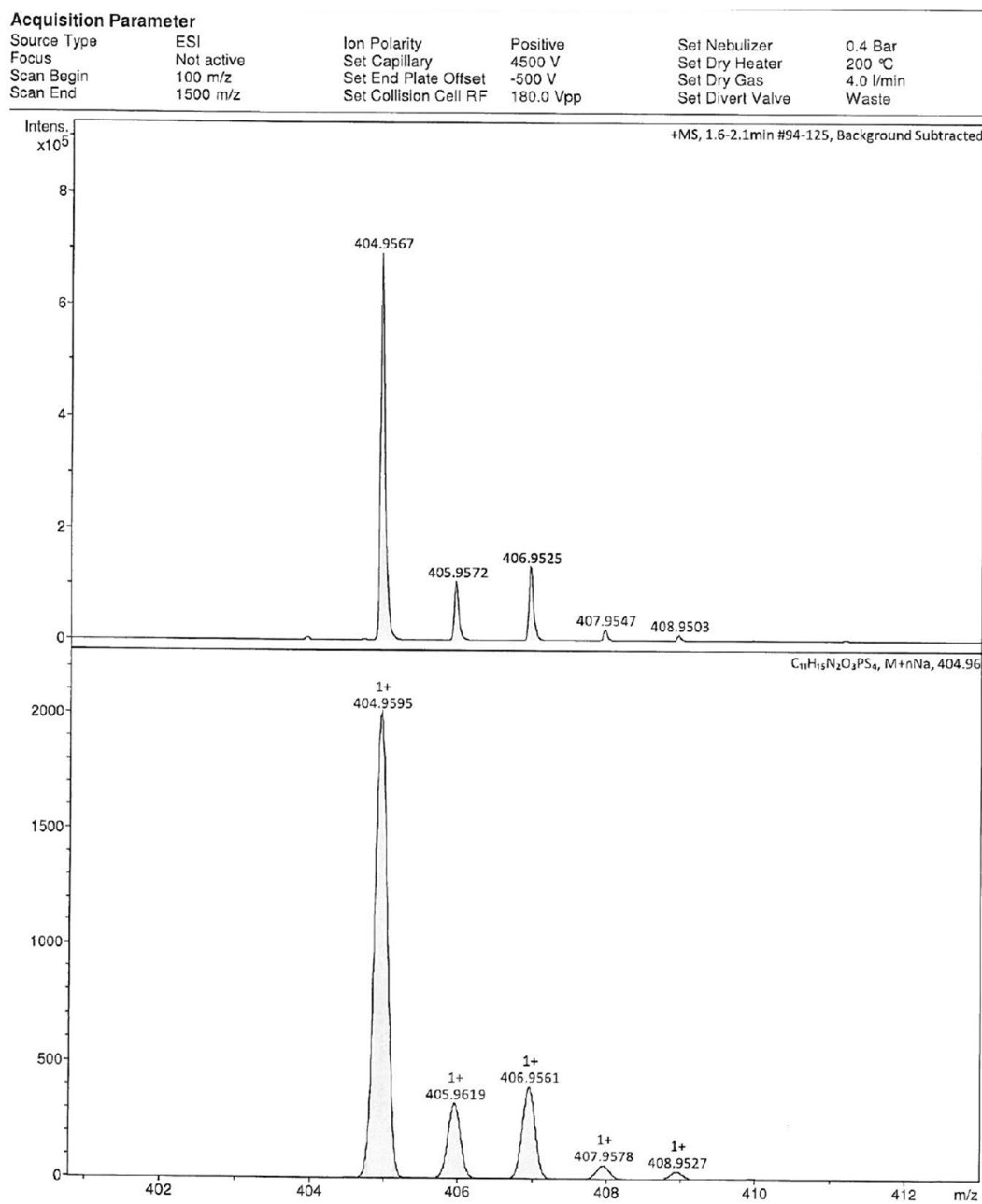**Figure 7.52.** ESI(+)-HRMS spectrum of **dmdtSEt[EtCN]**.

dmdtP[EtCN]

Acquisition Parameter

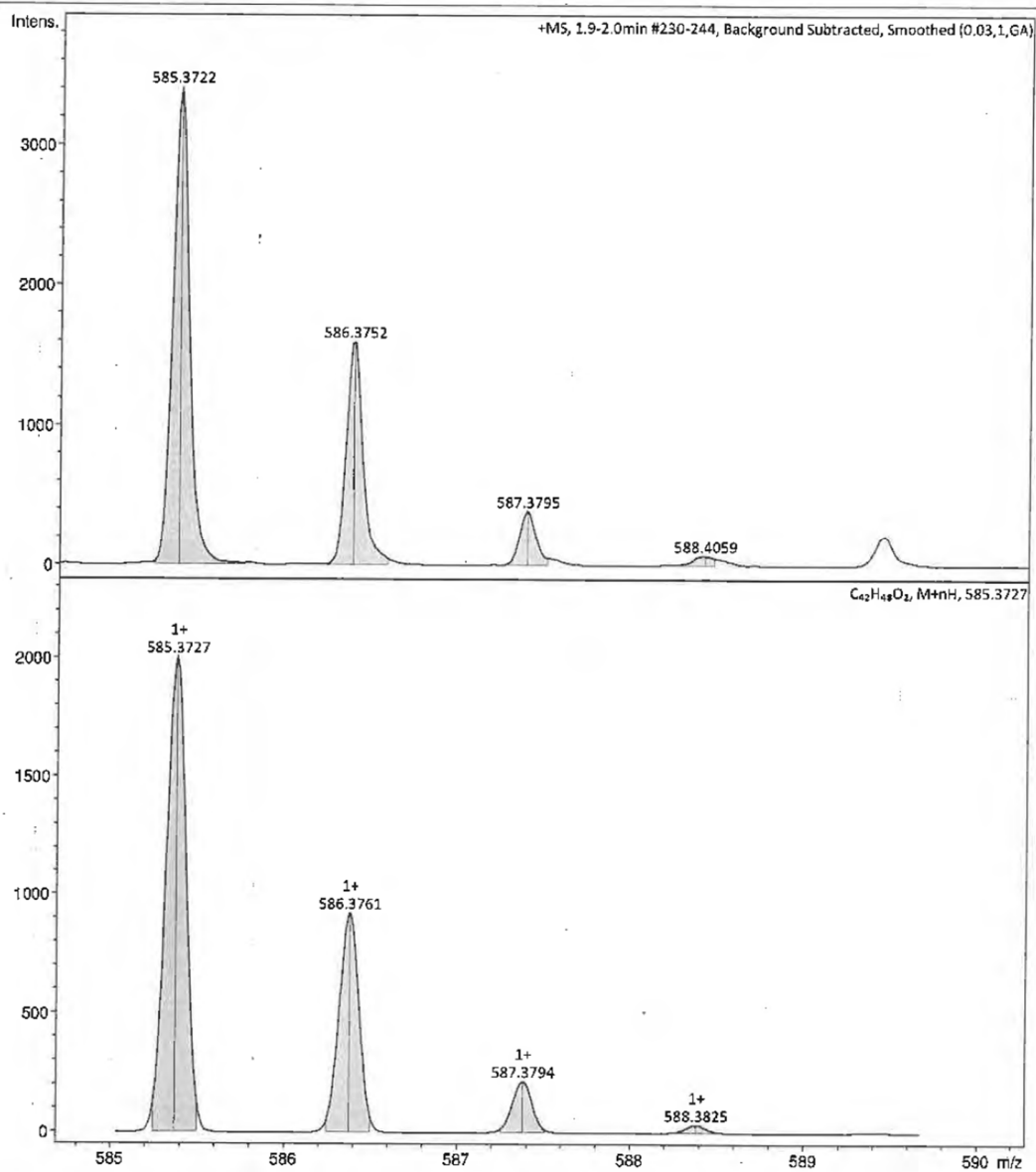|					
Source Type	ESI	Ion Polarity	Positive	Set Nebulizer	0.4 Bar
Focus	Not active	Set Capillary	4500 V	Set Dry Heater	200 °C
Scan Begin	100 m/z	Set End Plate Offset	-500 V	Set Dry Gas	4.0 l/min
Scan End	1500 m/z	Set Collision Cell RF	180.0 Vpp	Set Divert Valve	Waste

+MS, 1.6-2.1min #94-125, Background Subtracted

404.9567
405.9572
406.9525
407.9547
408.9503

$C_{11}H_{15}N_2O_3PS_4$, M+nNa, 404.96

1+ 404.9595
1+ 405.9619
1+ 406.9561
1+ 407.9578
1+ 408.9527

Figure 7.53. ESI(+)-HRMS spectrum of **dmdtP[EtCN]**.

2,6-Bis(m-di-tert-butylphenyl)anthraquinone

Figure 7.54. ESI(+)-HRMS spectrum of **2,6-bis(m-di-tert-butylphenyl)anthraquinone**.
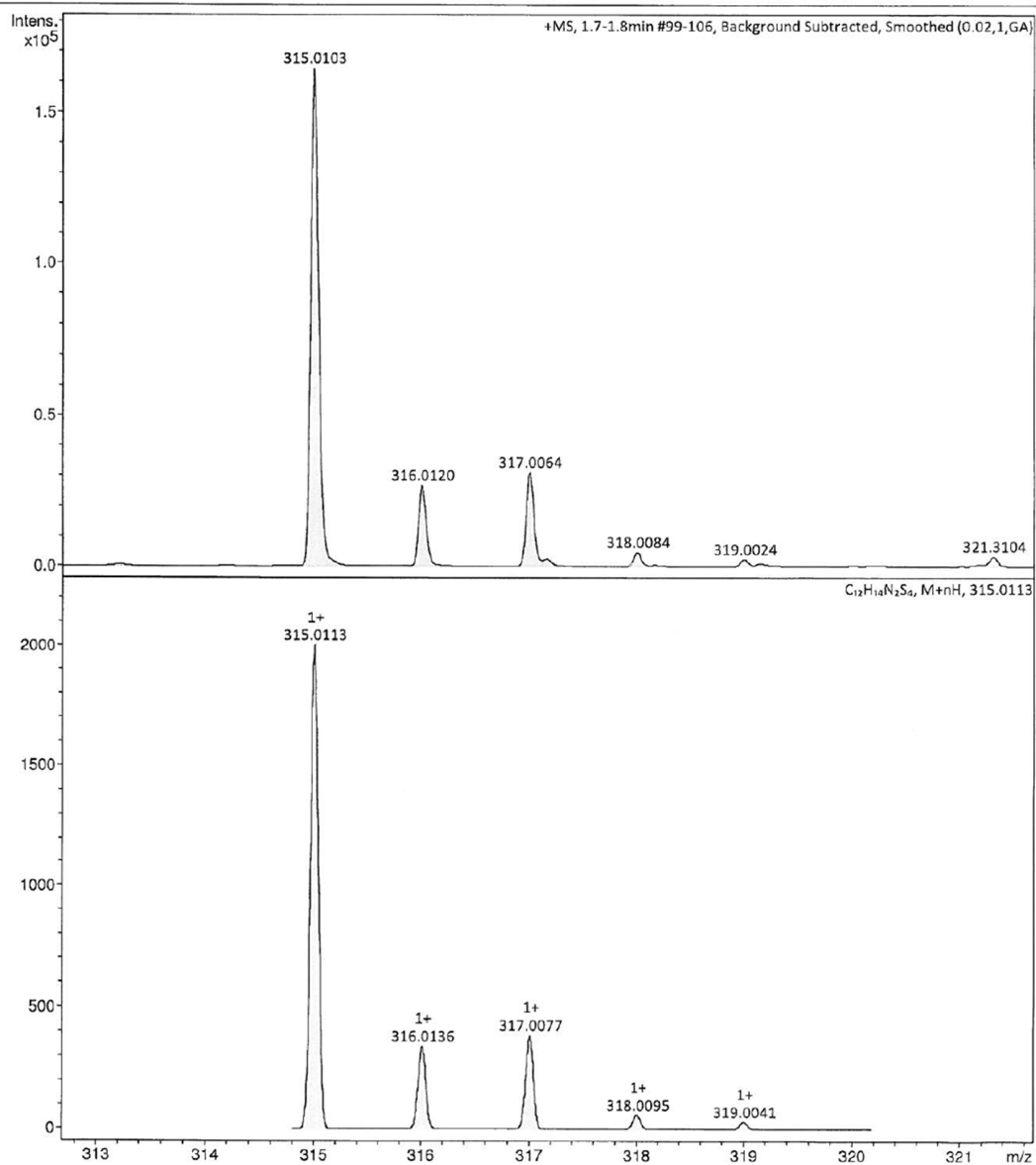
dmdtiPr[EtCN]

Figure 7.55.   ESI(+)-HRMS spectrum of **dmdtiPr[EtCN]**.

dmdtAd[EtCN]

Figure 7.56. ESI(+)-HRMS spectrum of **dmdtAd[EtCN]**.

dmdt$_2$Ad[EtCN]

Figure 7.57.   ESI(+)-HRMS spectrum of **dmdt$_2$Ad[EtCN]**.

dmdt₂Anthra[EtCN]

Figure 7.58. ESI(+)-HRMS spectrum of **dmdt₂Anthra[EtCN]**.

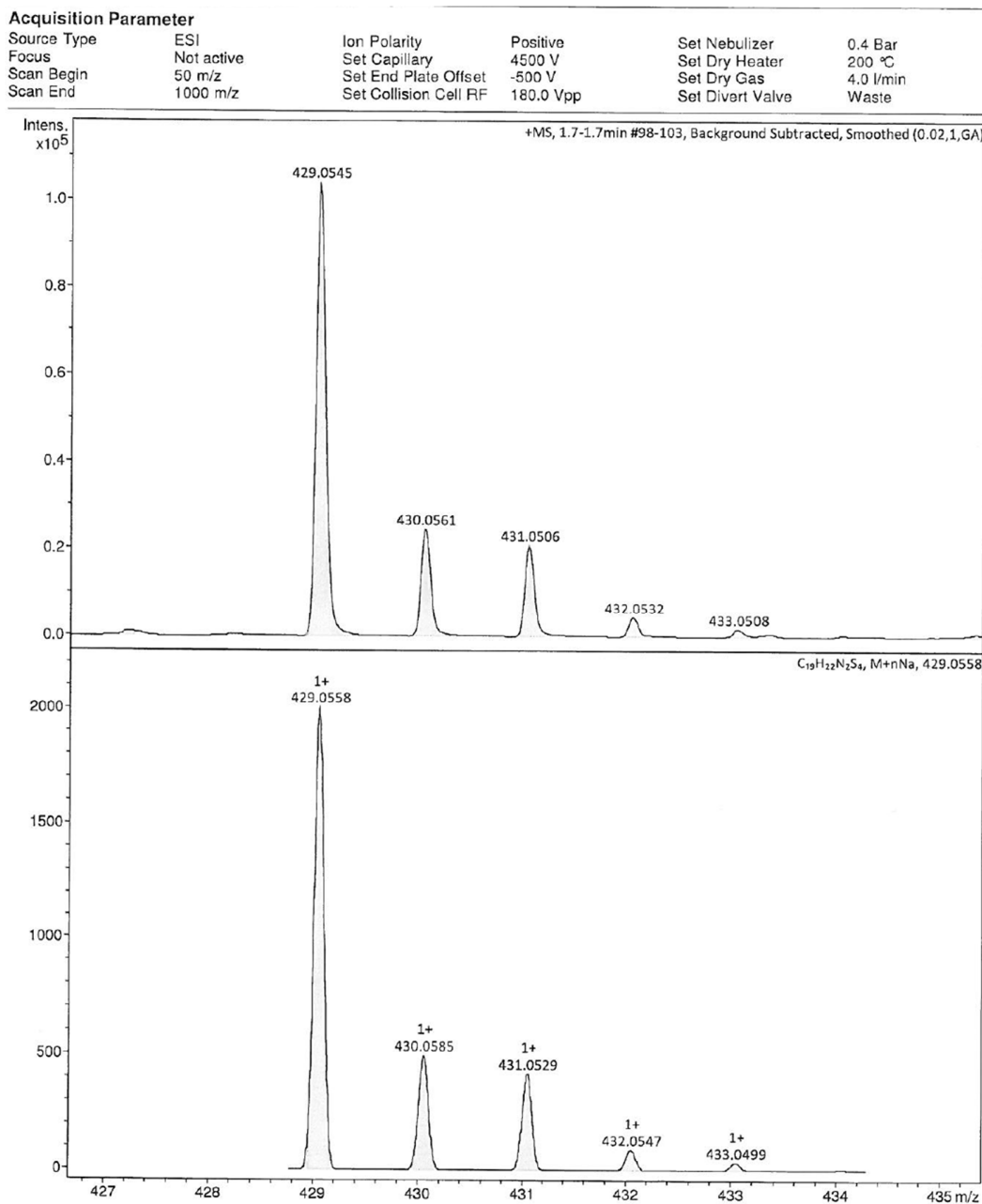**dmdt₂Penta[EtCN]**

Figure 7.59.   ESI(+)-HRMS spectrum of **dmdt₂Penta[EtCN]**.

dmdtAd[TiCp₂]

Acquisition Parameter
Source Type   ESI   Ion Polarity   Positive   Set Nebulizer   0.4 Bar
Focus   Not active   Set Capillary   4500 V   Set Dry Heater   200 °C
Scan Begin   50 m/z   Set End Plate Offset -500 V   Set Dry Gas   4.0 l/min
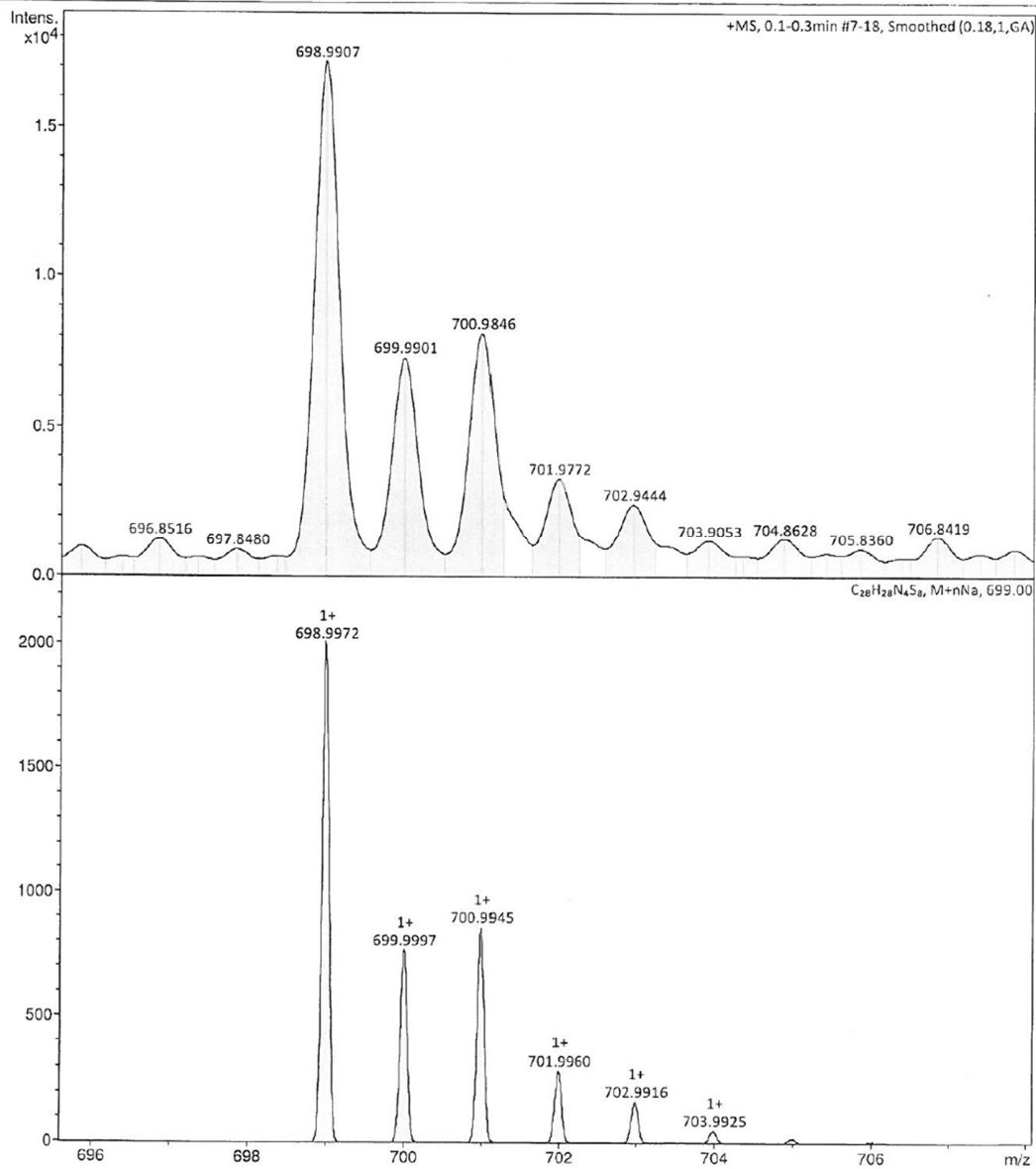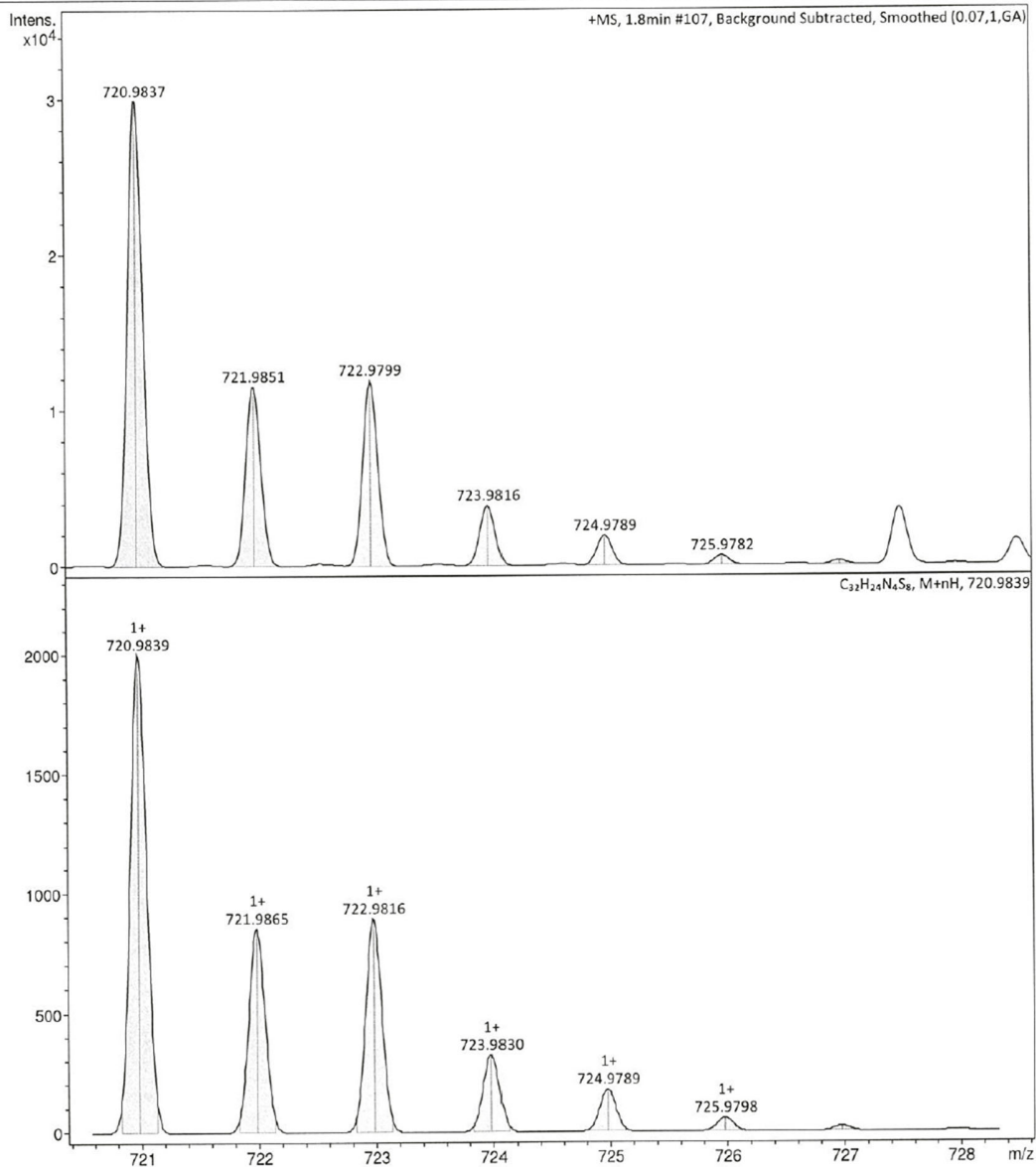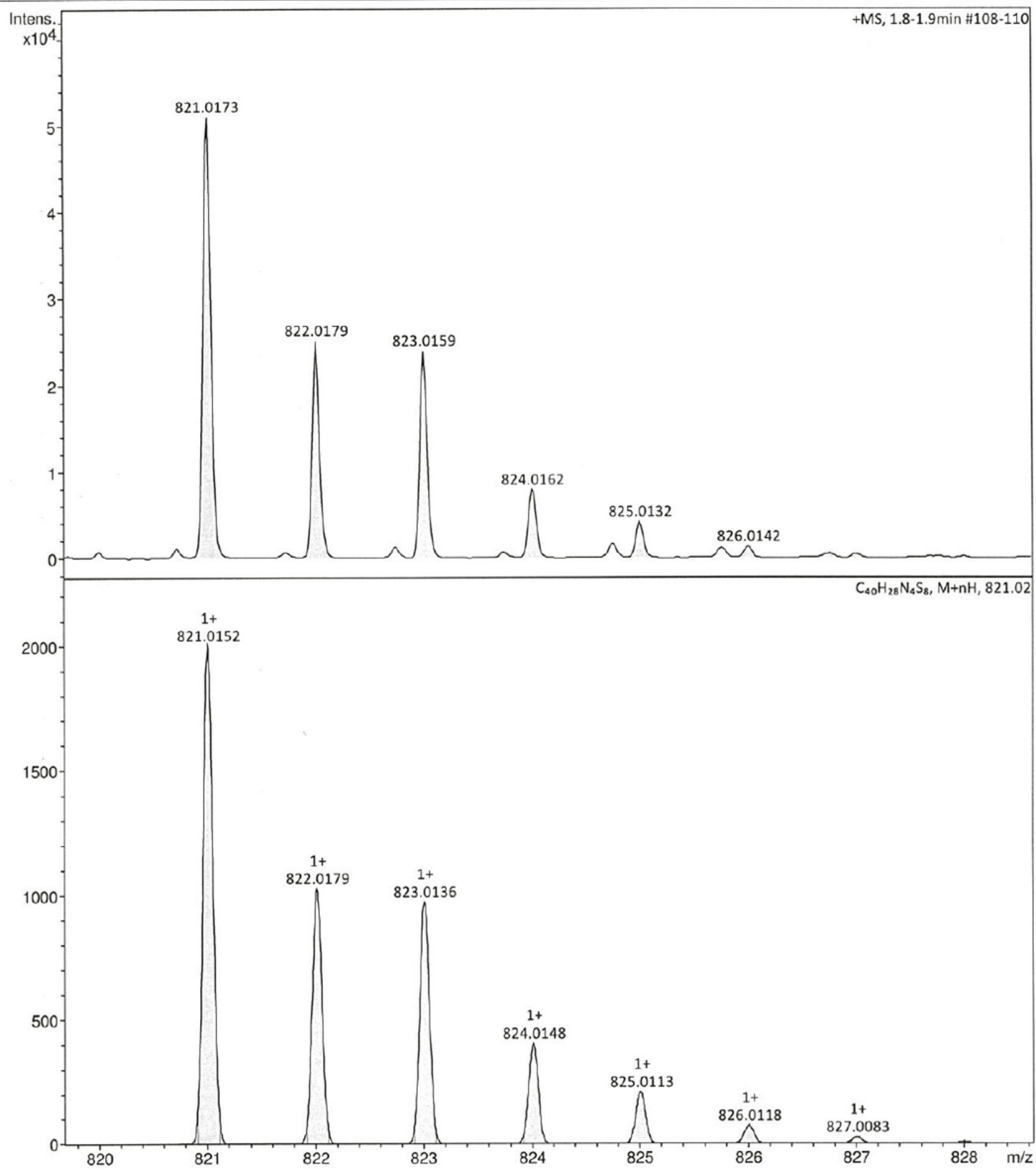Scan End   1500 m/z   Set Collision Cell RF 180.0 Vpp   Set Divert Valve   Waste
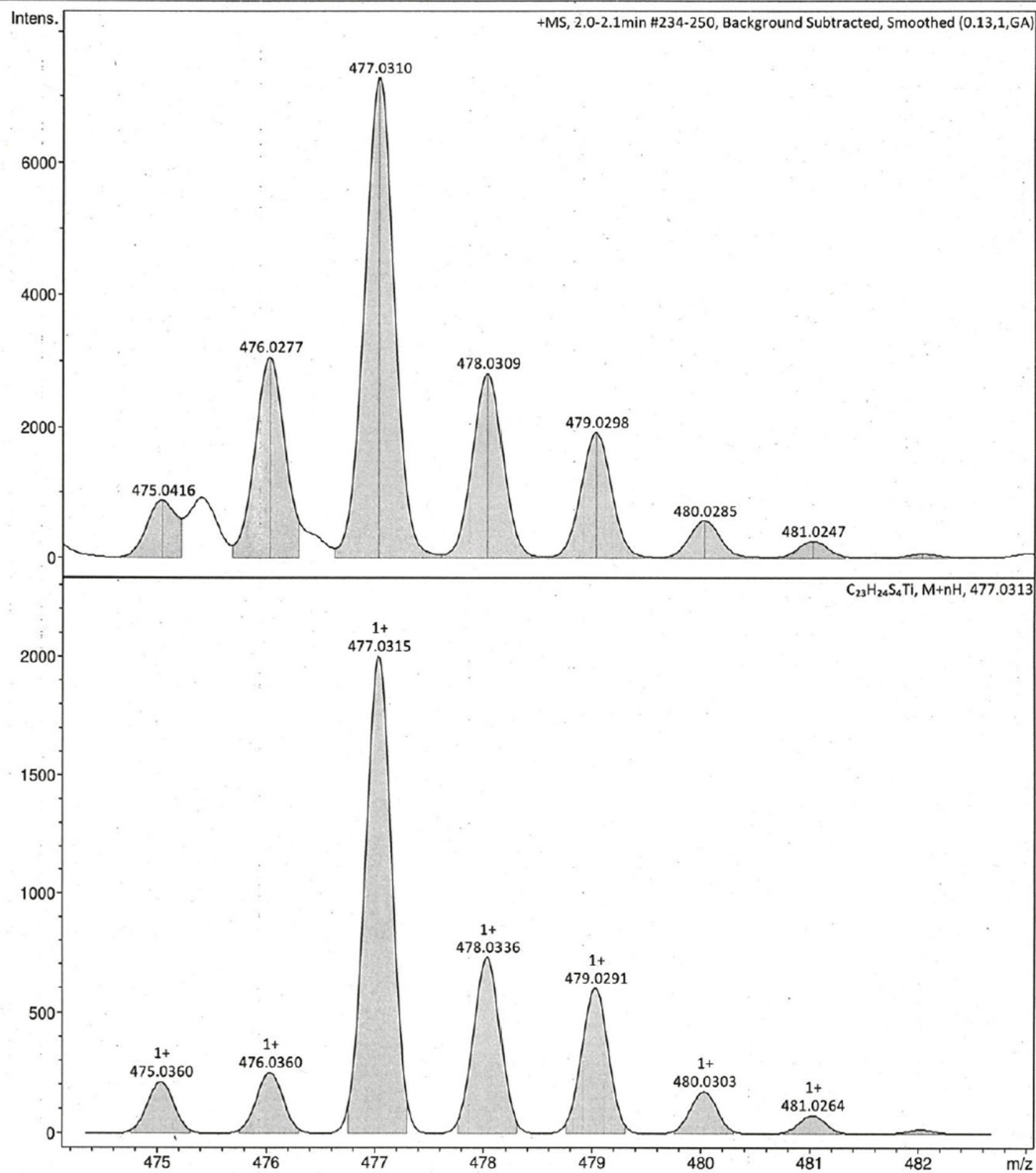
Figure 7.60. ESI(+)-HRMS spectrum of **dmdtAd[TiCp₂]₂**.

dmdt₂Ad[TiCp₂]

Figure 7.61.   ESI(+)-HRMS spectrum of **dmdt₂Ad[TiCp₂]₂**.

dmdt₂Anthra[TiCp₂]

Acquisition Parameter

Source Type	ESI	Ion Polarity	Positive	Set Nebulizer	0.4 Bar
Focus	Not active	Set Capillary	4500 V	Set Dry Heater	200 °C
Scan Begin	250 m/z	Set End Plate Offset	-500 V	Set Dry Gas	4.0 l/min
Scan End	3000 m/z	Set Collision Cell RF	500.0 Vpp	Set Divert Valve	Waste
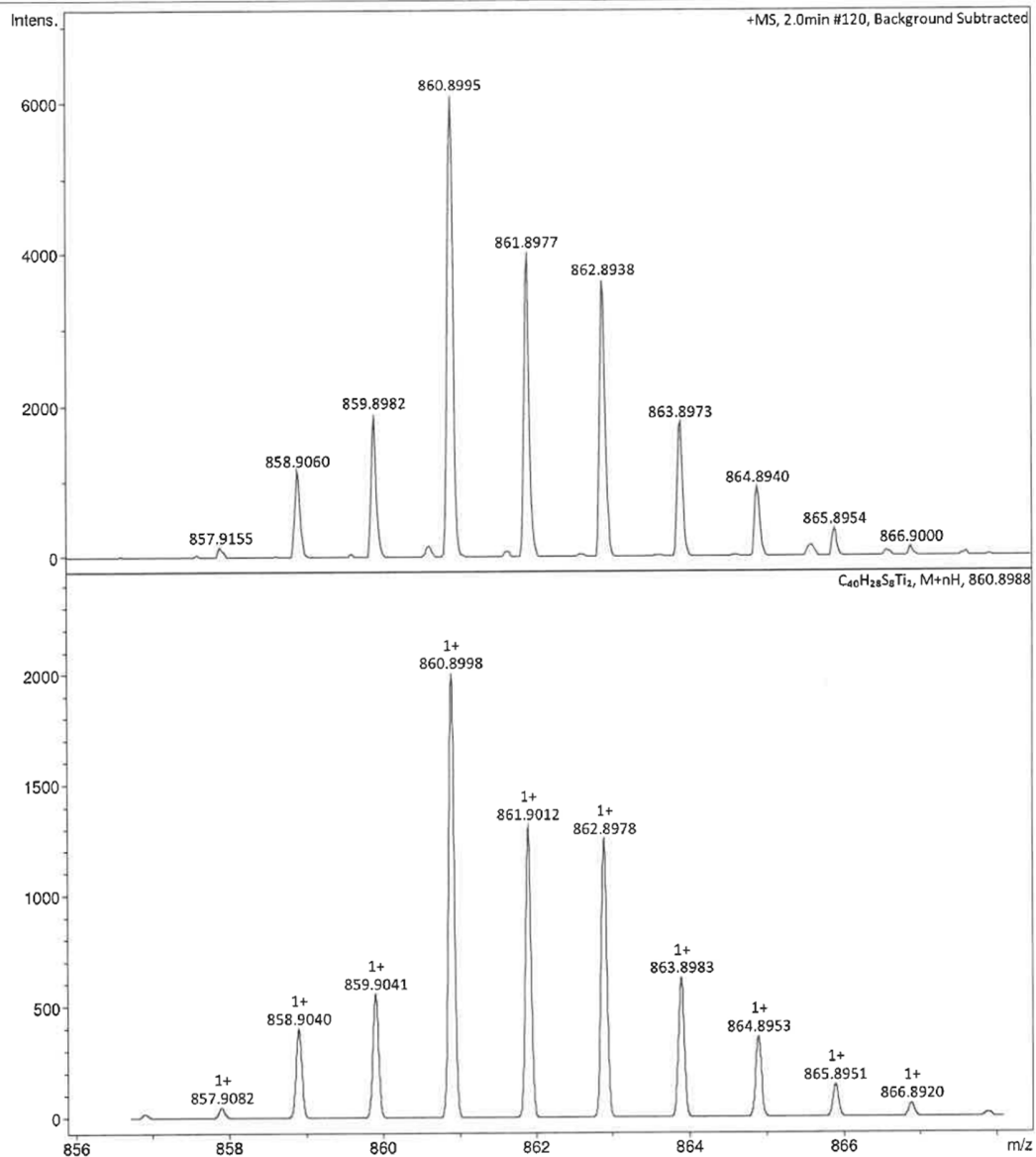
Figure 7.62.   ESI(+)-HRMS spectrum of **dmdt₂Anthra[TiCp₂]₂**.
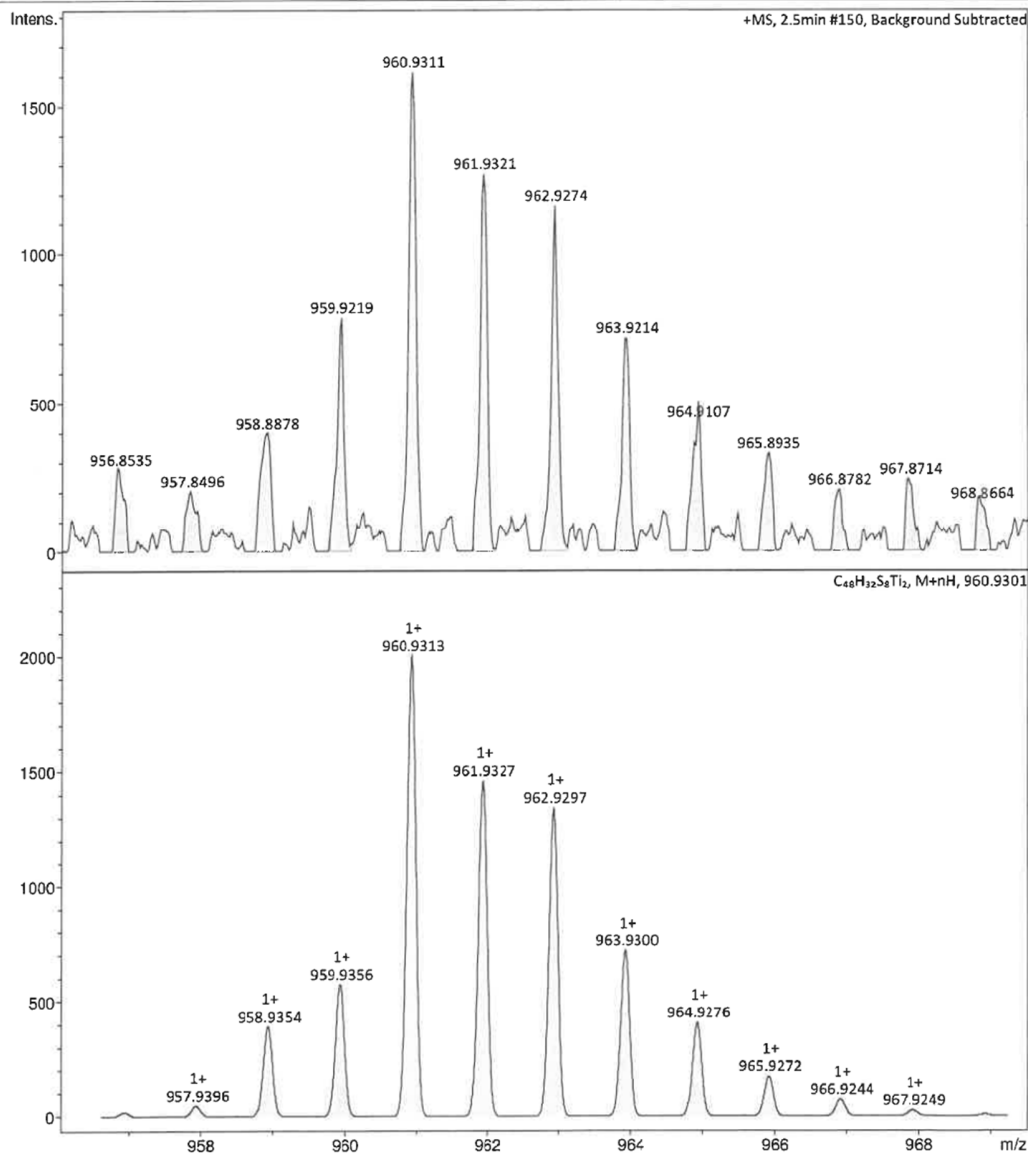
dmdt₂Penta[TiCp₂]

Figure 7.63. ESI(+)-HRMS spectrum of **dmdt₂Penta[TiCp₂]₂**.

dmdt₂Dtbpa[TiCp₂]

Figure 7.64. ESI(+)-HRMS spectrum of **dmdt₂Anthra[Pt]**.
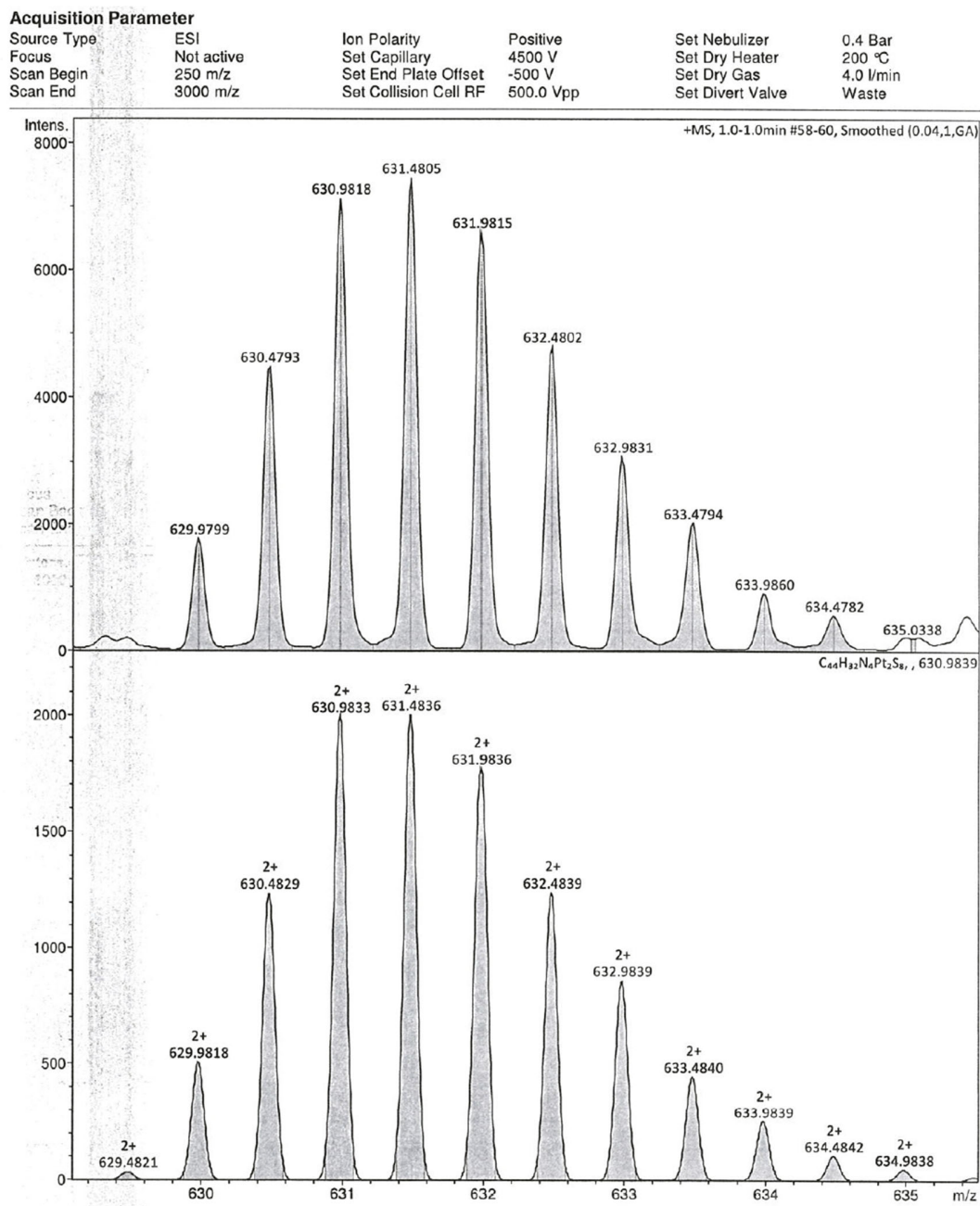
7.4. Crystal Structures
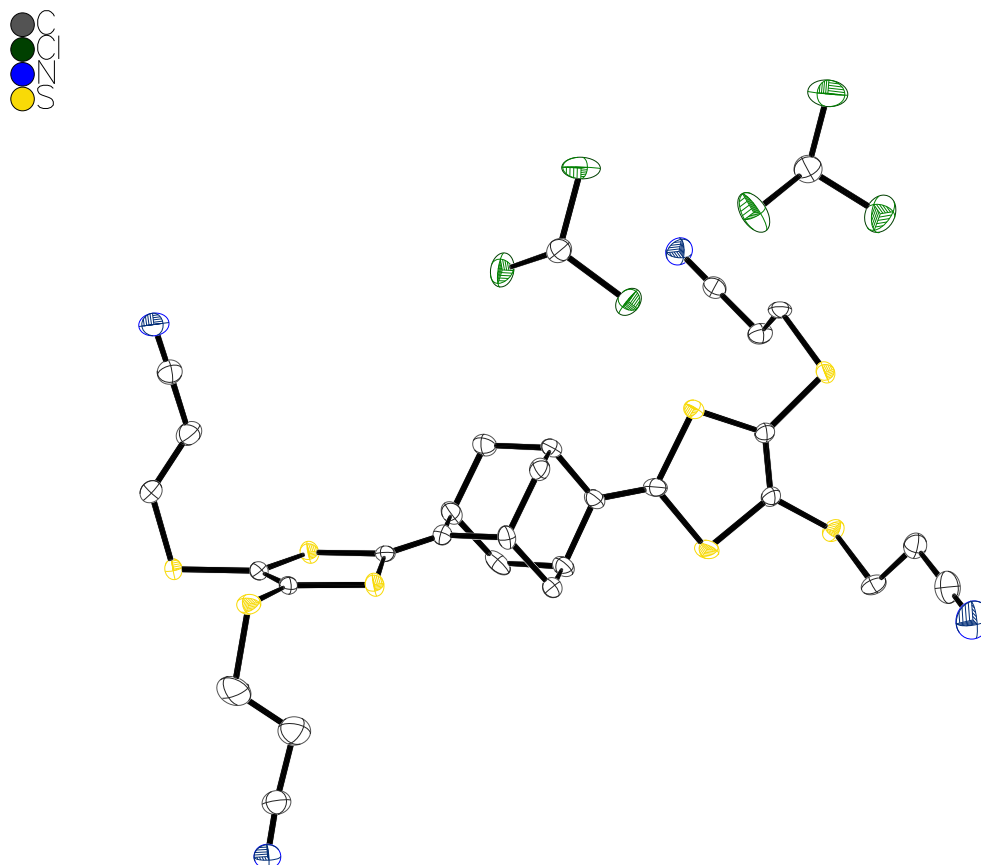
Figure 7.65. Representation of the molecular structure of **dmdt₂Ad[EtCN] · 2 CDCl₃** in the crystal. Hydrogens are omitted for clarity and thermal ellipsoids are drawn at 50% probability level. Color code: Carbon (white), Chlorine (green), Nitrogen (blue), Sulfur (yellow).
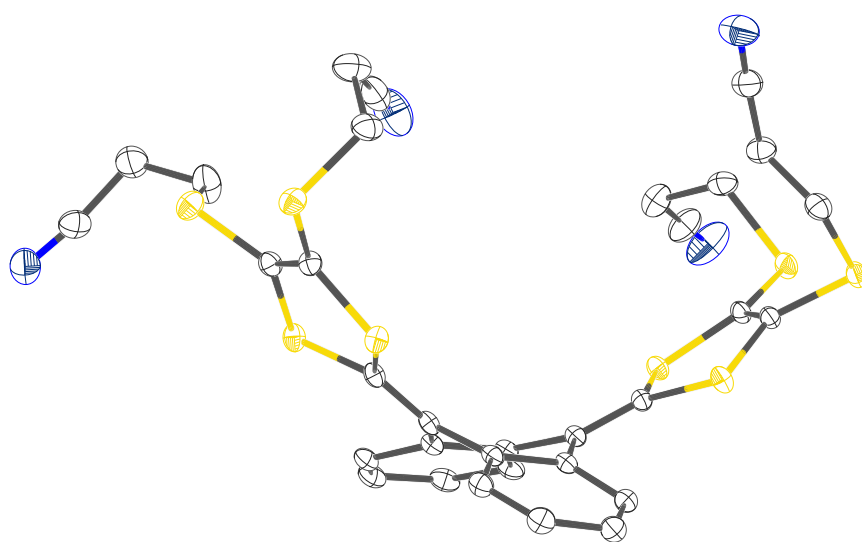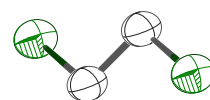
Figure 7.66. Representation of the molecular structure of **dmdt₂Anthra[EtCN] · DCE** in the crystal. Hydrogens are omitted for clarity and thermal ellipsoids are drawn at 50% probability level. Color code: Carbon (white), Chlorine (green), Nitrogen (blue), Sulfur (yellow).
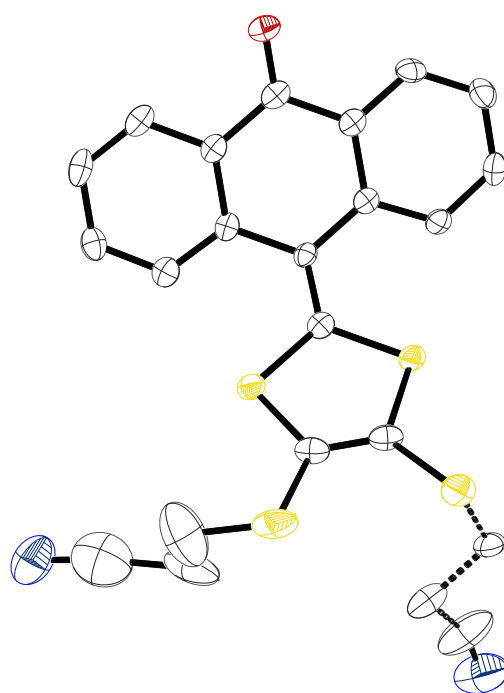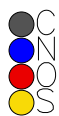
Figure 7.67. Representation of the molecular structure of **dmdtAnthrene[EtCN]** in the crystal. Hydrogens are omitted for clarity and thermal ellipsoids are drawn at 50% probability level. Color code: Carbon (white), Nitrogen (blue), Oxygen (red), Sulfur (yellow).

7.5. In Situ SEC-EPR X-Band spectra
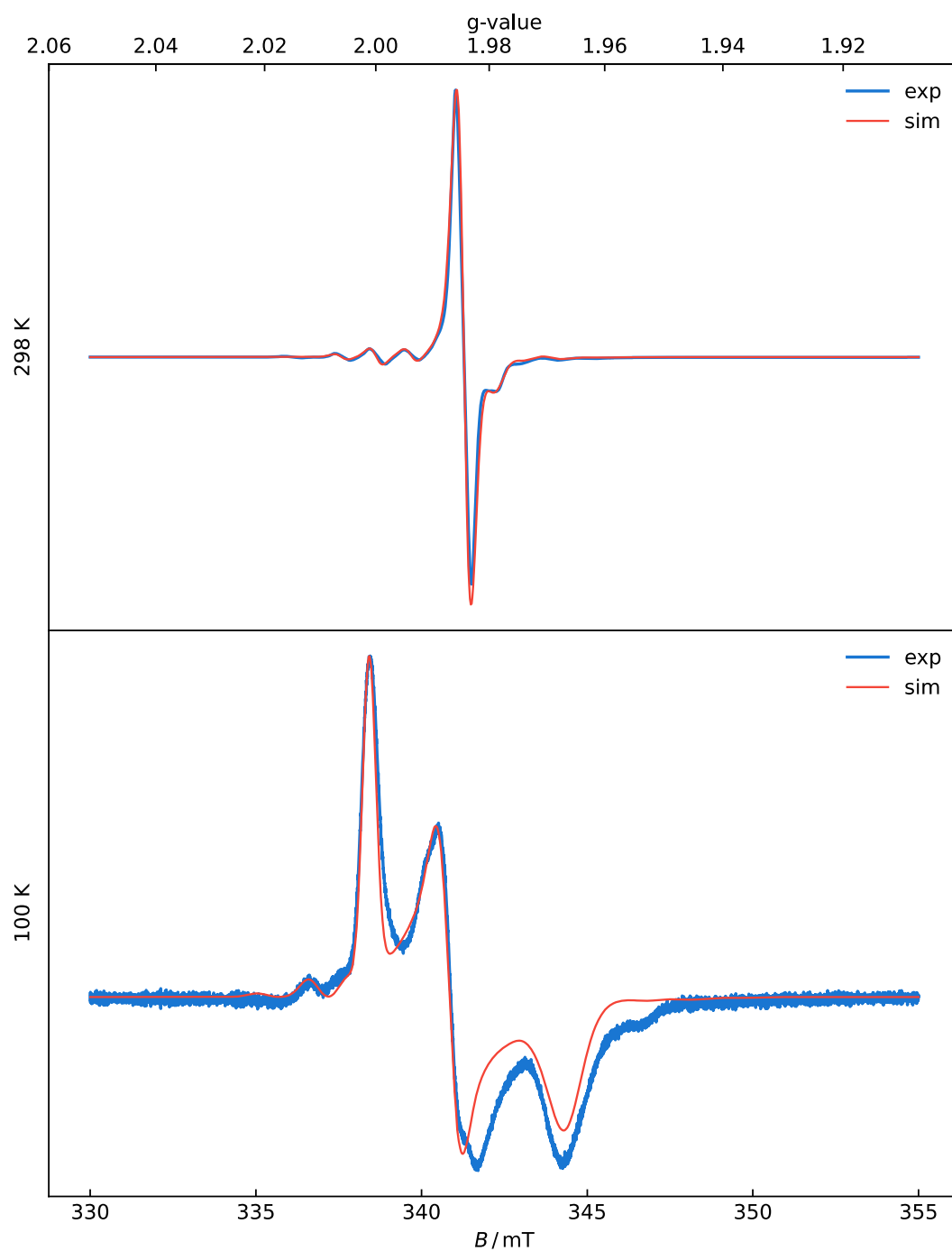
Figure 7.68. EPR spectra of the in situ SEC EPR reduction of **dmdt$_2$Ad[TiCp$_2$]** to **dmdt$_2$Ad[Ti(III)Cp$_2$]** in THF / 0.1 M [NBu$_4$][PF$_6$] at 293 K and 100 K. Simulation in red with exact simulation parameters taken from **Table 4.7** and a second underlying $S = 1/2$ species with $g = 1.981(2)$ and a weight of 10%.
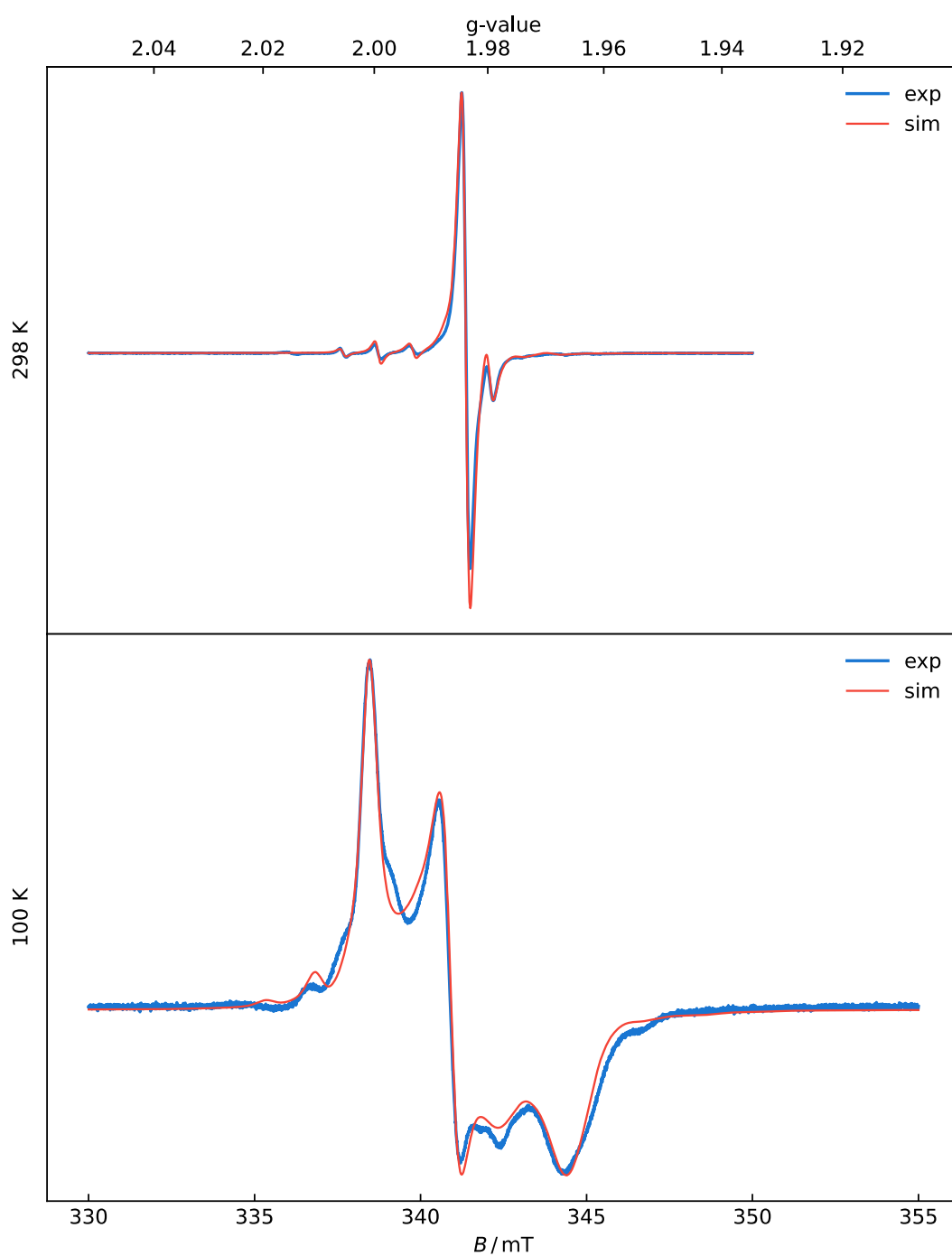
Figure 7.69. EPR spectra of the in situ SEC EPR reduction of **dmdt₂Anthra[TiCp₂]** to **dmdt₂Anthra[Ti(III)Cp₂]** in THF / 0.1 M [NBu₄][PF₆] at 293 K. Different run as the one shown in the main chapter, showing that the second underlying $S = 1/2$ species formation is dependent on the electrolysis itself. In addition, it is visible that the additional impurity signal is truly from an impurity on the electrodes. Simulation in red with exact simulation parameters taken from **Table 4.7** and a second underlying $S = 1/2$ species with $g = 1.981(2)$ and a weight of 10%.
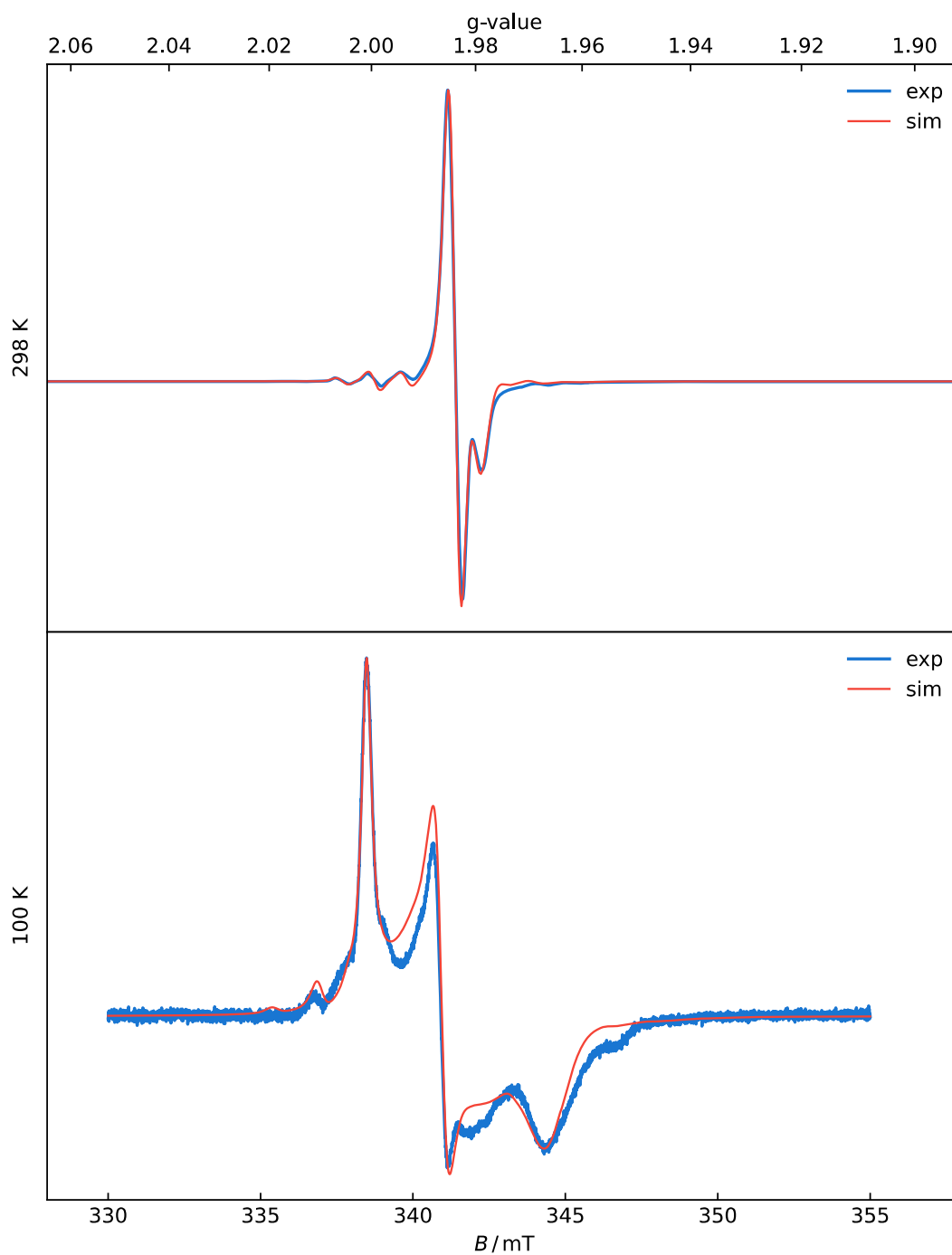
Figure 7.70. EPR spectra of the in situ SEC EPR reduction of **dmdt₂Anthra[TiCp₂]** to **dmdt₂Anthra[Ti(III)Cp₂]** in THF / 0.1 M [NBu₄][PF₆] at 293 K. Much slower ramping to the reduction voltage of $U = -2.0$ V as the one shown in the main chapter, showing that the second underlying $S = 1/2$ species formation is stronger upon slow sweeping. In addition, it is visible that the additional impurity signal is truly from an impurity on the electrodes. Simulation in red with exact simulation parameters taken from **Table 4.7** and a second underlying $S = 1/2$ species with $g = 1.981(2)$ and a weight of 22%.
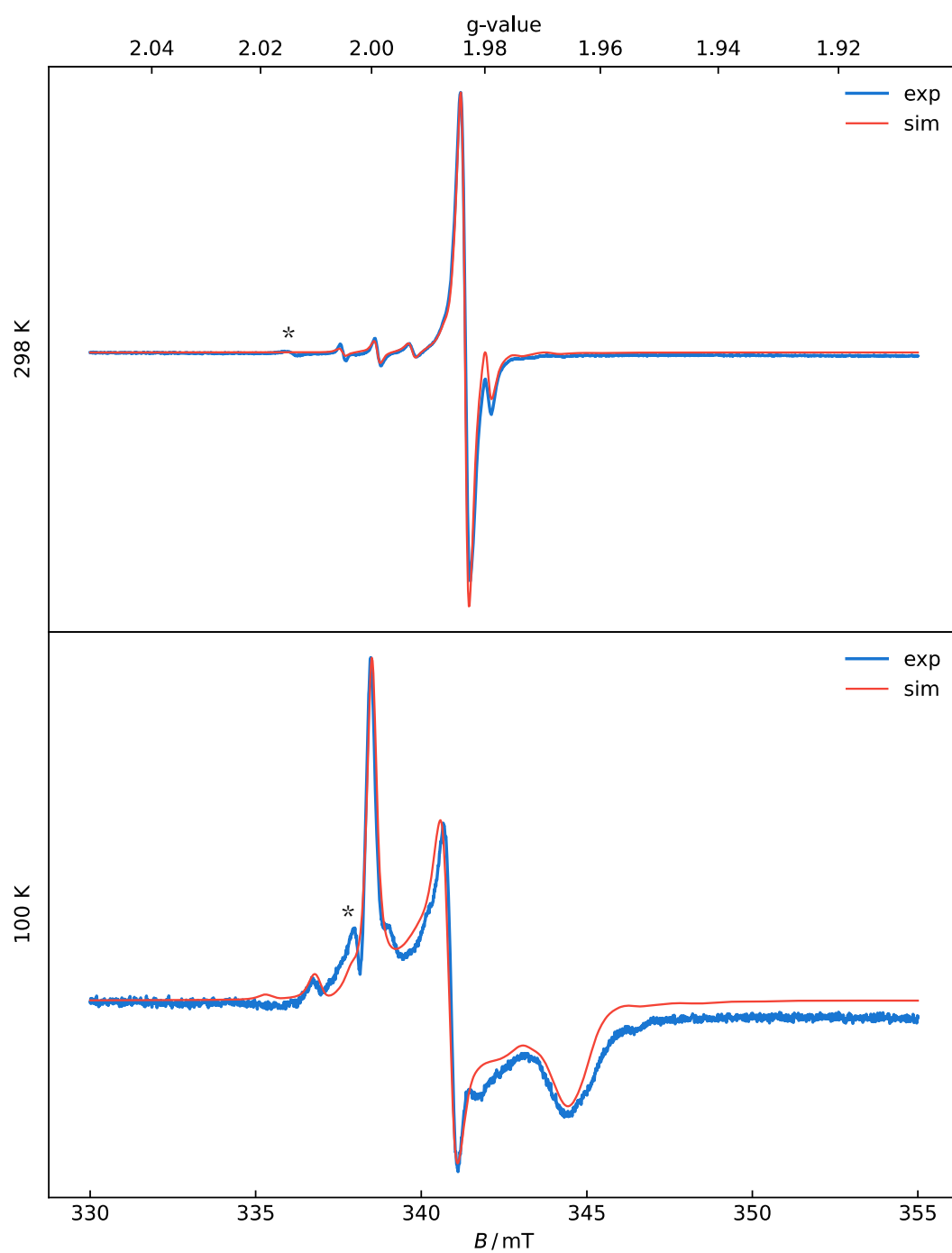
Figure 7.71. EPR spectra of the in situ SEC EPR reduction of **dmdt₂Penta[TiCp₂]** to **dmdt₂Penta[Ti(III)Cp₂]** in THF / 0.1 M [NBu₄][PF₆] at 293 K and 100 K. Simulation in red with exact simulation parameters taken from **Table 4.7** and a second underlying $S = 1/2$ species with $g = 1.981(2)$ and a weight of 9%. Signals indicated with * originate from the electrode.
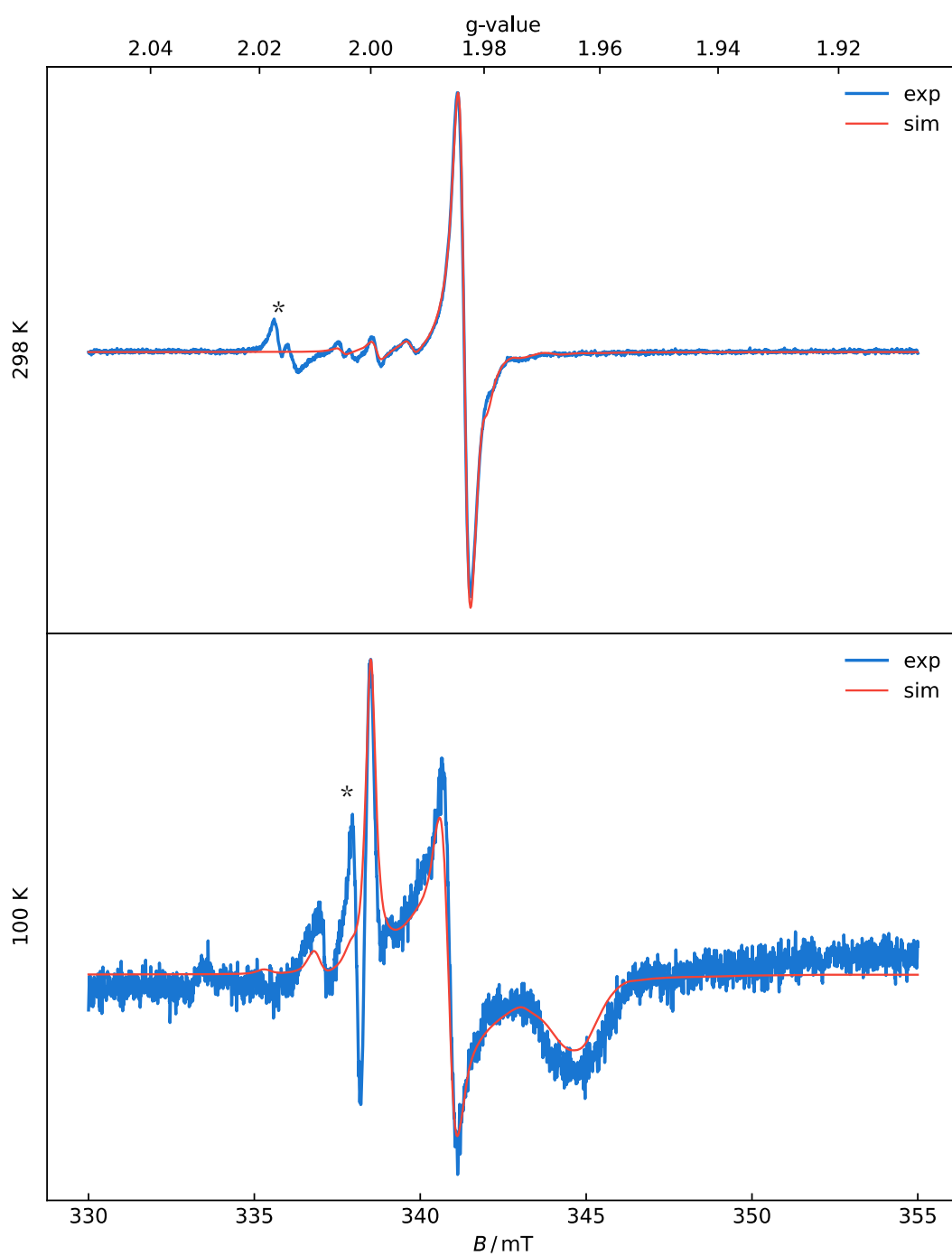
Figure 7.72. EPR spectra of the in situ SEC EPR reduction of **dmdt₂Dtbpa[TiCp₂]** to **dmdt₂Dtbpa[Ti(III)Cp₂]** in THF / 0.1 M [NBu₄][PF₆] at 293 K and 100 K. Simulation in red with exact simulation parameters taken from **Table 4.7** and a second underlying $S = 1/2$ species with $g = 1.981(2)$ and a weight of 20%. Signals indicated with * originate from the electrode.

7.6. Electrochemistry
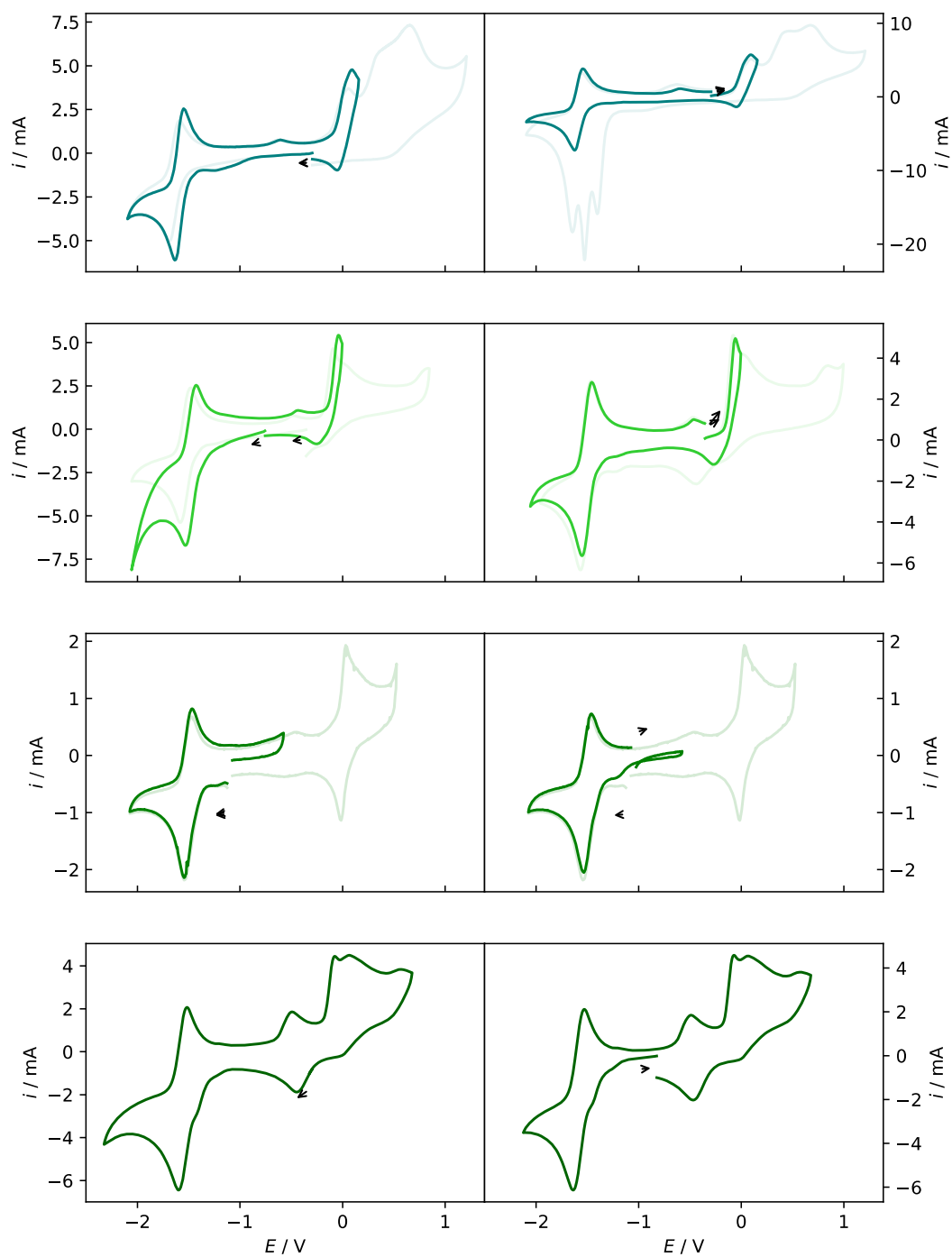
Figure 7.73. Cyclic voltammogram of (1st) **dmdt₂Ad[TiCp₂]**, (2nd) **dmdt₂Anthra[TiCp₂]**, and (3rd) **dmdt₂Penta[TiCp₂]** and (4th) **dmdt₂Dtbpa[TiCp₂]** in DCM / 0.1 M [NBu₄][PF₆] at 100 mV s⁻¹. Left column represents a sweep into the reduction, while right represents a sweep into the oxidation first. Less opaque cyclic voltammograms are representing full sweeps, while solid colors represent only the first waves.

7.7. Computations

dmdt₂Anthra[TiCp₂]
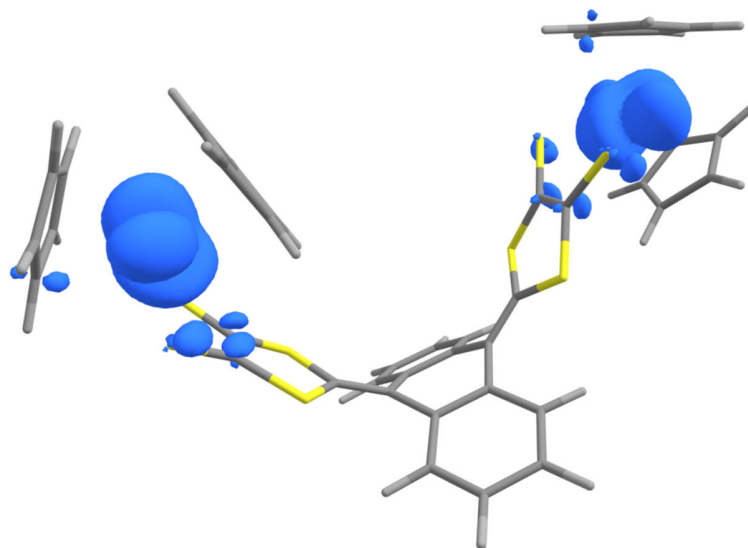
Figure 7.74.   Spin density of **trans-dmdt₂Anthra[Ti(III)Cp₂]** calculated by DFT (PBE0/def2-tzvp).
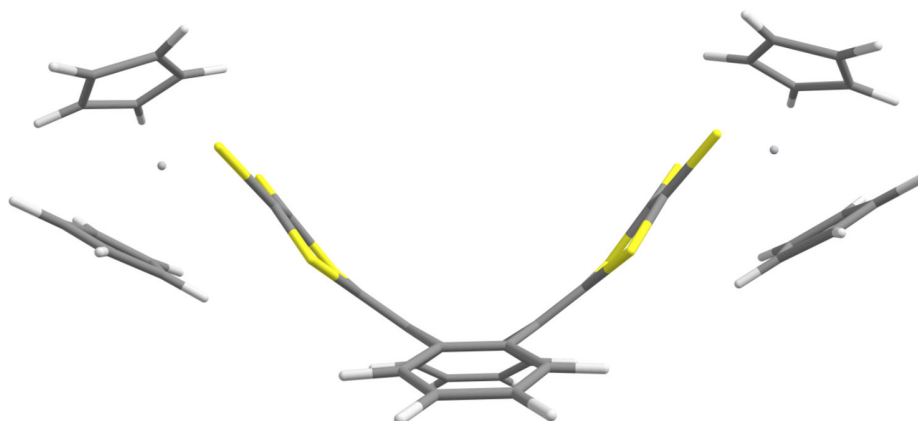
Figure 7.75.   Structure of **cis-dmdt₂Anthra[TiCp₂]** calculated by DFT (PBE0/def2-tzvp).
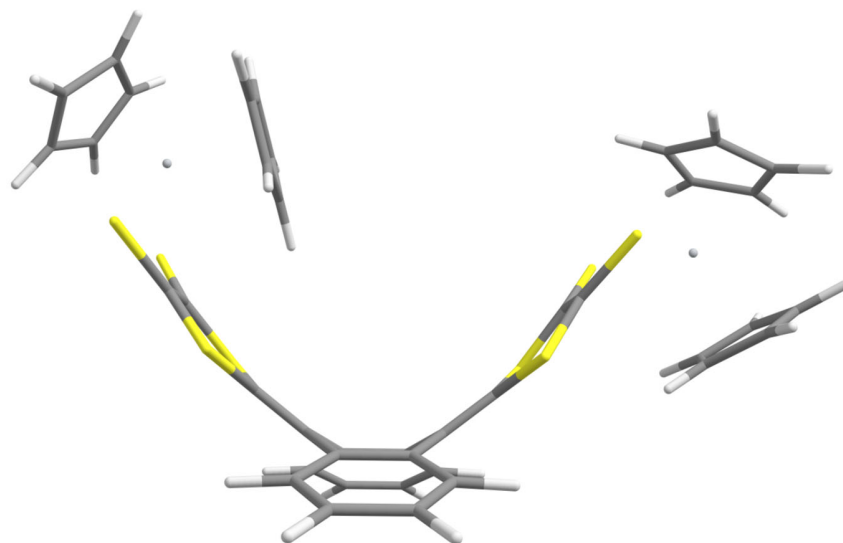
Figure 7.76.   Structure of **trans-dmdt₂Anthra[TiCp₂]** calculated by DFT (PBE0/def2-tzvp).

dmdt₂Ad[TiCp₂]
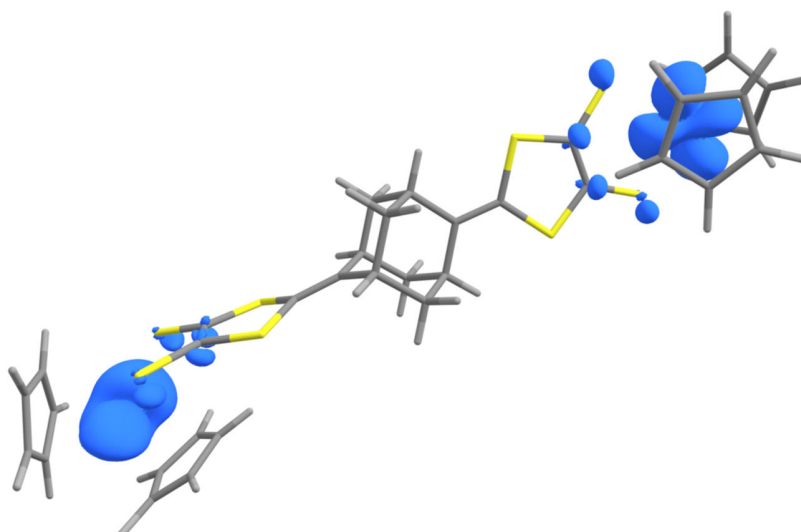
Figure 7.77.   Spin density of **dmdt₂Ad[Ti(III)Cp₂]** calculated by DFT (PBE0/def2-tzvp).

7.8. PTM Radical
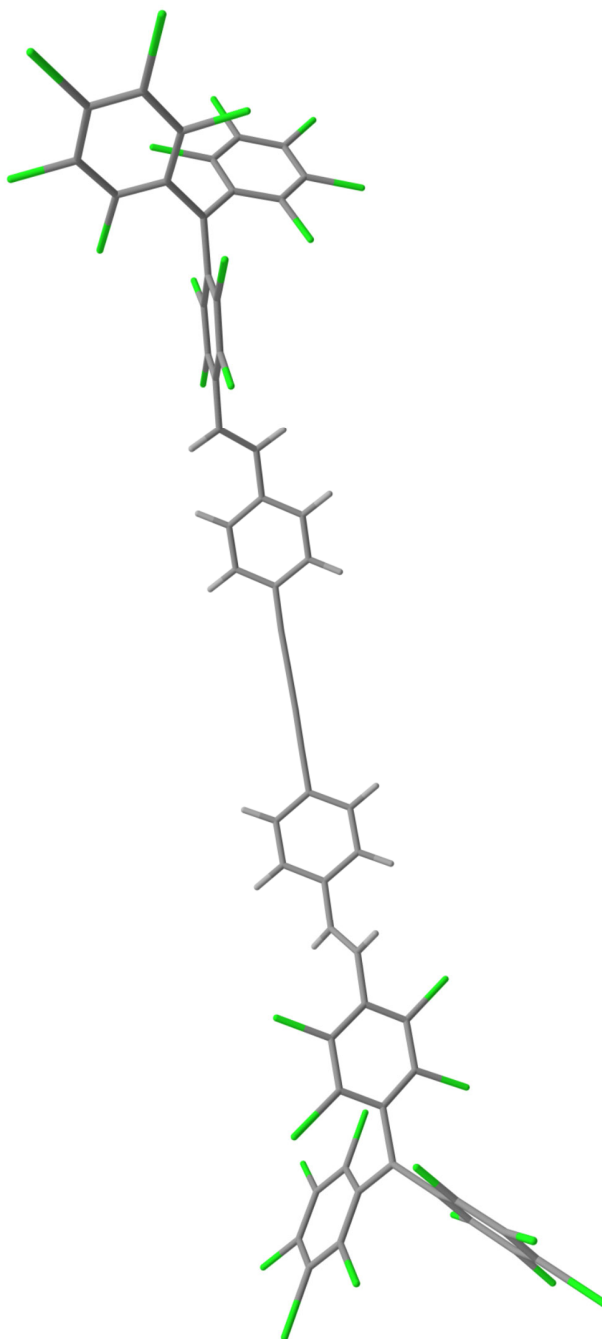
Figure 7.78.   Force-field optimized (UFF) molecular structure of the **PTM-di** radical. The distance between the two radical centers is calculated to be 2.76 nm. Color code: Carbon (grey), Chlorine (green), Hydrogen (white).

7.9. Phase Memory Times of Different Molecular Qubits

Table 7.1. Experimentally determined phase memory times of different monomeric and dimeric qubits at low temperatures found in literature. Summarized by Joris van Slageren.

Qubit	T_m/ μs	Ref.
[V(dbddto)$_3$]$^{2-}$	675	[10]
N@C$_{60}$	230	[188]
graphenoid	80	[189]
[Cu(mnt)$_2$]$^{2-}$	68	[15]
CuPc	41	[33]
[Cu(dbm)$_2$]	25	[190]
[Au^{III}(adt$_2$$^{3-·}$)]	21	[191]
CTM	13	[192]
Blatter	7.8	[193]
triplet C$_{60}$	6.2	[194]
NitSAc	5.41	[195]
TTM	5.1	[150]
dpph	3.9	[196]
TEMPO	3.2	[197]
CTPO	2.79	[195]
BDPA	2.3	[198]

Qubit 1	Qubit 2	T_m/ μs	Ref.
CuPor	TiCp	20.77, 8.20	[199]
TTM	triplet C$_{60}$	2.2, 6.2	[194]
CuZnHPDK	CuZnHPDK	6.03	[200]
CuNiHPDK	CuNiHPDK	3.59	[200]
MnDOTA	MnDOTA	5.9	[201]
TTM	TEMPO	3.8	[202]
TTM	TTM	3.3	[203]
Cr$_7$Ni	Cr$_7$Ni	3.239	[204]
Y@C$_{82}$	Y@C$_{82}$	2	[205]
GDPyMTA	GdPyMTA	1.4	[206]
TEMPO	Mn-tpy	1.0	[207]
VOCat	VOCat	1	[208]
Cu	Cu$_7$Ni	1, 0.6	[209]
VO-ON	VO-ON	0.26	[41]

8

REFERENCES

8. REFERENCES

[1]   Feynman, R. P. *Int. J. Theor. Phys.* **1982**, *217* (6).

[2]   Deutsch, D. *Proc. R. Soc. London, Ser. A Math. Phys. Sci.* **1985**, *400* (1818), 97–117, doi:10.1098/rspa.1985.0070.

[3]   Grover, L. K. *A fast quantum mechanical algorithm for database search*; arXiv: quant-ph/9605043, 1996.

[4]   Shor, P. W. *SIAM Rev.* **1999**, *41* (2), 303–332, doi:10.1137/S0036144598347011.

[5]   Bernstein, D. J.; Lenstra, A. K. *A general number field sieve implementation*; Springer, Berlin, Heidelberg, 1993.

[6]   Rivest, R. L.; Shamir, A.; Adleman, L. *Commun. ACM* **1978**, *21* (2), 120–126, doi:10.1145/359340.359342.

[7]   Ayoade, O.; Rivas, P.; Orduz, J. *Data* **2022**, *7* (3), 1–16, doi:10.3390/data7030028.

[8]   Broughton, M.; Verdon, G.; McCourt, T.; Martinez, A. J.; Yoo, J. H.; Isakov, S. V.; Massey, P.; Halavati, R.; Niu, M. Y.; Zlokapa, A.; Peters, E.; Lockwood, O.; Skolik, A.; Jerbi, S.; Dunjko, V.; Leib, M.; Streif, M.; Von Dollen, D.; Chen, H.; Cao, S.; Wiersema, R.; Huang, H.-Y.; McClean, J. R.; Babbush, R.; Boixo, S.; Bacon, D.; Ho, A. K.; Neven, H.; Mohseni, M. **2020**, 1–56.

[9]   DiVincenzo, D. P. *Fortschritte der Phys.* **2000**, *48* (9–11), 771–783, doi:10.1002/1521-3978(200009)48:9/11<771::AID-PROP771>3.0.CO;2-E.

[10]   Zadrozny, J. M.; Niklas, J.; Poluektov, O. G.; Freedman, D. E. *ACS Cent. Sci.* **2015**, *1* (9), 488–492, doi:10.1021/acscentsci.5b00338.

[11]   Kaminski, D.; Webber, A. L.; Wedge, C. J.; Liu, J.; Timco, G. A.; Vitorica-Yrezabal, I. J.; McInnes, E. J. L.; Winpenny, R. E. P.; Ardavan, A. *Phys. Rev. B - Condens. Matter Mater. Phys.* **2014**, *90* (18), 1–4, doi:10.1103/PhysRevB.90.184419.

[12]   Barenco, A.; Bennett, C. H. C. H.; Cleve, R.; DiVincenzo, D. P. D. P.; Margolus, N.; Shor, P. W. P.; Sleator, T.; Smolin, J. A. J. A.; Weinfurter, H. *Phys. Rev. A* **1995**, *52* (5), 3457–3467, doi:10.1103/PhysRevA.52.3457.

[13]   Yu, C. J.; Graham, M. J.; Zadrozny, J. M.; Niklas, J.; Krzyaniak, M. D.; Wasielewski, M. R.; Poluektov, O. G.; Freedman, D. E. *J. Am. Chem. Soc.* **2016**, *138* (44), 14678–14685, doi:10.1021/jacs.6b08467.

[14]   Bader, K.; Schlindwein, S. H.; Gudat, D.; Van Slageren, J. *Phys. Chem. Chem. Phys.* **2017**, *19* (3), 2525–2529, doi:10.1039/c6cp08161d.

[15]   Bader, K.; Dengler, D.; Lenz, S.; Endeward, B.; Jiang, S. Da; Neugebauer, P.; Van Slageren, J. *Nat. Commun.* **2014**, *5* (May), 1–5, doi:10.1038/ncomms6304.

[16]   Wedge, C. J.; Timco, G. A.; Spielberg, E. T.; George, R. E.; Tuna, F.; Rigby, S.; McInnes, E. J. L.; Winpenny, R. E. P.; Blundell, S. J.; Ardavan, A. *Phys. Rev. Lett.* **2012**, *108* (10), 107204, doi:10.1103/PhysRevLett.108.107204.

[17]   Graham, M. J.; Yu, C.-J.; Krzyaniak, M. D.; Wasielewski, M. R.; Freedman, D. E. *J. Am. Chem. Soc.* **2017**, *139* (8), 3196–3201, doi:10.1021/jacs.6b13030.

[18]   Zadrozny, J. M.; Niklas, J.; Poluektov, O. G.; Freedman, D. E. *J. Am. Chem. Soc.* **2014**, *136* (45), 15841–15844, doi:10.1021/ja507846k.

[19]   Eaton, S. S.; Eaton, G. R. *Distance Measurements in Biologic Systems by EPR*; Springer.

[20]   Wolfe, J. P. *Phys. Rev. Lett.* **1973**, *31* (15), 907–910, doi:10.1103/PhysRevLett.31.907.

[21]   NuDat 2.8 https://www.nndc.bnl.gov/nudat3/.

[22]   Bader, K. Spin dynamics in transition metal compounds: towards nuclear-spin-free molecular quantum bits, University of Stuttgart, Germany, 2016.

[23]   Moore, W.; Huffman, J. L.; Driesschaert, B.; Eaton, S. S.; Eaton, G. R. *Appl. Magn. Reson.* **2021**, No. 0123456789, doi:10.1007/s00723-021-01405-3.

[24]   Paniagua, J. C.; Mugnaini, V.; Gabellieri, C.; Feliz, M.; Roques, N.; Veciana, J.; Pons, M. *Phys. Chem. Chem. Phys.* **2010**, *12* (22), 5824, doi:10.1039/c003291n.

[25]   Moreno-Pineda, E.; Martins, D. O. T. A.; Tuna, F. *Molecules as qubits, qudits and quantum gates*; 2021; Vol. 27.

[26]   Bartolomé, E.; Arauzo, A.; Luzón, J.; Bartolomé, J.; Bartolomé, F. *Handb. Magn. Mater.* **2017**, *26*, 1–289, doi:10.1016/bs.hmm.2017.09.002.

[27]   Liddle, S. T.; Van Slageren, J. *Chem. Soc. Rev.* **2015**, *44* (19), 6655–6669, doi:10.1039/c5cs00222b.

[28]   Sproules, S. *Electron Paramagnetic Resonance: Molecules as electron spin qubits*, Volume 25.; Royal Society of Chemistry, 2016.

[29]   Ladd, T. D.; Jelezko, F.; Laflamme, R.; Nakamura, Y.; Monroe, C.; O'Brien, J. L. *Nature* **2010**, *464* (7285), 45–53, doi:10.1038/nature08812.

[30]   Bar-Gill, N.; Pham, L. M.; Jarmola, A.; Budker, D.; Walsworth, R. L. *Nat. Commun.* **2013**, *4*, doi:10.1038/ncomms2771.

[31]   Lewis, G. R.; Dance, L. *J. Chem. Soc. Dalt. Trans.* **2000**, No. 18, 3176–3185, doi:10.1039/b000093k.

[32]   Okubo, T.; Maeda, R.; Kondo, M.; Mitani, T.; Kitagawa, S. *Chem. Lett.* **2006**, *35* (1), 34–35, doi:10.1246/cl.2006.34.

[33]   Bader, K.; Winkler, M.; van Slageren, J. *Chem. Commun.* **2016**, *52* (18), 3623–3626, doi:10.1039/c6cc00300a.

[34]   Keller, K.; Ritsch, I.; Hintz, H.; Hülsmann, M.; Qi, M.; Breitgoff, F. D.; Klose, D.; Polyhach, Y.; Yulikov, M.; Godt, A.; Jeschke, G. *Phys. Chem. Chem. Phys.* **2020**, *22* (38), 21707–21730, doi:10.1039/d0cp03105d.

[35]   Godt, A.; Franzen, C.; Veit, S.; Enkelmann, V.; Pannier, M.; Jeschke, G. *J. Org. Chem.* **2000**, *65* (22), 7575–7582, doi:10.1021/jo005556j.

[36]   Nakazawa, S.; Nishida, S.; Ise, T.; Yoshino, T.; Mori, N.; Rahimi, R. D.; Sato, K.; Morita, Y.; Toyota, K.; Shiomi, D.; Kitagawa, M.; Hara, H.; Carl, P.; Höfer, P.; Takui, T. *Angew. Chemie - Int. Ed.* **2012**, *51* (39), 9860–9864, doi:10.1002/anie.201204489.

[37]   Boulon, M.-E.; Fernandez, A.; Moreno Pineda, E.; Chilton, N. F.; Timco, G.; Fielding, A. J.; Winpenny, R. E. P. P. *Angew. Chemie Int. Ed.* **2017**, *56* (14), 3876–3879, doi:10.1002/anie.201612249.

[38]   Ferrando-Soria, J.; Moreno Pineda, E.; Chiesa, A.; Fernandez, A.; Magee, S. A.; Carretta, S.; Santini, P.; Vitorica-Yrezabal, I. J.; Tuna, F.; Timco, G. A.; McInnes, E. J. L.; Winpenny, R. E. P. *Nat. Commun.* **2016**, *7*, 11377, doi:10.1038/ncomms11377.

[39]   Luis, F.; Repollés, A.; Martínez-Pérez, M. J.; Aguilà, D.; Roubeau, O.; Zueco, D.; Alonso, P. J.; Evangelisti, M.; Camón, A.; Sesé, J.; Barrios, L. A.; Aromí, G. *Phys. Rev. Lett.* **2011**, *107* (11), 1–5, doi:10.1103/PhysRevLett.107.117203.

[40]   Dengler, D. ESR-Untersuchungen an molekularen Ein- und Zwei-Quantenbit-Systemen, 2016.

[41]   Borilovic, I.; Alonso, P. J.; Roubeau, O.; Aromí, G. *Chem. Commun.* **2020**, *56* (21), 3139–3142, doi:10.1039/C9CC09817H.

[42]   Borbat, P. P.; Freed, J. H. *Chapter 20 Dipolar Spectroscopy – Single-resonance Methods*; 2018.

[43]   Goldfarb, D.; Stoll, S. *EPR Spectroscopy: Fundamentals and Methods*; WILEY-VCH Verlag, 2018.

[44]   Schweiger, A.; Jeschke, G. *Principles of Pulse Electron Paramagnetic Resonance*; Oxford University Press, 2001.

[45]   Akhmetzyanov, D. Pulsed EPR Dipolar Spectroscopy with Novel Paramagnetic Tags, 2016.

[46]   Pake, G. E. *J. Chem. Phys.* **1948**, *16* (4), 327–336, doi:10.1063/1.1746878.

[47]   Ernst, R. R. *Principles of Nuclear Magnetic Resonance in One and Two Dimensions*; Oxford Science Publications, 1997.

[48]   Shriver, J. *Concepts Magn. Reson.* **1992**, *4* (1), 1–33, doi:10.1002/cmr.1820040102.

[49]   Milov, A. D.; Salikhov, K. M.; Shirov, M. D. *Fiz. Tverd. Tela* **1981**, *23* (4), 975–982.

[50]   Jeschke, G. *eMagRes* **2016**, *5* (3), 1459–1476, doi:10.1002/9780470034590.emrstm1518.

[51]   Pannier, M.; Veit, S.; Godt, A.; Jeschke, G.; Spiess, H. . *J. Magn. Reson.* **2000**, *142* (2), 331–340, doi:10.1006/jmre.1999.1944.

[52] Borbat, P. P.; Freed, J. H. *Pros and Cons of Pulse Dipolar ESR: DQC & DEER*; EPR Newsletter, 2007; Vol. 17.

[53] Borbat, P. P.; Mchaourab, H. S.; Freed, J. H. *J. Am. Chem. Soc.* **2002**, *124* (19), 5304–5314, doi:10.1021/ja020040y.

[54] Jeschke, G.; Pannier, M.; Godt, A.; Spiess, H. W. *Chem. Phys. Lett.* **2000**, *331* (2–4), 243–252, doi:10.1016/S0009-2614(00)01171-4.

[55] Chiang, Y. W.; Borbat, P. P.; Freed, J. H. *J. Magn. Reson.* **2005**, *172* (2), 279–295, doi:10.1016/j.jmr.2004.10.012.

[56] Edwards, T. H.; Stoll, S. *J. Magn. Reson.* **2018**, *288* (10), 58–68, doi:10.1016/j.jmr.2018.01.021.

[57] Jeschke, G. DEER Software https://epr.ethz.ch/software.html.

[58] Bernhard, S.; Belser, P. *Synth. Commun.* **1996**, *26* (19), 3559–3563, doi:10.1080/00397919608003765.

[59] De Cola, L.; Belser, P.; von Zelewsky, A.; V??gtle, F. *Inorganica Chim. Acta* **2007**, *360* (3), 775–784, doi:10.1016/j.ica.2006.10.039.

[60] Balzani, V.; Barigelletti, F.; Belser, P.; Bernhard, S.; De Cola, L.; Flamigni, L. *J. Phys. Chem.* **1996**, *100* (42), 16786–16788, doi:10.1021/jp962366x.

[61] Belser, P.; Bernhard, S.; Blum, C.; Beyeler, A.; De Cola, L.; Balzani, V. *Coord. Chem. Rev.* **1999**, *190–192*, 155–169, doi:10.1016/S0010-8545(99)00075-2.

[62] Bernhard, S.; Belser, P. *Synthesis (Stuttg).* **1996**, *1996* (02), 192–194, doi:10.1055/s-1996-4183.

[63] Sandín, P.; Martínez-Grau, A.; Sánchez, L.; Seoane, C.; Pou-Amérigo, R.; Ortí, E.; Martín, N. *Org. Lett.* **2005**, *7* (2), 295–298, doi:10.1021/ol047681d.

[64] Christensen, M. A.; Parker, C. R.; Sørensen, T. J.; De Graaf, S.; Morsing, T. J.; Brock-Nannestad, T.; Bendix, J.; Haley, M. M.; Rapta, P.; Danilov, A.; Kubatkin, S.; Hammerich, O.; Nielsen, M. B. *J. Mater. Chem. C* **2014**, *2* (48), 10428–10438, doi:10.1039/c4tc02178a.

[65] Hardouin-Lerouge, M.; Chesneau, B.; Allain, M.; Hudhomme, P. *J. Org. Chem.* **2012**, *77* (5), 2441–2445, doi:10.1021/jo300101c.

[66] Kato, M.; Fujita, Y.; Yamauchi, T.; Mori, S.; Shirahata, T.; Misaki, Y. *Org. Lett.* **2018**, *20* (17), 5121–5125, doi:10.1021/acs.orglett.8b01985.

[67] Gleiter, R.; Gaa, B.; Sigwart, C.; Lange, H.; Borzyk, O.; Rominger, F.; Irngartinger, H.; Oeser, T. *European J. Org. Chem.* **1998**, No. 1, 171–176, doi:10.1002/(SICI)1099-0690(199801)1998:1<171::AID-EJOC171>3.0.CO;2-M.

[68] Kusamoto, T.; Kume, S.; Nishihara, H. *J. Am. Chem. Soc.* **2008**, *130* (42), 13844–13845, doi:10.1021/ja805751h.

[69] Fetkenheuer, B.; Fetkenheuer, H.; Lecus, H. *Berichte der Dtsch. Chem. Gesellschaft (A B Ser.* **1927**, *60* (11), 2528–2537, doi:10.1002/cber.19270601120.

[70] Steimecke, G.; Kirmse, R.; Hoyer, E. *Zeitschrift für Chemie* **2010**, *15* (1), 28–29, doi:10.1002/zfch.19750150117.

[71] Recatalá, D.; Gushchin, A. L.; Llusar, R.; Galindo, F.; Brylev, K. A.; Ryzhikov, M. R.; Kitamura, N. *Dalt. Trans.* **2013**, *42* (36), 12947, doi:10.1039/c3dt51102b.

[72] Pedersen, D. S.; Rosenbohm, C. *Synthesis (Stuttg).* **2001**, No. 16, 2431–2434, doi:10.1055/s-2001-18722.

[73] Yzambart, G.; Fabre, B.; Roisnel, T.; Dorcet, V.; Ababou-Girard, S.; Meriadec, C.; Lorcy, D. *Organometallics* **2014**, *33* (18), 4766–4776, doi:10.1021/om5000369.

[74] Halton, B.; Jones, C. S. *European J. Org. Chem.* **2004**, *2004* (1), 138–146, doi:10.1002/ejoc.200300619.

[75] Kolodiazhnyi, O. I. *Phosphorus Ylides*; WILEY-VCH Verlag, 1999.

[76] Hasegawa, M.; Endo, Y.; Honda, Y.; Mazaki, Y. *Chem. Lett.* **2017**, *46* (7), 964–967, doi:10.1246/cl.170257.

[77] Yu, W.-T.; Xue, G.; Fang, Q.; Liu, G.-Q. *Zeitschrift für Krist. - New Cryst. Struct.* **2003**, *218* (4), 545–546, doi:10.1524/ncrs.2003.218.4.545.

[78] Dolomanov, O. V.; Bourhis, L. J.; Gildea, R. J.; Howard, J. A. K.; Puschmann, H. *J. Appl. Crystallogr.* **2009**, *42* (2), 339–341, doi:10.1107/S0021889808042726.

[79] Yamakado, T.; Takahashi, S.; Watanabe, K.; Matsumoto, Y.; Osuka, A.; Saito, S. *Angew. Chemie - Int. Ed.* **2018**, *57* (19), 5438–5443, doi:10.1002/anie.201802185.

[80] Xu, F.; Peng, L.; Shinohara, K.; Morita, T.; Yoshida, S.; Hosoya, T.; Orita, A.; Otera, J. *J. Org. Chem.* **2014**, *79* (23), 11592–11608, doi:10.1021/jo502248p.

[81] Lin, C. H.; Lin, K. H.; Pal, B.; Tsou, L. Der. *Chem. Commun.* **2009**, No. 7, 803–805, doi:10.1039/b814840f.

[82] Einholz, R. Über die Reaktivität Großer Acene - In Lösung, in Matrix und unter sauer-oxidativen Bedingungen, Eberhard Karls Universität Tübingen, 2019.

[83] Kubo, K.; Nakao, A.; Ishii, Y.; Kato, R.; Matsubayashi, G. E. *Synth. Met.* **2005**, *153* (1–3), 425–428, doi:10.1016/j.synthmet.2005.07.322.

[84] Murata, M.; Kaji, S.; Nishimura, H.; Wakamiya, A.; Murata, Y. *Eur. J. Inorg. Chem.* **2016**, *2016* (20), 3228–3232, doi:10.1002/ejic.201600595.

[85] Liu, W.; Wang, R.; Zhou, X. H.; Zuo, J. L.; You, X. Z. *Organometallics* **2008**, *27* (1), 126–134, doi:10.1021/om700776s.

[86] Fujiwara, E.; Hosoya, K.; Kobayashi, A.; Tanaka, H.; Tokumoto, M.; Okano, Y.; Fujiwara, H.; Kobayashi, H.; Fujishiro, Y.; Nishibori, E.; Takata, M.; Sakata, M. *Inorg. Chem.* **2008**, *47* (3), 863–874, doi:10.1021/ic701100r.

[87] Zhou, B.; Idobata, Y.; Kobayashi, A.; Cui, H.; Kato, R.; Takagi, R.; Miyagawa, K.; Kanoda, K.; Kobayashi, H. *J. Am. Chem. Soc.* **2012**, *134* (30), 12724–12731, doi:10.1021/ja3044757.

[88] Nishikawa, H.; Yasuoka, W.; Sakairi, K.; Oshio, H. *Polyhedron* **2009**, *28* (9–10), 1634–1637, doi:10.1016/j.poly.2008.10.012.

[89] Fujiwara, E.; Zhou, B.; Kobayashi, A.; Kobayashi, H.; Fujishiro, Y.; Nishibori, E.; Sakata, M.; Ishibashi, S.; Terakura, K. *Eur. J. Inorg. Chem.* **2009**, No. 12, 1585–1591, doi:10.1002/ejic.200900008.

[90] Baudron, S. A.; Hosseini, M. W.; and, S. A. B.; Hosseini*, M. W. *Inorg. Chem.* **2006**, *45* (14), 5260–5262, doi:10.1021/ic0603510.

[91] Kawabata, K.; Nakano, M.; Tamura, H.; Matsubayashi, G. E. *Inorganica Chim. Acta* **2004**, *357* (15), 4373–4378, doi:10.1016/j.ica.2004.06.054.

[92] Dias, S. I. G.; Rabaça, S.; Santos, I. C.; Pereira, L. C. J.; Henriques, R. T.; Almeida, M. *Inorg. Chem. Commun.* **2012**, *15*, 102–105, doi:10.1016/j.inoche.2011.10.001.

[93] Filatre-Furcate, A.; Bellec, N.; Jeannin, O.; Auban-Senzier, P.; Fourmigué, M.; Íniguez, J.; Canadell, E.; Brière, B.; Ta Phuoc, V.; Lorcy, D. *Inorg. Chem.* **2016**, *55* (12), 6036–6046, doi:10.1021/acs.inorgchem.6b00556.

[94] Yzambart, G.; Bellec, N.; Nasser, G.; Jeannin, O.; Roisnel, T.; Fourmigué, M.; Auban-Senzier, P.; Íñiguez, J.; Canadell, E.; Lorcy, D. *J. Am. Chem. Soc.* **2012**, *134* (41), 17138–17148, doi:10.1021/ja3065649.

[95] Vuong, T. M. H.; Bui, T. T.; Sournia-Saquet, A.; Moreau, A.; Ching, K. I. M. C. *Inorg. Chem.* **2014**, *53* (6), 2841–2847, doi:10.1021/ic402528j.

[96] Le Gal, Y.; Roisnel, T.; Dorcet, V.; Guizouarn, T.; Sady, L. P.; Lorcy, D. *J. Organomet. Chem.* **2015**, *794*, 323–329, doi:10.1016/j.jorganchem.2015.07.021.

[97] Bellec, N.; Vacher, A.; Barrière, F.; Xu, Z.; Roisnel, T.; Lorcy, D. *Inorg. Chem.* **2015**, *54* (10), 5013–5020, doi:10.1021/acs.inorgchem.5b00632.

[98] Bsaibess, T.; Guerro, M.; Le Gal, Y.; Sarraf, D.; Bellec, N.; Fourmigué, M.; Barrière, F.; Dorcet, V.; Guizouarn, T.; Roisnel, T.; Lorcy, D. *Inorg. Chem.* **2013**, *52* (4), 2162–2173, doi:10.1021/ic3025606.

[99] Rabaça, S.; Oliveira, S.; Belo, D.; Santos, I. C.; Almeida, M. *Inorg. Chem. Commun.* **2015**, *58*, 87–90, doi:10.1016/j.inoche.2015.06.001.

[100] Kusamoto, T.; Kume, S.; Nishihara, H. *Angew. Chemie - Int. Ed.* **2010**, *49* (3), 529–531, doi:10.1002/anie.200905132.

[101] Tanushi, A.; Kusamoto, T.; Hattori, Y.; Takada, K.; Nishihara, H. *J. Am. Chem. Soc.* **2015**, *137* (20), 6448–6451, doi:10.1021/jacs.5b02118.

[102] Schallenberg, D.; Neubauer, A.; Erdmann, E.; Tänzler, M.; Villinger, A.; Lochbrunner, S.; Seidel, W. W. *Inorg. Chem.* **2014**, *53* (17), 8859–8873, doi:10.1021/ic4031206.

[103] Shin, K. S.; Han, Y. K.; Noh, D. Y. *Bull. Korean Chem. Soc.* **2003**, *24* (2), 235–238, doi:10.5012/bkcs.2003.24.2.235.

[104] Ogura, S.; Idobata, Y.; Zhou, B.; Kobayashi, A.; Takagi, R.; Miyagawa, K.; Kanoda, K.; Kasai, H.; Nishibori, E.; Satoko, C.; Delley, B. *Inorg. Chem.* **2016**, *55* (15), 7709–7716, doi:10.1021/acs.inorgchem.6b01166.

[105] Pintus, A.; Aragoni, M. C.; Bellec, N.; Devillanova, F. A.; Lorcy, D.; Isaia, F.; Lippolis, V.; Randall, R. A. M.; Roisnel, T.; Slawin, A. M. Z.; Woollins, J. D.; Arca, M. *Eur. J. Inorg. Chem.* **2012**, No. 22, 3577–3594, doi:10.1002/ejic.201200346.

[106] Ji, Y.; Hu, L.; Zhang, R.; Li, Y. Z.; Zuo, J. L.; You, X. Z. *Gaodeng Xuexiao Huaxue Xuebao/Chemical J. Chinese Univ.* **2011**, *32* (3), 545–551.

[107] Kusamoto, T.; Takada, K.; Sakamoto, R.; Kume, S.; Nishihara, H. *Inorg. Chem.* **2012**, *51* (22), 12102–12113, doi:10.1021/ic300581a.

[108] McCall, K. L.; Morandeira, A.; Durrant, J.; Yellowlees, L. J.; Robertson, N. *Dalt. Trans.* **2010**, *39* (17), 4138–4145, doi:10.1039/b924660f.

[109] Erdmann, E.; Lütgens, M.; Lochbrunner, S.; Seidel, W. W. *Inorg. Chem.* **2018**, *57* (9), 4849–4863, doi:10.1021/acs.inorgchem.7b02840.

[110] Saito, K.; Nakano, M.; Tamura, H.; Matsubayashi, G. E. *Inorg. Chem.* **2000**, *39* (21), 4815–4820, doi:10.1021/ic0000348.

[111] Eid, S.; Roisnel, T.; Lorcy, D. *J. Organomet. Chem.* **2008**, *693* (16), 2755–2760, doi:10.1016/j.jorganchem.2008.05.021.

[112] Saito, K.; Nakano, M.; Tamura, H.; Matsubayashi, G. *J. Organomet. Chem.* **2001**, *625* (1), 7–12, doi:10.1016/S0022-328X(00)00621-5.

[113] Misaki, Y.; Nishikawa, H.; Fujiwara, H.; Kawakami, K.; Yamabe, T.; Yamochi, H.; Saito, G. *J. Chem. Soc. Chem. Commun.* **1992**, *0* (19), 1408, doi:10.1039/c39920001408.

[114] Zeltner, S.; Dietzsch, W.; Olk, R.-M.; Kirmse, R.; Richter, R.; Schröder, U.; Olk, B.; Hoyer, E. *Chem. Ber.* **1994**, *127* (1), 67–71, doi:10.1002/cber.19941270110.

[115] Bordinhão, J.; Comerlato, N. M.; Cortas, L. C.; Ferreira, G. B.; Howie, R. A.; Wardell, J. L. *Inorganica Chim. Acta* **2010**, *363* (14), 4074–4079, doi:10.1016/j.ica.2010.08.014.

[116] Pullen, A. E.; Olk, R. M. *Coord. Chem. Rev.* **1999**, *188* (1), 211–262, doi:10.1016/S0010-8545(99)00031-4.

[117] Atzori, M.; Morra, E.; Tesi, L.; Albino, A.; Chiesa, M.; Sorace, L.; Sessoli, R. *J. Am. Chem. Soc.* **2016**, *138* (35), 11234–11244, doi:10.1021/jacs.6b05574.

[118] Vacher, A.; Le Gal, Y.; Roisnel, T.; Dorcet, V.; Devic, T.; Barrière, F.; Lorcy, D. *Organometallics* **2019**, doi:10.1021/acs.organomet.9b00485.

[119] Michel, S. L. J.; Goldberg, D. P.; Stern, C.; Barrett, A. G. M.; Hoffman, B. M. *J. Am. Chem. Soc.* **2001**, *123* (20), 4741–4748, doi:10.1021/ja003702x.

[120] Viard, B.; Amaudrut, J.; Sala-Pala, J.; Fakhr, A.; Mugnier, Y.; Moise, C. *J. Organomet. Chem.* **1985**, *292* (3), 403–409, doi:10.1016/0022-328X(85)80226-6.

[121] Köpf, H.; Balz, H. *J. Organomet. Chem.* **1990**, *387* (1), 77–81, doi:10.1016/0022-328X(90)87301-S.

[122] Hori, A.; Kim, Y.; Tahara, K.; Kadoya, T.; Yamada, J. ichi; Kubo, K. *Eur. J. Inorg. Chem.* **2021**, *2021* (11), 1023–1027, doi:10.1002/ejic.202001014.

[123] Bartlett, M. A.; Sundermeyer, J. *Dalt. Trans.* **2020**, *49* (35), 12180–12183, doi:10.1039/d0dt02060e.

[124] Watanabe, L. K.; Wrixon, J. D.; Ahmed, Z. S.; Hayward, J. J.; Abbasi, P.; Pilkington, M.; MacDonald, C. L. B.; Rawson, J. M. *Dalt. Trans.* **2020**, *49* (26), 9086–9093, doi:10.1039/d0dt01678k.

[125] Vitushkina, S. V.; Starodub, V. A. *Bull. Charkiv Natl. Univ. Ukr.* **2009**, *17* (40), 213–221.

[126] Chandrasekaran, P.; Greene, A. F.; Lillich, K.; Capone, S.; Mague, J. T.; Debeer, S.; Donahue, J. P. *Inorg. Chem.* **2014**, *53* (17), 9192–9205, doi:10.1021/ic501273b.

[127] Fourmigué, M. *Coord. Chem. Rev.* **1998**, *178–180*, 823–864, doi:10.1016/S0010-8545(98)00104-0.

[128] Guyon, F.; Jourdain, I. V.; Knorr, M.; Lucas, D.; Monzon, T.; Mugnier, Y.; Avarvari, N.; Fourmigué, M. *Eur. J. Inorg. Chem.* **2002**, *2002* (8), 2026–2033, doi:10.1002/1099-0682(200208)2002:8<2026::AID-EJIC2026>3.0.CO;2-0.

[129] Stephan, D. W. *Inorg. Chem.* **1992**, *31* (21), 4218–4223, doi:10.1021/ic00047a003.

[130] Hartke, K.; Rauschen, F. *Zeitschrift für Naturforsch. B* **1996**, *51* (11), 1611–1617, doi:10.1515/znb-1996-1114.

[131] Misaki, Y.; Nishikawa, H.; Kawakami, K.; Uehara, T.; Yamabe, T. *Tetrahedron Lett.* **1992**, *33* (30), 4321–4324, doi:10.1016/S0040-4039(00)74250-X.

[132] Bard, A. J.; Faulkner, L. R. *Electrochemical Methods: Fundamentals and Applications, 2nd Edition*, 2nd editio.; WILEY-VCH Verlag, 2000.

[133] Guyon, F.; Fourmigué, M.; Audebert, P.; Amaudrut, J. *Inorganica Chim. Acta* **1995**, *239* (1–2), 117–124, doi:10.1016/0020-1693(95)04728-X.

[134] Liedtke, T.; Spannring, P.; Riccardi, L.; Gansäuer, A. *Angew. Chemie* **2018**, *130* (18), 5100–5104, doi:10.1002/ange.201800731.

[135] Krejčik, M.; Daněk, M.; Hartl, F. *J. Electroanal. Chem.* **1991**, *317* (1–2), 179–187, doi:10.1016/0022-0728(91)85012-E.

[136] Camargo, L. C.; Briganti, M.; Santana, F. S.; Stinghen, D.; Ribeiro, R. R.; Nunes, G. G.; Soares, J. F.; Salvadori, E.; Chiesa, M.; Benci, S.; Torre, R.; Sorace, L.; Totti, F.; Sessoli, R. *Angew. Chemie Int. Ed.* **2021**, *60* (5), 2588–2593, doi:10.1002/anie.202009634.

[137] Connelly, N. G.; Geiger, W. E. *Chem. Rev.* **1996**, *96* (2), 877–910, doi:10.1021/cr940053x.

[138] Hodge, S. A.; Buckley, D. J.; Yau, H. C.; Skipper, N. T.; Howard, C. A.; Shaffer, M. S. P. *Nanoscale* **2017**, *9* (9), 3150–3158, doi:10.1039/c6nr10004j.

[139] Bajgur, C. S.; Tikkanen, W.; Petersen, J. L. *Inorg. Chem.* **1985**, *24* (16), 2539–2546, doi:10.1021/ic00210a015.

[140] Tkach, I.; Baldansuren, A.; Kalabukhova, E.; Lukin, S.; Sitnikov, A.; Tsvir, A.; Ischenko, M.; Rosentzweig, Y.; Roduner, E. *Appl. Magn. Reson.* **2008**, *35* (1), 95–112, doi:10.1007/s00723-008-0141-5.

[141] Stoll, S.; Schweiger, A. *J. Magn. Reson.* **2006**, *178* (1), 42–55, doi:10.1016/j.jmr.2005.08.013.

[142] Neese, F. *Wiley Interdiscip. Rev. Comput. Mol. Sci.* **2012**, *2* (1), 73–78, doi:10.1002/wcms.81.

[143] Grimme, S.; Antony, J.; Ehrlich, S.; Krieg, H. *J. Chem. Phys.* **2010**, *132* (15), doi:10.1063/1.3382344.

[144] Grimme, S.; Ehrlich, S.; Goerigk, L. *J. Comput. Chem.* **2011**, *32* (7), 1456–1465, doi:10.1002/jcc.21759.

[145] Dhimitruka, I.; Velayutham, M.; Bobko, A. A.; Khramtsov, V. V.; Villamena, F. A.; Hadad, C. M.; Zweier, J. L. *Bioorganic Med. Chem. Lett.* **2007**, *17* (24), 6801–6805, doi:10.1016/j.bmcl.2007.10.030.

[146] Shchepinov, M. S.; Korshun, V. A. *Chem. Soc. Rev.* **2003**, *32* (3), 170–180, doi:10.1039/b008900l.

[147] Gomberg, M. *J. Am. Chem. Soc.* **1900**, *22* (11), 757–771, doi:10.1021/ja02049a006.

[148] Andersson, S.; Rydbeck, A.; Servin, R.; Wistrand, L.-G.; Radner, F. Heterocyclic methyl free radicals as image enhancing agents. WO1996039367A1, 1996.

[149] Yong, L.; Harbridge, J.; Quine, R. W.; Rinard, G. A.; Eaton, S. S.; Eaton, G. R.; Mailer, C.; Barth, E.; Halpern, H. J. *J. Magn. Reson.* **2001**, *152* (1), 156–161, doi:10.1006/jmre.2001.2379.

[150] Fielding, A. J.; Carl, P. J.; Eaton, G. R.; Eaton, S. S. *Appl. Magn. Reson.* **2005**, *28* (3–4), 231–238, doi:10.1007/BF03166758.

[151] Hintz, H.; Vanas, A.; Klose, D.; Jeschke, G.; Godt, A. *J. Org. Chem.* **2019**, *84* (6), 3304–3320, doi:10.1021/acs.joc.8b03234.

[152] Ratera, I.; Vidal-Gancedo, J.; Maspoch, D.; Bromley, S. T.; Crivillers, N.; Mas-Torrent, M. *J. Mater. Chem. C* **2021**, *9* (33), 10610–10623, doi:10.1039/d1tc02196f.

[153] de Sousa, J. A. Stable perchlorinated trityl radicals on surfaces for molecular (opto)electronics and spintronics, University of Barcelona, 2022.

[154] Ballester, M.; Riera, J.; Castafier, J.; Badía, C.; Monsó, J. M. *J. Am. Chem. Soc.* **1971**, *93* (9), 2215–2225, doi:10.1021/ja00738a021.

[155] Harbridge, J. R.; Eaton, S. S.; Eaton, G. R. *J. Phys. Chem. A* **2003**, *107* (5), 598–610, doi:10.1021/jp021504h.

[156] Eaton, S. S.; Eaton, G. R. **2002**, *19*, 29–154, doi:10.1007/0-306-47109-4_2.

[157] Zhou, Y.; Bowler, B. E.; Eaton, G. R.; Eaton, S. S. *J. Magn. Reson.* **1999**, *139* (1), 165–174, doi:10.1006/jmre.1999.1763.

[158] Takahashi, S.; Van Tol, J.; Beedle, C. C.; Hendrickson, D. N.; Brunel, L. C.; Sherwin, M. S. *Phys. Rev. Lett.* **2009**, *102* (8), 1–4, doi:10.1103/PhysRevLett.102.087603.

[159] Meyer, A.; Jassoy, J. J.; Spicher, S.; Berndhäuser, A.; Schiemann, O. *Phys. Chem. Chem. Phys.* **2018**, *20* (20), 13858–13869, doi:10.1039/c8cp01276h.

[160] Jeschke, G. DeerAnalysis https://epr.ethz.ch/software.html.

[161] Warner, M.; Din, S.; Tupitsyn, I. S.; Morley, G. W.; Stoneham, A. M.; Gardener, J. A.; Wu, Z.; Fisher, A. J.; Heutz, S.; Kay, C. W. M.; Aeppli, G. *Nature* **2013**, *503* (7477), 504–508, doi:10.1038/nature12597.

[162] Bonizzoni, C.; Ghirri, A.; Atzori, M.; Sorace, L.; Sessoli, R.; Affronte, M. *Sci. Rep.* **2017**, *7* (1), 13096, doi:10.1038/s41598-017-13271-w.

[163] Cimatti, I.; Bondì, L.; Serrano, G.; Malavolti, L.; Cortigiani, B.; Velez-Fort, E.; Betto, D.; Ouerghi, A.; Brookes, N. B.; Loth, S.; Mannini, M.; Totti, F.; Sessoli, R. *Nanoscale Horizons* **2019**, *4* (5), 1202–1210, doi:10.1039/C9NH00023B.

[164] Atzori, M.; Tesi, L.; Morra, E.; Chiesa, M.; Sorace, L.; Sessoli, R. *J. Am. Chem. Soc.* **2016**, *138* (7), 2154–2157, doi:10.1021/jacs.5b13408.

[165] Aleksey Kuznetsov. *Metalloporphyrins*; Kuznetsov, A., Ed.; De Gruyter, 2021.

[166] Pereira, M. M.; Dias, L. D.; Calvete, M. J. F. *ACS Catal.* **2018**, 10784–10808, doi:10.1021/acscatal.8b01871.

[167] Jurow, M.; Schuckman, A. E.; Batteas, J. D.; Drain, C. M. *Coord. Chem. Rev.* **2010**, *254* (19–20), 2297–2310, doi:10.1016/j.ccr.2010.05.014.

[168] Gotico, P.; Halime, Z.; Aukauloo, A. *Dalt. Trans.* **2020**, *49* (8), 2381–2396, doi:10.1039/c9dt04709c.

[169] Chandra, S. Porphyrin and Redox Active Ligands-Based Metal Complexes - Studies on Electrocatalytic Activity and Electronic Structure of Redox-Active Compounds, University of Stuttgart, 2021.

[170] Vinck, E.; Van Doorslaer, S. *Phys. Chem. Chem. Phys.* **2004**, *6* (23), 5324–5330, doi:10.1039/b411444b.

[171] Walker, F. A. *Inorg. Chem.* **2003**, *42* (15), 4526–4544, doi:10.1021/ic026245p.

[172] Van Doorslaer, S.; Schweiger, A. *Phys. Chem. Chem. Phys.* **2001**, *3* (2), 159–166, doi:10.1039/b008083g.

[173] Di Valentin, M.; Albertini, M.; Dal Farra, M. G.; Zurlo, E.; Orian, L.; Polimeno, A.; Gobbo, M.; Carbonera, D. *Chem. - A Eur. J.* **2016**, *22* (48), 17204–17214, doi:10.1002/chem.201603666.

[174] Urtizberea, A.; Natividad, E.; Alonso, P. J.; Andrés, M. A.; Gascón, I.; Goldmann, M.; Roubeau, O. *Adv. Funct. Mater.* **2018**, *28* (31), 1–15, doi:10.1002/adfm.201801695.

[175] Yu, C. J.; Krzyaniak, M. D.; Fataftah, M. S.; Wasielewski, M. R.; Freedman, D. E. *Chem. Sci.* **2019**, *10* (6), 1702–1708, doi:10.1039/c8sc04435j.

[176] Graham, M. J.; Zadrozny, J. M.; Shiddiq, M.; Anderson, J. S.; Fataftah, M. S.; Hill, S.; Freedman, D. E. *J. Am. Chem. Soc.* **2014**, *136* (21), 7623–7626, doi:10.1021/ja5037397.

[177] Du, J.-L.; Eaton, G. R.; Eaton, S. S. *J. Magn. Reson. Ser. A* **1996**, *119* (2), 240–246, doi:10.1006/jmra.1996.0079.

[178] Scheidt, W. R.; Mondal, J. U.; Eigenbrot, C. W.; Adler, A.; Radonovich, L. J.; Hoard, J. L. *Inorg. Chem.* **1986**, *25* (6), 795–799, doi:10.1021/ic00226a014.

[179] Wili, N.; Richert, S.; Limburg, B.; Clarke, S. J.; Anderson, H. L.; Timmel, C. R.; Jeschke, G. *Phys. Chem. Chem. Phys.* **2019**, *21* (22), 11676–11688, doi:10.1039/c9cp01760g.

[180] Preiß, S.; Melomedov, J.; Wünsche Von Leupoldt, A.; Heinze, K. *Chem. Sci.* **2016**, *7* (1), 596–610, doi:10.1039/c5sc03429a.

[181] Preiß, S. Gold(II) Porphyrins as Key Intermediates in Novel Artificial Photosynthetic Systems, Johannes Gutenberg-Universität Mainz, 2019.

[182] Cremers, J. Electronic Communication in Heterometallated Porphyrin Oligomers, Springer International Publishing, 2020.

[183] Koseki, S.; Matsunaga, N.; Asada, T.; Schmidt, M. W.; Gordon, M. S. *J. Phys. Chem. A* **2019**, *123* (12), 2325–2339, doi:10.1021/acs.jpca.8b09218.

[184] Shanavas, K. V.; Popović, Z. S.; Satpathy, S. *Phys. Rev. B - Condens. Matter Mater. Phys.* **2014**, *90* (16), 1–9, doi:10.1103/PhysRevB.90.165108.

[185] Herman, F.; Kuglin, C. D.; Cuff, K. F.; Kortum, R. L. *Phys. Rev. Lett.* **1963**, *11* (12), 541–545, doi:10.1103/PhysRevLett.11.541.

[186] Mirzoyan, R.; Kazmierczak, N. P.; Hadt, R. G. *Chem. - A Eur. J.* **2021**, *27* (37), 9482–9494, doi:10.1002/chem.202100845.

[187] Khaetskii, A. V.; Nazarov, Y. V. *Phys. Rev. B - Condens. Matter Mater. Phys.* **2001**, *64* (12), 1253161–1253166, doi:10.1103/physrevb.64.125316.

[188] Schiemann, O.; Heubach, C. A.; Abdullin, D.; Ackermann, K.; Azarkh, M.; Bagryanskaya, E. G.; Drescher, M.; Endeward, B.; Freed, J. H.; Galazzo, L.; Goldfarb, D.; Hett, T.; Esteban Hofer, L.; Fábregas Ibáñez, L.; Hustedt, E. J.; Kucher, S.; Kuprov, I.; Lovett, J. E.; Meyer, A.; Ruthstein, S.; Saxena, S.; Stoll, S.; Timmel, C. R.; Di Valentin, M.; McHaourab, H. S.; Prisner, T. F.; Bode, B. E.; Bordignon, E.; Bennati, M.; Jeschke, G. *J. Am. Chem. Soc.* **2021**, *143* (43), 17875–17890, doi:10.1021/jacs.1c07371.

[189] Lombardi, F.; Lodi, A.; Ma, J.; Liu, J.; Slota, M.; Narita, A.; Myers, W. K.; Müllen, K.; Feng, X.; Bogani, L. *Science (80-.).* **2019**, *366* (6469), 1107–1110, doi:10.1126/science.aay7203.

[190] Lenz, S.; Bader, K.; Bamberger, H.; van Slageren, J. *Chem. Commun.* **2017**, *53* (32), 4477–4480, doi:10.1039/C6CC07813C.

[191] McGuire, J.; Miras, H. N.; Richards, E.; Sproules, S. *Chem. Sci.* **2019**, *10* (5), 1483–1491, doi:10.1039/c8sc04500c.

[192] Dai, Y.-Z. Z.; Dong, B.-W. W.; Kao, Y.; Wang, Z.-Y. Y.; Un, H.-I. I.; Liu, Z.; Lin, Z.-J. J.; Li, L.; Xie, F.-B. B.; Lu, Y.; Xu, M.-X. X.; Lei, T.; Sun, Y.-J. J.; Wang, J.-Y. Y.; Gao, S.; Jiang, S.-D. Da; Pei, J. *ChemPhysChem* **2018**, *19* (22), 2972–2977, doi:10.1002/cphc.201800742.

[193] Poryvaev, A. S.; Gjuzi, E.; Polyukhov, D. M.; Hoffmann, F.; Fröba, M.; Fedin, M. V. *Angew. Chemie - Int. Ed.* **2021**, *60* (16), 8683–8688, doi:10.1002/anie.202015058.

[194] Krumkacheva, O. A.; Timofeev, I. O.; Politanskaya, L. V.; Polienko, Y. F.; Tretyakov, E. V.; Rogozhnikova, O. Y.; Trukhin, D. V.; Tormyshev, V. M.; Chubarov, A. S.; Bagryanskaya, E. G.; Fedin, M. V. *Angew. Chemie Int. Ed.* **2019**, *58* (38), 13271–13275, doi:10.1002/anie.201904152.

[195] Collauto, A.; Mannini, M.; Sorace, L.; Barbon, A.; Brustolon, M.; Gatteschi, D. *J. Mater. Chem.* **2012**, *22* (41), 22272, doi:10.1039/c2jm35076a.

[196] Meyer, V.; Eaton, S. S.; Eaton, G. R. *Appl. Magn. Reson.* **2013**, *44* (4), 509–517, doi:10.1007/s00723-012-0417-7.

[197] Rajca, A.; Kathirvelu, V.; Roy, S. K.; Pink, M.; Rajca, S.; Sarkar, S.; Eaton, S. S.; Eaton, G. R. *Chem. - A Eur. J.* **2010**, *16* (19), 5778–5782, doi:10.1002/chem.200903102.

[198] Bonizzoni, C.; Maksutoglu, M.; Ghirri, A.; van Tol, J.; Rameev, B.; Affronte, M. *Appl. Magn. Reson.* **2022**, doi:10.1007/s00723-022-01505-8.

[199] von Kugelgen, S.; Krzyaniak, M. D.; Gu, M.; Puggioni, D.; Rondinelli, J. M.; Wasielewski, M. R.; Freedman, D. E. *J. Am. Chem. Soc.* **2021**, *143* (21), 8069–8077, doi:10.1021/jacs.1c02417.

[200] Uber, J. S.; Estrader, M.; Garcia, J.; Lloyd-Williams, P.; Sadurní, A.; Dengler, D.; van Slageren, J.; Chilton, N. F.; Roubeau, O.; Teat, S. J.; Ribas-Ariño, J.; Aromí, G.; Lloyd-Williams, P.; Sadurní, A.; Dengler, D.; van Slageren, J.; Chilton, N. F.;

Roubeau, O.; Teat, S. J.; Ribas-Ariño, J.; Aromí, G. *Chem. – A Eur. J.* **2017**, *23* (55), 13648–13659, doi:10.1002/chem.201702171.

[201] Akhmetzyanov, D.; Ching, H. Y. V.; Denysenkov, V.; Demay-Drouhard, P.; Bertrand, H. C.; Tabares, L. C.; Policar, C.; Prisner, T. F.; Un, S. *Phys. Chem. Chem. Phys.* **2016**, *18* (44), 30857–30866, doi:10.1039/C6CP05239H.

[202] Moore, W.; Yao, R.; Liu, Y.; Eaton, S. S.; Eaton, G. R. *J. Magn. Reson.* **2021**, *332*, 107078, doi:10.1016/j.jmr.2021.107078.

[203] Wili, N.; Hintz, H.; Vanas, A.; Godt, A.; Jeschke, G. *Magn. Reson.* **2020**, *1* (1), 75–87, doi:10.5194/mr-1-75-2020.

[204] Ardavan, A.; Bowen, A. M.; Fernandez, A.; Fielding, A. J.; Kaminski, D.; Moro, F.; Muryn, C. A.; Wise, M. D.; Ruggi, A.; McInnes, E. J. L.; Severin, K.; Timco, G. A.; Timmel, C. R.; Tuna, F.; Whitehead, G. F. S.; Winpenny, R. E. P. *npj Quantum Inf.* **2015**, *1* (1), 15012, doi:10.1038/npjqi.2015.12.

[205] Gil-Ramírez, G.; Shah, A.; El Mkami, H.; Porfyrakis, K.; Briggs, G. A. D.; Morton, J. J. L.; Anderson, H. L.; Lovett, J. E. *J. Am. Chem. Soc.* **2018**, *140* (24), 7420–7424, doi:10.1021/jacs.8b03889.

[206] Azarkh, M.; Bieber, A.; Qi, M.; Fischer, J. W. A.; Yulikov, M.; Godt, A.; Drescher, M. *J. Phys. Chem. Lett.* **2019**, *10* (7), 1477–1481, doi:10.1021/acs.jpclett.9b00340.

[207] Akhmetzyanov, D.; Plackmeyer, J.; Endeward, B.; Denysenkov, V.; Prisner, T. F. *Phys. Chem. Chem. Phys.* **2015**, *17* (10), 6760–6766, doi:10.1039/C4CP05362A.

[208] Atzori, M.; Chiesa, A.; Morra, E.; Chiesa, M.; Sorace, L.; Carretta, S.; Sessoli, R. *Chem. Sci.* **2018**, *9* (29), 6183–6192, doi:10.1039/C8SC01695J.

[209] Fernandez, A.; Moreno Pineda, E.; Muryn, C. A.; Sproules, S.; Moro, F.; Timco, G. A.; McInnes, E. J. L.; Winpenny, R. E. P. *Angew. Chemie Int. Ed.* **2015**, *54* (37), 10858–10861, doi:10.1002/anie.201504487.